Dipl.-Ing. Andreas Johann Lesch, BSc

Application of Variational Methods for Field Mapping in Magnetic Resonance Imaging

DOCTORAL THESIS

to achieve the university degree of
“Doktor der technischen Wissenschaften”

submitted to

Graz University of Technology

Supervisor

Univ.-Prof. Dipl-Ing. Dr. techn. Rudolf Stollberger
Institute of Medical Engineering
Graz University of Technology, Austria

2nd Reviewer

Univ.-Prof. Dr. Maxim Zaitsev
Center for Medical Physics and Biomedical Engineering
Medical University of Vienna

Graz, Austria, August 2020

> Iron rusts from disuse; water loses its purity from stagnation... even so does inaction sap the vigor of the mind.
>
> ---
>
> *Leonardo da Vinci (1452 - 1519)*

Abstract

Over the years, magnetic resonance imaging (MRI) has evolved to one of the leading imaging modalities in medical diagnosis, because of its high soft tissue contrast without deposing ionizing radiation. Besides pure morphological imaging, MRI can also provide quantitative or semi-quantitative information about physical and physiological processes or the micro-structure of the tissue, which can serve as biomarker for several diseases. Among others, these are blood flow, diffusion, perfusion, quantitative susceptibility, fat content or tissue relaxation times. The main drawback of MRI is the inherently long acquisition time. To overcome this problem, several strategies were proposed over the years, by improving imaging sequences and data acquisition trajectories to increase the acquired data per time. With this development in combination with improved hardware, the physiological limits in terms of peripheral nerve stimulation and RF energy deposition were reached.

Another way to accelerate the MR data acquisition is to reduce the amount of acquired data below the Nyquist limit and to reconstruct the image using mathematical methods. Because of the ill-posedness of this inverse problem, regularization becomes necessary to stabilize the solution of the reconstruction. The theory of variational methods is perfectly suited for this purpose.

Some applications have very high requirement according the homogeneity of the fields necessary to obtain an MRI signal. These are the static magnetic field B_0 and the radio frequency (RF) field B_1. Careful coil design, low manufacturing tolerances, and shimming approaches for B_0 and B_1 lead already to very homogeneous field distributions, but the magnetic and electric properties of biological tissue lead to field distortions which are specific for a certain patient. To correct for influences arising from that, filed mapping becomes necessary.

This thesis covers the physical background of field inhomogeneities in B_0 and B_1, as well as the most important mapping methods and shimming approaches to increase their homogeneity. Moreover, the mathematical background of image reconstruction is described, as well as a deviation of the most important regularization functionals and their numerical solution. This thesis also considers the questions, how variational methods can be applied to either increase the accuracy of an acquired field map or to reconstruct highly accurate field maps from highly undersampled data. For this purpose, two different algorithms are described, one to gain highly accurate B_0 maps dedicated for the separation of fat and water signal components and the other one for the reconstruction of B_1^+ field maps from highly accelerated Bloch-Siegert data. Several examples are shown for phantom and in-vivo measurements at 3 T and 7 T.

Keywords: magnetic resonance imaging (MRI), field mapping, B_1 mapping, B_0 mapping, water/fat separation, variational methods, Bloch-Siegert shift imaging

Kurzfassung

Die Magnetresonanz Tomographie (MRT) hat sich über die Jahre zu einer der führenden Bildgebungs-Modalitäten in der medizinischen Diagnose entwickelt, aufgrund des hohen Weichteilkontrasts ohne die Verwendung ionisierender Strahlung. Neben der reinen morphologischen Bildgebung bietet die MRT auch eine Reihe von quantitativen und semi-quantitativen Informationen über physikalische und physiologische Prozesse oder die Gewebsmikrostruktur, die als Biomarker für verschiedene Krankheiten dienen können. Unter anderem sind dies: Blutfluss, Diffusion, Perfusion, quantitative Suszeptibilität, Fettgehalt oder Gewebsrelaxationszeiten. Der größte Nachteil dieser Technologie ist die messprinzipbedingte hohe Akquisitionszeit. Um dieses Problem zu lösen wurden über die Jahre etliche Strategien vorgestellt, die vorrangig die Bildgebungssequenzen und die Akquisitionstrajektorien verbessern um die aufgenommenen Daten pro Zeiteinheit zu vergrößern. Diese Entwicklung führte in Kombination mit verbesserter Hardware dazu, dass die physiologischen Grenzen für periphere Nervenstimulationen und HF-Energiedeposition im Gewebe erreicht wurden.

Die MR Datenakquisition kann auch über eine Reduktion der aufgenommenen Daten unter die Nyquistrate beschleunigt werden, wobei das Bild unter Verwendung mathematischer Methoden rekonstruiert werden muss. Da dieses inverse Problem äußerst schlecht gestellt sein kann, wird die Verwendung von Regularisierung notwendig um das Rekonstruktionsergebnis zu stabilisieren. Zu diesem Zweck ist die Theorie der varationellen Methoden hervorragend geeignet.

Viele Anwendungen stellen hohe Anforderungen an die Homogenität der verwendeten Felder, die notwendig sind um ein MR Signal zu erzeugen. Dies sind das statische Magnetfeld B_0 und das Hochfrequenzfeld (HF) B_1. Sorgfältiges Spulendesign, geringe Fertigungstoleranzen und Shimming Ansätze für B_0 und B_1 führen bereits zu äußerst homogenen Feldverteilungen, aber die elektrischen und magnetischen Eigenschaften von biologischem Gewebe führen zu Feldverzerrungen, die auch noch patientenabhängig sind.

Um die daraus resultierenden Einflüsse zu korrigieren, ist es notwendig die Feldverteilung zu messen.

Diese Arbeit umfasst den physikalischen Hintergrund der Entstehung von Feldinhomogenitäten für B_0 und B_1, sowie die wichtigsten Methoden zu deren Messung und die wichtigsten Ansätze deren Homogenität zu erhöhen (Shimming). Weiters wird der mathematische Hintergrund der Bildrekonstruktion beschrieben, sowie die wichtigsten Regularisierungsfunktionale und deren numerische Lösung hergeleitet. Diese Arbeit beschäftigt sich mit der Frage, wie varationelle Methoden angewendet werden können um entweder die Genauigkeit einer akquirierten "field map" zu erhöhen oder eine sehr genaue "field maps" aus hoch unter-abgetasteten Daten zu rekonstruieren. Zu diesem Zweck werden zwei Algorithmen beschrieben, einer um die Genauigkeit der B_0 Schätzung zu erhöhen, speziell zugeschnitten für die Anwendung um Fett und Wasser Signalkomponenten zu trennen und ein zweiter für die Rekonstruktion von B_1^+ maps aus hoch unter-abgetasteten Daten der Bloch-Siegert Methode. Einige Beispiele für Phantom- und in-vivo Messungen auf 3 T und 7 T werden vorgestellt.

Schlüsselwörter: Magnetresonanz Tomographie (MRT), Feld mapping, B_1 mapping, B_0 mapping, Wasser/Fett Signal Trennung, variationelle Methoden, Bloch-Siegert shift imaging

Affidavit

I declare that I have authored this thesis independently, that I have not used other than the declared sources/resources, and that I have explicitly indicated all material which has been quoted either literally or by content from the sources used.
The text document uploaded to TUGRAZonline is identical to the present doctoral thesis.

Date

Signature

Eidesstattliche Erklärung

Ich erkläre an Eides statt, dass ich die vorliegende Arbeit selbstständig verfasst, andere als die angegebenen Quellen/Hilfsmittel nicht benutzt, und die den benutzten Quellen wörtlich und inhaltlich entnommenen Stellen als solche kenntlich gemacht habe.
Das in TUGRAZonline hochgeladene Textdokument ist mit der vorliegenden Dissertation identisch.

Datum

Unterschrift

Acknowledgments

This work was carried out on the "Institute of Medical Engineering" at "Graz University of Technology" during the years from 2014 to 2020. Now it is time to say "thank you" to those people who supported me during this time, making this thesis possible.

First and foremost I would like to thank my supervisor Prof. Stollberger, giving me the opportunity to do my PhD thesis, introducing me to the interesting field of MRI and his support over the last years. It was a pleasure for me to work in this great team, with many interesting an talented people. I also want to express my gratitude to my collaboration partners from the "Institute of Mathematics and Scientific Computing" (University of Graz) Martin Holler and Kristian Bredies for their very important contribution to this work and the fruitful collaboration. I also want to thank my further coauthors Matthias Schlögl, Christoph Aigner, Clemens Diwoky, Stefan Spann, Andreas Petrovic, Tilman Sumpf and Rudolf Stollberger for their contributions. Moreover, I want to thank Martin Söllradl, Bernhard Neumayer, Oliver Maier, Christina Graf and Stefan Spann for our strong collaboration and joint research output.

I want to thank my former colleagues Clemens Diwoky, Peter Opriessnig, Markus Kraiger, Andreas Petrovic, Christoph Aigner, Matthias Schlögl and Johannes Strasser supporting me doing my first steps in this field and their patience and fruitful discussions. Furthermore, I want to thank my colleagues on the "Institute of Medical Engineering": Christina Graf, Markus Bödenler, Oliver Maier, Stefan Spann, Christian Gössweiner, Isabella Radl, Hermann Scharfetter, and Ingmar Middelhoff for the many hours of interesting and highly productive discussions and providing a relaxed and inspiring working atmosphere. I am thankful for the great time we had together.

I also want to thank our collaboration partners from the "Ludwig Boltzmann Institute for Clinical Forensic Imaging": Martin Urschler, Bernhard Neumayer, Alexander Bornik, Bridgette Webb and Thomas Widek; from the "Neuroimaging Research Unit" (Medical University of Graz): Martin Söllradl, Lukas Pirpamer, Johannes Strasser, Christoph

Birkl, Stefan Ropele, and Christian Langkammer; “Institute of Mathematics and Scientific Computing” (University of Graz): Martin Holler, Kristian Bredies, Armin Rund, Christian Clason, and Gundolf Haase; from the “Institute of Psychology” (University of Graz): Karl Koschutnig and Thomas Zussner; from the “Institute of Computer Graphics and Vision” (Graz University of Technology): Kerstin Hammernik and Thomas Pock for the good collaboration and many inspiring discussions.

Last but not least, I also want to thank Daniela Agrinz for her administrative support and organizing our trips to Buschenschank in summer; and Walter Gmeindl for his technical support. Very special thanks goes to Christina Graf and my friend Muaaz Abdul Hadi for proofreading this thesis.

Finally, I want to express my deepest gratitude to my parents Anna and Walter and my sister Susanne, supporting me during my whole life. Without you, it would have not been possible to finish my studies and reach this point. I would like to thank my girlfriend Christina for everything and her deprivations during the last months.

Contents

1 Introduction and Motivation **1**
1.1 Introduction 1
1.2 Contribution and Outline 5

2 Physical Principles of Magnetic Resonance Imaging and Field Mapping **7**
2.1 Signal Generation and involved Fields 7
2.1.1 Nuclear Spin 8
2.1.2 Macroscopic Magnetization and Boltzmann Distribution 10
2.1.3 Classical Description 11
2.1.4 RF–Excitation and Rotating Coordinate System 13
2.1.4.1 Polarization of the B_1^+ Field 16
2.1.5 Relaxation and Bloch-Equations 18
2.1.5.1 Longitudinal Relaxation T_1 18
2.1.5.2 Transverse Relaxation T_2 18
2.1.6 Receiving Signal and SNR 20
2.1.7 Spatial Encoding 22
2.1.7.1 Slice Selective Excitation 22
2.1.7.2 Fourier Encoding and k-space 23
2.1.8 Imaging Sequences 26
2.1.8.1 Gradient Echo Sequence (GRE) 26
2.1.8.2 Spin Echo Sequence (SE) 26
2.1.8.3 Echo Planar Imaging (EPI) 28
2.2 Homogeneity Limitations of the B_0 Field 29
2.2.1 Field Generation – Technical Limits of Homogeneity 29
2.2.2 Influence of Matter on the Magnetic Field Homogeneity 30
2.2.2.1 Material dependent Influence – Magnetic Susceptibility χ . 31

2.2.2.2 Shape dependent Influence – Demagnetization Factor ξ . . 33
2.2.3 Influence on the MR-Signal 38
2.2.3.1 Spatially varying Signal Phase 38
2.2.3.2 Geometric Distortions and Echo Shifting 38
2.2.3.3 Signal Loss due to Dephasing 41
2.2.4 Spatial Behavior of the B_0 Field 42
2.2.5 Active Shimming 43
2.3 Homogeneity Limitations of the B_1 field 46
2.3.1 Technical Limitations – Transmit/Receive Coils 46
2.3.2 Influence of Matter on the RF Field 49
2.3.3 Spatial behavior of the B_1 Field 52
2.3.4 Energy Deposition – Specific Absorption Rate (SAR) 53
2.3.5 Influence on the MR Signal 54
2.3.6 B_1 Shimming 55
2.3.7 Combination of Signals from Phased Array Coils 57
2.4 Mapping the Static Magnetic Field – B_0 Mapping 59
2.4.1 Phase Unwrapping 60
2.4.2 Influence of Echo Time and Chemical Shift 61
2.4.3 Influence due to Eddy-Currents and Hardware Imperfections 62
2.5 Mapping the RF Field – B_1^+ Mapping 63
2.5.1 Mapping the Magnitude of the B_1^+ Field 64
2.5.1.1 Double Angle Method (DAM) 64
2.5.1.2 Stimulated Echo – Spin Echo Imaging (STESE) 66
2.5.1.3 Actual Flip-Angle Imaging (AFI) 67
2.5.1.4 Saturated Turob FLASH (satTFL) 68
2.5.1.5 180° Signal Null 69
2.5.1.6 Dual Refocusing Echo Acquisition Mode (DREAM) 70
2.5.1.7 Phase Imaging 73
2.5.1.8 Orthogonal Alpha 74
2.5.1.9 Hyperbolic Secant 75
2.5.1.10 Bloch–Siegert Shift Imaging (BS) 77
2.5.2 Mapping the Phase of the B_1^+ Field 81
2.5.2.1 Absolute Phase of the B_1^+ Field 81
2.5.2.2 Relative Phase of the B_1^+ Field between Transmit Channels 82

3 Basic Principles of MR-Image Reconstruction **85**
3.1 Accelerated MR Data Acquisition and Parallel Imaging 86
3.1.1 General 86
3.1.2 Parallel Imaging 88
3.1.2.1 Sensitivity Encoding (SENSE) 91
3.2 Image Reconstruction as an Optimization Problem – Variational Methods . 92

3.2.1 The inverse Problem in MRI 93
3.2.2 Probabilistic Point of View 94
3.2.3 The MR Forward/Backward Operator 95
3.2.4 Incorporation of Prior Knowledge – Regularization 97
3.2.4.1 Tikhonov Regularization 97
3.2.4.2 H_1 – Regularization 97
3.2.4.3 Total Variation (TV) 98
3.2.4.4 Total Generalized Variation (TGV) 98
3.2.5 Numerical Solution 99
3.2.5.1 Gradient based Minimization – Steepest Descend and Conjugate Gradient 100
3.2.5.2 Primal Dual 102
3.2.6 Convexity 105
3.2.7 Determination of Receive Coil Sensitivity Profiles 106
3.2.8 Iterative Image Reconstruction and Compressed Sensing 108
3.3 Variational Methods in Field Mapping 109

4 Applications **111**
4.1 Chemical Shift Imaging (Water/Fat Separation) 112
4.1.1 Physical Principles of Water/Fat Separation 112
4.1.2 Signal Model and Fat Quantification 114
4.1.3 Methods for Water/Fat Signal Separation 119
4.1.3.1 Initially proposed Two-Point Dixon 119
4.1.3.2 Three-Point / Multi-Point Dixon Methods 120
4.1.3.3 Region Growing based Methods 122
4.1.3.4 Iterative Decomposition and Variants of IDEAL 123
4.1.3.5 General Aspects 125
4.1.3.6 Recent Developments 125
4.2 Quantitative MRI 134

5 Bloch–Siegert based B_1^+ Mapping **137**
5.1 Robust Implementation of 3D Bloch-Siegert B_1^+ Mapping 140
5.1.1 Methods 140
5.1.2 Results 141
5.1.3 Discussion 142
5.1.4 Conclusion 143
5.2 Highly accelerated 3D Bloch-Siegert B_1^+ Mapping 143
5.2.1 Theory 143
5.2.1.1 Bloch-Siegert Approach for B_1^+ Mapping 143
5.2.1.2 Variational BS Reconstruction from highly subsampled Data 144
5.2.2 Methods 146

5.2.2.1 Implementation . . . 146
5.2.2.2 Validation and parameter optimization . . . 147
5.2.3 Results . . . 149
5.2.4 Discussion . . . 160
5.2.5 Conclusions . . . 163
5.3 3D Bloch-Siegert EPI B_1^+ Mapping . . . 163
5.3.1 Methods . . . 163
5.3.2 Results . . . 165
5.3.3 Discussion and Conclusion . . . 166
5.4 Highly accelerated 3D Bloch Siegert B_1^+ Mapping at 7T . . . 167
5.4.1 Theory and Methods . . . 167
5.4.2 Results and Discussion . . . 170
5.4.3 Conclusion . . . 172

6 Chemical Shift based Fat-Water Separation using a Variational Approach for B_0 Correction **175**
6.1 Theory and Methods . . . 176
6.2 Results . . . 181
6.3 Discussion . . . 183

7 Summary, Conclusion and Outlook **193**
7.1 Highly accelerated B_1^+ Mapping . . . 193
7.2 Chemical Shift based Fat-Water Separation . . . 195
7.3 Conclusion and Outlook . . . 196

A Appendix I **199**
A.1 Spherical Harmonics . . . 199
A.2 Definitions . . . 204
A.2.1 Rotation Matrices . . . 204
A.2.2 Norms . . . 204
A.2.3 Finite Differences Operators . . . 205
A.2.4 Discrete Gradient Operators . . . 206
A.2.5 Analytic Gradient Operators . . . 208
A.2.6 Convex Optimization . . . 208

B List of Acronyms **211**

C List of Symbols **215**

D List of Publications **223**

Bibliography **227**

List of Figures

2.1 Schematic representation of the Zeeman energy splitting in a magnetic field. 10
2.2 Net magnetization due to spin orientation with and without magnetic field. 12
2.3 Classical description of the interaction of the spin magnetic moment in an external magnetic field. 12
2.4 RF excitation in the static and rotating coordinate system and transverse magnetization after excitation. 14
2.5 Effective magnetic field: Excitation in the presence of a resonance offset. . . 17
2.6 Longitudinal T_1 and transverse relaxation T_2. 19
2.7 Slice selective excitation, relation between slice selective gradient, RF pulse bandwidth and slice thickness. 24
2.8 Sequence diagram and corresponding k-space trajectory for a gradient echo sequence. 27
2.9 Sequence diagram and corresponding k-space trajectory for a spin echo sequence. 27
2.10 Sequence diagram and corresponding k-space trajectory for an EPI sequence. 28
2.11 Different behavior of paramagnetic and diamagnetic materials. 31
2.12 Demagnetization factor for ellipsoids of revolution depending on their aspect ratio. 34
2.13 Surface plot for field distortions caused by a sphere and a long cylinder with a susceptibility difference equal to that between air and tissue with different orientations. 36
2.14 Contour plot and field lines for field distortions caused by a sphere and a long cylinder with a susceptibility difference equal to that between air and tissue. 37
2.15 Geometric distortions for a TSE and GRE sequence with different readout bandwidths. 39

2.16 Geometric distortions for TSE and EPI sequence under an externally applied field gradient for different phase encoding directions. 40
2.17 Measured influence on the field distribution of first and second order spherical harmonic shimming. 44
2.18 Law of Biot-Savart for a loop coil. 47
2.19 Schematic representation of the currents in a birdcage coil. 48
2.20 Comparison of the field distributions generated by a birdcage and a surface coil in air. 49
2.21 Simulated RF field distribution for different permittivity and conductivity values in a cylinder phantom. 50
2.22 Simulated RF field distribution in magnitude and phase for 3 T and 7 T. . . 51
2.23 Simulated RF field distribution for discontinuous permittivity and conductivity distributions in a cylinder phantom. 52
2.24 Coil combined images with different methods in magnitude and phase. . . . 59
2.25 Sequence diagram of the stimulated echo – spin echo imaging method. . . . 66
2.26 Sequence diagram of the AFI method. 67
2.27 Sequence diagram of the DREAM method 70
2.28 Theoretical position of the magnetization vector in the transverse plane for the “phase imaging” method. 73
2.29 Sequence diagram for the hyperbolic secant method. 76
2.30 Sequence diagram of the BS shift method and the corresponding field configuration. 77

3.1 Visualization of the general relation between k-space and image space in terms of FOV, image resolution Δx and Δy, k-space resolution Δk_x and Δk_y, and the maximum acquired spatial frequency $k_{x,max}$ and $k_{y,max}$, as well as the concepts of reduced resolution and rectangular FOV. 87
3.2 Effect of aliasing for different acceleration factors in the regular Cartesian case. 88
3.3 Coil images, receive coil sensitivity maps and k-space data of each receive coil from 5 exemplary channels from a 64-channel head coil data set. 89
3.4 Visualization of the principle of SENSE for 3 receive coils and $R_{\text{acc}} = 2$. . . 91
3.5 Comparison of the convergence rate of steepest descent and CG on an arbitrary 2D problem. 101
3.6 1D example of convex and non-convex function 106

4.1 FID signal for voxel containing fat and water. 113
4.2 Sequences used to encode the fat water shift. 114
4.3 Fat molecule with its different chemical groups as well as the resulting fat spectrum as simulation and measurement. The spectral components are referred to its originating chemical group. 118

4.4 Residuum of fat water signal for equal and non equal echo spacing. 126
4.5 T_1 map gained with VFA with and without B_1 correction and the corresponding B_1 map. 135

5.1 Schematic illustration of sequential and interleaved sampling scheme. 140
5.2 Unwrapped phase drift measured at the end of 3 regular measurement days over a time period of 6 h. 141
5.3 Comparison between BS based B_1^+ maps obtained with sequential and interleaved acquisition as central slice of a 3D data set. 141
5.4 2D BS B_1^+ maps with different delay times between positive and negative resonance offset acquisition compared to a DAM reference. 142
5.5 Schematic representation of the block pattern and the irregular pattern with Gaussian density function. 148
5.6 Reconstruction results for retrospectively subsampled data compared to zero padding and a fully sampled reference for different pattern sizes. 150
5.7 Error histogram for retrospectively subsampled data for different pattern sizes compared to zero padding. 152
5.8 Reconstruction error depending on the regularization parameters λ_2 and σ for different pattern sizes. 153
5.9 Reconstruction results and error maps for retrospectively subsampled data for different undersampling patterns with equal acceleration. 154
5.10 Reconstruction results and corresponding error maps for prospectively subsampled data in head and knee for two different pattern sizes. 155
5.11 Zero padded results and corresponding error maps for prospectively subsampled data in head and knee for two different pattern sizes. 156
5.12 Reconstruction results for prospectively subsampled data in a liver data set for different pattern sizes compared to zero padding. 157
5.13 Reconstruction results and corresponding error maps for retrospectively undersampled data in the head for four different pattern sizes, with coil sensitivity maps estimated directly from the undersampled data. 158
5.14 Intermediate reconstruction results given as magnitude and phase after the first step, the TGV part, and after the second step, the H_1 part of the reconstruciton for a block pattern size of 12×4. 160
5.15 Reconstruction result for prospectively subsampled data for a cylindrical object placed close to the rod of a small animal birdcage coil, leading to stronger field variations. 162
5.16 Sequence diagram for the BS EPI-SE sequence. 164
5.17 Resulting B_1^+ map obtained with BS SE-EPI acquisition compared to a more robust GRE acquisition with difference map. 165

5.18 Resulting B_1^+ maps for the retrospectively undersampled BS SE-EPI data using different block pattern sizes, obtained with zero padding and the two step reconstruction approach. Results are compared to a fully sampled reference. 166
5.19 B_1^+ map in µT measured in a spherical phantom at 7 T. Reconstruction results for retrospectively subsampled data are compared to zero padding and a fully sampled reference for different pattern sizes. 168
5.20 B_1^+ map in µT from an in-vivo measurement at 7 T. Reconstruction results for retrospectively subsampled data are compared to zero padding and a fully sampled reference for different pattern sizes. 169
5.21 Error histogram for the retrospectively subsampled in-vivo dataset acquired at 7 T compared to the fully sampled reference and zero padding. 170
5.22 B_1^+ map in µT from an in-vivo measurement at 7 T from 3 different subjects. Reconstruction results for retrospectively subsampled data are compared a fully sampled reference (first row) for two different pattern sizes. 173

6.1 Visualization of the root finding problem and the corresponding convex relaxation of the problem to gain solvability. 177
6.2 Fat fraction, frequency offset due to ΔB_0 inhomogeneity, fat and water image are shown for the acquired dataset. 181
6.3 Fat fraction, frequency offset due to ΔB_0 inhomogeneity, fat and water image are shown for dataset 7 of the ISMRM fat/water challenge 2012. 182
6.4 Fat fraction, frequency offset due to ΔB_0 inhomogeneity, fat and water image are shown for dataset 8 of the ISMRM fat/water challenge 2012. 183
6.5 Provided reference fat fraction maps and the obtained results for fat fraction maps, field maps and the fat and water images with the proposed TGV regularized algorithm for the datasets 1–9 of the ISMRM fat water challenge of 2012. 187
6.6 Provided reference fat fraction maps and the obtained results for fat fraction maps, field maps and the fat and water images with the proposed TGV regularized algorithm for the datasets 10–17 of the ISMRM fat water challenge of 2012. 188
6.7 Provided reference fat fraction maps and the obtained results with the proposed TGV regularized algorithm with different levels of additive complex Gaussian noise for the datasets 1–9 of the ISMRM fat water challenge of 2012. 189
6.8 Provided reference fat fraction maps and the obtained results with the proposed TGV regularized algorithm with different levels of additive complex Gaussian noise for the datasets 10–17 of the ISMRM fat water challenge of 2012. 190

6.9 ΔB_0 maps obtained with the proposed TGV regularized algorithm with different levels of additive complex Gaussian noise for the selected datasets of the ISMRM fat water challenge of 2012. 191
6.10 Boxplot of the fat fraction deviation for the noise analysis without noise and with 5 different levels of additive Gaussian noise using all datasets provided by the ISMRM fat water challenge of 2012. 192

A.1 Spherical harmonics shown on the surface of a sphere for order $l \leq 3$. . . . 202
A.2 Spherical harmonics shown as cross section in Cartesian coordinates for order $l \leq 3$. 203

List of Tables

2.1 Spin quantum number, gyromagnetic ratio and the average tissue concentration for biologically relevant nuclei. 10
2.2 Magnetic susceptibility values and mass density for some biological relevant materials. 33

4.1 Spectral position of 9 different fat components and their chemical group, which are summarized to the usually modeled 6 main peaks. 115
4.2 Spectral position and relative contribution of the 6 main fat peaks in %, as well as their resonance offset in Hz relative to water at 3 T. For some peaks also the T_1 and T_2 relaxation time constants are given. 116

5.1 MAE, medAE and $q_{99\%}$ errors for retrospectively subsampled data for different pattern sizes compared to zero padding. 152
5.2 Error measures MAE, medAE and$q_{99\%}$ are given for reconstruction results obtained with the proposed variational reconstruction approach for "individually optimized regularization parameters", "globally optimized regularization parameters" and coil sensitivity maps estimated directly from the undersampled data. 159
5.3 MAE, medAE and $q_{99\%}$ errors for retrospectively subsampled data acquired with the BS SE-EPI sequence for different pattern sizes compared to zero padding. 167
5.4 MAE, medAE and $q_{90\%}$ inside the cranial bone structure of the in-vivo dataset acquired at 7 T using different block sizes, obtained with the proposed reconstruction algorithm compared to zero padding. 171
5.5 MAE, medAE and $q_{90\%}$ inside the cranial bone structure of three different subjects acquired at 7 T using different block sizes, obtained with the proposed reconstruction algorithm. 174

6.1 Used values for the parameters in the fat signal model from the ISMRM fat water challenge 2012. 177
6.2 Parameters for of the datasets served as test cases for the ISMRM fat water challenge 2012. 179
6.3 Scoring values $\mathcal{S}$ for the datasets 1–12 of the ISMRM fat water challenge of 2012 for the results obtained with the proposed TGV regularized algorithm and a comparison to those obtained with 11 state of the art algorithms. . . 185
6.4 Scoring values $\mathcal{S}$ for the datasets 13–17 of the ISMRM fat water challenge of 2012 and a mean value over all datasets for the results obtained with the proposed TGV regularized algorithm and a comparison to those obtained with 11 state of the art algorithms. 186

A.1 Expressions for spherical harmonics functions given in Cartesian and spherical polar coordinates up to 3^{rd} order. 201

1

Introduction and Motivation

> Genius is one percent inspiration and ninety-nine percent perspiration.
>
> *Thomas Edison*

Contents

1.1 Introduction 1
1.2 Contribution and Outline 5

1.1 Introduction

Since the 1980s, Magnetic Resonance Imaging (MRI) established as a powerful tomographic imaging modality in clinical practice. Compared to the x-ray based Computer Tomography (CT), the main advantages of *MRI* is the absence of ionizing radiation making this technology non-invasive. Also, it gives a much better soft tissue contrast. Over the years continuous improvements in hardware, sequence design, and image reconstruction led to higher resolutions with better Signal-to-Noise Ratio (SNR) in a shorter acquisition time. Besides the pure morphological imaging with different contrasts, the development also led to a variety of different methods enabling the possibility to investigate different physical and physiological quantities. These quantities are an important source of information in clinical research and for the diagnosis of many diseases, which cannot be provided by any other imaging modality. For example, Diffusion Weighted Imaging (DWI) [44, 171, 298] or Diffusion Tensor Imaging (DTI) [5, 10] enables the possibility to measure the micro-structural orientation of, e.g., axon fibers with diameters in the range of µm; Arterial Spin Labeling (ASL) [3, 66] which is a method to quantify the perfusion in a certain tissue without contrast agents; blood flow velocity which is used in Phase Contrast Angiography (PCA) [74, 224, 310] or functional MRI (fMRI) [164] where the signal is proportional to the activity in a certain brain region. Further examples are Quantitative Susceptibility Mapping (QSM) [316, 330] or fat/water separation (chemical-shift imaging) [67, 239], where the signal is separated in its water and fat content according their shift in resonance (Larmor) frequency.

To generate an *MRI* signal, two different magnetic fields are necessary: The static magnetic field (B_0 field) and the Radio Frequency (RF) field (B_1 field) with a frequency that is matched to the Larmor-frequency of the investigated nucleus. From the macroscopic point of view, the B_0 field leads to a partial alignment of the magnetic moments in the observed nuclei (usually hydrogen) along the direction of the B_0 field, resulting in a net magnetization along that direction. Furthermore, the magnetic moments start to precess around this direction with a frequency (Larmor frequency) proportional to the field strength and the nucleus dependent gyromagnetic ratio γ. If the frequency of the B_1 field is matched to the Larmor frequency, it deflects the net magnetization out of its equilibrium direction resulting in a coherent precession in the transverse plane perpendicular to the main field direction, which induces a measurable signal in properly oriented receive coil. [104]

Because the resonance frequency depends on the B_0 field strength, the spatial homogeneity requirements on the magnet hardware are very high. Differences in field strength of only 10 ppm would change the resonance frequency by $\approx 1.2\,\mathrm{kHz}$ (at 3 T), which is already a large value for many applications. Modern *MRI* systems can reach a peak to peak homogeneity in a spherical volume with a diameter of 45 cm lower then 5 ppm and lower than 2 ppm for a diameter of 30 cm [120, Part I.]. These values are already very impressive and can only be reached with an enormous effort in designing the supra-conducting main field coil and the static and dynamic shim hardware. In standard morphological imaging, the achieved homogeneity is sufficient to generate high quality images in different anatomical regions. However, some applications have much stronger requirements on the main field homogeneity such as chemical shift imaging (fat/water separation) [67, 239] or *QSM* [316, 330]. The different chemical environment of hydrogen in fat and water leads to different resonance frequencies, which are 3.5 ppm apart (chemical shift). The simplest way to separate these two signal components is to acquire an in-phase and an opposed-phase echo. The sum and the difference of these two signals result in the pure water or pure fat signal, respectively [67]. If the additional main field inhomogeneity is greater then half the chemical shift, a water signal appears as a fat signal and vice versa, which leads to so called fat water swaps. The above mentioned peak to peak field deviation of 2 ppm in the 30 cm sphere is already in that range. Beside these technical sources, the patient itself introduces additional inhomogeneities due to discontinuous susceptibility variations along tissue borders; most problematic are air/tissue interfaces, which are typically in the range of a few ppm. If an accurate B_0 field map is available, the adverse effects can be corrected to a certain degree e.g. to remove the unwanted fat water swaps.

Also, the B_1 field suffers from inhomogeneous distribution over the Field of View (FOV), which is basically a result of the interaction of the *RF* field with the biological tissue. Due to the high frequency, eddy currents are induced inside the tissue which consists of displacement and conducting currents depending on the conductivity σ and permitivity ϵ distribution inside the body. These currents interact with the incident field and alter the effectively "seen" field in a certain voxel, leading to an inhomogeneous distribution. The situation gets worse, if the main field strength and with that the corresponding Larmor frequency increases. The increasing frequency leads to a reduction in wavelength, which is about 15 cm at the maximum available clinical field strength of 7 T, being in the range of the dimension of the usually examined anatomy e.g. the head. If the wavelength is smaller than the object of interest, standing wave phenomena can occur which can lead to a complete cancellation of the B_1 field at certain points. Currently the highest field strength for a human system is 10.5 T (2018) and a system with 11.7 T is under construction [165], which makes the problem more severe. The achieved flip angle, which is very important for image contrast, is proportional to the magnitude of the actual B_1 field reached at a certain position in space. Inhomogeneities in the B_1 field lead to an inhomogeneous flip angle distribution, which is responsible for a very inhomogeneous image contrast and introduces modeling errors in several applications related to quantitative MRI (qMRI) in which the fitting model depends on the flip angle [65, 257]. To correct these errors, an accurate mapping of the B_1 field distribution is necessary. If more than one transmit channel is available (parallel transmit (pTX) systems) and the magnitude along with the phase of each channel can be controlled independently, then this inhomogeneities can be balanced out to a certain degree, which is called B_1 shimming [149, 303, 337]. Nevertheless, for the calibration of such a system the actual subject dependent magnitude and phase of the individual B_1 field distributions of each channel must be measured in advance.

In contrast to other imaging modalities, *MRI* is a quite slow technique, because data is acquired successively line by line with a certain Repetition Time (TR) which can be in the order of seconds. Over the years many things were done to reduce the acquisition time in *MRI* examinations by the development of faster and more effective sequences. A few developments are worth to mention here such as Multiple Spin Echo (MSE) [78] or Turbo Spin Echo (TSE) [119] where the signal is refocused many times in a Spin Echo (SE) sequence [107], interleaved acquisition of different slices in a volume to make use of the waiting time during a *TR* or imaging in a kind of steady state where no full relaxation of the magnetization is needed to reduce the *TR* as it is done in spoiled Gradient Recalled Echo (GRE) [105] or balanced Steady State Free Precession (bSSFP) [112, 338] type sequences. For very special applications this even led to the development of a sequence where the whole data space (k-space) is acquired after a single excitation by continuous refocusing the signal with gradients of different polarity the so called Echo Planar Imaging (EPI) sequence [210]. This sequence is very prone to artifacts which can be corrected to a certain degree. Furthermore, the requirements on the imaging hardware concerning timing, B_0 field homogeneity, gradient linearity and eddy current compensation are very high.

Besides acceleration through faster and more efficient data acquisition, people started to develop methods to reconstruct images from under-sampled data. According to Shannon's and Nyquist's sampling theorem [223, 263, 264] for a given *FOV* and resolution, a minimum amount of data has to be acquired to guarantee a unique reconstruction. If less data is acquired it is called under-sampling. In the Cartesian case e.g. a 2-fold acceleration is reached by leaving out every second line in k-space, which leads to artifacts known as back-folding. The first methods used to reconstruct artifact free images out of under-sampled data are know as Parallel Imaging (PI) where the coil sensitivity profiles (*RF* receive field B_1^-) of a phased array receive coil are used to unfold the images. The two most prominent variants are Sensitivity Encoding (SENSE) [234] and Generalized Auto-calibrating Partial Parallel Acquisition (GRAPPA) [99]. Over the time more sophisticated algorithms developed known as Compressed Sensing (CS) in combination with random under-sampling patterns and data acquisition trajectories like radial, golden angle radial, spiral, and many more [194, 195], enabling a much higher acceleration potential than classical *PI* methods. Here, the reconstruction is typically performed by solving an optimization problem, searching for an image which fits best to the measured data. The solution of these optimization problems can be be quite ill-posed where variational modeling is used to stabilize the solution by the incorporation of prior knowledge about the spacial structure of the image to be reconstructed. First it was introduced by Rudin et al. [247] for the purpose of image denoising, where a Total Variation (TV) image prior was used. In *MRI*, the concept of variational modeling was first introduce by Block et al. [28] for the reconstruction of undersampled radial k-space data, where the same *TV* prior was used. The drawback of *TV* is that this functional is not accurate enough to capture the image structure, which led to the development of higher order functionals like Total Generalized Variation (TGV) [38] for image reconstruction [159] and Infimal Convolution Total Generalized Variation (ICTGV) for the reconstruction of dynamic image series [255]. Both image priors lead to more natural appearing images and enable a higher acceleration potential.

However, acceleration of *MRI* data acquisition is still an important research topic. In sequence design, a technique called Simultaneous Multi-Slice (SMS) [7, 169] gains more and more interest, where the first ideas already date back to the 1980s [212]. Recent developments showed the application of *SMS* to *EPI* with improved slice separation with blipped-Controlled Aliasing in Parallel Imaging (CAIPI) [262] or wave-*CAIPI* [22] for 3D acquisition. Furthermore, for the application of high resolution diffusion imaging a combination of *SMS* and in-slab 3D-phase encoding was developed [261]. Another recent development is Echo Planar Time-resolved Imaging (EPTI) [313] enabling high temporal resolution and an enormous distortion reduction in *EPI* acquisition, also in a motion robust variant [77]. Nowadays, in image reconstruction methods of machine learning and Artificial Intelligence (AI) are getting of increasing importance as it was shown by Hammernik et al. [110] that artifact free images can be gained out of Cartesian undersampled data and a similar approach is described for dynamic imaging also by Hammernik et al. [109].

In terms of field mapping two things are very important, where variational modeling can be beneficial: First the acquisition time and second the accuracy. Due to the fact that field mapping is only used as a calibration or a correction method without any diagnostic information, the acquisition speed is even more important, which can be improved by under-sampling. As stated above, variational modeling can be used to enforce a certain spacial property of the reconstruction result, which is very beneficial especially in combination with under-sampling. Field variations are usually smooth in space which can be enforced by proper regularization. According to accuracy, if field mapping is used i.e., for fat/water imaging to avoid fat/water swaps, an accurate field estimate is required. In order to achieve that, variational modeling can be used to separate the frequency shift induce by the chemical shift between water and fat and that one induce by the underlying field distribution, without acquiring additional data. This is possible because the spatial behavior of these two effects are different.

1.2 Contribution and Outline

Variational modeling is a widely used technique for many applications in computer vision. Among others, it is used for image denoising [247], image deblurring [47] or image segmentation [40]. As already mentioned, the main applications for variational modeling in *MRI* are image denoising and to stabilize the solution for the reconstruction from undersampled data. In this thesis, the application of variational modeling for Magnetic Resonance (MR) field mapping is exploited according to several aspects. The main contribution of this thesis is the development of a reconstruction algorithm, based on variational modeling, to obtain highly accurate *RF* field maps (B_1^+ mapping) from highly undersampled data using the method of Bloch-Siegert (BS). The performance of this algorithm is investigated with respect to its acceleration potential, the applicability of different undersampling patterns, the use of different acquisitions sequences and the influence of very high field strengths, i.e., 7 T. Another contribution is the application of variational modeling to obtain highly accurate B_0 field maps, for the separation of the signal contributions from fat and water.

The outline of this thesis is as follows: Chapter 2 starts with an overview of the principles of *MRI*, and describes the contribution of the involved field to generate an Nuclear Magnetic Resonance (NMR) signal in Section 2.1. The technical limitations in generating homogeneous fields and the involved coils for both B_0 and B_1 fields, as well as the physical principles of their interaction with matter and these additional influences on field homogeneity are considered in Sections 2.2 and 2.3. At the end of Chapter 2, different methods and important aspects for the mapping of the B_0 and B_1 field are considered in Sections 2.4 and 2.5. In Chapter 3, the basics of *MR* image reconstruction from undersampled data are reviewed. Furthermore, common regularization functionals which are used throughout this thesis including their applicability in field mapping and suitable algorithms to solve these optimization problems are described. Chapter 4 considers potential applications for field mapping, with special focus on the separation of fat and water signal contributions. Here, the basic principles from the early beginning with the seminal work of Dixon [67], over several improvements to current state of the art methods incorporating approaches similar to variational modeling are reviewed in Section 4.1. In Section 4.2, some commonly used model for *qMRI* are introduced to show their dependence on the flip angle and the B_1^+ field distribution. In Chapter 5, the contributions of this thesis to *BS* based B_1^+ mapping and undersampled data acquisition is described. Section 5.1 describes a robust data acquisition scheme for *BS* based B_1^+ mapping to be robust against phase variations during the acquisition. In Section 5.2, the reconstruction algorithm to obtain accurate B_1^+ field maps from highly undersampled data is described as well as its performance for the application of different undersampling patterns. In Section 5.3, the combination of undersampling and *EPI* readout is considered, and in Section 5.4, the application of the reconstruction algorithm and its acceleration potential under the conditions of a field strength of 7 T is investigated. In Chapter 6, a method to obtain a reliable B_0 field map for the separation of the fat and water contributions to the *MRI* signal based on *TGV* regularization is introduced and Chapter 7 gives a summary of the outcome of this thesis and gives a future outlook.

2

Physical Principles of Magnetic Resonance Imaging and Field Mapping

> Life is like riding a bicycle. To keep your balance, you must keep moving.
>
> *Albert Einstein*

Contents

2.1 Signal Generation and involved Fields 7

2.2 Homogeneity Limitations of the B_0 Field 29

2.3 Homogeneity Limitations of the B_1 field 46

2.4 Mapping the Static Magnetic Field – B_0 Mapping 59

2.5 Mapping the RF Field – B_1^+ Mapping 63

In this chapter, the basic physical principles of Magnetic Resonance Imaging (MRI), from the quantum mechanical point of view to a macroscopic signal description as a fundamental interaction with different kind of magnetic fields, are discussed. Furthermore, the limitations in field homogeneity including technical and physiological origins of field distortion for both the static magnetic field and the Radio Frequency (RF) field are described. Furthermore, the technical methods to improve field homogenity are elaborated. At the end of this chapter, different methods for mapping inhomogeneous field distributions are considered.

2.1 Signal Generation and involved Fields

The signal in *MRI*, or more general Nuclear Magnetic Resonance (NMR), is the result of the interaction of a nuclear quantum mechanical spin with an external magnetic field $\vec{B}_0$.

In this section, the properties of the quantum mechanical nuclear spin and its behavior in the presence of an external magnetic field are described. Moreover, a model to describe the signal from a phenomenological point of view (classical description) is introduced. Thus, in combination with relaxation, it gives the famous Bloch equations [27]. As an important part in signal generation, the interaction of the nuclear spins with an on-resonant *RF* field is described from a macroscopic point of view. Furthermore, the signal demodulation during receive and the signal to noise behavior is considered. At the end of this section, spatial signal encoding is described, in particular slice selective excitation and Fourier encoding leading to the so called k-space. This section is mainly based on Haacke et al. "*Magnetic Resonance Imaging*" [104].

2.1.1 Nuclear Spin

Subatomic particles such as electrons, protons, and neutrons have an angular momentum $\vec{J}$, which is a quantum mechanical property and has contributions from the orbital motion $\vec{L}$ and the intrinsic spin $\vec{S}$ of a certain particle

$$\vec{J} = \vec{L} + \vec{S}. \tag{2.1}$$

In *NMR*, the observed signal is only gained by an interaction with the nucleus, so that the orbital contribution $\vec{L}$ to the total angular momentum $\vec{J}$ can be neglected or is identical zero ($\vec{L} = 0$) for the most important nuclei, leading to

$$\vec{J} = \vec{S}. \tag{2.2}$$

In an external magnetic field $\vec{B}_0$, the z-component μ_z of the magnetic moment $\vec{\mu}$ (see Eq. (2.6)) and therefore also the corresponding angular momentum J_z can only have discrete values. The z-direction is given by the direction of $\vec{B}_0$. This behavior was first shown in the famous experiment by Stern and Gerlach [91], where only two spots were observed for the deflection of silver of a silver atom ray in an inhomogeneous magnetic field. The z-component of the angular momentum J_z must be an integer or half integer multiply m_j of the Plank's constant $\hbar = {}^{h}/_{2\pi}$ ($h = 6.626 \cdot 10^{-34}$ J s)

$$J_z = m_j \hbar. \tag{2.3}$$

The factor m_j, called the magnetic quantum number, can take $2j + 1$ values according to

$$m_j = -j, -j + 1, \ldots, j - 1, j, \tag{2.4}$$

where, j is the spin quantum number which can take positive integer and half integer values. This means that the z-component of a nucleus with spin quantum number of $j = 1/2$ can be aligned parallel ($m_j = +1/2$) or antiparallel ($m_j = -1/2$) to the external field, as it is for the hydrogen nucleus. The total angular momentum is related to the

Planck's constant by

$$J = \sqrt{j(j+1)}\,\hbar. \tag{2.5}$$

The combination of an angular momentum with an electrical charge, which can be seen as a circling current, results in a magnetic moment $\vec{\mu}$. $\vec{J}$ and $\vec{\mu}$ are connected by a proportionality constant γ (gyromagnetic ratio) which is specific for every nucleus or particle

$$\vec{\mu} = \gamma \vec{J}. \tag{2.6}$$

The associated energy E of a magnetic moment $\vec{\mu}$ in a magnetic field $\vec{B}_0$ is given by their dot product and can be written by using Eqs. (2.3) and (2.6) as

$$E = -\vec{\mu} \cdot \vec{B}_0 = -\gamma m_j \hbar B_0. \tag{2.7}$$

The energy difference ΔE between the two possible energy states is

$$\Delta E = E\left(m_j = -\frac{1}{2}\right) - E\left(m_j = +\frac{1}{2}\right) = \frac{1}{2}\gamma\hbar B_0 - \left(-\frac{1}{2}\gamma\hbar B_0\right) = \hbar\omega_0, \tag{2.8}$$

which denotes that a transition from the parallel to the antiparallel state or vice versa is equivalent by absorbing or emitting a photon with the angular frequency ω_0, respectively. This is visualized in Figure 2.1. The transition frequency ω_0 is the well known Larmor frequency, which is proportional to the magnitude of the external field B_0 and is equivalent to the precession frequency of $\vec{\mu}$ derived from the classical model in Section 2.1.3 given as

$$\omega_0 = \gamma B_0. \tag{2.9}$$

The most important nucleus in medical imaging is the ^{1}H-nucleus, which consists of a single proton with a gyromagnetic ratio of $\gamma = 2\pi \cdot 42.58\,\mathrm{MHz\,T^{-1}}$ and a spin quantum number of $j = 1/2$. The high importance in *MRI* comes from the high gyromagnetic ratio and more important the high concentration in human tissue (see Table 2.1). Not all nuclei show magnetic resonance behavior, because, according to Pauli's principle [228], the nucleons (protons and neutrons) in a nucleus group with opposing sign in magnetic spin quantum number, leading to a zero net magnetic moment. Only nuclei with an unpaired magnetic moment can be "seen" in *NMR*. Beside the ^{1}H nucleus, other *NMR*-nuclei in human tissue exist, e.g. ^{23}Na, ^{31}P, ^{17}O, and ^{19}F, but their relevance is restricted to very special applications which are far beyond the scope of this thesis. Their properties are shown in Table 2.1. All further considerations are tailored to the ^{1}H nucleus.

In general, also shell electrons show magnetic resonance behavior, called Electron Spin Resonance (ESR), nevertheless, in medical imaging *ESR* is of no importance due to several reasons e.g. the much higher frequency and the lower signal. This section is mainly based on Haacke et al. "*Magnetic Resonance Imaging*" [104, Ch.5].

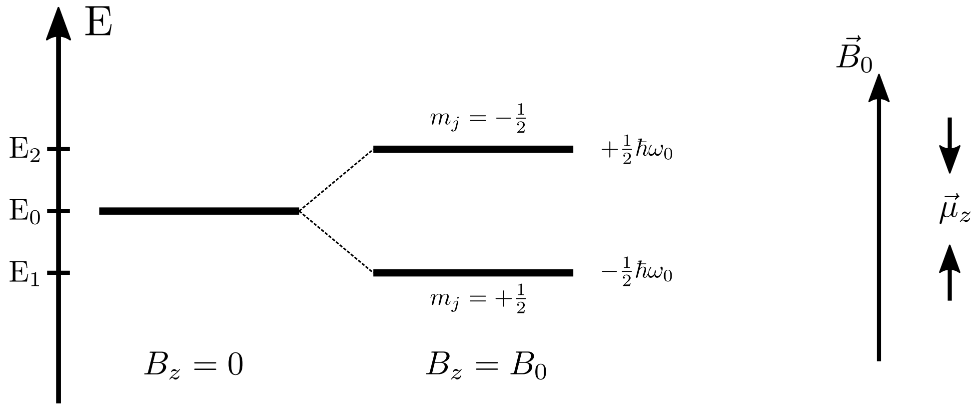

Figure 2.1: Schematic representation of the Zeeman energy splitting for a $j = 1/2$ nucleus in a magnetic field $\vec{B}_0$ and the direction of the corresponding magnetic moment $\vec{\mu}_z$. The magnetic moment parallel to $\vec{B}_0$ with $m_j = +1/2$ has the lower energy. Figure inspired by Haacke et al. "*Magnetic Resonance Imaging*" [104, p.71].

nucleus	spin quantum number j	γ in $2\pi\cdot$MHz T^{-1}	av. concentration in human tissue
^{1}H	1/2	42.58	88 M
^{23}Na	3/2	11.27	80 mM
^{31}P	1/2	17.25	75 mM
^{17}O	5/2	-5.77	16 mM
^{19}F	1/2	40.08	4 µM
^{13}C	1/2	10.71	–
^{15}N	1/2	-4.31	–

Table 2.1: Biologically relevant nuclei with their spin quantum number j, gyromagnetic ratio γ and their average concentration in human tissue. Negative γ indicates that angular momentum $\vec{J}$ and magnetic moment $\vec{\mu}$ point in the opposite direction. Values are from Haacke et al. "*Magnetic Resonance Imaging*" [104, p.27] and Westbrook et al. [319, p.5].

2.1.2 Macroscopic Magnetization and Boltzmann Distribution

In thermal equilibrium, the direction of the spins' magnetic moments is arbitrarily distributed and macroscopically no net magnetization can be observed. In an external static magnetic field $\vec{B}_0$, the nuclear magnetic moments $\vec{\mu}$ undergo a partial alignment parallel and antiparallel to the direction of $\vec{B}_0$ according to Eqs. (2.3) and (2.6). The energy for the parallel orientation $m_j = +1/2$ is lower than for the antiparallel orientation $m_j = -1/2$ (Eq. (2.7)), so that the probability for the parallel state is slightly higher, which leads to a macroscopic observable magnetization $\vec{M}_0$ along the field direction (see Figure 2.2). The macroscopic magnetization is the sum over all nuclear magnetic moments inside the observed volume V normalized to it

$$\vec{M} = \frac{1}{V} \sum_V \vec{\mu}_i. \tag{2.10}$$

The probability for a certain spin to be either in $+1/2$ or in $-1/2$ state follows the Boltzmann distribution

$$p_\pm = \frac{e^{\pm \frac{\gamma \hbar B_0}{2kT}}}{e^{+\frac{\gamma \hbar B_0}{2kT}} + e^{-\frac{\gamma \hbar B_0}{2kT}}}, \tag{2.11}$$

where k is the Boltzmann constant ($k = 1.38 \cdot 10^{-23} \mathrm{J\,K^{-1}}$) and T the absolute temperature in K. Out of Eq. (2.11), the relation between the number of parallel $N_{+1/2}$ and antiparallel $N_{-1/2}$ aligned spins is given by

$$\frac{N_{+1/2}}{N_{-1/2}} = e^{\frac{\gamma \hbar B_0}{kT}}. \tag{2.12}$$

With that and a 1^{st}-order Taylor series expansion of the exponential function, the magnitude of the thermal equilibrium magnetization M_0 is given by

$$M_0 = \rho_0 \frac{\gamma^2 \hbar^2 B_0}{4kT}, \tag{2.13}$$

where, ρ_0 is the spin density ($\rho_0 = N/V$) with the total number of spins in a volume $N = N_{+1/2} + N_{-1/2}$. M_0 is very important, because it is direct proportional to the maximum available signal. However, the *NMR* signal is based on the quantum mechanical property of a certain nucleus, the signal behavior can be described exactly by methods of classical physics. In Hanson et al. [113], it is described why quantum mechanics is not necessary to understand the signal behavior in *MRI*. In the next section, a model will be derived arising from the mechanical equivalent, the gyroscopic equations. However, the same equations can be derived as solution of the Schrödinger equation by using the Hamiltonian operators. However, this topic is beyond the scope of this thesis, but for the interested reader a detailed deviation is described in Haacke et al. "*Magnetic Resonance Imaging*" [104, Ch.5, and 6].

2.1.3 Classical Description

In classical physics, every object carrying a magnetic moment $\vec{\mu}$ (e.g. an electric current flowing through a loop coil ($\vec{\mu} = I_c A_c \vec{n}$)) tends to align the magnetic moment along the direction of an external applied magnetic field $\vec{B}_0$. The generated torque $\vec{D}$ is proportional to the crossproduct between magnetic moment $\vec{\mu}$ and external field $\vec{B}$

$$\vec{D} = \vec{\mu} \times \vec{B}. \tag{2.14}$$

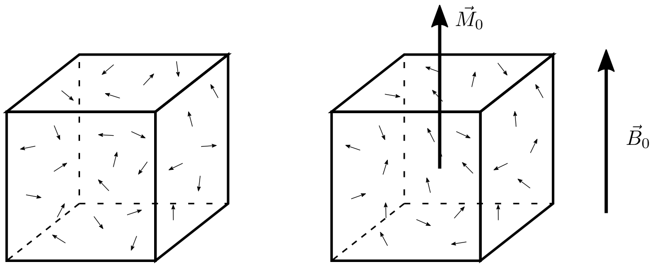

Figure 2.2: Without magnetic field the spin's magnetic moments are arbitrarily orient so that no net magnetization can be observed. Partial alignment of the magnetic moments and the higher probability for the $m_j = +1/2$ state lead to a net magnetization $\overrightarrow{M}_0$ it the direction of the magnetic field $\overrightarrow{B}_0$.

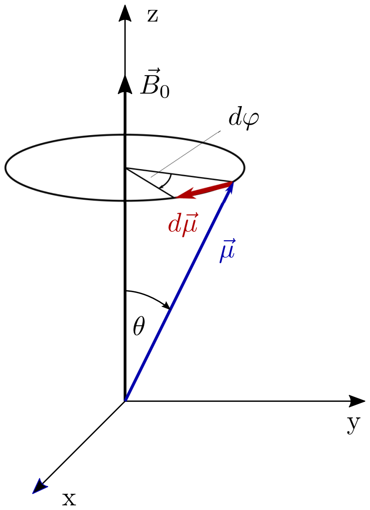

Figure 2.3: In the classical description the magnetic moment of a spin behaves such as a gyroscope. The change of the magnetic moment due to the torque generated between $\overrightarrow{B}$ and $\overrightarrow{\mu}$ leads to a precession movement of the magnetic moment around the magnetic field direction. Figure inspired by Haacke et al. "*Magnetic Resonance Imaging*" [104, p.29].

Any non-zero torque applied to a system results in a change of its angular momentum $\overrightarrow{J}$

$$\frac{d\overrightarrow{J}}{dt} = \overrightarrow{D}. \tag{2.15}$$

Since $\overrightarrow{J}$ and $\overrightarrow{\mu}$ are related to each other by Eq. (2.6), the following relation can be derived by combining Eqs. (2.14) and (2.15)

$$\frac{d\overrightarrow{\mu}}{dt} = \gamma\overrightarrow{\mu} \times \overrightarrow{B}, \tag{2.16}$$

which is the analogue to the gyroscopic equation. Out of this relation, where the time derivative of a vector is given by a cross product involving itself, the change in $\overrightarrow{\mu}$ is perpendicular to $\vec{\mu}$ and $\vec{B}_0$ where the magnitude of $\vec{\mu}$ stays unchanged. This leads to a circular precession around the external field direction $\vec{B}$, which is depicted in Figure 2.3. Calculating the angular frequency of the precession out of Eq. (2.16) comes to the same result as Eq. (2.9) derived from the energy level difference, the already described Larmor frequency.

$$\omega_0 = \gamma B_0 \tag{2.17}$$

The solution of Eq. (2.16) describes the precession of one single magnetic moment $\vec{\mu}$ around the $\vec{B}_0$ direction as

$$\begin{aligned} \mu_x(t) &= \mu_x(0)\cos\omega_0 t + \mu_y(0)\sin\omega_0 t, \\ \mu_y(t) &= \mu_y(0)\cos\omega_0 t - \mu_x(0)\sin\omega_0 t, \\ \mu_z(t) &= \mu_z(0), \end{aligned} \tag{2.18}$$

with $\mu_x(t)$, $\mu_y(t)$ and $\mu_z(t)$ being the Cartesian components of $\vec{\mu}$. Eq. (2.18) can also be written by using the rotation matrix $\mathbf{R}_z$ defined in the Appendix (see Eq. (A.12))

$$\vec{\mu}(t) = \mathbf{R}_z(\omega_0 t)\vec{\mu}(0). \tag{2.19}$$

Rather than using the magnetic moment of a single spin, which follows quantum mechanical rules (see Section 2.1.1), $\vec{\mu}$ in Eq. (2.16) can be replaced by the macroscopic magnetization $\vec{M}$ from Eq. (2.10) leading to

$$\begin{aligned} \frac{d\vec{M}(t)}{dt} &= \gamma\vec{M}(t) \times \vec{B}(t), \\ \vec{M}(0) &= \vec{M}_0, \end{aligned} \tag{2.20}$$

with the boundary condition that the magnetization at time point $t = 0$ is the thermal equilibrium magnetization from Eq. (2.13), which is aligned to the external field. However, the static magnetic field alone cannot create a measurable *MRI* signal, an additional time varying *RF* field is necessary. The previous section is mainly based on Haacke et al. "*Magnetic Resonance Imaging*" [104, Ch.2].

2.1.4 RF–Excitation and Rotating Coordinate System

To gain an *MRI* signal, the net magnetization $\vec{M}_0$ has to be deflected out of its thermal equilibrium direction. For that purpose, an *RF* field (B_1^+) is applied, whose frequency ω has to be matched to the Larmor frequency ω_0 of the nucleus of interest. This is where the term "resonance" in *NMR* and *MRI* originates. If the resonance condition is fulfilled ($\omega = \omega_0$), the magnetization vector $\vec{M}$ is pushed down on a spiral path as depicted in

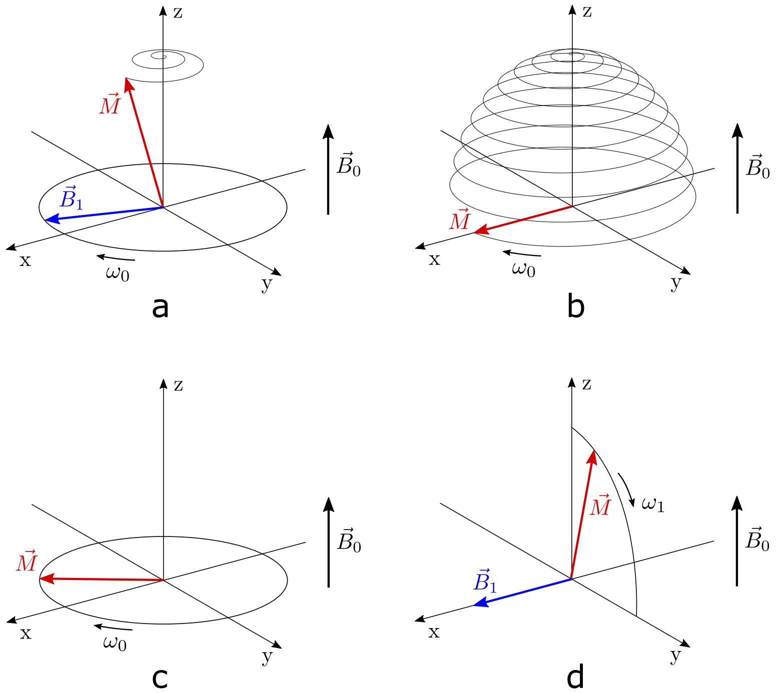

Figure 2.4: Excitation by applying an RF field in the laboratory frame versus rotating frame for the onresonant case ($\omega = \omega_0$). (a) and (b) Excitation in the laboratory frame, the active component of the $\overrightarrow{B}_1$ filed rotates in the transverse plane ($x - y$ plane) and the magnetization vector $\overrightarrow{M}$ is pushed downwards on a spiral path. The path is simulated for $\omega_0 = 40\omega_1$. (c) Magnetization $\overrightarrow{M}$ is rotating in the transverse plane with ω_0 after excitation, producing a detectable signal. (d) Excitation in the rotating frame, the coordinate system is rotating with ω_0, such that $\overrightarrow{B}_1$ is oriented along an axis of the transverse plane. $\overrightarrow{M}$ is moved downwards by a simple rotation with ω_1. Figure is inspired by Haacke et al. "*Magnetic Resonance Imaging*" [104, p.6 and 44].

Figure 2.4(a) and (b). For example, by applying an external field of the form of

$$\overrightarrow{B}(t) = \begin{pmatrix} B_1(t)\cos\omega t \\ -B_1(t)\sin\omega t \\ B_0 \end{pmatrix}, \tag{2.21}$$

with the circular polarized *RF* component rotating in the transverse ($x - y$) plane, the magnetization vector $\overrightarrow{M}$ can be described by rewriting Eq. (2.20) leading to the following differential equation

$$\frac{d\overrightarrow{M}}{dt} = \gamma \begin{pmatrix} M_y B_0 + M_z B_1 \sin\omega t \\ M_z B_1 \cos\omega t - M_x B_0 \\ -M_x B_1 \sin\omega t - M_y B_1 \cos\omega t \end{pmatrix}. \tag{2.22}$$

However, Eq. (2.22) seems to be quite simple, it can only be solved numerically, because a closed form solution does not exist. To simplify the equations, the magnetization behavior is usually described in a rotating coordinate system (rotating frame), which is rotating around the z-axis of the corresponding static coordinate system (laboratory frame) with the angular frequency ω of the incident *RF* field. In the rotating frame, the $\vec{B}_1^+$ field vector stands still with a certain orientation in the transverse plane described by the initial phase ϕ_0. In the ideal onresonant case ($\omega = \omega_0$), also the magnetization vector $\vec{M}$ stands still, which means that the magnetization undergoes a simple rotation around the applied $\vec{B}_1^+$ field with angular frequency $\omega_1 = \gamma B_1^+$, as shown in Figure 2.4(d). Because of the coordinate transformation from the laboratory frame to the rotating frame, the effective field $\vec{B}_{eff}$ has to be introduced which is defined by

$$\vec{B}_{eff} = \vec{B} - \frac{\vec{\omega}}{\gamma}, \tag{2.23}$$

where $\vec{\omega}$ is the direction of the coordinate system's rotation (typically, the z-axis). For the applied field in Eq. (2.21), this means that the z-component becomes zero, such that the precession of $\vec{M}$ stops and the *RF* component is aligned along the x-axis

$$\vec{B}_{eff}(t) = \begin{pmatrix} B_1(t) \\ 0 \\ 0 \end{pmatrix}. \tag{2.24}$$

With that, the magnetization $\vec{M}$ will undergo a simple rotation around the x-axis in the rotating frame. If $B_1(t)$ is constant over time, $\vec{M}$ can be described as follows

$$\begin{array}{rcl} M_x(t) & = & M_x(0), \\ M_y(t) & = & M_y(0)\cos\omega_1 t - M_z(0)\sin\omega_1 t, \\ M_z(t) & = & -M_y(0)\sin\omega_1 t + M_y(0)\cos\omega_1 t. \end{array} \tag{2.25}$$

Similar to Eq. (2.19), this can also be rewritten in vector/matrix notation with the rotation matrix $\mathbf{R}_x$ defined in the Appendix (see Eq. (A.10))

$$\vec{M}(t) = \mathbf{R}_x(\omega_1 t)\vec{M}(0). \tag{2.26}$$

This means that a constant *RF* field B_1^+ applied for a certain time T_p along an arbitrary axis in the transverse plane of the rotating frame leads to a flip of the magnetization by an angle α. The flip angle α is defined with respect to the z-axis and is given by

$$\alpha = \gamma B_1^+ T_p. \tag{2.27}$$

The B_1^+ field is usually applied with a time varying magnitude $B_1(t)$ (*RF* envelop), the so called *RF* pulse, where the changes in $B_1(t)$ are several orders of magnitude slower then

ω. The resulting flip angle is given by

$$\alpha = \gamma \int_0^{T_p} B_1^+(t) dt. \tag{2.28}$$

However, in practice the onresonant case is nearly never fulfilled, so for $\omega \neq \omega_0$, the more general form of a rotation around the effective field, introduced in Eq. (2.23), must be considered. For B_1^+ along the x-axis of the rotating frame, $\vec{B}_{eff}(t)$ is calculated by

$$\vec{B}_{eff}(t) = \begin{pmatrix} B_1(t) \\ 0 \\ B_0 - \frac{\omega}{\gamma} \end{pmatrix}. \tag{2.29}$$

In this case, $\vec{M}$ rotates around the direction of $\vec{B}_{eff}$ with the angular frequency ω_{eff}

$$\omega_{eff} = \gamma B_{eff} = \gamma \sqrt{\left(B_0 - \frac{\omega}{\gamma}\right)^2 + B_1^2} = \sqrt{(\omega_0 - \omega)^2 + \omega_1^2}, \tag{2.30}$$

graphically visualized in Figure 2.5. The angle θ between $\vec{B}_{eff}$ and the transverse plane and is given by

$$\theta = \arccos\left(\frac{B_0 - \omega/\gamma}{B_1}\right). \tag{2.31}$$

Assuming again that the B_1^+ field is aligned with the x-axis in the rotating frame, the behavior of $\vec{M}$ can be calculated by a coordinate transformation, where the whole coordinate system is rotated by $-\theta$ such that $\vec{B}_{eff}$ is in the transverse plane (along the x-axis in this case). After the rotation around $\vec{B}_{eff}$, the coordinate system is rotated back into the initial orientation.

$$\vec{M}(t) = \mathbf{R}_y(\theta)\mathbf{R}_x(\omega_{eff}t)\mathbf{R}_y(-\theta)\vec{M}(0) \tag{2.32}$$

The process of tilting $\vec{M}$ is called excitation and leads to a coherent precession of the transverse component of $\vec{M}$ with the Larmor frequency ω_0 (see Figure 2.4(c)). The transverse component of $\vec{M}$, which is proportional to $\sin(\alpha)$, induces measurable signal in an external receive coil oriented perpendicular to the transverse plane. The rotation matrices $\mathbf{R}_x$, $\mathbf{R}_y$, and $\mathbf{R}_z$ are defined in the Appendix (see Eqs. (A.10) to (A.12)).

2.1.4.1 Polarization of the $\mathbf{B}_1^+$ Field

Polarization refers to the oscillation direction of the *RF* field. Consider a linearly polarized coil producing a $\vec{B}_1^+$ field along the x-axis of the laboratory frame given by

$$\vec{B}_1^{lin}(t) = \begin{pmatrix} B_1 \cos \omega t \\ 0 \end{pmatrix}. \tag{2.33}$$

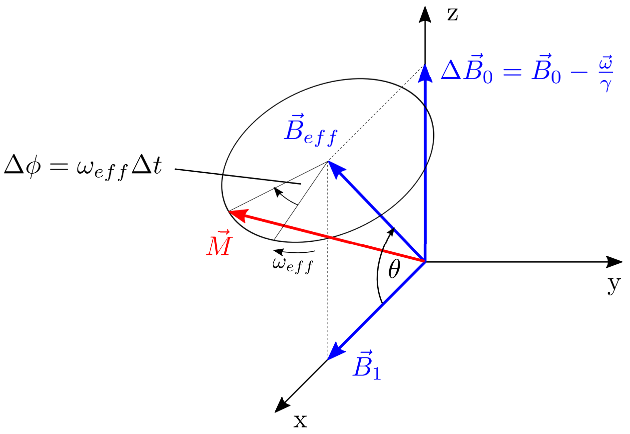

Figure 2.5: Excitation in the general case $\omega \neq \omega_0$ in the rotating frame. The magnetization vector $\overrightarrow{M}$ is rotating around an effective field $\overrightarrow{B}_{eff}$ with ω_{eff}, resulting as the vectorial sum of the RF field $\overrightarrow{B}_1$ and the resonance offset $\Delta\overrightarrow{B}_0$. Figure inspired by Haacke et al. "*Magnetic Resonance Imaging*" [104, p.47].

Mathematically, this can be separated into two circularly polarized fields with clockwise $\overrightarrow{B}_1^{cw}(t)$ and counterclockwise $\overrightarrow{B}_1^{ccw}(t)$ rotation with half the magnitude, given as

$$\overrightarrow{B}_1^{lin}(t) = \frac{1}{2}\left(\overrightarrow{B}_1^{cw}(t) + \overrightarrow{B}_1^{ccw}(t)\right) = \frac{1}{2}\left[\begin{pmatrix} B_1 \cos\omega t \\ B_1 \sin\omega t \end{pmatrix} + \begin{pmatrix} B_1 \cos\omega t \\ -B_1 \sin\omega t \end{pmatrix}\right]. \tag{2.34}$$

With the representation in the rotating frame, it is obvious that only the component rotating in the same direction as the precession of the magnetization vector $\overrightarrow{M}$ (the clockwise direction) has a tilting contribution. So in this case, half the energy of the transmit coil is dissipated in the tissue without any active contribution. However, the counterclockwise part also contributes in tissue heating, leading to twice the Specific Absorption Rate (SAR). The *SAR* is a measure how much energy is dissipated in the subject per unit body mass (see Section 2.3.4). Instead of a linear polarized field, usually, a clockwise circularly polarized *RF* field $\overrightarrow{B}_1^{cw}(t)$ is used for *MRI* excitation. This can be reached by applying two linear polarized fields which are phase shifted by 90° and applied perpendicular to each other. It can be realized using a birdcage coil, where only the clockwise circularly polarized field $\overrightarrow{B}_1^{cw}$ is generated.

$$\overrightarrow{B}_1^{cw}(t) = \begin{pmatrix} B_1 \cos\omega t \\ -B_1 \sin\omega t \end{pmatrix} \tag{2.35}$$

The whole previous section (Section 2.1.4) is mainly based on Haacke et al. "*Magnetic Resonance Imaging*" [104, Ch.3].

2.1.5 Relaxation and Bloch-Equations

To fully describe the magnetization behavior, the term relaxation must also be introduced. After tilting the magnetization $\overrightarrow{M}$ out of its equilibrium direction by an *RF* field, $\overrightarrow{M}$ precesses around the main field direction in the transverse plane, leading to a measurable signal. Of course, this signal is not present forever, $\overrightarrow{M}$ tends to reach thermal equilibrium again which is called relaxation. There are two independent relaxation phenomena, the longitudinal (T_1) relaxation and the transversal (T_2) relaxation, where both phenomena are induced by an interaction of the nuclear spin with its surrounding.

2.1.5.1 Longitudinal Relaxation $\mathbf{T_1}$

The longitudinal relaxation is induced by random thermal fluctuations in the surrounding lattice (Brown's molecular movement), leading to an energy exchange between the nuclear spin and the lattice. Coincidentally, the frequency of the thermal fluctuations match the Larmor frequency of the nuclear spin, leading to a photon exchange and a state change from $m_j = -1/2$ to $m_j = 1/2$ or vice versa. In thermal equilibrium, the probability for both quantum state changes are equal, so macroscopically no change can be observed. After an *RF* excitation, of course, the transition from $m_j = -1/2$ to $m_j = 1/2$ is more likely until the thermal equilibrium is reached again. The quantum mechanical description of relaxation is very complicated and not necessary to describe the macroscopic signal evolution in *MRI*, so a phenomenological description is preferred. The longitudinal relaxation is described by a constant growth rate of the longitudinal magnetization M_z with an empirically determined time constant T_1, leading to

$$\frac{dM_z}{dt} = \frac{1}{T_1}(M_0 - M_z). \tag{2.36}$$

The solution of Eq. (2.36) leads to the well known monoexponential T_1 relaxation relation with the time course shown in Figure 2.6(a)

$$M_z(t) = M_z(t_0)e^{-\frac{t-t_0}{T_1}} + M_0\left(1 - e^{-\frac{t-t_0}{T_1}}\right). \tag{2.37}$$

2.1.5.2 Transverse Relaxation $\mathbf{T_2}$

The transverse relaxation is induced by spin - spin interactions without an energy exchange. The magnetic field produced by each nuclear spin overlays with the external static magnetic field $\vec{B}_0$, influencing the precession frequency of other spins near by, so that the precession frequency of each spin is slightly different. This difference leads to a constant dephasing of the coherent precession in the transverse plane. Due to thermal fluctuations, the spin-spin interaction is an irreversible random process and ones the signal is lost due to dephasing, it cannot be recovered again. The transverse relaxation is also

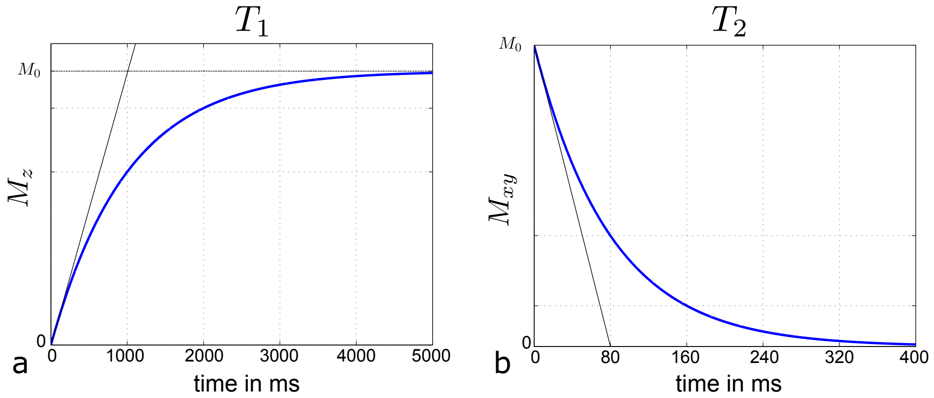

Figure 2.6: Magnetization time course for longitudinal (a) and transverse relaxation (b) with initial slope, simulated for $T_1 = 1000\,\mathrm{ms}$ and $T_2 = 80\,\mathrm{ms}$.

described by a constant decay rate and the empirically determined time constant T_2

$$\frac{dM_{xy}}{dt} = -\frac{1}{T_2} M_{xy}. \tag{2.38}$$

The solution of Eq. (2.38) leads to the well known exponential T_2 decay with the time course shown in Figure 2.6(b)

$$M_{xy}(t) = M_{xy}(0) e^{-\frac{t}{T_2}}. \tag{2.39}$$

Besides the dephasing introduced by the spin-spin interaction, there is an additional dephasing phenomenon induced by an inhomogeneous B_0 field distribution in a certain voxel, which is constant in time. This additional signal loss is described by an additional time constant T_2'. In combination, the total signal loss can be described by replacing T_2 in Eqs. (2.38) and (2.39) with

$$T_2^* = \frac{1}{\dfrac{1}{T_2} + \dfrac{1}{T_2'}}. \tag{2.40}$$

In contrast to pure T_2 relaxation, this additional dephasing can be recovered with a refocusing pulse in a spin echo sequence, because the causing inhomogeneities are time constant. For more details see Section 2.2.3.3. By combining Eqs. (2.20), (2.36) and (2.38), we get a differential equation for the full description of the magnetization behavior

$$\frac{d\overrightarrow{M}(t)}{dt} = \gamma \overrightarrow{M}(t) \times \overrightarrow{B}(t) + \begin{pmatrix} -\frac{1}{T_2} M_x \\ -\frac{1}{T_2} M_y \\ \frac{1}{T_1}(M_0 - M_z) \end{pmatrix}, \tag{2.41}$$

the famous Bloch equations [26]. The solution for the Bloch equation in the laboratory frame where only the static magnetic field $\vec{B}_0$ along the z-direction is applied is given by

$$\begin{aligned}
M_x(t) &= e^{-\frac{t}{T_2}}\left(M_x(0)\cos\omega_0 t + M_y(0)\sin\omega_0 t\right), \\
M_y(t) &= e^{-\frac{t}{T_2}}\left(M_y(0)\cos\omega_0 t - M_x(0)\sin\omega_0 t\right), \\
M_z(t) &= M_z(0)e^{-\frac{t}{T_1}} + M_0\left(1 - e^{-\frac{t}{T_1}}\right).
\end{aligned} \tag{2.42}$$

The information in this section is mainly based on Haacke et al. “*Magnetic Resonance Imaging*” [104, Ch.4].

2.1.6 Receiving Signal and SNR

After applying a 90° excitation pulse, the whole magnetization M_0 is flipped to the transverse plane, starting a coherent precession according to Eq. (2.42). This precessing movement induces a voltage $u_c(t)$ in a receive coil oriented perpendicular to the transverse plane, which is proportional to the flux through it, given as

$$u_c(t) \propto -\frac{d}{dt}\int_V \vec{M}(\vec{r},t)\vec{B}_1^-(\vec{r})d^3r. \tag{2.43}$$

Here, $\vec{B}_1^-(\vec{r})$ is the sensitivity profile of the receive coil (receive field), which is given as the field which would be produced at spatial point $\vec{r}$ for a unit current flowing through the coil. Further description is given in Section 2.3. If all quantities inside the integral are assumed to be constant in space, the signal can be rewritten with the sample volume V_s and an arbitrary flip angle α as

$$u_c(t) \propto \omega_0 M_0 \sin(\alpha) B_1^- V_s \sin(\omega_0 t + \phi_0). \tag{2.44}$$

The received signal is further quadratur demodulated with angular frequency ω of the incident *RF* field during excitation. For the demodulation, two orthogonal reference signals are used, $\sin(\omega t)$ and $-\cos(\omega t)$, leading to a complex signal $s(t)$ describing the magnetization behavior in the rotating frame. The double frequency component arising from the demodulation is filtered out, such that the signals after demodulation for both channels $s_1(t)$ and $s_2(t)$ are given by

$$\begin{aligned}
s_1(t) &\propto \sin(\omega_0 t + \phi_0)\cdot\sin(\omega t) &&\Rightarrow \frac{1}{2}\cos\left(\Delta\omega t + \phi_0\right) &&= \Re(s(t)), \\
s_2(t) &\propto \sin(\omega_0 t + \phi_0)\cdot(-\cos(\omega t)) &&\Rightarrow \frac{1}{2}\sin\left(\Delta\omega t + \phi_0\right) &&= \Im(s(t)),
\end{aligned} \tag{2.45}$$

with $\Delta\omega = \omega_0 - \omega$. Furthermore, s_1 and s_2 can be seen as real and imaginary part of the complex signal $s(t)$

$$s(t) = s_1(t) + is_2(t). \tag{2.46}$$

After spacial encoding (see Section 2.1.7) and assuming that all quantities under the integral in Eq. (2.43) are at least constant over the voxel dimensions, V_s in Eq. (2.44) can be replaced with the voxel volume V_{vox} and $u_c(t)$ by the voxel signal $S_{\text{vox}}(\vec{r}, t)$.

$$S_{\text{vox}}(\vec{r}, t) \propto \omega_0(\vec{r}) M_0(\vec{r}) \sin(\alpha(\vec{r})) B_1^-(\vec{r}) V_{\text{vox}} \sin(\omega_0(\vec{r}) t + \phi_0(\vec{r})). \tag{2.47}$$

According to Eqs. (2.13), (2.17) and (2.44), the signal $s(t)$ is proportional to the squared main field strength ($s(t) \propto B_0^2$), because ω_0 and M_0 in Eq. (2.44) is proportional to B_0. Furthermore, according to Eq. (2.47), the signal is also proportional to the voxel volume. This means, by reducing the dimension Δx of an isotropic voxel with a constant factor a, the voxel signal S_{vox} reduces with $1/a^3$.

As any other signal, the *MRI* signal is also corrupted with noise, where 3 main sources can be identified: the thermal noise in the receiving coil and the following electronic circuits arising from charge fluctuations due to thermal motion, as well as the thermal fluctuations in the tissue of the subject contribute to the total noise. In general, the standard deviation of the noise in the measured signal σ_{meas} is given by

$$\sigma_{\text{meas}} = \sqrt{4kT\Delta f_{\text{BW}} R_{\text{eff}}}, \tag{2.48}$$

where Δf_{BW} is the measurement bandwidth according to Eq. (2.67) and R_{eff} is the effective resistance. Because all contributions are Gaussian distributed and statistically independent, the variances of each can be summed up and therefore also the corresponding noise resistances

$$R_{\text{eff}}(\omega) = R_{\text{coil}}(\omega) + R_{\text{electronics}}(\omega) + R_{\text{body}}(\omega). \tag{2.49}$$

Typically, the noise resistance contributions depend on the operation frequency ω and therefore they are also field strength dependent. The contribution from the coil and the electronics depend marginally on the frequency; and at very low frequencies, these sources dominate the total noise. At clinically relevant field strength, the noise is highly dominated by the contribution of the body, the coil load. R_{body} highly depends on the frequency ($R_{\text{body}} \propto \omega^2$), so that the noise is proportional to ω (Eq. (2.48)). The consequence of this is that the Signal-to-Noise Ratio (SNR) only increases linearly with the field strength and not quadratically as it might be assumed at the first glance

$$\text{SNR} \propto B_0. \tag{2.50}$$

Generally, when using multiple receive coils, the noise standard deviations $\sigma_{\text{meas},n}$ of each receive coil $n \in [1, N_c]$ are different and can be correlated due to inductive coupling. To account for this, the noise correlation matrix $\boldsymbol{\Psi}$ is introduced, which can be determined out of noise samples η_n for each channel by

$$\Psi_{k,l} = \frac{1}{N_{\text{noise}}} \langle \eta_k, \eta_l \rangle, \tag{2.51}$$

where $\langle\cdot\rangle$ defines the scalar product. Eq. (2.51) is only valid if a sufficient number of noise samples N_{noise} is available, and as a rule of thumb $N_{\text{noise}} \geq 10^5$. The noise samples for each channel η_i can be acquired, by data sampling without previous excitation. The noise variances $\sigma^2_{\text{meas},n}$ of each channel are the diagonal elements of $\boldsymbol{\Psi}$. This section is mainly based on Haacke et al. "*Magnetic Resonance Imaging*" [104, Ch.7 and 15].

2.1.7 Spatial Encoding

According to Eq. (2.17), the precesssion frequency and with that the signal frequency depends on the static magnetic field strength B_0. To encode the signal according to its spatial origin, typically an additional linearly varying field along either the x, y or z axis is applied, which is called gradient field G_x, G_y or G_z respectively. It is important to mention that only the z-component of the field varies linearly along the specified direction, leading to the following relation for the z-component of the local magnetic field strength

$$B_z = B_0 + G_x x + G_y y + G_z z. \tag{2.52}$$

The coordinates x, y and z are referred to the laboratory frame. Typical maximum gradient field strengths in human imaging are $< 100\,\mathrm{mT\,m^{-1}}$. In *MRI*, we can basically distinguish between two types of spatial encoding with gradients, the slice selective excitation and the Fourier encoding in k-space.

2.1.7.1 Slice Selective Excitation

In 2D-imaging, the excitation of a well delimited slice is very important. For that purpose, a gradient field G_z along the z-axis is applied. According to Eq. (2.52), this leads to a variation of the resonance frequency $\omega(z)$ in the laboratory frame given by

$$\omega(z) = \omega_0 + \gamma G_z z. \tag{2.53}$$

Transferring Eq. (2.53) to the rotating frame the effective frequency variation $\omega'(z)$ reduces to

$$\omega'(z) = \gamma G_z z. \tag{2.54}$$

By applying an *RF* pulse with a time varying envelope $B_1^+(t)$, modulated to the center frequency $\omega = \omega_0$ and with a duration T_p, the magnetization behavior in every point along the z-direction can be described by Eqs. (2.30) to (2.32). The envelop function $B_1^+(t)$ defines the bandwidth of the *RF* pulse and with that the shape of the excited slice, the slice profile. The slice thickness is determined by the bandwidth of the pulse in combination with the magnitude of gradient G_z and is usually defined as the Full Width Half Maximum (FWHM) of the slice profile. This is visualized in Figure 2.7. According to Eq. (2.23), the effective field $\vec{B}_{eff}(t)$ in the rotating frame is given as

$$\vec{B}_{eff}(t) = \begin{pmatrix} B_1(t) \\ 0 \\ \gamma G_z z \end{pmatrix}. \tag{2.55}$$

By introducing the complex transverse magnetization $M_\perp$,

$$M_\perp = M_x + iM_y, \tag{2.56}$$

and using Eq. (2.20), the transverse magnetization in the rotating frame along the slice direction (z-axis) can be described by

$$M_\perp(t, z) = i\gamma e^{-i\gamma G_z z t} \int_0^t M_z(\tau) B_1(\tau) e^{i\gamma G_z z \tau} d\tau. \tag{2.57}$$

Under the assumption that M_z is time independent ($M_z(t) = M_0$), $M_\perp$ along the slice direction at the end of the pulse (at time point T_p) can be described by

$$M_\perp(T_p, z) \approx i\gamma M_0 e^{-i\gamma G_z z \frac{T_p}{2}} \int_{-\frac{T_p}{2}}^{\frac{T_p}{2}} B_1(\tau) e^{i\gamma G_z z \tau} d\tau = \mathcal{F}^{-1}\{B_1(t)\}. \tag{2.58}$$

Using $\gamma G_z z = \Delta\omega$, it can be seen that this is the inverse Fourier transform of the applied *RF* envelope, which is known as the small flip angle approximation valid for flip angles $\alpha \leq 30°$. For higher flip angles, the magnetization profile must be calculated numerically for every spatial point in z-direction and for every time point of the *RF* envelop $B_1^+(t)$ by using Eqs. (2.31) and (2.32). Furthermore, an additional gradient pulse has to be applied after the excitation, typically with half the gradient moment and opposite polarity as the slice selective gradient for symmetric *RF* pulses. This is necessary to compensate the accumulated phase in Eqs. (2.57) and (2.58), in order to prevent a dephasing along the slice. This section is mainly based on [18, Ch.3] and [104, Ch.10].

2.1.7.2 Fourier Encoding and k-space

After the excitation of a single slice, the gained signal must be spatially encoded as well. Thus, gradient fields perpendicular to the slice selection direction are used. According to Eq. (2.18), the magnetization vector $\vec{M}$ is rotating in the transverse plane with the angular frequency ω_0 in the laboratory frame. If $\omega = \omega_0$, the magnetization vector $\vec{M}$ stands still in the rotating frame, with a certain orientation ϕ_0 gained from the *RF* excitation. For the moment, let us assume $\phi_0 = 0$ by rotating the coordinate system such that $\vec{M}$ is aligned with the x-axis. By applying a time constant gradient field along the x-axis, the

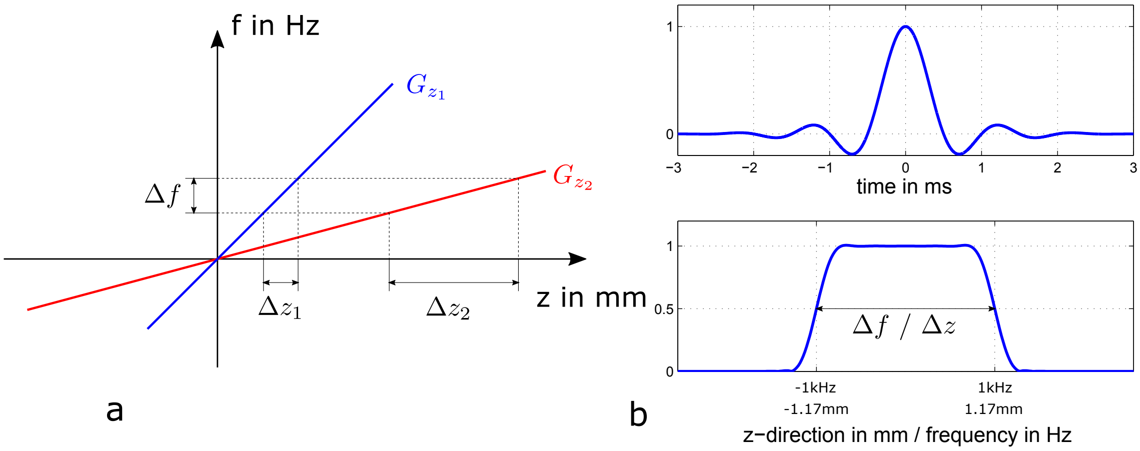

Figure 2.7: Influence of the slice selective gradient strength G_z and pulse bandwidth Δf on the slice thickness Δz. (a) Slice thickness for different gradient strengths and constant bandwidth. (b) Simulated slice profile for a 6 ms Hanning filtered sinc shaped RF pulse for a gradient strength of $G_z = 20\,\mathrm{mT\,m^{-1}}$ using the small flip angle approximation.

frequency distribution is given as

$$\omega(x) = \gamma G_x x. \tag{2.59}$$

Again, by using the complex transverse magnetization $M_\perp(x, y)$ depending on the spatial location (x, y) in the transverse plane, the signal $s(t)$ can be written by using $k_x = \gamma G_x t$

$$s(t) = \int M_\perp(x, y) e^{-i\gamma G_x x t} dx dy = \int M_\perp(x, y) e^{-i k_x x} dx dy. \tag{2.60}$$

This is called frequency encoding, because the resonance frequency is varying linearly along the x-direction. The relation in Eq. (2.60) shows that the measured signal is the one dimensional Fourier transform of the magnetization along the x-direction with the spatial frequency k_x. With that the spatial contributions to the signal can be resolved at least in one direction. To reach a spatial encoding in the second direction (here, y-direction) as well, an additional linear gradient field along the y-direction is applied for a certain time T_{G_y} between excitation and readout, leading to an additional spatial dependent phase term, which is called phase encoding. After one excitation, only one phase encoding step can be measured, so that this experiment has to be repeated until the whole k-space is acquired. With that the signal formula can be extended by

$$s(t) = \int M_\perp(x, y) e^{-i\gamma G_x x t} e^{-i\gamma G_y y T_{G_y}} dx dy. \tag{2.61}$$

By using the more general form of the spatial frequencies k_x and k_y for time varying gradient fields $G_x(t)$ and $G_y(t)$, which reduce to a simple multiplication if the gradients are constant in time

$$
\begin{aligned}
k_x &= \gamma \int_0^t G_x(\tau)d\tau = \gamma G_x t, \\
k_y &= \gamma \int_0^{T_{G_y}} G_y(\tau)d\tau = \gamma G_y T_{G_y},
\end{aligned}
\tag{2.62}
$$

the signal can be written in terms of k_x and k_y

$$
s(k_x, k_y) = \int M_\perp(x, y) e^{-ik_x x} e^{-ik_y y} dxdy. \tag{2.63}
$$

This is the origin of the famous name k-space, the *MRI* data space. The measured signal is given by the 2D-Fourier transform of the complex transverse magnetization $M_\perp$, which is proportional to the actual image of interest. Because the Magnetic Resonance (MR) signal is sampled at discrete points in k-space, where a number of N_x and N_y samples are acquired in k_x and k_y direction respectively, Eq. (2.63) has to be discretized leading to the 2-dimensional Discrete Fourier Transform (DFT)

$$
\begin{aligned}
s(l_x \Delta k_x, l_y \Delta k_y) = \mathcal{F}\left\{M_\perp(m_x \Delta x, m_y \Delta y)\right\} = \\
\sum_{m_x = -\frac{N_x}{2}}^{\frac{N_x}{2}-1} \sum_{m_y = -\frac{N_y}{2}}^{\frac{N_y}{2}-1} M_\perp(m_x \Delta x, m_y \Delta y) e^{-il_x \Delta k_x m_x \Delta x} e^{-il_y \Delta k_y m_y \Delta y} \Delta x \Delta y.
\end{aligned}
\tag{2.64}
$$

This can be described as linear time invariant operator, the discrete 2D-Fourier operator $\mathcal{F}$. Based on Eq. (2.64), the image can be reconstructed by applying the inverse linear discrete 2D-Fourier operator $\mathcal{F}^{-1}$ to the acquired k-space. The resolution in k-space Δk_x and Δk_y is given by the dwell time of the sampling system Δt in the the frequency encoding direction and the difference in the gradient strength ΔG_y from one phase encoding step to the other in the phase encoding direction

$$
\begin{aligned}
\Delta k_x &= \gamma G_x \Delta t, \\
\Delta k_y &= \gamma \Delta G_y T_{G_y}.
\end{aligned}
\tag{2.65}
$$

The image resolution Δx and Δy and the Field of View (FOV) in both spatial directions x and y are related to the k-space resolution Δk_x and Δk_y; and the maximum acquired k-space frequency $k_{x,max}$ and $k_{y,max}$ by

$$
\begin{aligned}
\Delta x &= \frac{1}{N_x \Delta k_x} = \frac{1}{2k_{x,max}}, & \Delta y &= \frac{1}{N_y \Delta k_y} = \frac{1}{2k_{y,max}}, \\
\mathrm{FOV}_x &= N_x \Delta x = \frac{1}{\Delta k_x}, & \mathrm{FOV}_y &= N_y \Delta y = \frac{1}{\Delta k_y}.
\end{aligned}
\tag{2.66}
$$

This concept is schematically visualized for a Spin Echo (SE) sequence in Figure 2.9 and for a Gradient Recalled Echo (GRE) sequence in Figure 2.8. The readout bandwidth Δf

is determined by the magnitude of the readout gradient G_x by

$$\Delta f_{\mathrm{BW}} = \gamma G_x \Delta x = \frac{1}{\Delta t}. \tag{2.67}$$

In Section 2.1.8 three basic sequences to cover the k-space are described. This concept can be easily extended by a second phase encoding direction for 3D acquisition. This section is mainly based on Haacke et al. "*Magnetic Resonance Imaging*" [104, Ch.9 and 10] and Bernstein et al. "*Handbook of MRI pulse sequences*" [18, Ch.8].

2.1.8 Imaging Sequences

In this section, three basic sequences to cover the k-space are described: the *GRE*, the *SE* and the Echo Planar Imaging (EPI) sequence. The description includes the applied *RF* and gradient objects and the corresponding k-space trajectory.

2.1.8.1 Gradient Echo Sequence (GRE)

The simplest sequence to acquire *MR* data in k-space is the *GRE* sequence, with its sequence diagram and the corresponding k-space trajectory shown in Figure 2.8. It consists of an excitation *RF* pulse with arbitrary flip angle α and a corresponding slice selective gradient, according to Sections 2.1.4 and 2.1.7.1. To acquire a symmetric echo, a prephasing gradient in read direction is necessary with half the gradient moment (area) and opposite polarity of the actual read out gradient. After the excitation, all spins perform a coherent precession, which corresponds to the central k-space position ((1) in Figure 2.8). The prephasing corresponds to a movement to the left margin of the k-space ((2) in Figure 2.8). The phase encoding gradient is necessary to perform a phase encoding according to Eq. (2.62), leading to a movement in vertical direction in k-space ((2)-(3) in Figure 2.8). Magnitude and timing of the readout gradient determine the echo time, where a Free Induction Decay (FID) echo is recalled at the center of the readout gradient, when the prephasing gradient moment is compensated ((4) in Figure 2.8). The magnitude of the readout gradient determines the velocity traveling in k_x direction and with that the readout bandwidth according to Eq. (2.67) in Hz/pix. The signal for *GRE* sequences decays with T_2^*.

2.1.8.2 Spin Echo Sequence (SE)

The *SE* sequence also starts with a slice selective excitation pulse with a typical flip angle of $\alpha = 90°$. Compared to *GRE*, in the *SE* sequence an additional *RF* pulse is applied after TE/2, the so called refocusing pulse, with a typical flip angle of $\beta = 180°$. Due to this 180° flip, all dephasing induced by time constant field inhomogeneities inside a voxel, can be recovered at echo time TE, so that the signal at TE decays with T_2 rather than T_2^*. To reach the maximum signal, the center of the readout gradient has to be exactly at

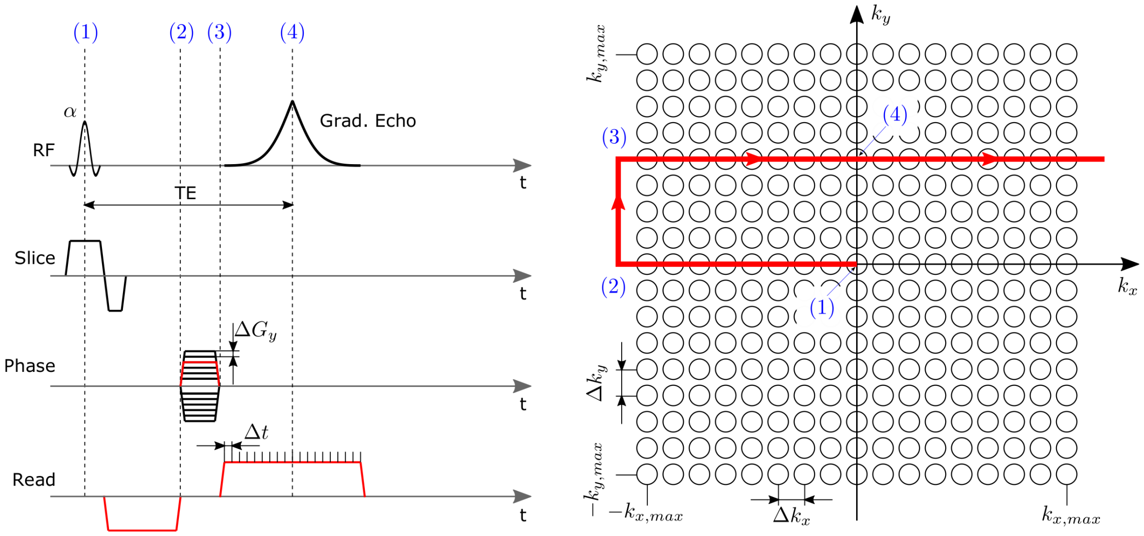

Figure 2.8: (Left): Sample sequence diagram for a GRE sequence showing RF, and the gradients in slice selection, phase and frequency encoding (read) direction. (Right): Corresponding k-space trajectory. Numbers from 1 to 4 indicate prominent points in the sequence diagram and the corresponding position in k-space. The sample trajectory for one TR and the corresponding gradients are highlighted in red.

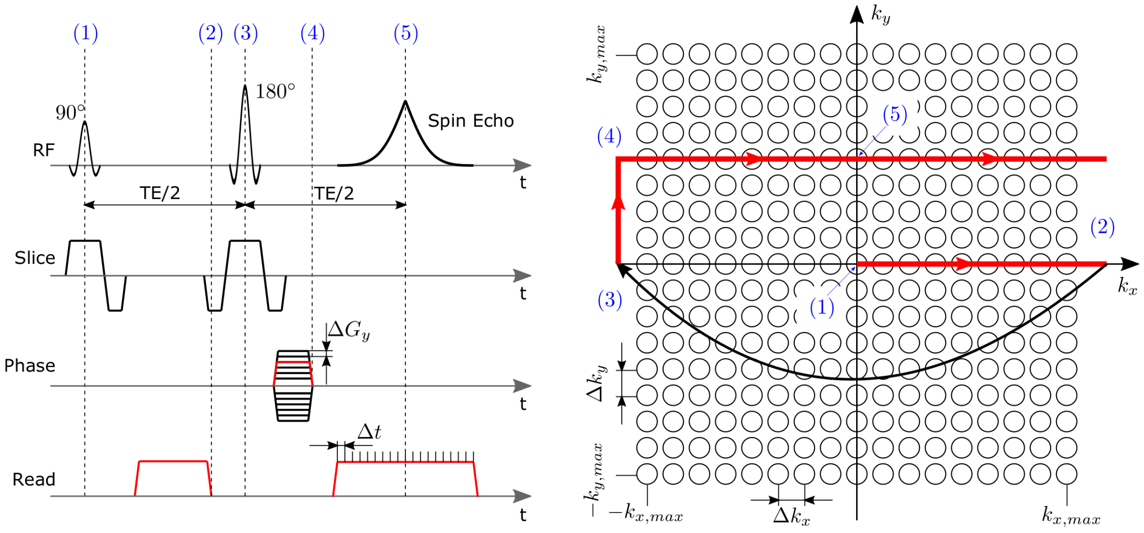

Figure 2.9: (Left): Sample sequence diagram for a SE sequence showing RF, and the gradients in slice selection, phase and frequency encoding (read) direction. (Right): Corresponding k-space trajectory. Numbers from 1 to 5 indicate prominent points in the sequence diagram and the corresponding position in k-space. The sample trajectory for one TR and the corresponding gradients are highlighted in red.

TE, otherwise additional T_2^* decay is present. The prephasing gradient is usually applied before the refocusing pulse, so that it has the same polarity as the readout gradient, because the acquired phase is reversed by the refocusing pulse ((2)-(3) in Figure 2.9). The

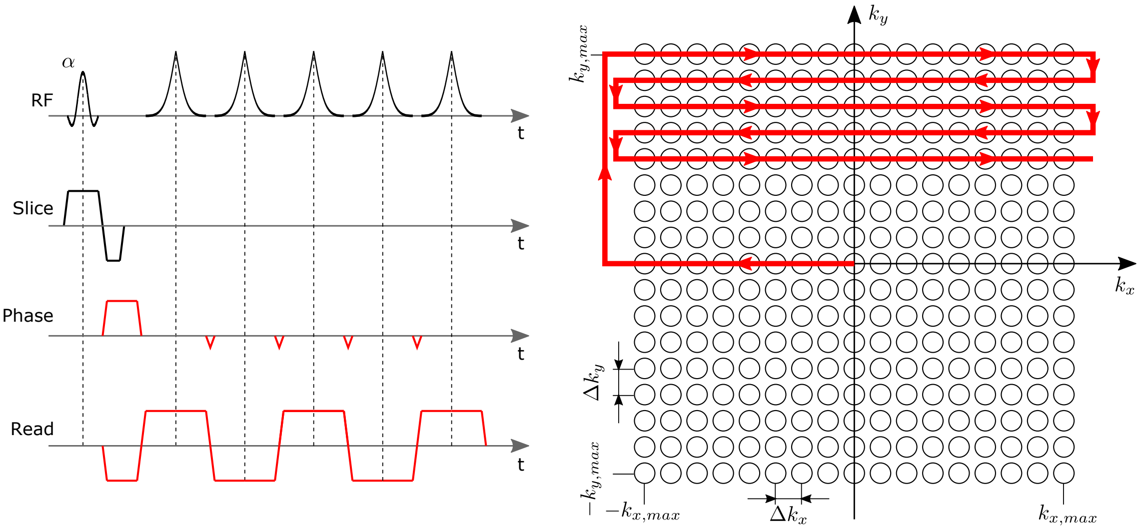

Figure 2.10: (Left): Sample sequence diagram for a EPI sequence showing RF, and the gradients in slice selection, phase and frequency encoding (read) direction. (Right): Corresponding k-space trajectory. The sample trajectory for the first four echos and the corresponding gradients are highlighted in red.

phase encoding gradient can be applied before or after the refocusing pulse. In general, the *SE* sequence has a higher signal depending on the T_2 to T_2^*, but a longer minimum TE and an increased *SAR* due to the additional *RF* pulse. The sequence diagram is shown in Figure 2.9.

2.1.8.3 Echo Planar Imaging (EPI)

The *EPI* sequence is one of the fastest acquisition strategies in *MRI*, where the whole k-space data is acquired after a single excitation pulse. This is achieved by periodically inverting the polarity of the readout gradient, so that the signal gets refocused multiple times. The phase encoding is changed from line to line by a small gradient blip during the readout gradient slope. To reach the edges of k-space, a prephasing gradient is applied in phase and readout direction directly before the readout train begins. Due to the long readout train, this sequence is very prone to artifacts due to offresonances, timing errors, relaxation, and other hardware imperfections which can be corrected to a certain degree. The sequence diagram is shown in Figure 2.10.

2.2 Homogeneity Limitations of the B$_0$ Field

In this section, all aspects concerning static magnetic field homogeneity/inhomogeneity are considered. This includes the generation of the magnetic field with the involved coils and the the technical limitations. Furthermore, the influence of matter on the magnetic field is considered, which is described by the material dependent magnetic susceptibility χ. The shape of an object inside a magnetic field has a strong influence on the field inside and outside the object as well, described by the concept of a demagnetization factor, which is also considered on the example of ellipsoids of revolution. The influence of inhomogeneities in the B_0 field strength on the signal is described, as well as its spatial behavior. This section ends by a description of active shimming, a method to dynamically improve the field homogeneity in a certain volume.

2.2.1 Field Generation – Technical Limits of Homogeneity

In the early days of *MRI*, the static magnetic field was generated with permanent magnets or resistive coils at room temperature. With these settings, only a low degree of spatial homogeneity can be reached, and the thermal and temporal field stabilities are quite low. Furthermore, these systems are restricted to quite low field strength $< 500\,\mathrm{mT}$. Except some few applications such as Fast Field Cycling (FFC), where the B_0 field strength is changed during the acquisition [30, 43], today, the $\vec{B}_0$ field is generated by a superconducting magnet lying at temperature of liquid helium ($\approx 4\,\mathrm{K}$) in nearly every clinically relevant case. It is already a huge technical effort, to generate a magnetic field of 1.5 T in air in dimensions that a human can be investigated. The necessary effort increases with field strength, so that only one company exists world wide producing commercial systems at 7 T, which can be used clinically. The effort producing a magnet with this field strength fulfilling the homogeneity requirements to perform magnetic resonance imaging increases further. Even though, the magnets are quite big and heavy, there only exist a very small spherical volume in the center of the bore of about 45 cm in diameter with a peak to peak homogeneity $< 5\,\mathrm{ppm}$, the so called iso-center. The temporal field stability of such a magnet is about $< 0.05\,\mathrm{ppm/h}$ [120, Part I., Ch.1]. For a 3 T magnet, this means that the static field inside this region does not deviate more than $\approx \pm 7.5\,\mu\mathrm{T}$, this range is about one third of the earth magnetic field of about 48 µT. However, outside this investigation region, the homogeneity decreases rapidly. To reach such values, a careful coil design with several superconducting coils in perfect geometrical orientation is required. This also includes the active shield coils reducing the magnetic field outside the bore. The field generated by each coil has to fulfill the Maxwell's equations (Eq. (2.89)) for the magnetostatic case, in particular the Biot-Savart's law, described later (Eq. (2.87)). The simplest configuration to produce a homogeneous field is between two parallel oriented coils, placed in a distance equal to their diameter (Helmholtz configuration). Beside that, also the magnetic properties of the whole housing, including the cyrostat, and all mounting devices, which mostly consist of stainless steal, must be considered in magnet design in order to produce such a homogeneous field. However, manufacturing tolerances occur during the production process, leading to a certain deviation of the expected main field homogeneity. These deviations have to be corrected individually after the system setup, which is called passive or active shimming. Passive shimming is performed by placing ferromagnetic objects (e.g. iron plates) at a certain position, which influences the main field in a way to improve its homogeneity. Active shimming is done by additional shim coils, which are usually able to correct inhomogeneities up to 2^{nd} order spherical harmonics, where their default currents are determined during set up, which is called "Tune-Up". Furthermore, the shim currents are adapted before each measurement to compensate patient induced field distortions (for more details, see Section 2.2.5). Also, the dimensions of the magnet itself influence the homogeneity inside. In recent years, manufactures tried to reduce the magnet dimensions, to reduce the required space in clinics, and to increase the size of the bore diameter (e.g. 70 cm) to increase patient comfort. In both cases, in general, the homogeneity suffers and also shimming gets more difficult.

Even though, these methods allow to build magnets with already impressive homogeneity, but for many applications in *MRI* this is still not sufficient. For the separation of fat and water signals [67], which lie 3.5 ppm apart, the deviation of ≈ 5 ppm is already to much. Therefore, an additional field mapping is required to correct its influence. This section is based mainly on Hennig et al. "*High-Field MR Imaging*" [120, Part I., Ch.1].

2.2.2 Influence of Matter on the Magnetic Field Homogeneity

Beside the technical influences on the field homogeneity caused by hardware imperfections (see Section 2.2.1), the human body itself leads to a distortion of the magnetic field. These "body"-induced distortions are usually much more local and dominate the overall inhomogeneity for in-vivo applications. Of course, the patient induced distortions vary from subject to subject, and hence, the currents in the shim coils have to be adjusted before each scan, to maximize the homogeneity in the specific volume of interest. As already mentioned, global shim coils are usually able to produce spherical harmonic correction fields of up to 2^{nd} order, nevertheless, the shim capability for local distortions is limited. Today huge improvements are achieved by using local shim coils integrated, e.g., in the head coil, which are much better suited to correct these local variations.

The influence of matter on the magnetic field homogeneity can be separated into two different contributions: the first contribution arises form the magnetization behavior which is specific for a certain material and can be described by the magnetic susceptibility χ. The second contribution arises from the object's shape, leading to a so called demagnetization field inside the object counteracting the externally applied field, if the susceptibility inside differs from that outside the object. This can be described by the demagnetization factor ξ for specific object shapes.

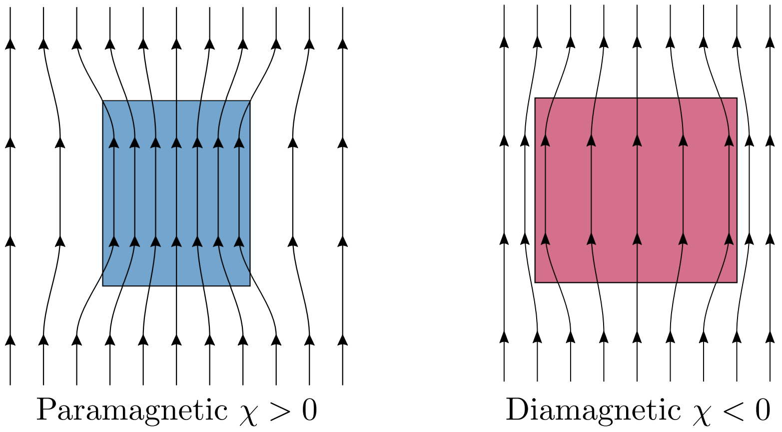

Figure 2.11: The general magnetic material behavior is described by the magnetic susceptibility χ. In paramagnetic materials $\chi > 0$ the field strength inside increases, so that the field lines are "pulled" into the material. In diamagnetic materials the field lines are "pushed" out of the material, leading to a reduced field strength inside.

2.2.2.1 Material dependent Influence – Magnetic Susceptibility χ

The main reason for patient induced field distortions is a variation in the magnetic susceptibility between different kind of tissues. The most severe distortions occur at air/tissue interfaces, where air chambers inside the body (e.g. nasal sinuses or the lung) are most problematic. The magnetic susceptibility χ describes the interaction of matter with the external magnetic field (see Figure 2.11), where χ theoretically can have values in the range of $\chi = [-1, +\infty)$. In *MRI*, the magnetic field strength is referred to the $\vec{B}$ field, which is actually called magnetic flux density or magnetic induction in electrodynamics. To account for the material behavior, an additional field (the $\vec{H}$ field) is introduced, which is referred to as magnetic field strength in electrodynamics. In vacuum both fields are proportional to each other by the permeability constant $\mu_0 = 1.256637 \cdot 10^{-6}\mathrm{V\,s\,A^{-1}\,m^{-1}}$

$$\vec{B} = \mu_0 \vec{H}. \tag{2.68}$$

If matter is placed in the field, it gets magnetized, where the gained magnetization $\vec{M}$ acts back onto the external field. The dimensionless susceptibility χ describes the magnetizability of the matter according to the $\vec{H}$ field

$$\vec{M} = \chi \vec{H}. \tag{2.69}$$

Using Eqs. (2.68) and (2.69), the $\vec{B}$-field can be written as

$$\vec{B} = \mu_0(\vec{H} + \vec{M}) = \mu_0(1 + \chi)\vec{H} = \mu_0 \mu_r \vec{H}, \tag{2.70}$$

with the relative permeability μ_r given as $\mu_r = (1+\chi)$. χ is not necessarily a scalar value, in non-isotropic media it can also have the form of a tensor, meaning that $\vec{B}$ and $\vec{H}$ are pointing in different directions. It was shown by Li et al. [182] that human brain tissue shows slight anisotropic behavior, but in general, χ is assumed to be scalar in *MRI*. In general, we can distinguish between three kinds of behavior:

- **Diamagnetic materials** ($\chi < 0$): The orbiting electrons in diamagnetic atoms can be seen as circular currents in the classical description. This circular currents are influenced by induction according to Lenz's law, so that they counteract the external field. This means, the magnetic field is reduced inside diamagnetic materials, which can be visualized by "pushing" the field lines out of the material. The perfect diamagnetic material is a superconductor ($\chi = -1$), where the field inside is perfectly canceled. Diamagnetism is present in every material.

- **Paramagnetic materials** ($\chi > 0$): Similar to the nuclear spin (see Section 2.1.1), the electron has also a magnetic moment due to its quantum mechanic angular momentum which is responsible for the paramagnetic behavior. If the atom has an uncompensated magnetic moment, it is partially aligned with the direction of the external field, leading to an amplification of the field inside. The magnetic moment of the nucleus can be neglected in this consideration, since the magnitude is lower by three orders and hence the contribution to paramagnetism can be neglected. Paramagnetism usually dominates over the diamagnetic effect, which is always present.

- **Ferromagnetic materials** ($\chi \gg 0$): In ferromagnetic materials, a strong orientational alignment of the atomic magnetic moments occur, leading to a massive amplification of the external field and magnetization can be present even without an external field. The susceptibility values are in a range of $\chi \approx 10^3 \dots 10^6$, showing strong saturation at higher field strength. Due to the high level of magnetization, the force acting on objects containing ferromagnetic materials is very high. Thus, due to safety, objects containing such materials should never be inside the magnet room. Besides safety, the only relevance of ferromagnetic materials in *MRI* is passive shimming.

Magnetic susceptibility spans a range over more than 6 orders of magnitude, but most biological tissues are slightly diamagnetic with susceptibility values in the range of $\chi_{\text{tissue}} = -11 \dots -7\,\text{ppm}$. This is approximately in a range of $\pm 20\,\%$ around the susceptibility of water ($\chi_{H_2O} = -9.053\,\text{ppm}$ at $37\,^\circ\text{C}$) [253]. There are only a few exceptions in biological tissue which are paramagnetic, mostly molecules containing iron, such as hemoglobin for the oxygen transport in red blood cells, and ferritin which is mostly stored in brain and liver tissue. For example, hemoglobin is only paramagnetic in the deoxygenated form, however, even in venous blood the diamagnetic behavior of water and proteins is dominant. Air is also slightly paramagnetic $\chi_{\text{Air}} = 0.36\,\text{ppm}$, which is responsible for comparable strong field distortions at air/tissue interfaces.

Material	**Mass Density** ρ $\mathrm{kg\,m^{-3}}$	**Susceptibility** χ ppm
Stearic Acid (Lipid)	–	-10.0
Iron free Hemoglobin	–	-9.91
Water (37 °C)	993.35	-9.053
Blood Plasma	1027	-9.05
Water (20 °C)	998.23	-9.032
Human Tissues	$\approx 1000 \dots 1050$	$\approx -11.0 \dots -7.0$
Cortical Bone	–	-8.86
Whole Blood (deoxygenated)	1057	-7.9
Red Blood Cell (deoxygenated)	1093	-6.52
Liver (severe iron overload)	–	≈ 0.0
Vacuum	0	0
Hemoglobin Molecule (deoxygenated)	1335	+0.15
Air	1.29	+0.36
Ferritin	1494	520

Table 2.2: Magnetic susceptibility χ and the corresponding density ρ for some biological tissues and biological relevant materials in MRI according to Schenck [252] and Schenck [253].

Typical values for biological relevant materials are given in Table 2.2. In daily life and also in most common technical applications, the susceptibility of non-ferromagnetic materials (including biological tissue) is so low (a few ppm), that it normally cannot be distinguished from vacuum; and hence, such materials are referred to as non-magnetic. Also when considering the *RF* field (see Section 2.3), the susceptibility is usually neglected by using $\mu_r \approx 1$ or $\chi \approx 0$. However, for the consideration of the static magnetic field homogeneity, the susceptibility of the involved materials plays a central role, because of the very high homogeneity requirements in *MRI*. If an object consists of a material with a certain susceptibility χ, is brought into a magnetic field $\vec{B}_0$, the field inside the object changes and also the field around it, is influenced. This influence depends on χ, the shape of the object and the orientation of it with respect to the external field direction. The previous considerations are partially based on Preis K. Lecture notes "*Elektrodynamik TE*" [232, Ch.3 and 4] and Schenck [253].

2.2.2.2 Shape dependent Influence – Demagnetization Factor ξ

In general, Eqs. (2.69) and (2.70) are only valid when the whole volume is filled with the given material. If an object with homogeneous and isotropic susceptibility is placed in a magnetic field, the material is magnetized according to Eq. (2.69) and the field generated by this magnetization $\vec{M}$ overlays with the external causing field in such a way that the Maxwell equations Eq. (2.89) are fulfilled. For an arbitrary shape, the calculation of these field distortions can be very troublesome and some methods to tackle this problem

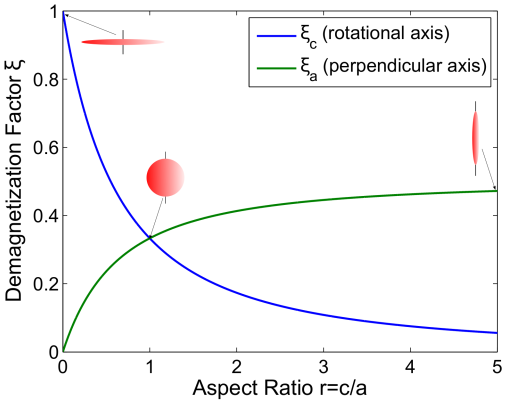

Figure 2.12: Demagnetization factor ξ for ellipsoids of revolution along its rotational axis and the axis perpendicular to it depending on their aspect ratio r, according to Eq. (2.74). For aspect ratio i$r = 1$ the rotational ellipsoid is a sphere, for $r \gg 1$ it has the shape of a sharp needle approximating a long cylinder and for $r \approx 0$ it is a thin disk approximating a plate.

are described later. For one class of geometrical objects, the ellipsoid, the field distortion calculation can be achieved with algebraic equations instead of differential equations. This is considered here, since many objects can be approximated with an ellipsoid such as a thin disk, a long cylinder or a sphere (exactly), and the general behavior of certain shapes can be estimated. For an ellipsoidal object with homogeneous susceptibility placed in a homogeneous external field, the field inside is constant over the whole object. If the ellipsoid is placed in such a way that one of its principle axes is aligned along the external field $\vec{H_0}$, the internal induced field $\vec{H_i}$ can be described by the demagnetization factor ξ and the magnetization $\vec{M}$ of the material

$$\vec{H_i} = -\xi\vec{M}. \tag{2.71}$$

Using $\vec{H} = \vec{H_0} + \vec{H_i}$, Eqs. (2.68), (2.69) and (2.71), and plugging into Eq. (2.70), this leads to an expression for the resulting total internal magnetic field $\vec{B}$ depending on the shape, susceptibility, and the external field $\vec{B}_0$

$$\vec{B} = \vec{B}_0 \frac{1+\chi}{1+\xi\chi}. \tag{2.72}$$

If the applied external field is not parallel to one of the principle axes, the resulting field can be calculated by a superposition of the projected components onto the principle axes of the ellipsoid. In this case, the internal field is not parallel to the applied external field any more, not even with isotropic susceptibility χ. A general ellipsoid has three principle axes with a length of each semi-axis of a, b, and c, respectively. In this case, also three independent demagnetization factors, one for each axes ξ_a, ξ_b, and ξ_c exist with the condition

$$\xi_a + \xi_b + \xi_c = 1. \tag{2.73}$$

In the next step, the current consideration is further restricted to ellipsoids of revolution, which are rotational symmetric. In this case, the length of two principle semi-axes are equal ($a = b$) leading to $\xi_a = \xi_b$, with an axis of rotational symmetry along the third principle semi-axis c. The demagnetization factors can be expressed in terms of the ratio between the two independent semi-axes $r_a = c/a$. In the special case of $r_a = 1$, the object becomes a sphere, where all three semi-axes are equal to the radius R of the sphere, leading to $\xi_a = \xi_b = \xi_c = 1/3$ under the condition of Eq. (2.73). For $r_a \gg 1$, the ellipsoid is shaped as a needle approximating a long thin cylinder leading to $\xi_a = \xi_b = 1/2$ and $\xi_c = 0$ as limit of Eqs. (2.74) and (2.75). This special case also holds for a real cylinder at least in its center, whereas the field distributions around the top and bottom of the cylinder are completely different. For $r_a \ll 1$, the ellipsoid is shaped as a disk approximating a flat circular plate leading to $\xi_c = 1$ and $\xi_a = \xi_b = 0$. For the general case, the demagnetization factors are given by the following relations, which is further depicted in Figure 2.12,

$$\begin{aligned}
\xi_c &= \frac{1}{r_a^2 - 1}\left(\frac{r_a}{\sqrt{r_a^2-1}}\log\left(r_a + \sqrt{r_a^2-1}\right) - 1\right) && \dots \quad r_a > 1,\\
\xi_c &= 1 - \left(\frac{r_a}{\sqrt{1-r_a^2}}\right)^2\left(\frac{\sin^{-1}\left(\sqrt{1-r_a^2}\right)}{r_a\sqrt{1-r_a^2}} - 1\right) && \dots \quad r_a < 1,\\
\xi_c &= \tfrac{1}{3} && \dots \quad r_a = 1.
\end{aligned} \tag{2.74}$$

The demagnetization factor for the two perpendicular principle axis is given by Eq. (2.73) and $\xi_a = \xi_b$ as

$$\xi_a = \frac{1 - \xi_c}{2}. \tag{2.75}$$

The demagnetization factor can vary in the range $\xi = [0, 1]$, where a value of $\xi = 0$ means that the field inside the object does not depend on the shape, but only on the susceptibility of the object, so that Eq. (2.72) reduces to $\vec{B} = \vec{B}_0(1 + \chi)$. A value of $\xi = 1$ denotes that the shape dependency compensates the influence of the susceptibility on the field inside the object. The field inside is the same as the externally applied field and Eq. (2.72) reduces to $\vec{B} = \vec{B}_0$. The field outside the ellipsoid, which leads to a field distortion in the surrounding, is given as a simple dipole field with a magnetic moment of $\vec{\mu} = V\vec{M}$, where $\vec{M}$ is the magnetization inside the volume V of the object. In the general case, this stray field cannot be described in terms of simple functions, but only by the use of ellipsoidal harmonics. However, for two geometries, the sphere and the cylinder, the external field can be expressed with very simple relations. Under the assumption $\|\chi\| \ll 1$, expressions for the z-component of the $\vec{B}$ field distributions ΔB_z are given for the following three cases below, where $\Delta\chi = \chi_{\text{inside}} - \chi_{\text{outside}}$. This is further visualized as contour plot with the corresponding field lines in Figure 2.14 and as 3D surface plot in Figure 2.13.

1. Sphere with radius a centered at origin:

$$\begin{aligned} \Delta B_{z_{in}} &= \frac{2\Delta\chi B_0}{3} \\ \Delta B_{z_{out}} &= \frac{\Delta\chi B_0}{3}\frac{a^3\left(2z^2-x^2-y^2\right)}{\left(x^2+y^2+z^2\right)^{5/2}} \end{aligned} \tag{2.76}$$

2. Cross-section in the center of a cylinder with radius a and its long axis parallel to $\vec{B}_0$:

$$\begin{aligned} \Delta B_{z_{in}} &= \Delta\chi B_0 \\ \Delta B_{z_{out}} &= 0 \end{aligned} \tag{2.77}$$

3. Cross-section in the center of a cylinder with radius a and its long axis perpendicular to $\vec{B}_0$:

$$\begin{aligned} \Delta B_{z_{in}} &= \frac{\Delta\chi B_0}{2} \\ \Delta B_{z_{out}} &= \frac{\Delta\chi B_0}{c}\frac{a^2\left(z^2-x^2\right)}{\left(x^2+z^2\right)^2} \end{aligned} \tag{2.78}$$

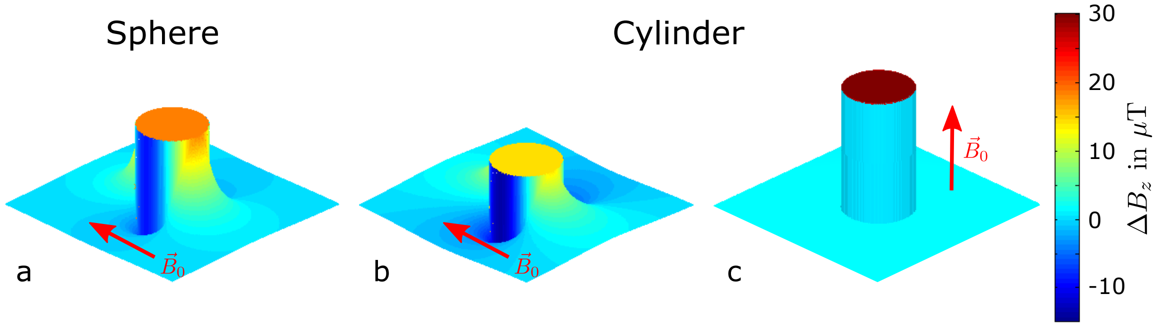

Figure 2.13: Surface plot for the field distortion ΔB_z introduced by a spherical object (a) and a cylindrical object (b) and (c) around it according to Eqs. (2.76) to (2.78). For the cylindrical object it is shown for two field orientations, one perpendicular to the long axis (b) and one parallel to it (c). The simulation was performed for a susceptibility difference between in- and outside of $\Delta\chi = 9.36\,\text{ppm}$ which is approximately the same as between air and tissue. Furthermore, the continuity condition for the $\vec{B}$ field component normal to the interface can be seen in (a) and (b). The field inside and outside the object is equal at the boarder surface, when only the perpendicular component to the surface is present.

The consideration of the demagnetization factor is based on a very detailed description by Schenck [253] for ellipsoids of revolution. A much more detailed mathematical description for general ellipsoids is given by Stoner [287] and Osborn [225]. However, the concept of the demagnetization factor can be extended to other shapes as well, e.g. for several rotational symmetric objects [272]. This concept is further extended to non-ellipsoidal objects by Joseph and Schlöemann [145], leading to a kind of demagnetization factor field with varying values over the object. Of course, no closed form solution exist for arbitrary shaped objects; hence, the calculation of the field distortion can only be done numerically.

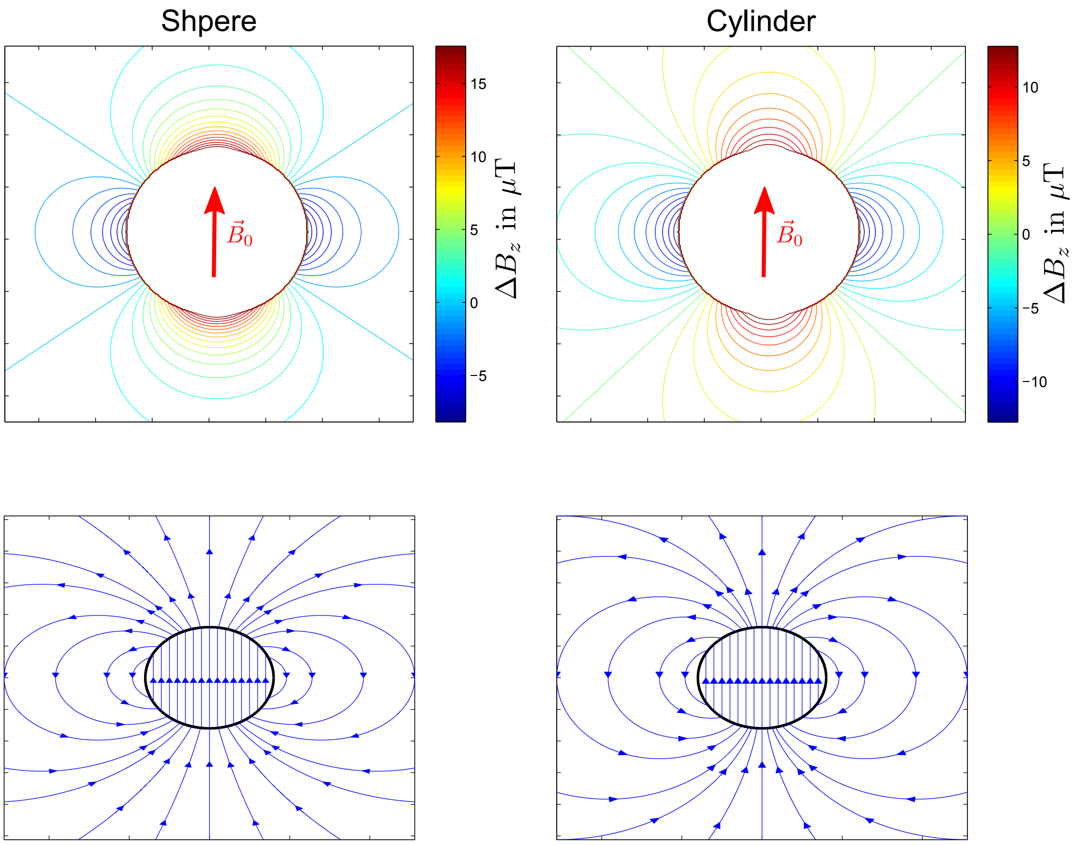

Figure 2.14: 1st row: Contour plots for the field distortion ΔB_z introduced by a spherical (left) / cylindrical object (right) around it according to Eqs. (2.76) and (2.78). Inside the object the field is constant. For the cylindrical shape this is only valid in the center of a long cylinder. The simulation was performed for a susceptibility difference between in- and outside of $\Delta\chi = 9.36\,\text{ppm}$ which is approximately the same as between air and tissue. 2nd row: Corresponding field lines gained by the magnetization of the material, sphere (left) and cylinder (right).

For this purpose, many methods were proposed, i.e., a method for arbitrary susceptibility distributions in 2D [20] and an extension for 3D geometries [19] evaluated on a two-compartment model, so that their results can be compared to the well known analytic solutions described above. Results for numerical field calculations in a two-compartment human head wire-grid model were presented by Li et al. [181]. Although, only air and normal tissue are modeled, the results are already in good accordance to measured data. Another numerical solution is presented in [295] based on the algorithm of [19], where a four-compartment tissue model is derived from a Computer Tomography (CT) scan.

Despite the negative effects occurring due to the susceptibility induced field perturbations, this can also be used as a feature as it is done in Quantitative Susceptibility Mapping (QSM) and Susceptibility Weighted Imaging (SWI). These techniques use the susceptibility distribution in tissue as a biomarker for several diseases [316, 330] or for the quantification of iron in white matter brain tissue [103, 167]. Furthermore, the susceptibility difference of deoxygenated blood is used to image the venous vascular system [54].

2.2.3 Influence on the MR-Signal

The influence of inhomogeneous static magnetic field on the *MR* signal is very versatile and depends on the spatial distribution of the field distortion, the field strength, and the also the imaging sequence. In general, one can distinguish between macroscopic, mesoscopic, and microscopic field variations. The influence of macroscopic field variations (larger than the voxel size) basically consists of a spatially varying signal phase and geometric distortions in Fourier encoding and slice selective excitation. Mesoscopic field variations are smaller than the voxel size and lead to a signal loss due to dephasing and microscopic field variations have a range smaller than the diffusion length of water, so that they cannot be treated as time independent. This section is mainly based on Hennig et al. "*High-Field MR Imaging*" [120, Part III.] and Haacke et al. "*Magnetic Resonance Imaging*" [104, Ch.20], where a very detailed description of this topic is given. Furthermore, a good overview over the influence of the combination of static and *RF* field inhomogeneities on the signal of *SE* and *GRE* sequences and the corresponding image artifacts is described by Truong et al. [294].

2.2.3.1 Spatially varying Signal Phase

Macroscopic field variations mainly arise as a consequence of tissue interfaces, especially between air and tissue, according to the principles described above and can be expressed as a distortion field $\Delta B_0(\vec{r})$. Due to this, field distortion the local Larmor frequency changes according to

$$\Delta\omega_0(\vec{r}) = \gamma \Delta B_0(\vec{r}), \tag{2.79}$$

leading to phase variations of the complex signal over the entire object

$$\phi(\vec{r}) = \Delta\omega_0(\vec{r})\mathrm{TE} + \phi_0(\vec{r}). \tag{2.80}$$

This phase effect is used to map the field distribution (see Section 2.4). Field distortions are considered to be macroscopic if their spatial range is larger than the spatial resolution. Only if this is the case, a coherent signal inside a voxel can be gained, with varying phase over the *FOV*. This phase effect can only be seen in a *GRE* sequence, in a *SE* sequence the effect compensates due to the refocusing pulse in the second half of the echo time period, if the field variations are constant in time.

2.2.3.2 Geometric Distortions and Echo Shifting

Another very important effect caused by static magnetic field variations, $\Delta B_0(x, y, z)$, are geometrical distortions. According to Section 2.1.7, the spatial encoding is based

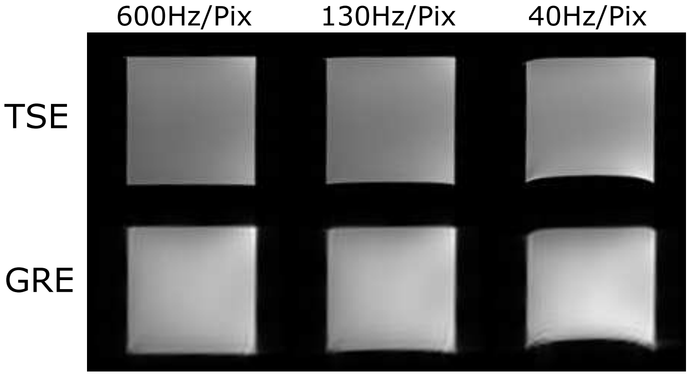

Figure 2.15: Geometric distortions measured on a cubic phantom with different readout bandwidths for a TSE and a GRE sequence. The slice is placed parallel to the surface of the cube. For 600 Hz/pix the distortions is smaller than the voxel size, whereas for 40 Hz/pix severe distortions can be seen, which are the same for both sequences. Distortions introduced by non-linear gradients are corrected by the scanner software.

on linearly varying gradient fields along the tree spatial axes, which leads to a linear frequency variation along the corresponding axis, see Eqs. (2.52) and (2.59). If additional field distortions occur, Eq. (2.52) changes to

$$B_z(x,y,z) = B_0 + G_x x + G_y y + G_z z + \Delta B_0(x,y,z). \tag{2.81}$$

Because the underlying Fourier transform inherently assumes Eq. (2.52) to be valid, this leads to a misregistration of the spin's spatial location. A certain frequency component is mapped to the wrong position in space. The shape and degree of the distortion depend on the relation between the gradient of the underlying field variation, $\nabla(\Delta B_0(x,y,z))$, and the strength of the actual imaging gradient. A constant field offset would simply shift an arbitrary object proportional to the field offset, because the spin's frequency is shifted. If the gradient of the distortion field points along the readout direction, then the investigated object is stretched / compressed if the field distortion increases / decreases the actual imaging gradient, because the frequencies in the object vary over a larger / smaller range. If in the extreme case, the field distortion compensates the imaging gradient the object will collapse to a Dirac delta, because no spatial encoding is present any more. If the gradient of the distortion field points along the phase encoding direction, the reconstructed image suffers from shearing distortion, because the axis of frequency encoding is rotated by a certain angle depending on the ratio between field distortion gradient and frequency encoding gradient. If a certain field distortion is present, the effect can be reduced by increasing the readout gradient, which on the other hand leads to a decrease in *SNR* because the receiving bandwidth has to be increased as well (see Eq. (2.48)). If the frequency variation is below the bandwidth per voxel, no image distortion can be seen in the reconstructed image. *GRE* and *SE* based sequences are effected equally by these kind of distortions, because the readout gradient is effected. However, the *EPI* sequence

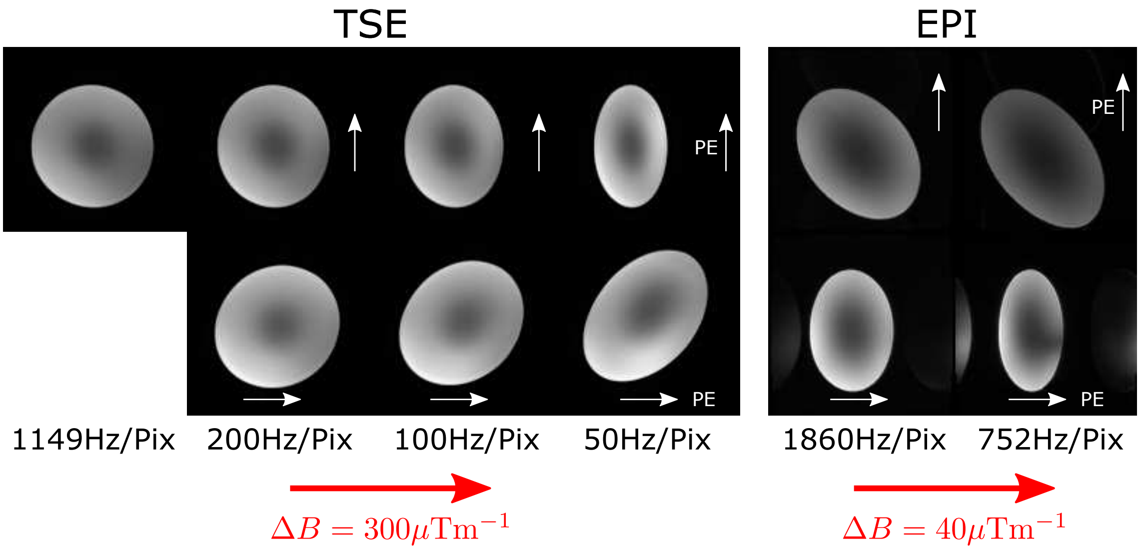

Figure 2.16: Influence of the phase encoding direction on geometrical distortions measured on a cylindrical phantom for a TSE and an EPI sequence. Top-left: Reference image with readout bandwidth of 1149 Hz/pix to be distortion insensitive. Left: Distortions are shown for the TSE sequence with a readout bandwidth of 200 Hz/pix, 100 Hz/pix and 50 Hz/pix with phase encoding direction (anterior-posterior) (1^{st} row) and (left-right) (2^{nd} row). To introduce distortions, a field gradient of $300\,\mu\mathrm{T\,m}^{-1}$ is applied for the TSE and of $40\,\mu\mathrm{T\,m}^{-1}$ for the EPI measurement on the right side. EPI data is measured with a readout bandwidth of 1860 Hz/pix and 752 Hz/pix.

is very prone to this kind of artifacts, because of the long readout duration and especially the low bandwidth in phase encoding direction. Even very low field variations can lead to severe distortion artifacts. Some examples for field distortions are shown in Figure 2.15 for the influence of different readout bandwidths on a *GRE* and a Turbo Spin Echo (TSE) sequence, measured on a cubic phantom, and in Figure 2.16 for different phase encoding directions for an *EPI* and a *TSE* sequence. Haacke et al. “*Magnetic Resonance Imaging*” [104, Ch.20]

Also, the slice selection is influenced by field distortions. According to the same ideas described for frequency encoding, the excited slice can be shifted, stretched or compressed if the field distortions is a constant offset, increases or decreases the slice selection gradient, respectively, because the bandwidth of the excitation pulse is constant. If the gradient of the distortion field is perpendicular to the slice selection gradient, the slice changes its orientation or gets bent according to the spatial variation of the field distortion. Also, the slice selection refocusing gradient can be affected, leading to incomplete phase refocusing along the slice after the excitation with the consequence of signal loss. Haacke et al. “*Magnetic Resonance Imaging*” [104, Ch.20]

However, the susceptibility of biological tissue is so low, that it will be far away from getting saturated (even at very high field strength), and hence, the susceptibility is independent of B_0. Therefore, the relative field change introduced by susceptibility variations is constant with field strength, nevertheless; the absolute value in Hz or µT varies linearly with B_0. Using the same readout bandwidth, the distortion artifacts increase with field strength. Hennig et al. "*High-Field MR Imaging*" [120, Part III., Ch.1]

Another effect occurring only in *GRE* sequences is the echo shifting. According to Section 2.1.8.1, the *GRE* sequence consists of a prephasing gradient with half the area of the following readout gradient with opposite polarity, so that the maximum echo amplitude occurs at the center of the readout gradient. An additional gradient arising from variations in the field distribution increasing / decreasing the prephasing gradient, leads to a decrease / increase of the readout gradient. This leads to the situation that the prephasing gradient is compensated after / before the center of the readout, so that the time point of the maximal echo amplitude is shifted. Furthermore, this offset is not constant over space leading to a spatial dependent echo time and a blurred k-space center. The consequence of this effect is an additional phase term and signal loss. Haacke et al. "*Magnetic Resonance Imaging*" [104, Ch.20]

2.2.3.3 Signal Loss due to Dephasing

Compared to macroscopic field variations, mesoscopic field variations which are below the voxel size lead to phase variations over the entire voxel resulting in a signal loss due to dephasing. Mesoscopic field variations can have different sources, e.g., the gradient of macroscopic field variations, as described above, also leads to a field variation over the voxel size. Furthermore, biological tissue is very inhomogeneous containing many different kind of microstructure, which is a potential source of mesoscopic field variations. One example would be, a red blood cell containing deoxygenated hemoglobin with different susceptibility compared to the surrounding tissue (see Table 2.2). As already described in Section 2.1.5.2, besides the transverse relaxation time T_2 arising from spin-spin interaction, this additional dephasing due to field inhomogeneity can be described by an additional time constant T_2'. This leads to an apparent transverse relaxation time T_2^* given in Eq. (2.40), under the assumption that this additional signal loss also behaves monoexponentially. However, this is only true for a very special hypothetical case, where a Lorentzian spin density distribution with a *FWHM* of $2\Delta x$ is assumed, where Δx is the voxel size and N_0 a normalization constant

$$\rho_0(x) = N_0 \frac{4\pi\Delta x}{4\pi^2\left(\Delta x^2 + x^2\right)}. \tag{2.82}$$

Using Eq. (2.82), and assuming a linear gradient of the background field distortion over the whole space, the integration over x leads to an ideal monoexponential decay with the time constant T_2' given as

$$\frac{1}{T_2'} = \gamma \|\Delta B_0\|. \tag{2.83}$$

Here, ΔB_0 is the field variation over the voxel size Δx. In practice, this is never fulfilled, which leads in the best case to a deviation of the time constant given in Eq. (2.83). Normally, the dephasing behavior differs from the monoexponential decay, where also damped oscillations similar to a “sinc” function can occur. The actual dephasing function depends on the subject, the hardware, the current shim state, and the patient positioning. Nevertheless, in most cases, the monoexponential decay with the appearing time constant T_2^* is used as a sufficient approximation. Very important for this consideration is that the field variations leading to T_2' are constant over time, so that they can be recovered after the refocusing in a *SE* sequence, whereas *GRE* sequences are affected by this additional decay.

The spatial extension of microscopic field variations is in the order of the diffusion length of the water molecules, so that the field variation can not be treated as constant over time. These field variations are introduced by spin-spin interaction on a microscopic level, leading to the irreversible T_2 decay described in Section 2.1.5.2. This section is mainly based on Haacke et al. “*Magnetic Resonance Imaging*” [104, Ch.20].

2.2.4 Spatial Behavior of the B_0 Field

The spatial behavior of the B_0 field can be derived from interface conditions of the different field quantities in electrodynamics. In the static or at least stationary case, which is fulfilled for B_0, there exist exact conditions for the behavior of the described field quantities at certain material interfaces. For that purpose, each field quantity $\vec{X}$ is separated into a component perpendicular to the surface $X_\perp$ and a component parallel to it $X_\parallel$. The rules are as follows, where the index a and b indicate medium a and medium b:

- $\vec{B}$ field: The component perpendicular to the surface $B_\perp$ behaves continuously, $B_{\perp_a} = B_{\perp_b}$ at the surface, whereas the parallel component $B_\parallel$ has to fulfill $B_{\parallel_a}/B_{\parallel_b} = \mu_a/\mu_b$ at the surface.

- $\vec{H}$ field: The component parallel to the surface $H_\parallel$ behaves continuously, $H_{\parallel_a} = H_{\parallel_b}$ at the surface, whereas the normal component $H_\perp$ has to fulfill $H_{\perp_a}/H_{\perp_b} = \mu_b/\mu_a$ at the surface.

All effects in *MRI* depend on the magnetic flux density $\vec{B}$ (in *MRI* denoted as magnetic field strength), so that only this quantity is of interest. Inside an object with homogeneous media, all field variations are continuous in space, only at interfaces between different media the parallel component of the magnetic field shows a discontinuity. The behavior of the magnetic field at material interfaces for both components can be seen in Figures 2.13 and 2.14. However, because the susceptibility variations in biological tissue are very low, also the discontinuities are very low, so that the spatial behavior is approximated in many cases as a continuous and smoothly varying function. This consideration is important for the development of proper regularization functionals, describing this characteristics. This section is mainly based on Preis K. Lecture notes “*Elektrodynamik TE*” [232, Ch.4].

2.2.5 Active Shimming

Besides the passive shim, where iron plates are placed at dedicated positions to compensate field inhomogeneities arising from hardware imperfections, the active shim is adjusted before each examination. As described in Section 2.2.2, the patient induced field distortions dominate over the hardware induced ones, and therefore a subject dependent local field distortion occurs. With active shimming, it is tried to compensate these local distortions to a certain degree in the desired measurement volume by using resistive shim coils, which are usually located around the bore.

According to Maxwell's equations Eq. (2.89), the magnetic field in any region without current sources has to satisfy the Laplace equation $\nabla^2\vec{B} = 0$. Compared to the z-component of the static magnetic field, the x and y-components are negligible and therefore, the Laplace equation can be written in terms of the z-component $\nabla^2 B_z = 0$. A complete basis of the solution space for the Laplace equation is given by the set of spherical harmonic functions with order of $l = [0, \infty)$ and degree of $m = [-l, l]$. Spherical harmonic functions are usually defined in spherical polar coordinates with radius r, polar angle $\vartheta = [0, \pi]$ and azimuthal angle $\varphi = [0, 2\pi]$. A short description and some examples up to 3rd order are given in Appendix A.1. Due to the cylindrical symmetry, every field configuration inside the magnet's bore can be described by a weighted sum of spherical harmonics X_l^m with the weighting coefficient A_{lm}

$$B_z(r, \vartheta, \varphi) = \sum_{l=0}^{\infty} \sum_{m=-l}^{l} A_{lm} r^l X_l^m(\vartheta, \varphi). \tag{2.84}$$

A very detailed description of the underlying math for the generation of axially symmetric magnetic fields is given by Garrett [88], including an error analysis for the achievable homogeneity up to 8th order. Therefore, shim coils are designed to produce a spherical harmonic field distribution, so that distortions until n^{th} order can be compensated, where n is the highest implemented order. Some exemplary coil geometries are described in Romeo and Hoult [245], and Figure 2.17 shows field distribution for 1st and 2nd order spherical harmonics measured on a spherical phantom. Commercially available scanners used in clinical practice normally use shim coils up to 2nd order, whereas the linear first order is implemented as offset in the gradient coils. However, there also exist experimental systems with higher order shim coils up to 4th [127] and 5th order [148], but 4th and 5th order are not complete. In Spielmann et al. [282], the effect of higher order shimming is investigated compared to solely linear correction; hence, showing massive improvements in field homogeneity, B_0 shifts, and line broadening in dedicated Region Of Interests (ROIs).

To adjust the current in the shim coils, so that the field gets maximal homogeneous, two thing are necessary: First the B_0 field distribution has to be measured and second the measured field distribution must be transformed into a current for each shim channel. For that purpose, several methods were proposed. In the early stage, shimming was

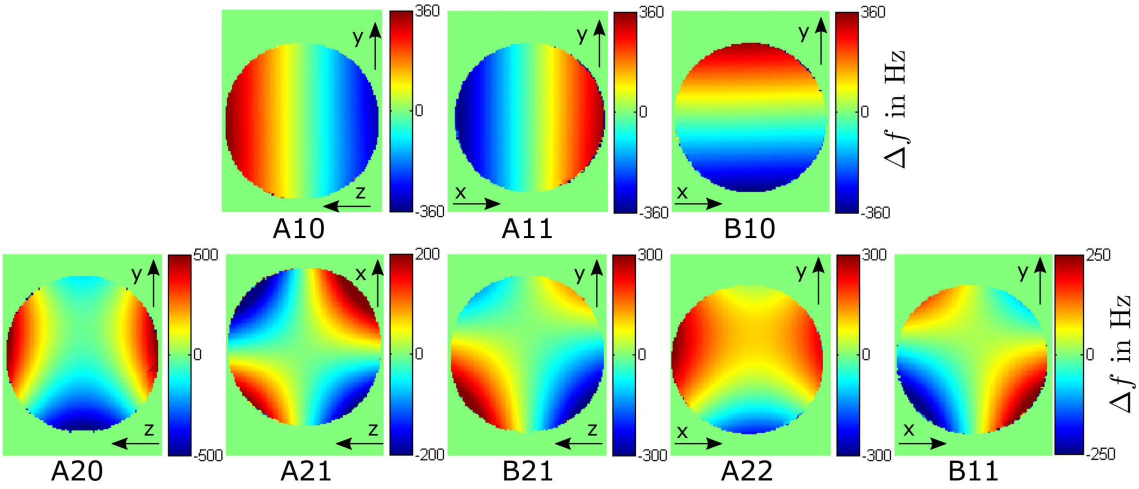

Figure 2.17: Influence of 1^{st} (first row) and 2^{nd} order (second row) shim coils measured on a spherical phantom. For each channel the field distribution is given as frequency shift in Hz.

mainly applied for spectroscopic applications, such that the B_0 field distribution was simply measured by the area under the *FID* [127]. This is equivalent to the line width of water, by using a Stimulated Echo Acquisition Mode (STEAM) sequence. The adaption of the shim currents was performed by doing a line search for every channel to reach the maximum *FID* area or the minimum line width. In [205], the B_0 field distribution is measured spectroscopically as the shift of the water peak gained by a *STEAM* sequence on a 31 dedicated positions. The values gained are used to fit the weighting factors of the spherical harmonics, which are proportional to the current in the corresponding shim coil. Also, a *STEAM* sequence is used in [101] to measure the field distribution along a few linear projections to decrease the acquisition time, under the assumption the shim coil behave perfectly spherical harmonic. Under this assumption, the measurement of such projections is enough to characterize the field in terms of spherical harmonics, which was shown by Gruetter and Boesch [102]. Modern shimming methods usually acquire a 3D low resolution field map ΔB_0 by acquiring *GRE* images with different TE, which is done in [148, 158, 258, 317] considering different aspects regarding to field mapping, where more details are described in Section 2.4. To determine the current in each shim coil I_{shim}, a reference measurement is necessary for each channel on a homogeneous phantom, while applying a unit current. This can be done once during system setup. The resulting field map for each channel at unit current is represented by the matrix $\mathbf{B}_0^{\text{shim}}(\vec{r})$ with size $N_x N_y N_z \times N_c^{\text{shim}}$, where N_x, N_y, and N_z represent the size of the field map in each direction and N_c^{shim} is the available number of shim coils. The optimal currents $\hat{I}_{\text{shim}}$ for each channel are determined by the least square solution between the measured field map $\Delta B_0(\vec{r})$ and the applied correction field for I_{shim}

$$\hat{I}_{\text{shim}} = \arg\min_{I_{\text{shim}}} \|\mathbf{B}_0^{\text{shim}}(\vec{r}) I_{\text{shim}} - \Delta B_0(\vec{r})\|_2^2. \tag{2.85}$$

This approach has the advantage that no assumption regarding the shim coil (perfect spherical harmonic behavior) is necessary; the current is determined based on the true influence of each coil on the resulting correction field. This so far is the standard on today's available commercial scanners, with up to second order spherical harmonic shim. However, many improvements were proposed over the last two decades, especially for the application on 7 T, where the most important are shortly summarized here.

The optimization problem to determine the shim coil currents (Eq. (2.85)) can get ill-posed when using higher order shim coils in combination with a small shimming volume and a low *SNR*. A regularized solution for this problem is proposed by Kim et al. [155], by using truncated Singular Value Decomposition (SVD). An investigation of the effect and necessity of higher order shimming was done by Pan et al. [226], where a 4th order spherical harmonics shim coil was used. Additionally, a head shim insert with up to 5th order is presented. It was shown by measurements that massive improvements could be reached by applying 4th order shimming over the whole head. Furthermore, it was shown by simulations up to 15th order that an improvement in field homogeneity can be gained up to 8th order spherical harmonic shim. For higher orders, no further improvement is possible. This indicates that the intrinsic limit for global shimming, given by local susceptibility variations between brain tissues, is reached. Further improvements could be reached with the introduction of dynamic shimming, where the shim currents are adjusted during the measurement to optimize the field homogeneity for every slice instead of the whole imaging volume in a multi-slice acquisition, using first order [25, 217] and second order [64, 163] spherical harmonics. Furthermore, dynamic shimming was also applied to compensate dynamic field fluctuations due to the change in air volume during breathing. According to reference scans to capture the chest motion, the shim currents are adjusted in real time during the breathing cycle with up to 2nd order [308] and up to 5th order spherical harmonics [21]. Shim coils are usually not equipped with an active shield winding, so that eddy currents produced by dynamic shimming can lead to a problem, which are usually compensated by a proper preemphasis.

Besides that, also other shimming methods were developed with small local shim array coils, producing non-spherical harmonic field distributions. Of course these fields are non-orthogonal, requiring a much higher number of channels to achieve the same performance. The adjustment procedure is the same as for spherical harmonic shimming (see Equation (2.85)), but the solution can be ill-posed, because of the linearly dependent contribution of the individual coils. However, there are many advantages which can overcome the loss of orthogonality. First, the constructions is much easier, because they usually consist of simple loop coils, which can be placed much closer to the shimming volume. The smaller coverage volume leads to a lower inductance and a lower power consumption. Due to the larger distance to the cryo-shield, no significant eddy currents are created, which leads in combination with the lower inductance to faster response times and much better behavior in dynamic shimming applications. A 48-channel multi-coil shimming system for dynamic shimming in the human brain was introduced by Juchem et al. [146] and a comparison to standard spherical harmonic shimming is given by Juchem et al. [147]. It was shown that the 48-channel multi-coils shim can reduce the average standard deviation of the global off-resonance over 5 subjects from 32.3 Hz to 13.3 Hz compared to 3rd order spherical harmonics. It was further shown that this system outperforms up to 5th order static and up to 4th order dynamic spherical harmonic global shim. Because space is limited and local shim coils compete with *RF* receive arrays, the latest improvement is to combine both functionalities into one coil winding. This is usually done by bridging the tuning capacitor with an additional inductance for the DC shim current. In [111], a proof of concept with a two coil array was presented, which was extended to 32 channels in [284, 296]. This technique was further improved, such that each *RF* element is subdivided into multiple shim elements to increase shimming capability [62]. However, local shimming is still not standard in clinical practice, most systems are custom made and only for research purposes. In the latest generation of commercially available scanners, local shim is already implemented, but only for dedicated regions with a low number of channels. For more details on the current state of the art in B_0 shimming, the reader is referred to a review given by Stockmann and Wald [283]. This section is partly based on Hennig et al. [119].

2.3 Homogeneity Limitations of the B$_1$ field

In this section, all necessary aspects concerning the homogeneity of the *RF* field are described. First, the difference between receive B_1^- and transmit field B_1^+ is discussed, including the influence of the corresponding coils. Furthermore, a method to calculate the field distribution of a certain coil, the Biot-Savart's law, is described and the influence of matter on the *RF* field is considered. When talking about the B_1 field, the energy deposition in the tissue under investigation is also a very important topic, as well as the influence of inhomogeneous *RF* field distributions on the *MR* signal. This section ends with a consideration of B_1 shimming, a method to increase the *RF* homogeneity in a certain volume by multiple transmit coils, and how to combine signals from multiple receive coils.

2.3.1 Technical Limitations – Transmit/Receive Coils

When talking about B_1 inhomogeneities, we have to distinguish between inhomogeneities of the transmit (B_1^+) and receive sensitivity (B_1^- field). As described in Section 2.1.4, the B_1^+ field is the magnitude of the *RF* field, which is proportional to the achieved flip angle in the object of interest (see Eqs. (2.27) and (2.28)). If the B_1^+ field varies over the measurement volume, also the flip angle does, leading to spatially varying signal and contrast. The absolute value of the B_1^+ field magnitude has to be determined to correct for such influences, many methods were proposed for that purpose and the most important are described in Section 2.5. The maximum magnitude for human full body imaging is

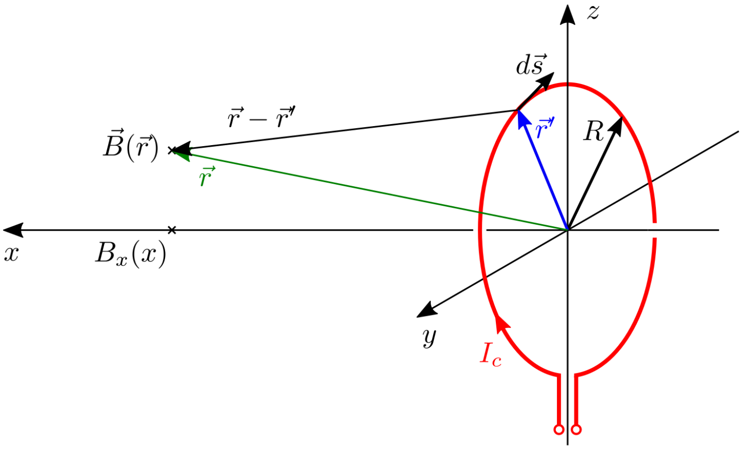

Figure 2.18: The magnetic field $\vec{B}(\vec{r})$ at position $\vec{r}$ is given by the current I_c in the loop coil placed in the $y-z$ plane according to Eq. (2.87).

usually in the range of $\approx 20\,\mu\mathrm{T}$, with dedicated small volume extremity coils values of about $\approx 45\,\mu\mathrm{T}$ can be achieved. According the principle of reciprocity, B_1^+ and B_1^- are identical for a specific coil. The principle of reciprocity says that the receive field B_1^- (receive sensitivity) for detecting a magnetization at a point $\vec{r}$ in space is equal to the necessary current in the coil to produce the same magnetization at point $\vec{r}$. In *MRI* usually different coils are used for transmit and receive, so that in general B_1^+ and B_1^- are completely different. On systems with a field strength of maximum 3 T, usually birdcage coils are used for transmit because of their better homogeneity. For receive, usually phased arrays of surface coils are used because of the better *SNR* independent on the field strength. The receive field B_1^- is a measure for the sensitivity of a certain coil to a signal arising from a specific point $\vec{r}$ in the measurement volume. To ideally combine the signals from such an array coil with a certain number of receive channels, the B_1^- from every channel should be known [246] (for more details see Section 2.3.7). Furthermore, B_1^- is also necessary for most reconstruction algorithms, when using undersampled multichannel data. In contrast to B_1^+, B_1^- usually can only be determined relatively, which is sufficient for coil combination and reconstruction purposes. A short description of methods to determine the B_1^- filed is given in Section 3.2.7. Due to the principle of reciprocity, the sources of inhomogeneity are the same for both B_1^+ and B_1^-.

There are several sources that lead to spatial inhomogeneous B_1 field distributions. First, of course, there is the coil geometry leading to an inhomogeneous field distribution. The field distribution $\vec{B}(\vec{r})$ at point $\vec{r}$ in space for any current density distribution $\vec{j}(\vec{r}')$ at point $\vec{r}'$ is given by the Biot-Savart's law, as integral over the contributing volume V. The Biot-Savart's law is derived from the Maxwell's equations and is given as

$$\vec{B}(\vec{r}) = \frac{\mu_0}{4\pi}\int_V \vec{j}(\vec{r}') \times \frac{\vec{r}-\vec{r}'}{\|\vec{r}-\vec{r}'\|^3} dV. \tag{2.86}$$

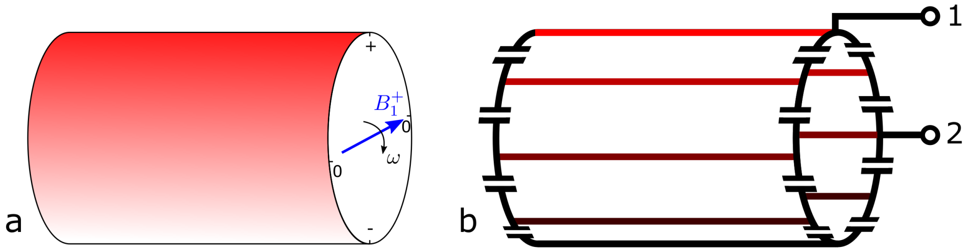

Figure 2.19: (a) A perfectly homogeneous B_1 field would be gained inside a cylinder for a sinusoidal current distribution on its surface. (b) The birdcage coil is an approximation for that, realized with a certain number of rods, connected by a ring on each side. The ring is cut up between each rod and connected with capacitor to induce a phase shift between the rods. Two sinusoidal signals are feed into port 1 and 2 in order to produce the desired current distribution. This figure is inspired by Hennig et al. "*High-Field MR Imaging*" [120, p.43].

This means for any point in space, the magnetic field strength depends on the current density in the whole volume. For a circular loop coil, which is a usual geometry for one element of an *MRI* receive array coil, the current density is restricted by the leads of the coil carrying the current I_c with the number of N_w windings. With that, Eq. (2.86) can be rewritten to an integral along the coil direction

$$\vec{B}(\vec{r}) = \frac{N_w I_c \mu_0}{4\pi} \oint_C d\vec{s}(\vec{r}\,') \times \frac{\vec{r} - \vec{r}\,'}{\|\vec{r} - \vec{r}\,'\|^3}, \tag{2.87}$$

where $d\vec{s}$ is pointing along the current direction (see Figure 2.18). Solving Eq. (2.87) for the central axis of the loop coil (with a normal vector along the x-direction), a closed form solution for the field component along that direction $B_x(x)$ is given as

$$B_x(x) = \frac{N_w I_c \mu_0}{2} \frac{R^2}{(R^2 + x^2)^{3/2}}, \tag{2.88}$$

where R is the coil radius [90]. The field strength for the loop coil decrease with $\approx 1/r^3$, leading to a quite inhomogeneous field distribution. This is shown as a simulation in Figure 2.20(b).

The birdcage coil, on the other hand, provides a much more homogeneous field distribution than the surface coil. The birdcage coil arises from a discrete approximation of a sinusoidal current distribution on the surface of a cylinder, which would lead to a perfectly homogeneous B_1 field, at least in air. In the birdcage coil, this is reached with discrete rods connected by a ring on each side. To reach the desired current distribution at Larmor frequency, the rings on each side of the coil are interrupted and connected with capacitors of equal value between each rod, as shown in Figure 2.19. Furthermore, two *RF* signals at ω_0 with 90° phase shift to each other are fed into the coil at connections perpendicular to each other to achieve a circular polarization (see Eq. (2.35)). This is a very good approximation, where the homogeneous field distribution is only disturbed close

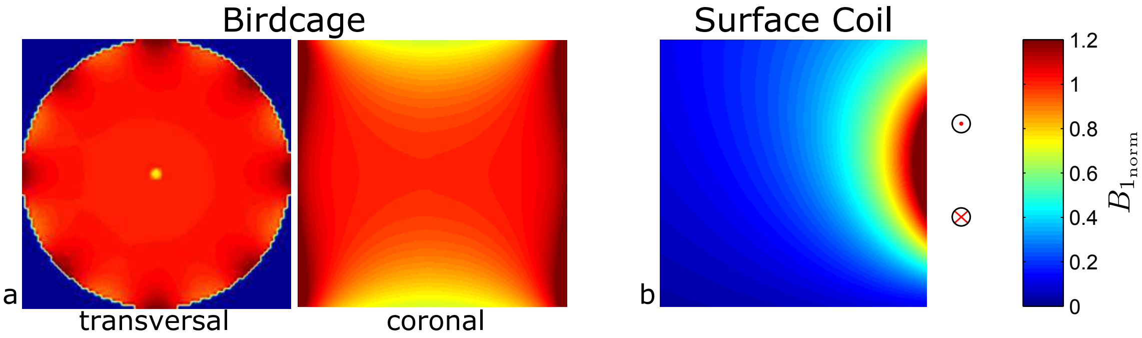

Figure 2.20: Simulated B_1^+ distribution for a birdcage coil in transverse and coronal orientation (a) and for a surface coil (b) in air. The field distribution inside the birdcage coil is very homogeneous especially in the center. Only near the rods a slight increase and near the upper and lower end a slight decrease can be observed. The birdcage coil has a diameter of 240 mm and a length of 250 mm. The surface coil shows a very rapid decay according the $1/r^3$ relation out of Biot-Savart's law. The surface coil is place 100 mm to the right of the image center, indicated by the two circles, and has a diameter of 64 mm. The birdcage simulation was performed with an FDTD solver [185] described by Liebig et al. [186] for 3 T, and the surface coil simulation was performed with a modified version of the Biot-Savart's law described by Gebhart et al. [89].

to the rods, which are usually far away of the tissue under investigation. A simulation for the field distribution in the birdcage coil is shown in Figure 2.20(a). This section is partly based on Hennig et al. "*High-Field MR Imaging*" [120, Part I., Ch.3] and Preis K. Lecture notes "*Elektrodynamik TE*" [232, Ch.3].

2.3.2 Influence of Matter on the RF Field

Beside the coil itself, also the coil load, the investigated subject, introduces inhomogeneities in the field distribution, which are usually much more severe and change from patient to patient. The law of Biot-Savart is valid for static fields, but yields a very good approximation in the stationary case, when the dimensions of the imaged object are smaller than the wavelength. This can be seen as fulfilled for field strength up to 3 T. Nevertheless, even in the stationary case, the time varying current in the coil does not only generate a time varying magnetic field $\vec{B}$, it also generates a vortex electric field $\vec{E}$ and displacement currents according to the 3rd and 4th Maxwell's equation [232, Ch.5]

$$\begin{aligned}
\nabla \cdot \vec{E} &= \frac{\rho_c}{\epsilon_0 \epsilon_r} \\
\nabla \cdot \vec{B} &= 0 \\
\nabla \times \vec{E} &= -\frac{\partial \vec{B}}{\partial t} \\
\nabla \times \vec{B} &= \mu_0 \mu_r \vec{j} + \mu_0 \mu_r \epsilon_0 \epsilon_r \frac{\partial \vec{E}}{\partial t}.
\end{aligned} \tag{2.89}$$

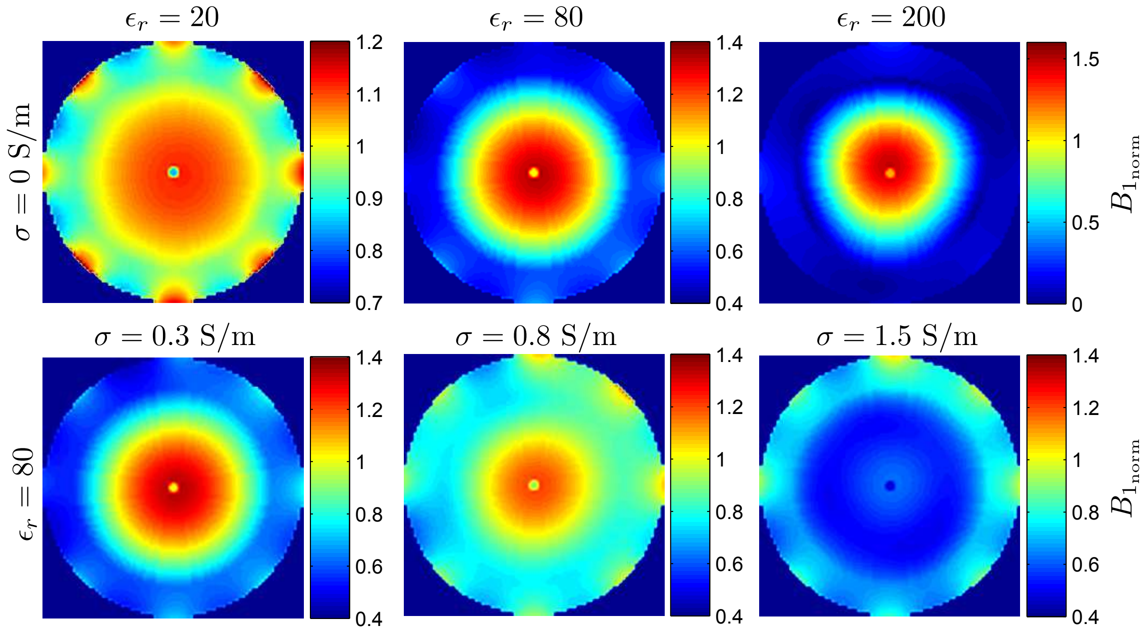

Figure 2.21: Simulated B_1^+ distribution for a cylindrical phantom with different electrical properties. First row: Permittivity variation in the range of $\epsilon_r = [20, 200]$ with no conductivity ($\sigma = 0\,\mathrm{S\,m^{-1}}$). Second row: Conductivity variation in the range of $\sigma = [0.3, 1.5]\mathrm{S\,m^{-1}}$ with constant permittivity ($\epsilon_r = 80$). Increasing permittivity leads to a localized maximum in the center of the cylinder with increasing height and stronger variations, whereas increasing sensitivity damps the B_1^+ field. Simulation was performed with an FDTD solver [185] described by Liebig et al. [186] for 3 T.

If an object is placed inside the transmit coil (e.g. birdcage coil), the field distribution is heavily influenced by the electrical parameter distribution (conductivity $\sigma(\vec{r})$ and permittivity $\epsilon_r(\vec{r})$) of the tissue under investigation. ϵ_0 is the permittivity in vacuum with a value of $\epsilon_0 \approx 8.8542 \cdot 10^{-12}\mathrm{A\,s\,V^{-1}\,m^{-1}}$. Beside the displacement currents arising from $\epsilon_0\epsilon_r\partial\vec{E}/\partial t$, also conducting currents $\vec{j}$ occur according to

$$\vec{j}(\vec{r}) = \sigma(\vec{r}) \cdot \vec{E}(\vec{r}). \tag{2.90}$$

All three occurring fields, the magnetic field $\vec{B}$, the electric field $\vec{E}$, and the current density $\vec{j}$ influence each other in a way so that the Maxwell's equations with the material properties σ and ϵ_r are fulfilled. This can lead to quite inhomogeneous distributions. As described in Section 2.2.2.1, biological tissue behaves diamagnetic with a susceptibility of $\chi \approx 10\,\mathrm{ppm}$, so that the relative permeability μ_r is very close to 1 (with an accuracy $\approx 10^{-5}$). Compared to the influence of the permittivity ($\epsilon_{r_\mathrm{tissue}} \approx 60 \ldots 80$), the influence of μ_r can be neglected in *RF* field calculations, although it is the main influence for static magnetic field perturbations (see Section 2.2.2.1). Typically, the tissue parameters σ and ϵ_r show also a strong frequency dependence, where in general $\sigma(\omega)$ increases and $\epsilon_r(\omega)$ decreases with increasing frequency ω. Typical values for σ and ϵ_r and their frequency

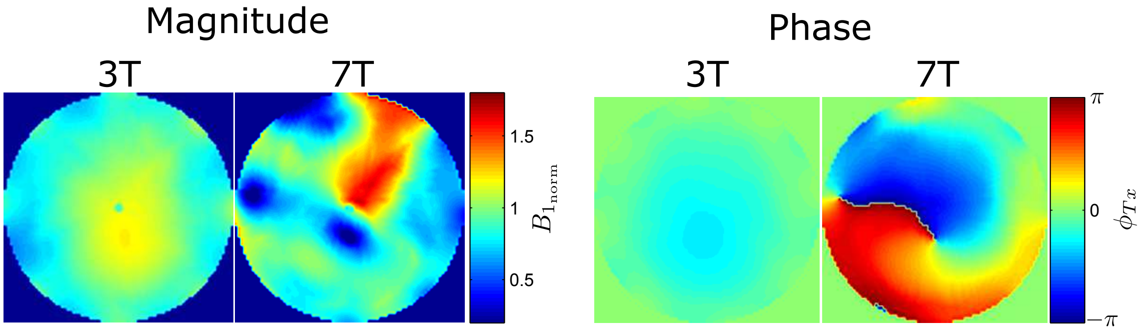

Figure 2.22: Simulated B_1^+ magnitude (left) and phase distribution (right) for 3 T and 7 T on a numerical in-vivo phantom with 116 classified tissues with values of density, permittivity and conductivity for each. The model is out of [132] with values from [190]. The field at 7 T suffers from heavy distortions compared to 3 T in magnitude and phase. Simulation was performed with an FDTD solver [185] described by Liebig et al. [186] for 3 T.

dependence in healthy biological tissue can be found in [85, 86] and [87, 214], and for some cancerous tissues in [143, 289]. The influence of ϵ_r and σ are shown by simulations on a cylindrical phantom in Figure 2.21. As a side note, this behavior is also used to map σ and ϵ_r called Electrical Property Tomography (EPT) [150, 335] out of measuring magnitude and phase of the current B_1^+ field distribution.

A very important parameter for the B_1 field homogeneity is the wavelength λ_{mat} in the investigated matter, which is given by

$$\lambda_{\mathrm{mat}} = \frac{2\pi c_0}{\omega\sqrt{\epsilon_r \mu_r}} \approx \frac{2\pi c_0}{\omega\sqrt{\epsilon_r}}, \tag{2.91}$$

where c_0 is the speed of light in vacuum ($c_0 \approx 3 \cdot 10^8\ \mathrm{m\,s^{-1}}$) and ω the angular frequency of the *RF* field. With $\mu_r \approx 1$, λ_{mat} is proportional to $1/\sqrt{\epsilon_r}$. In water and also in tissue, the value for the relative permittivity is approximately $\epsilon_{r_{\mathrm{tissue}}} \approx 60 \ldots 80$, as stated above, meaning that the vacuum wavelength λ_{vac} is reduced by a factor of $\approx 7 \ldots 9$. For main field strengths up to 3 T, with $\lambda_{\mathrm{vac}} \approx 2.3\,\mathrm{m}$ and $\lambda_{\mathrm{mat}} \approx 30\,\mathrm{cm}$, the situation can be considered as stationary, leading to quite homogeneous B_1 field distributions with deviations of $\approx \pm 20 \ldots 30\%$ inside the human head. By increasing the field strength to 7 T or 12 T, the wavelength reduces to $\lambda_{\mathrm{mat}} = 13\,\mathrm{cm}$ and $\lambda_{\mathrm{mat}} = 7.6\,\mathrm{cm}$, which is much shorter than the typical extensions of human body parts to be imaged. In this high frequency range, the stationary assumption is not valid any more leading to much more severe B_1 field distortions. At 7 T, B_1 field variations of around $\approx \pm 60 \ldots 70\%$ in a human head are common, even complete cancellations due to zero crossings of the standing wave have to be expected inside the *FOV*. At such high field strengths, the excitation with a transmit birdcage body coil does not work any more, because of the inhomogeneous field distribution, such that typically multiple stripe line elements in Circular Polarized (CP) mode are used. More on that is given in the B_1 shimming section (Section 2.3.6).

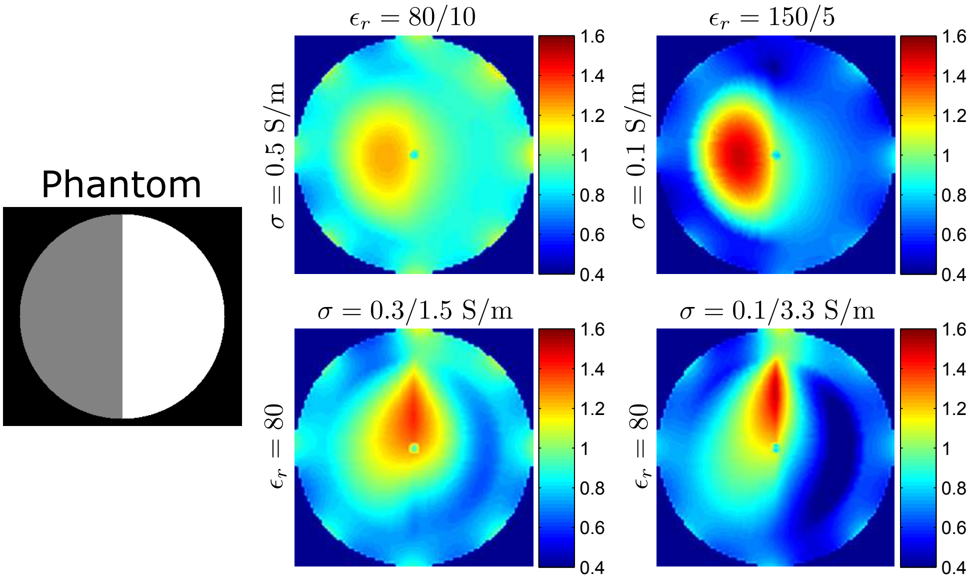

Figure 2.23: Simulated B_1^+ distribution for a cylindrical phantom, divided into 2 compartments along the long axis of the cylinder (perpendicular to the shown plane) to simulate a discontinuity in the electric properties. First row: Discontinuous variation in ϵ_r with constant conductivity in both compartments. Second row: Discontinuous variation in σ with constant permittivity in both compartments. Simulation was performed with an FDTD solver [185] described by Liebig et al. [186] for 3 T.

However, also at high frequencies the $\vec{B}_1$, $\vec{E}$, and $\vec{j}$ field distributions always have to fulfill the Maxwell equations (Eq. (2.89)). The simulated *RF* field distribution inside the human head is shown in Figure 2.22 for 3 T and 7 T in magnitude and phase. The field distribution is calculated by a numerical method, the Finite Differences Time Domain (FDTD) method, described by Liebig et al. [185, 186]. For the simulation, a volume based human head neck model containing 116 different classified tissues with an isotropic resolution of 0.5 mm was used. The model is described by Iacono et al. [132] and the corresponding values for each tissue are out of [190]. This section is partly based on Hennig et al. "*High-Field MR Imaging*" [120, Part II. and Part III].

2.3.3 Spatial behavior of the B_1 Field

The spatial behavior of the B_1 field has to be considered in order to develop a suitable regularization functional for the reconstruction from undersampled data. In general, the solutions of the Maxwell equations in vacuum or in a homogeneous medium are continuous and smooth in space. However, the conductivity $\sigma(\vec{r})$ and permittivity distribution $\epsilon_r(\vec{r})$ in biological tissue are very inhomogeneous, with discontinuities at tissue boundaries and a quite large range of values if we consider e.g. the interface between air (nasal sinuses) and the surrounding tissue with following values: air $\epsilon_{\text{air}} = 1$ and $\sigma_{\text{air}} = 0$ and tissue $\epsilon_{\text{tissue}} \approx 30 \ldots 60$ and $\sigma_{\text{tissue}} \approx 0.1 \ldots 1\,\text{S}\,\text{m}^{-1}$ at 3 T. As already described in Section 2.2.4, the spatial behavior in the static or at least stationary case can be derived from interface conditions of the involved field quantities. For that purpose every field $\vec{X}$ is separated into a component perpendicular to the surface $X_\perp$ and a component parallel to it $X_{||}$. These rules are as follows, where the index a and b indicate medium a and medium b (derived form Preis K. Lecture notes "*Elektrodynamik TE*" [232, Ch.1, 2 and 4]):

- $\vec{E}$ field: The component parallel to the surface $E_{||}$ behaves continuous, $E_{||_a} = E_{||_b}$ at the surface, whereas the normal component $E_\perp$ has to fulfill $E_{\perp_a}/E_{\perp_b} = \epsilon_b/\epsilon_a$ at the surface.

- $\vec{j}$ field: The component perpendicular to the surface $j_\perp$ behaves continuous, $j_{\perp_a} = j_{\perp_b}$ at the surface, whereas the parallel component $j_{||}$ has to fulfill $j_{||_a}/j_{||_b} = \sigma_a/\sigma_b$ at the surface.

- $\vec{B}$ field: The component perpendicular to the surface $B_\perp$ behaves continuous, $B_{\perp_a} = B_{\perp_b}$ at the surface, whereas the parallel component $B_{||}$ has to fulfill $B_{||_a}/B_{||_b} = \mu_a/\mu_b$ at the surface.

In the case of the *RF* field, things are much more complicated. For inhomogeneous electrical property distributions, the field distributions can only be calculated numerically. All three fields influence each other according to Maxwell's equations, and due to several continuity conditions the macroscopical observable B_1 field is smooth and continuous over space. This is experimentally confirmed with measurements and simulations, e.g. simulations for the spatial behavior of the B_1^+ field for discontinuous variation in both σ and ϵ_r are shown in Figure 2.23.

2.3.4 Energy Deposition – Specific Absorption Rate (SAR)

Another important issue, which has to be considered when talking about *RF* fields is the energy deposition inside the body. A measure for that is the so called *SAR* in W kg^{-1}, which gives the energy deposition per kg body weight. The B_1^+ field does not directly contribute to the *SAR*, but indirectly over the $\vec{E}$ field which depends on $\vec{B}_1^+$. The $\vec{E}$ field is responsible for displacing free electrical charges, and the corresponding eddy currents are responsible for tissue heating. The local *SAR* can be calculated with the conductivity σ, charge density ρ_c and the magnitude of the $\vec{E}$ field

$$\mathrm{SAR} = \frac{\sigma \|\vec{E}\|^2}{\rho_c}. \tag{2.92}$$

Because of the 3rd Maxwell equation (Eq. (2.89)), the magnitude of the $\vec{E}$ field is proportional to the frequency, so that the *SAR* increases with the square of the frequency or field strength B_0 (SAR $\propto \omega^2 \propto B_0^2$). Because the $\vec{E}$ field cannot be measured in *MRI*, the *SAR* prediction is very complicated. Usually, for field strengths up to 3 T, a global

SAR estimation is performed to keep the exposure below the limits of regulatory authorities. This is done to keep the temperature increase inside the body below 1 °C. The current maximum SAR value is $2\,\mathrm{W\,kg^{-1}}$ in normal mode and $4\,\mathrm{W\,kg^{-1}}$ in the so called first level mode for whole body exposure. The limit for head exposure is $3.2\,\mathrm{W\,kg^{-1}}$ [120, p.84]. Unfortunately, at higher field strengths, also the $\vec{E}$ field and with that the SAR distribution get more and more inhomogeneous, which can lead to local SAR hot-spots far beyond the limits. This can lead to a local temperature increase of more than the allowed value of 1 °C, even if the global SAR constraint is fulfilled. The situation gets more severe, if more than one transmit channel is used to homogenize the B_1 field distribution (B_1 shimming Section 2.3.6). This can lead to more severe SAR hot-spots, because the $\vec{E}$ field distribution can suffer from severe constructive interference. Unfortunately, the local SAR estimation is very complicated and is usually done by numerical FDTD simulations using a standard human model for a course prediction for a certain coil configuration. Each patient of course deviates from the standard model, which means the local SAR distribution can be completely different. The local SAR issue is still an open research topic and in practice to consider patient safety, the global SAR limit is usually reduced drastically to avoid local hot-spots exceeding the limit. The actual quantity to be controlled is the temperature increase in the investigated tissue, which does not only depend on the SAR, but also on physiological parameters such as the thermal conductivity, the perfusion and the thermal regulatory system. A whole bunch of literature concerning field and SAR calculation exists, where a few are mentioned here [53, 56, 130, 140, 141, 189, 268]. The information in this section is mainly based on Hennig et al. "*High-Field MR Imaging*" [120, Part II. and III].

2.3.5 Influence on the MR Signal

The influence of an inhomogeneous B_1 field distribution on the MR signal can be quite complicated and depends on the flip angle, the sequence, and the used coils for receive and transmit. These complex interactions are described in the following section, which is mainly based on Hennig et al. "*High-Field MR Imaging*" [120, Part III]. According to Eqs. (2.27) and (2.28), the flip angle α is direct proportional to the transmit RF amplitude. This means, an inhomogeneous B_1^+ field distribution leads to an inhomogeneous flip angle distribution within the excited volume. The dependency of the signal on the flip angle highly depends on the sequence and is in general highly nonlinear. If the magnetization is in thermal equilibrium $TR > T_1$ and a GRE sequence is used, the signal is proportional to $\sin(\alpha)$ (see Eq. (2.44)). This means for low flip angles $< 60°$, the signal increases monotonically (approximately linearly) with α. If the flip angle approaches $90°$, an increase in α leads to a decrease in signal due to overflipping. To decrease acquisition time, GRE sequences are normally applied with a $TR \ll T_1$ leading to a much more nonlinear relation between signal and α. For a given $TR - T_1$ combination, there exists a flip angle where the signal reaches a maximum, the so called Ernst angle [76], so that the signal decreases if this angle is exceeded. In this case, the signal behavior also depends on the type of tissue. For *SE* sequences, the signal does not only depend on the excitation angle α, but also on the refocusing angle β, whose distributions suffers from the same inhomogeneity. In this case, the signal is proportional to $\sin(\alpha) \cdot \sin^2(\beta)$. If sequences in the steady state are used, such as balanced Steady State Free Precession (bSSFP), the relations get much more nonlinear.

The signal also depends on the receive field distribution $B_1^-(\vec{r})$, which describes the sensitivity of a certain coil to a spin at a certain position in space $\vec{r}$. Due to the principle of reciprocity, transmit B_1^+ and receive field B_1^- are the same. According to Eq. (2.44), the signal depends linearly on the receive sensitivity, which leads to a quadratic relation between signal and B_1 for low flip angles in *GRE* sequences ($TR > T_1$), if the same coil is used for receive and transmit, because of the linear approximation of $\sin(\alpha)$. For all other cases described above, transmit and receive inhomogeneity overlay each other. As already described, birdcage coils are usually used for transmit and surface coils for receive, so that their inhomogeneity profiles compensate each other to a certain degree. This is, because birdcage coils usually have a maximum in the middle of the object and surface coils have their maximum close to the surface. One aspect should not be forgotten in the consideration of B_1 inhomogeneity, the B_1 phase. Both the transmit and receive lead to an additional phase term in the resulting signal $\phi_{Tx}(\vec{r})$ and $\phi_{Rx}(\vec{r})$. At moderate field strength (up to $3\,\mathrm{T}$), the B_1 phase mainly depends on the geometrical orientation of the coil and the phase variation over the *FOV* is quite low. At higher field strength ($\geq 7\,\mathrm{T}$), when wave effect start to play a role, also the B_1 phase distribution gets severely affected, which has to be considered in B_1 shimming. Furthermore, the contrast usually depends on the flip angle, so that an inhomogeneous B_1 field also leads to a varying contrast over the *FOV*.

2.3.6 B$_1$ Shimming

Compared to B_0 shimming, B_1 shimming is a quite new technique and arises due to the highly inhomogeneous *RF* field distributions at ultra high field strength ($> 3\,\mathrm{T}$). For that purpose, the applicability of the commonly used whole body birdcage coil for transmit is limited, because the number of independent control variables is very low, restricted to magnitude and phase of the two channels. To overcome this problem, array coils are used also for transmit at higher field strength, similar to the receive array coils which are already used for more than two decades, however, the coil design is different. Compared to receive array coils which are usually built as loop coils, the transmit arrays are built up of stripe line elements in Transverse Electro-Magnetic (TEM) mode, where a number of N_{Tx} elements are placed around the body part under investigation. Each stripe line element consists of a stripe conductor separated by a dielectric material from a ground plate with larger geometrical extensions. The thickness of the dielectric media (e.g. Teflon) determines the penetration depth. Although, this coil is constructed as a capacitor, the inductive properties dominate at the frequency of operation. Typical dimensions of such a stripe element for a typical head coil are: stripe conductor 12 mm × 15 cm, ground plate 20 mm × 15 cm separated by a 5 mm thick Teflon plate. The advantage of this coil type is that it is very easy to construct and it is widely used in communication devices [120, Part I]. Compared to conventional systems, the hardware effort increases linearly with the number of transmit channels. The whole *RF* chain, including waveform generator, amplifier, and Tx/Rx switch, has to be built up separately for each channel, such that the current in each element can be controlled independently. The term B_1 shimming usually refers to an independent control of magnitude and phase of each channel, where the same waveform is used. This leads to $2N_{Tx}$ degrees of freedom. By allowing different waveforms for each channel, the degree of freedom is massively increased, which is usually referred to as full parallel transmit (pTX), which is not covered in this thesis.

According to Boernert et al. [31], the idea behind B_1 shimming is to control magnitude A_n and phase ϕ_n of the current in each transmit channel, such that the inhomogeneous *RF* field distributions are compensated up to a certain degree to reach a maximal homogeneous excitation. Because of superposition, the resulting active component of the B_1 field $B^+_{1_{res}}$ is given as

$$B^+_{1_{res}}(t,\vec{r}) = \sum_{n=1}^{N_{Tx}} A_n \cdot B^+_{1_n}(t,\vec{r}) e^{i\phi_n}, \tag{2.93}$$

where $B^+_{1_n}$ is the active component of the B_1 field generated by each element. To determine A_n and ϕ_n, the contribution of each channel $B^+_{1_n}$ has to be known over the whole volume, which can be determined using one of the B_1 mapping methods described in Section 2.5. In general, $B^+_{1_n}$ is complex and in order to get a coherent overlay not only the magnitude but also the spatially varying phase distribution $\phi_{B_{1n}}(\vec{r})$ of $B^+_{1_n}$ has to be determined, which is described in Section 2.5.2. The controls A_n and ϕ_n are determined as the solution of an optimization problem, such that the standard deviation of $B^+_{1_{res}}$ gets minimized. The cost function can also incorporate an additional constraint to reduce the global *SAR*, where λ is a regularization parameter balancing between field homogeneity and *SAR* reduction. The cost function writes as

$$(\tilde{\mathbf{A}}, \mathbf{\Phi}) = \arg\min_{\tilde{\mathbf{A}},\mathbf{\Phi}} \left\| B^+_{1_{res}}(\vec{r}) - \langle B^+_{1_{res}}(\vec{r})\rangle \right\|_2^2 + \frac{\lambda}{\langle B^+_{1_{res}}(\vec{r})\rangle^2} \sum_{n=1}^{N_{Tx}} A_n \left\| B^+_{1_n}(\vec{r}) \right\|_2^2, \tag{2.94}$$

where $\langle B^+_{1_{res}}\rangle$ is the mean value of $B^+_{1_{res}}(\vec{r})$ over the *FOV* and $\tilde{\mathbf{A}} = [A_1, \ldots, A_{N_{Tx}}]^T$ and $\mathbf{\Phi} = [\phi_1, \ldots, \phi_{N_{Tx}}]^T$ are the vectors containing A_n and ϕ_n, respectively. The *SAR* constraint is necessary, because at least partially destructive interference can occur in some regions, so that the magnitude of $B^+_{1_{res}}$ decreases, but the *SAR* contribution increases dramatically. Even though, the global *SAR* is under control, local *SAR* hot spots can not be excluded due to $\vec{E}$ field interferences. According to Section 2.3.4, *SAR* is proportional to $\|\vec{E}\|^2$ and the measurement does not provide any information about the $\vec{E}$ field. The local *SAR* can only be determined with a detailed tissue model of the current subject, including conductivity and permittivity distributions and a numerical simulation. Of course, in clinical practice this is usually not available and the calculation effort would be to high, so that B_1 shimming is still an experimental technique, which is only applied for research purposes under special conditions. However, such *TEM* transmit coil arrays can be switched to *CP* mode with equal amplification factors $A_1 = A_2 = \ldots = A_{N_{Tx}}$ and a phase relation $\phi_n = 2\pi(n-1)/N_{Tx}$, such that the current distribution and the B_1 behavior is similar to a birdcage coil. This operation mode can be used in clinical practice and it is the standard excitation mode for field strengths $\geq 7\,\mathrm{T}$.

Many studies were proposed showing the potential benefits of *RF* shimming. In [134], a massive improvement in field homogeneity could be proven by simulations with a 24-channel transmit array on a 18-tissue human head model. Furthermore, it was shown that the contribution of the phase is more important than of the magnitude. The same findings were confirmed by simulations on a torso model [151]. It was shown in [133], also by numerical simulations, that the same transmit array can be calibrated to perform either a homogeneous excitation over different slices, or a very localized excitation pattern in a defined *ROI* with nearly no excitation outside. This can be used for example to suppress surrounding tissue instead of saturation pulses. In [149] and [337], transmit arrays were used to produce very sharp 2D excitation profiles. In [213], B_1 shimming was used to maximize the available signal in a 7 T prostate examination instead of homogenizing the excitation pattern. In [211], the limits of *RF* shimming were examined and it was found that a 16-channel transmit array is sufficient to shim a single slice up to 600 MHz and the whole brain up to 300 MHz. For whole brain shimming up to 600 MHz, a 80-channel array is necessary. Also the local *SAR* problem was considered, but only in simulations for 3 T in [306] and 7 T in [307].

2.3.7 Combination of Signals from Phased Array Coils

One very important aspect concerning the B_1^- field (receive field) is the combination of signals received by a phased array coil to a single image. This can be done by directly combining the analog signals and sampling the combined one. This has the advantage that only one Analog to Digital Converter (ADC) is required and the amount of acquired data is massively reduced. However, this approach does not allow any spatial phase correction (see later) and the additional spatial information required for undersampled image reconstruction is lost (see Chapter 3). Today, every commercially available system samples the signal from each channel separately, such that the combination has to be done in image space. The simple complex addition, as it would be the first idea, does not work, because the spatially varying phase of the receive field $B_{1_n}^-$ in each receive channel may lead to destructive interference of the channel signals. In the worst case, this can lead to a complete signal dropout. The summation of the magnitudes of each channel also leads to an unnatural appearance of the image. One often used approach is the Sum of Squares

(SOS) method, where the squared magnitudes of each channel are summed up, so that the combined voxel signal S_{comb} is given by

$$S_{\mathrm{comb}}(\vec{r}) = \sqrt{\sum_{n=1}^{N_c} S_n(\vec{r})\overline{S}_n(\vec{r})}\,. \tag{2.95}$$

Here, S_n is the voxel signal of each channel with its complex conjugate $\overline{S}_n$, and N_c is the number of receive channels. This already leads to suitable images, but the phase information is completely lost. In the seminal work of Römer et al. [246], it was shown how to optimally combine the different coil signals on the basis of their individual spatial varying receive fields $B_{1_n}^-(\vec{r})$ to maximize the *SNR* in the combined image. The combined image is given by

$$S_{\mathrm{comb}}(\vec{r}) = \sum_{n=1}^{N_c} \overline{B}_{1_n}^-(\vec{r}) S_n(\vec{r}), \tag{2.96}$$

where $\overline{B}_{1_n}^-$ is the complex conjugate of the receive field. The basic idea is to remove the phase introduced by the receive field and to sum up the individual coil signals coherently. The magnitude weighting is used to suppress noise and artifacts appearing in non-sensitive regions of one coil. This can be written in vector matrix form

$$S_{\mathrm{comb}}(\vec{r}) = \mathbf{S}^T(\vec{r})\boldsymbol{\Psi}^{-1}\overline{\mathbf{B}}_1^-(\vec{r}), \tag{2.97}$$

such that the influence of the noise correlation matrix $\boldsymbol{\Psi}$, defined in Eq. (2.51), can be considered. The column vector $\mathbf{S} = [S_1, \ldots, S_{N_c}]^T$ contains the voxel signal and the column vector $\mathbf{B}_1^- = [B_{1_1}^-, \ldots, B_{1_{N_c}}^-]^T$ contains the the receive field of each receive coil in this voxel. The inverse of the noise correlation matrix leads to a weighting of the individual signals inverse to their average noise level. However, this kind of combination can lead to a very inhomogeneous intensity distribution over the image, according to the overall sensitivity. It is typically higher in regions close to the surface, which are closer to the receive coils than the center regions. To remove this inhomogeneities, also a pixel scaling factor was introduced, such that the combined image has uniform intensity which is given by

$$S_{\mathrm{comb}}(\vec{r}) = \frac{\mathbf{S}^T(\vec{r})\boldsymbol{\Psi}^{-1}\overline{\mathbf{B}}_1^-(\vec{r})}{{\mathbf{B}_1^-}^T(\vec{r})\boldsymbol{\Psi}^{-1}\overline{\mathbf{B}}_1^-(\vec{r})}. \tag{2.98}$$

Because the pixel value itself depends on the receive field, the normalization factor (denominator in Eq. (2.98)) is selected to make the voxel signal independent of the receive field. In practice, the receive fields $B_{1_n}^-$ can be determined by a reference scan with the birdcage body coil S_{ref} having a quite homogeneous receive profile by

$$B_{1_n}^-(\vec{r}) = \frac{S_n(\vec{r})}{S_{\mathrm{ref}}(\vec{r})}. \tag{2.99}$$

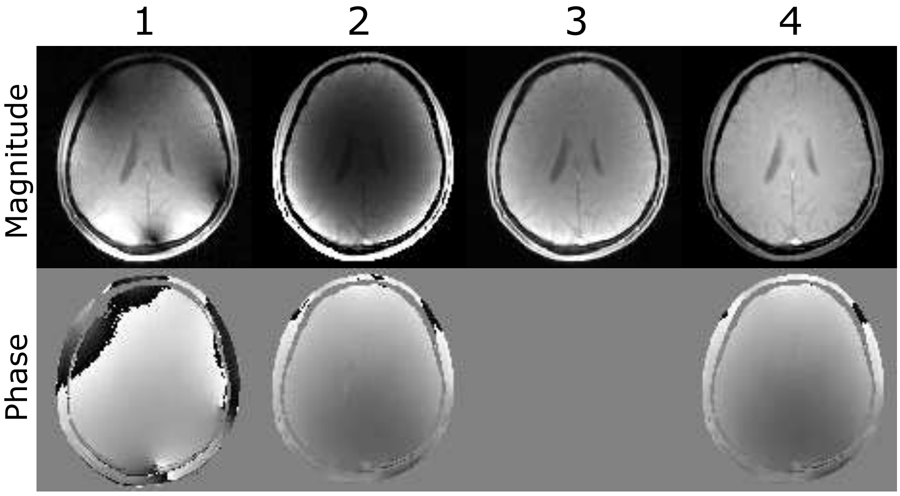

Figure 2.24: Results for different coil signal combinations applied to the same measurement acquired on a healthy volunteer at 3 T using a 64-channel head coil: (1) The direct complex addition of the individual coil signals leads to destructive interference in some regions. (2) Phase correct addition using the individual receive profiles $B_{1_n}^-$ according to Eq. (2.96) gives a very inhomogeneous signal distribution. (3) With the sum of squares combination according to Eq. (2.95), the phase information is lost. (4) Best results are gained with the uniform intensity combination according to Eq. (2.98). Residual signal inhomogeneities are due to transmit. The sensitivity profiles are gained through a reference measurement with the body coil.

Figure 2.24 shows the result for different coil signal combinations and their influence on the final image. Other approaches for phase coherent coil combination without reference scan are described by Robinson et al. [244], where the receive field determination is often based on the spatially smoothing constraints on the B_1^- field. The knowledge of receive profiles is also very important for image reconstruction from undersampled data, gaining additional spatial information and to set up the forward and backward operators (see Chapter 3). For that purpose, special methods were proposed to determine low resolution B_1^- distributions out of a fully sampled region in k-space center Auto Calibration Lines (ACLs) [301, 311].

2.4 Mapping the Static Magnetic Field – B$_0$ Mapping

The idea behind B_0 field mapping is quite simple. According to Eqs. (2.79) and (2.80) in Section 2.2.3.1, a map of macroscopic B_0 field variations can be gained as the phase difference between two *GRE* acquisitions S_{TE_1} and S_{TE_2} with different echo times

$$\Delta B_0(\vec{r}) = \frac{\angle S_{\mathrm{TE}_2}(\vec{r}) - \angle S_{\mathrm{TE}_1}(\vec{r})}{\gamma(\mathrm{TE}_2 - \mathrm{TE}_1)} = \frac{\Delta\phi(\vec{r})}{\gamma\Delta\mathrm{TE}}. \tag{2.100}$$

The phase difference is necessary to get rid of the background phase $\phi_0(\vec{r}) = \phi_{Tx}(\vec{r}) + \phi_{Rx}(\vec{r})$, which consists of the *RF* phase during transmit ϕ_{Tx} and receive ϕ_{Rx}, which is usually referred to as transceive phase (see Section 2.3.5). Moreover, a spin echo sequence can be used for that purpose if excitation and echo are placed asymmetrically around the refocusing pulse. In particular, the refocusing pulse is applied at time τ after the excitation and the readout gradient is applied such that, the echo forms at time $2\tau + \Delta t$ after the excitation. The phase gained in the time interval Δt is proportional to the field shift according to Eq. (2.80), described in [259]. Alternatively, a linear fit of the unwrapped phase of a multi-echo *GRE* acquisition with a number of N_{TE} echos can be performed [84], making the result more stable against noise. This leads to following minimization problem in every voxel

$$\Delta\omega_0, \phi_0 = \arg \min_{\Delta\omega_0, \phi_0} \left\| \begin{bmatrix} \mathrm{TE}_1 & 1 \\ \vdots & \vdots \\ \mathrm{TE}_{N_{\mathrm{TE}}} & 1 \end{bmatrix} \cdot \begin{bmatrix} \Delta\omega_0 \\ \phi_0 \end{bmatrix} - \begin{bmatrix} \phi_{\mathrm{TE}_1} \\ \vdots \\ \phi_{\mathrm{TE}_{N_{\mathrm{TE}}}} \end{bmatrix} \right\|_2^2, \tag{2.101}$$

which can be solved by using the pseudo-inverse. However, even though the math is quite simple, there are many influences and pitfalls which can lead to errors in the final map. Some examples might be phase wraps, infinite many solutions due to periodicity, chemical shift effects, and sequence specific influences such as eddy currents or timing errors. In the next few subsections, these topics are discussed in more detail.

2.4.1 Phase Unwrapping

As already mentioned, field mapping is based on phase information and therefore phase unwrapping has to be applied as a preprocessing step such that Eqs. (2.100) and (2.101) can be applied properly. The signal phase can only be determined on an open interval $\phi = [0, 2\pi)$ or $\phi = [-\pi, \pi)$, depending on the definition. The absolute phase value ϕ_{abs} is given by

$$\phi_{\mathrm{abs}}(\vec{r}) = \phi(\vec{r}) + 2\pi n(\vec{r}), \tag{2.102}$$

where n is an integer value, which has to be determined during phase unwrapping. For 1D signals, phase unwrapping is a quite simple task by simply adding or subtracting 2π for all following phase samples whenever a phase wrap is detected, under the condition that the phase difference between adjacent samples $\Delta\phi < \pi$, which is called the unwrapping condition. Even though, the principle is the same, phase unwrapping for 2D and 3D images can be quite challenging. In particular, regions with low *SNR* can lead to large errors which can propagate over the whole image. Another problem which can arise are open ended phase wraps, also known as fringe lines or residues which can occur due to a violation of the unwrapping condition. This can be the case because of low local *SNR* or improper combination of the different receiver coil signals. An important condition to prove the validity of the phase in a certain point in space is that the sum along any closed line around it has to be zero. If this is the case, the phase can be considered as valid. A detailed description of fringe lines and how to tackle this problem is given by Chavez et al. [49]. Furthermore, many algorithms were proposed in order to phase unwrap 2D and 3D images. Some approaches perform local phase unwrapping which are based on path following schemes [115] or quality guided region growing [81, 322, 326], where most of them require user interaction e.g. for selecting a proper seed point. Other algorithms based on cost function minimization [138], graph-cut methods [23], and Markov random field modeling [329] were also introduced. Beside that, there also exist global methods, where the unwrapping procedure is written as a global optimization problem with the advantage of no required user interaction and a solution independent of the processing path. Such an approach was presented by Song et al. [278] as a solution of the Poisson equation $\nabla^2\phi_{\text{abs}} = \nabla \cdot W(\nabla\phi)$ with $W(x)$ being the phase wrapping operator, where a solution is also described in Fourier space [6]. Other globally defined methods are based on polynomial fitting [184], Chebyshev polynomials [168] or the minimum L_p-norm [93]. This short summary, shows the huge variety of different phase unwrapping methods available, where all have their specific advantages and disadvantages, so that it is hard to determine the "best" one. However, one algorithm, which was also used throughout this thesis, should be highlighted because of its robust behavior and delivery of reliable results. This algorithm performs fully automatic unwrapping on the basis of a sorted list, multi-clustering approach [206]. Furthermore, an open source MATLAB implementation is available.

2.4.2 Influence of Echo Time and Chemical Shift

The next important aspect to be considered is the selection of suitable values for TE, where first the echo time difference ΔTE is considered. On the one hand, ΔTE directly determines the sensitivity of the measurement, the higher the better, but on the other hand a longer ΔTE restricts the range of ΔB_0 which can be unambiguously resolved, because of the periodicity of $\Delta\phi$ with respect to ΔB_0. Derived from Eqs. (2.79) and (2.80), the maximum field deviation $\Delta B_{0_{\text{max}}}$ which can be mapped so that the resulting phase difference lies in the range $\Delta\phi = [-\pi, \pi)$ is given by

$$\Delta B_{0_{\text{max}}} = \frac{2\pi}{\gamma \Delta \text{TE}}. \tag{2.103}$$

This means that there exists an infinite number of solutions for ΔB_0 for the measured phase difference $\Delta\phi$

$$\Delta B_0 = \Delta B_{0_{\text{calc}}} + n B_{0_{\text{max}}}, \tag{2.104}$$

where $B_{0_{\text{calc}}}$ refers to the solution gained with Eq. (2.100). This problem can be tackled by the application of an accurate phase unwrapping method as described above, whereas other approaches were presented using polynomial fitting [258] or a minimization approach where the gradient of the field distribution is minimized [148]. Even though, assuming perfect phase unwrapping over a wide range to get rid of the periodicity, ΔTE cannot be increased arbitrarily to increase the sensitivity of the field mapping. This is because of the

T_2^* decay in *GRE* based sequences (see Section 2.2.3.3), leading to a reduction in *SNR* of the phase signal with increasing TE. If only one chemical species is present, the absolute value of TE_1 and TE_2 from Eq. (2.100) can be adjusted such that TE_1 is as short as possible (maximum signal) and TE_2 should be chosen to be a good compromise between sensitivity versus periodicity and signal loss. However, in in-vivo measurements usually two dominant chemical species are present, water and fat, where their protons show a distinct frequency shift due to differences in the chemical environment which is about 3.5 ppm. This additional frequency shift overlays with that caused by macroscopic field variations and leads to errors especially if both are present in a voxel. To overcome this problem, the echo times can be restricted to values where both components are in phase [258], which approximately occurs every 2.2 ms ($2\pi/\Delta\omega_F$) at 3 T. However, this restricts TE and ΔTE to integer multiples of this field strength dependent value, leading to an intentional aliasing between those two signals. Another possibility is to apply spectral selective excitation pulses, such that only the water component is measured [317]. However, the efficiency of such pulses suffers under the presence of field inhomogeneities.

A special challenge is field mapping for the application of fat/water separation. To simultaneously obtain information about the different chemical species, the in-phase condition obviously cannot be fulfilled, which leads to ambiguous solutions requiring special treatment. Section 4.1 elaborates further on this topic.

2.4.3 Influence due to Eddy-Currents and Hardware Imperfections

Also, sequence specific parameters as the readout trajectory, *FOV*, and resolution combined with imperfections such as eddy currents, sequence timing errors, gradient waveform imperfections, and unequal areas for positive and negative gradient lobes can lead to errors in the final field map. All these errors lead to an echo-shift, and because of the Fourier shift theorem, the signal is corrupted by an additional phase term. According to Section 2.2.3.2, geometric distortions occur in the presence of field variations, whereas the distortion direction depends on the polarity of the readout gradient. By using a multi-echo *GRE* sequence with bipolar readout gradients, the occurring geometric distortions are different for odd and even echoes leading to a mismatch between those acquisitions. To compensate this influence, it is recommended to use a monopolar *GRE* readout [148]. Nevertheless, the resulting distortions are equal in all images used for calculating the field map, such that the field map is influenced by the same distortion. However, if a proper readout bandwidth is used, these distortions are usually smaller than the voxel size in a *GRE* sequence and therefore usually negligible.

Eddy currents are electric currents induced in the cryoshield of the magnet and other electric conducting materials of the hardware by switched gradient fields. These eddy currents produce time varying field distortions, additionally to the static field distortions, which also influence the field map. According to Section 2.1.7.2, every change in *FOV*, resolution or acquisition bandwidth changes the timing and strength of the applied gradients and with that the corresponding eddy currents. Eddy currents can be subdivided into short and long time constant eddy currents, where short time constants are on the order of gradient rise times and long time constants in the order of repetition times. Short time constant eddy currents basically distort the gradient shape, similar to a low-pass filter and have the same influence as timing errors. Long term eddy currents are very hard to consider, they build up a certain steady state depending on the gradient history, and their effect can hardly be distinguished from static field distortions. Another important influence are gradient amplifier asymmetries leading to different areas for positive and negative gradient lobes, which causes a phase error increasing with the echo number. Klassen and Menon [158] proposed a method, where all these influences were considered with a dedicated sequence design to separate all phase contributions from the effect of pure static field perturbations. For that purpose, the acquisition of two multi-echo *GRE* echo trains with bipolar readout and increasing echo spacing is proposed. The second echo train has the reversed read out gradient polarity of the first one and at least three echos have to be acquired, whereas more echos increase the noise robustness. The phase effects of short time constant eddy currents and timing errors depend on the gradient polarity and therefore they can be removed as a phase average between the two echo trains with identical timing. The effect of gradient amplifier asymmetries cannot be removed by averaging, because of the same phase sign in both echo trains. To separate this effect, the increasing echo spacing is applied, because its phase contribution depends on the number of refocused echos, whereas the phase contribution of the static field perturbation depends on the evolution time. Both effects can be separated by solving a linear system of equations. For equal echo spacing, these two effects are not separable. The last effect arising from long time constant eddy currents is corrected by navigator echos without phase encoding, acquired before and after the volume acquisitions. The phase contribution from long time constant eddy currents can be calculated out of the difference between both navigator echoes, because when the first one is acquired no steady state has established yet and the long time constant eddy currents effect is minimal. After the volume acquisition, the steady state has established and the long time constant eddy current effect is maximal. Additionally, before the volume acquisition starts, a certain number of gradient pulses is applied without acquiring data, until the steady state is reached. With that, the long time constant eddy current influence does not change over the acquisition time, so that it can be corrected with the navigator echos.

2.5 Mapping the RF Field – B_1^+ Mapping

Mapping the B_1 field is not that straight forward than mapping the B_0 field, because the relation between the *MRI* signal and the B_1 field is not trivial and depends on several factors, as the used sequence, the slice profile, and the resonance offset ΔB_0. For that purpose, the magnetization has to be prepared in a certain way so that all other influences except B_1 are compensated, or at least reduced to a negligible degree. Many methods were proposed, where most of them do not map the the magnitude of the *RF* field directly, but the achieved flip angle α instead. At least in the onresonant case, there is no difference because α is proportional to the B_1 magnitude according to Eqs. (2.27) and (2.28) in Section 2.1.4. If additional B_0 field inhomogeneities are present, hence, flip angle mapping and direct B_1 field mapping deliver different results. At least, the most important methods are reviewed here. However, most of these methods are only able to determine the magnitude of the B_1 field, which is sufficient for most applications, especially for field strength $\leq 3\,\mathrm{T}$, but for some applications also the spatial varying phase of the B_1 field is of interest e.g. B_1 shimming (see Section 2.3.6). A good review of state of the art methods for B_1 mapping, especially for the requirements at very high fields, is given by Pohmann and Scheffler [231], including an error and scan time efficiency analysis.

2.5.1 Mapping the Magnitude of the $\mathbf{B}_1^+$ Field

In this section, the most important methods to measure the spatial flip angle distribution are discussed. At the end, two methods to directly measure the magnitude of the B_1 field is described. Due to the proportionality, all are referred to as B_1 mapping.

2.5.1.1 Double Angle Method (DAM)

Fist attempts to map the spatial distribution of the *RF* field were already done by Hornak et al. [129], but the first reliable and quantitative method was presented by Stollberger et al. [285], the so called Double Angle Method (DAM). The main idea of this method is to get rid of signal influences from spatial varying spin density ρ, relaxation times T_1 and T_2, receiver sensitivity profiles B_1^-, and the refocusing flip angle β in a *SE* sequence. Under the condition that $\mathrm{TR} > 5T_{1_{max}}$, the *SE* signal can be described with

$$S(\vec{r}) = \rho(\vec{r}) B_1^-(\vec{r}) \cdot \sin(\alpha(\vec{r})) \cdot \sin^2\left(\frac{\beta(\vec{r})}{2}\right) e^{-\frac{\mathrm{TE}}{T_2(\vec{r})}}, \tag{2.105}$$

such that the ratio between two acquisitions with exactly the same sequence parameters, except the flip angle α, gets independent of all these disturbing influences. Under the condition of $\alpha_2 = 2\alpha_1$ for the second acquisition, the flip angle distribution $\alpha(\vec{r})$ can be calculated out of the ratio between the two acquired signals using

$$\alpha_1(\vec{r}) = \arccos\left(\frac{S_2(\vec{r})}{2S_1(\vec{r})}\right). \tag{2.106}$$

Due to the proportionality between B_1^+ and α, the magnitude of the *RF* field can be calculated using Eqs. (2.27) and (2.28).

In [135], two further methods were presented, one with the only difference of using a *GRE* sequence, compared to [285], leading to the same relation described in Eq. (2.106). The second one is based on a slightly different *SE* acquisition scheme, where not only the excitation flip angle α is varied between both acquisitions, but also the refocusing angle β, with the conditions $\beta_1 = 2\alpha_1$, $\beta_2 = 2\alpha_2$, and $\alpha_2 = 2\alpha_1$. With that, the signal depends on $\sin^3(\alpha)$ instead of $\sin(\alpha)$ leading to a much higher sensitivity for small changes. The resulting relation is given by

$$\alpha_1(\vec{r}) = \arccos\left(\sqrt[3]{\frac{S_2(\vec{r})}{8S_1(\vec{r})}}\right). \tag{2.107}$$

With that, the second scheme is better suited for volume coils, because of the higher sensitivity for the less severe flip angle variations. For surface coils, the method from [285] is better suited, because the flip angle rapidly decreases to values close to zero with increasing distance from the coils, where the second variant has a low sensitivity because of the $\sin^3(\alpha)$ relation. The suggested flip angle combination for the first method is $\alpha_1 = 60°$ and $\alpha_2 = 120°$. For the second method, the following flip angles are suggested: $\alpha_1 = 60°$, $\beta_1 = 120°$, $\alpha_2 = 120°$, and $\beta_2 = 240°$.

With these methods two problems arise. First, the assumed linearity between B_1 and α is not fulfilled for slice selective excitation and second, the very long acquisition time because of the restriction $\text{TR} > 5T_{1_{max}}$ to get rid of T_1 influence. In the human brain the T_1 time constants are in the order of 1 s (if Cerebrospinal Fluid (CSF) is neglected), so that the minimum repetition time is in the order of 5 s, leading to an acquisition time of 5 min for a single slice with a matrix size of 64 × 64. These two problems were tackled in Stollberger and Wach [286], where a compensated version of *DAM* was introduced as well as a correction for slice profile effects. For the compensated *DAM*, the sequence was modified using an additional *RF* pulse with a flip angle δ, applied directly after the readout gradient. The following condition must be met for the first and second acquisition, $\delta_1 = \alpha_2$ and $\delta_2 = \alpha_1$. With that, the total flip angle over one TR interval is the same and if the time between excitation and compensation pulse is small compared to TR, the z-component M_z of the magnetization shortly before the excitation is approximately the same for both acquisitions and can therefore be neglected. The TR can be reduced into the range of $T_{1_{max}}$. The nonlinearity effect between B_1 and α gets more severe, the higher α gets. This problem is solved with an acquired correction curve for the specific used *RF* pulse. For the sinc shaped pulse used in [286], the linearity condition was fulfilled for flip angles up to 140°.

Some further improvements should be mentioned concerning this method. In [61], the *DAM* method was improved by the application of a B_1 insensitive saturation pulse at the end of the sequence combined with a spiral readout, where acquisition times in the order of seconds were reached. A similar approach was presented by Wang et al. [312], where an *RF* pulse train was applied to maintain the same z-magnetization for both acquisitions. For readout, a more robust multi-echo *GRE* sequence was used. The *DAM* was combined with a *TSE* readout and a non-selective excitation pulse in [270] to decrease acquisition time and reduce slice profile effects, and in [314] it was combined with an *EPI* readout.

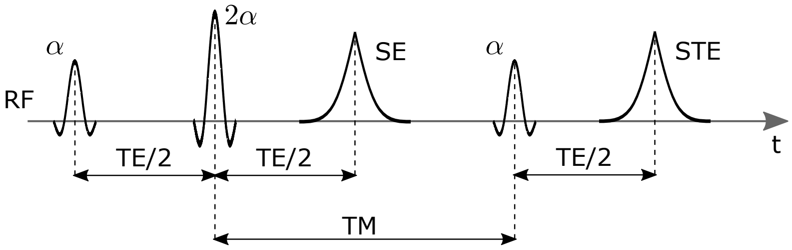

Figure 2.25: Sequence diagram of the stimulated echo – spin echo imaging method.

2.5.1.2 Stimulated Echo – Spin Echo Imaging (STESE)

In Akoka et al. [2], a B_1 mapping method based on the acquisition of a *SE* and a Stimulated Echo (STE) is proposed. For this purpose a three pulse experiment is carried out, and the *SE* after the second pulse and the *STE* after the third pulse is acquired with a flip angle scheme α–2α–α (see sequence diagram in Figure 2.25). An improved version of this method for 3D acquisition is described by Jiru and Klose [142], where the acquisition of both echos is performed by an *EPI* readout. The signals of the *SE* and the *STE* are given by

$$S_{\mathrm{SE}} = M_0 e^{-\frac{\mathrm{TE}}{T_2}} \sin^3(\alpha), \tag{2.108}$$

$$S_{\mathrm{STE}} = \frac{M_0}{2} e^{-\frac{\mathrm{TE}}{T_2}} e^{-\frac{\mathrm{TM}}{T_1}} \sin^2(\alpha)\sin(2\alpha), \tag{2.109}$$

where TM is the mixing time between second and third *RF* pulse. The flip angle in each voxel is calculated out of the relation between both echos, where the following relation is derived

$$\alpha = \arccos\left(\frac{S_{\mathrm{STE}} \cdot e^{\frac{\mathrm{TM}}{T_1}}}{S_{\mathrm{SE}}}\right). \tag{2.110}$$

If TM $\ll T_1$, the exponential term in Eq. (2.110) can be neglected as proposed in [2], due to the longer *EPI* readout in [142], it is suggest not to neglect it. For the correction, a T_1 map or simply an average T_1 value of the tissue under investigation can be used. Furthermore, an error estimate of the T_1 influence is given, which increases with increasing α and TM. However, the relation is independent of TR, such that it does not limit the acquisition time. With the *EPI* readout, a 3D volume can be acquired in 1.5 min. To reduce the influence of the slice profile, only the first pulse in the sequence is played out slice selective, the second and the third are applied non-selective. For the application of this method to 7 T, an improvement in dynamic range and a reduction to offresonances in combination with parallel imaging for faster acquisition was proposed by Lutti et al. [197].

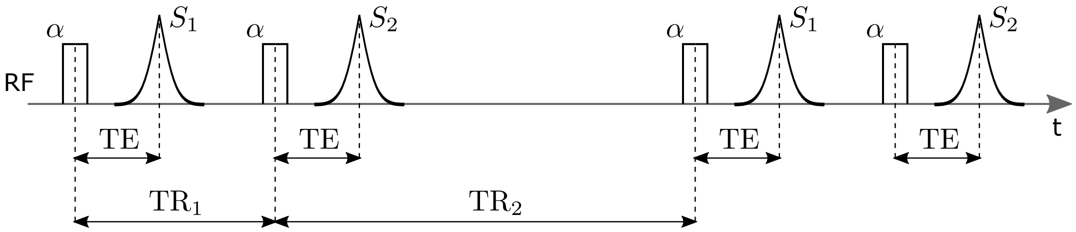

Figure 2.26: Sequence diagram of the AFI method.

2.5.1.3 Actual Flip-Angle Imaging (AFI)

A first variant of Actual Flip Angle Imaging (AFI) was introduced by Pan et al. [227], where two excitation pulses were applied with equal flip angle α, and a subsequent acquisition of a gradient echo after each excitation pulse. If the time between both excitations TR_1 is short enough that the longitudinal relaxation can be neglected during that time ($TR_1 \ll T_1$), the ratio between first and second echo signal is proportional to $\cos(\alpha)$, so that $\alpha(\vec{r})$ is given by

$$\alpha(\vec{r}) = \arccos\left(\frac{S_2(\vec{r})}{S_1(\vec{r})}\right). \tag{2.111}$$

This is, because both signals are proportional to M_0 and $\sin(\alpha)$, and the remaining longitudinal magnetization after the first excitation depends on $\cos(\alpha)$, all other contributions cancel out. However, full spoiling must be established between both excitations and full relaxation is required after the second echo acquisition. Compared to standard *DAM*, the acquisition time is at least halved.

A more general version of this approach is described by Yarnykh [327], where the imaging is performed in a certain steady state. The idea of applying two excitation pulses with equal flip angle α is the same as before, also a gradient echo is acquired after each excitation. With that, the sequence has two Repetition Times (TRs), TR_1 between first an second excitation pulse and TR_2 between the second excitation pulse and the start of the next repetition (see sequence diagram in Figure 2.26). Under the assumption of $\mathrm{TR}_1 < \mathrm{TR}_2 < T_1$ and perfect spoiling at the end of the TR_1 and TR_2 interval, the longitudinal magnetization reaches a steady state before first M_{z1} and second M_{z2} excitation pulse given as

$$M_{z1} = M_0 \frac{1 - E_{\mathrm{TR2}} + (1 - E_{\mathrm{TR1}})\, E_{\mathrm{TR2}} \cos(\alpha)}{1 - E_{\mathrm{TR1}} E_{\mathrm{TR2}} \cos^2(\alpha)}, \tag{2.112}$$

$$M_{z2} = M_0 \frac{1 - E_{\mathrm{TR1}} + (1 - E_{\mathrm{TR2}})\, E_{\mathrm{TR1}} \cos(\alpha)}{1 - E_{\mathrm{TR1}} E_{\mathrm{TR2}} \cos^2(\alpha)}, \tag{2.113}$$

with

$$E_{\mathrm{TR1,2}} = e^{-\frac{\mathrm{TR}_{1,2}}{T_1}}. \tag{2.114}$$

Because of equal TE and flip angle, the signal of first S_1 and second acquisition S_2 are proportional to the corresponding longitudinal steady state magnetization M_{z1} and M_{z1}, respectively, such that the ratio between both signals can be expressed as

$$r = \frac{S_2}{S_1} = \frac{1 - E_{\mathrm{TR1}} + (1 - E_{\mathrm{TR2}})\, E_{\mathrm{TR1}} \cos(\alpha)}{1 - E_{\mathrm{TR2}} + (1 - E_{\mathrm{TR1}})\, E_{\mathrm{TR2}} \cos(\alpha)}. \tag{2.115}$$

If TR_1 and TR_2 are small compared to T_1, Eq. (2.115) can be simplified by first-order Taylor series approximation of the exponential terms

$$r \approx \frac{1 + n\cos(\alpha)}{n + \cos(\alpha)}, \tag{2.116}$$

with

$$n = \frac{\mathrm{TR}_2}{\mathrm{TR}_1}, \tag{2.117}$$

such that the ratio r gets independent of T_1. By rearranging Eq. (2.116), the flip angle in each voxel can be expressed as

$$\alpha \approx \arccos\left(\frac{rn - 1}{n - r}\right). \tag{2.118}$$

With that, the overall repetition time ($\mathrm{TR} = \mathrm{TR}_1 + \mathrm{TR}_2$) comes into the order of $\mathrm{TR} < 100\,\mathrm{ms}$ such that a 3D acquisition gets feasible. With a non-selective or slab selective excitation pulse, the influence of the slice profile is eliminated. The limitations of this method are, due to high degree of approximation, low values of T_1 and high flip angles. The sensitivity of this method is determined by the ratio n between TR_1 and TR_2, where a higher n leads to an increase in sensitivity. It is recommended to keep TR_1 as low as possible due to sequence timing (practically $\mathrm{TR}_1 \approx 10\,\mathrm{ms}$) and the ratio n should be in the range of 4-6 to provide a good compromise between sensitivity and acquisition time. It is further recommended to keep α in the range of 40° to 80°, because lower flip angles lead to a decreased sensitivity and higher ones to an increased error.

2.5.1.4 Saturated Turob FLASH (satTFL)

The Saturated Turbo FLASH (satTFL) method was first described by Chung et al. [55] and is based on the acquisition of a turbo Fast Low Angle Shot (FLASH) readout, immediately after a slice selective preconditioning *RF* pulse with a certain flip angle α_{Pre}. The preconditioning pulse is played out slice selective, because it reduces the sensitivity to off-resonances. The turbo *FLASH* readout is performed with centric k-space ordering, the central k-space lines are acquired at the beginning, such that the main contrast in the image is determined by the preconditioning pulse. A spoiler gradient has to be applied between preconditioning pulse and turbo *FLASH* readout in order to dephase any transverse magnetization from the preconditioning. A second acquisition with the same sequence parameters has to be acquired, but without preconditioning, leading to proton density contrast. The flip angle distribution is again derived from the relation between both acquisitions. The signal intensities are proportional to the z-magnetization before the first *FLASH* readout pulse. Without preconditioning, the signal S_{PD} is proportional to M_0 and with preconditioning the signal S_{Pre} is proportional to $\cos(\alpha_{Pre})$, so that the relation is given by

$$\frac{S_{Pre}(\vec{r})}{S_{PD}(\vec{r})} = \frac{M_z(\vec{r})}{M_0(\vec{r})} = \cos(\alpha_{Pre}(\vec{r})). \tag{2.119}$$

With that, the flip angle distribution can be obtained with

$$\alpha_{Pre}(\vec{r}) = \arccos\left(\frac{S_{Pre}(\vec{r})}{S_{PD}(\vec{r})}\right). \tag{2.120}$$

It is suggested to select the preconditioning flip angle α_{Pre} to be around 60°, such that the effective flip angle for expected inhomogeneity variations in volume coils at 3 T does not exceed 90°. For $\alpha_{Pre} > 90°$, the solution in Eq. (2.120) is not unambiguous any more. The flip angle of the *FLASH* readout was set to $\alpha_{Ex} = 10°$. One very important assumption for the validity of Eq. (2.119) is that the appearing transient in the longitudinal magnetization during the turbo *FLASH* readout can be neglected. Because of that, the central k-space lines are acquired at the beginning, such that the influence of the overall contrast is quite low. It was proven to be $< 0.5\,\%$ Root Mean Squared Error (RMSE) for $T_1 \geq 500\,\text{ms}$. The influence of off-resonances was also shown to be $< 1.6\,\%$ *RMSE* for $\Delta\omega \leq 2\pi \cdot 500\,\text{Hz}$. However, slice profile effects might influence the accuracy of this method.

2.5.1.5 180° Signal Null

Compared to the previously described methods, the 180° signal null method, described by Dowell and Tofts [70], utilizes a completely different effect. Normally, the signal of a spoiled *GRE* sequence highly depends on the flip angle α, T_1, and TR in a highly nonlinear manner, but the point where the signal gets zero when α approaches 180° does not depend on T_1 and TR. If the effective flip angle is $\alpha_{eff} = 180°$, the signal gets identical zero, because this corresponds to a perfect inversion, so that no transverse magnetization is excited. Around the zero crossing, the signal varies approximately linear with flip angle which is also independent of T_1 and TR, such that a linear fit can be applied to determine the zero crossing out of three acquisitions around the nominal flip angle $\alpha_{nom} = 180°$. Simulations indicate that the variation of α_{nom} should be ±35°, such that three acquisitions are performed with nominal flip angles $\alpha_{nom_1} = 145°$, $\alpha_{nom_2} = 180°$ and $\alpha_{nom_3} = 215°$. In principle, two angles would be enough, but the robustness against noise increases with the proposed three acquisitions. The effective flip angle $\alpha_{eff}(\vec{r})$ in each voxel can be expressed by a scaling factor $\varrho(\vec{r})$ in each voxel as

$$\alpha_{eff}(\vec{r}) = \varrho(\vec{r})\alpha_{nom}. \tag{2.121}$$

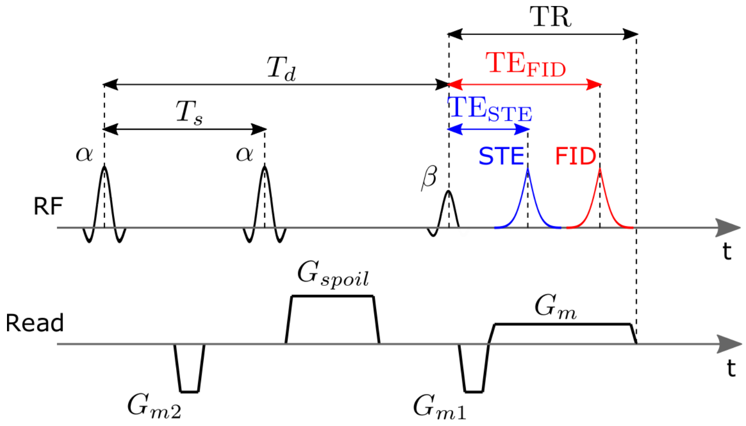

Figure 2.27: Sequence diagram of the DREAM method

Out of the linear fit in each voxel, the zero crossing $\alpha_{zero}(\vec{r})$ can be determined and with that the scaling factor map $\varrho(\vec{r})$ is given as

$$\varrho(\vec{r}) = \frac{180°}{\alpha_{zero}(\vec{r})}. \tag{2.122}$$

As already mentioned, the zero crossing is in principle independent of TR, but the slope of the function in that point is not independent. It can be shown that the slope and therefore the sensitivity of the method increases with increasing TR. Thus, the selection of TR is a compromise between sensitivity and acquisition time. In [70], a TR of 33 ms is suggested, leading to an acquisition time of ≈ 4 min for a 3D volume covering the entire brain. Another restriction of this method is that it is only suited for low flip angle variations, because the linear region around the zero crossing is limited. Due to that and the increase in *SAR* due to the high flip angle, this method is limited for volume coils at field strength ≤ 3 T.

2.5.1.6 Dual Refocusing Echo Acquisition Mode (DREAM)

The latest method based an the signal magnitude was described by Nehrke and Börnert [220], called Dual Refocusing Echo Acquisition Mode (DREAM) and is able to reach very low acquisition times in the order of < 1 s for a single slice, but with the drawback of a very low resolution. The method is based on a *STEAM* preparation module, followed by a rapid low-angle *GRE* single shot acquisition with flip angle β, where two echos, an *STE* and an *FID* echo, are acquired quasi simultaneously. The *STEAM* preparation consists of two *RF* pulses with equal flip angle α separated by the time interval T_S and a modulation gradient with strength G_{m2} inbetween. The transverse magnetization after the *STEAM* preparation is dephased utilizing a spoiler gradient. The longitudinal magnetization is prepared, such that a *STE* component $M_{z,\mathrm{STE}}$ and an unprepared component $M_{z,\mathrm{FID}}$ are present. The time between the center of the first preparation pulse and the first *GRE* readout pulse is denoted as delay time T_d (see sequence diagram in Figure 2.27). The phase introduced by G_{m2} is responsible that both echos are refocused at different echo times in the following *GRE* acquisition, at $\mathrm{TE}_{\mathrm{STE}}$ and $\mathrm{TE}_{\mathrm{FID}}$, which are acquired in a single readout period. The signal for the first *GRE* readout is given by

$$S_{\mathrm{STE}} = \sin(\beta) M_{z,\mathrm{STE}} = \frac{1}{2}\sin^2(\alpha) M_0 \sin(\beta), \tag{2.123}$$

$$S_{\mathrm{FID}} = \sin(\beta) M_{z,\mathrm{FID}} = \cos^2(\alpha) M_0 \sin(\beta). \tag{2.124}$$

The preparation flip angle α can be calculated out of the relation between the magnitude of the two signals as

$$\alpha = \arctan\left(\sqrt{\frac{2|S_{\mathrm{STE}}|}{|S_{\mathrm{FID}}|}}\right). \tag{2.125}$$

The echo time difference is determined by the modulation gradient G_{m2}, its pulse length T_{m2}, and the readout gradient G_m, which is given by

$$\mathrm{TE}_{\mathrm{STE}} - \mathrm{TE}_{\mathrm{FID}} = \frac{\int_0^{T_{m2}} G_{m2}(t)dt}{G_m}. \tag{2.126}$$

Different timing schemes were proposed in [220], however, only the most effective is considered, where T_S is selected to be

$$T_S = \mathrm{TE}_{\mathrm{STE}} + \mathrm{TE}_{\mathrm{FID}}. \tag{2.127}$$

This timing scheme was shown to be independent to T_2^* decay, ΔB_0 and chemical shift. It has to be noted that T_2^* and ΔB_0 effects are completely refocused in the *STE* only for $T_S = \mathrm{TE}_{\mathrm{STE}}$, for $T_S \neq \mathrm{TE}_{\mathrm{STE}}$ they are at least partially refocused, such that Eqs. (2.123) and (2.124) can be rewritten as

$$S_{\mathrm{STE}} = e^{i(\phi_{Tx}+\phi_{Rx})} \cdot e^{-\frac{|\mathrm{TE}_{\mathrm{STE}}-T_S|}{T_2^*}} \cdot e^{i\gamma\Delta B_0(\mathrm{TE}_{\mathrm{STE}}-T_S)} \cdot \sin(\beta) M_{z,\mathrm{STE}}, \tag{2.128}$$

$$S_{\mathrm{FID}} = e^{i(\phi_{Tx}+\phi_{Rx})} \cdot e^{-\frac{|\mathrm{TE}_{\mathrm{FID}}|}{T_2^*}} \cdot e^{i\gamma\Delta B_0 \mathrm{TE}_{\mathrm{FID}}} \cdot \sin(\beta) M_{z,\mathrm{FID}}. \tag{2.129}$$

By using Eq. (2.127), the relation in Eq. (2.125) gets independent of T_2^* and ΔB_0. If a fat-water in-phase echo time is used, also chemical shift effects cancel out. Moreover, additional information can be gained out of these two signals for free, a ΔB_0 dependent phase map and the transceive phase of the *RF* system by

$$\Delta B_0 = \frac{\angle(S_{\mathrm{FID}} \cdot \overline{S_{\mathrm{STE}}})}{2\gamma \mathrm{TE}_{\mathrm{FID}}}, \tag{2.130}$$

$$\phi_{Tx} + \phi_{Rx} = \frac{\angle(S_{\mathrm{FID}} \cdot S_{\mathrm{STE}})}{2}. \tag{2.131}$$

The influence of T_1 is determined by the delay time T_d, which should be kept as short as possible. For the timing chosen according to Eq. (2.127), the T_2 influence is determined by the echo time of the *STE*, which also should be kept as short as possible. For the experiments described by Nehrke and Börnert [220], reasonable values are given for $\mathrm{TE}_{\mathrm{STE}} = 1.7\,\mathrm{ms}$, $\mathrm{TE}_{\mathrm{FID}} = 2.3\,\mathrm{ms}$, $\mathrm{TR} = 3.2\,\mathrm{ms}$, and $T_d = 9\,\mathrm{ms}$, such that the relaxation influence can be neglected for typical tissue relaxation times. Because the acquisition has to be done in 2D, the slice profile influence has to be considered. For single slice acquisitions, the *STEAM* preparation pulses are carried out non-selective, with a slice selective *GRE* excitation pulse. This is, because β has no influence on the flip angle map. For multi-slice acquisitions, the *STEAM* preparation pulses are carried out with double the slice thickness of the *GRE* excitation pulse. To avoid influencing neighboring slices, an even–odd slice acquisition scheme has to be applied, such that the time between adjacent slices is at least $> T_1$. Also an error analysis is provided. According to that, the optimal preparation flip angle should be $\alpha \approx 55°$ and a *GRE* flip angle of $\beta = 15°$ is suggested. Furthermore, an error estimate is given by

$$\Delta\alpha \approx \frac{220°}{\mathrm{SNR}}. \tag{2.132}$$

The main advantages of this method are its very high motion robustness, because of the short acquisition time in the order of $\mathrm{TA} \approx 130\,\mathrm{ms}$ per slice and its insensitivity against ΔB_0 and relaxation. Furthermore, since it is not based on low bandwidth acquisition (e.g. *EPI* or spirals), this method is not prone to geometrical distortions. However, care has to be taken on signal variations during the readout pulse train, where the prepared longitudinal magnetization $M_{z,\mathrm{STE}}$ and $M_{z,\mathrm{FID}}$ changes due to influences of T_1 and β, such that only the first acquired echo fulfills Eq. (2.125). This effect is considered by Nehrke et al. [221], and it can be shown that this influence is negligible for the proposed center-out k-space ordering scheme with typically used flip angles, readout train lengths, and tissue T_1 times. Small influences were reported around edges. However, this effect limits the *DREAM* method to a very low resolution in the presented way. A segmented acquisition with several preparation modules would be possible in general, but this would require much longer acquisition times, because full relaxation is required between each shot. Furthermore, in [221], an additional timing scheme was proposed to compensate both, the influences of T_2^* and T_2. A further improvement of this method is described by Ehses [75], where the *DREAM* approach is extended to a single shot 3D acquisition. For that purpose, a 2D center-out spiral readout trajectory was combined with undersampling in both phase encoding directions and the application of a Controlled Aliasing in Parallel Imaging (CAIPI) [41] pattern and Generalized Auto-calibrating Partial Parallel Acquisition (GRAPPA) [99] reconstruction. Because of the strong blurring introduced by the long readouts, an iterative blurring compensation has to be applied, utilizing a global T_1 estimate and the gained flip angle values. With that a 3D volume with 5 mm isotropic resolution can be acquired in approximately 4 s.

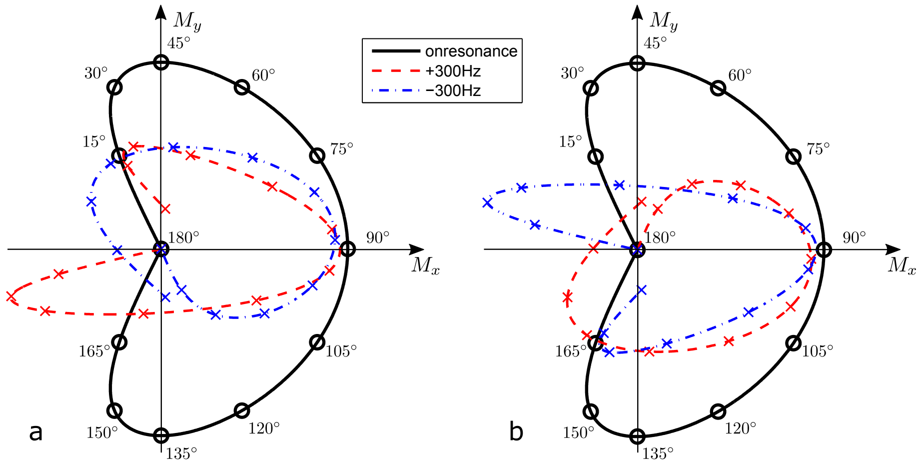

Figure 2.28: Theoretical position of the magnetization vector in the transverse plane after performing both excitation pulses for different α and different resonance offsets. (a) For first and (b) for second acquisition.

2.5.1.7 Phase Imaging

All previously described B_1 mapping methods are based on the signal's magnitude. A new method was proposed by Morrell [218] relying on the signals phase, with the advantage of an inherent T_1 independency and allowing a larger range of flip angle variations. The basic idea of this method is to apply two non-selective excitation pulses with a nominal flip angle of $\alpha_1 = 180°$ for the first *RF* pulse which is applied around the x-axis, and $\alpha_2 = 90°$ for the second pulse that is applied around the y-axis. Because of the unknown B_1 field variation, the effective flip angles are $\alpha_1 = 2\alpha$ and $\alpha_2 = \alpha$. Without off-resonances, the situation is quite simple, the first *RF* pulse flips the magnetization vector into the $y - z$ plane. The subsequent second pulse flips the magnetization into the transverse $x - y$ plane, where the phase is influenced by the first 2α pulse. The magnetization can be described by

$$\overrightarrow{M} = M_0 \begin{pmatrix} \sin(\alpha)\cos(2\alpha) \\ \sin(2\alpha) \\ \cos(\alpha)\cos(2\alpha) \end{pmatrix}. \tag{2.133}$$

Because the signal phase not only depends on the first 2α pulse, a second acquisition is necessary to get rid of other phase effects. The second acquisition is performed with the same sequence parameters except the first *RF* pulse is applied with opposite sign, such that the flip direction is reversed, and hence, the sign of the signal phase. The phase difference $\Delta\phi$ of both acquisitions is related through a lookup table to the value of interest, the flip angle α. If offresonances are present, the flip axis changes according to Eq. (2.29) in Section 2.1.4 and the expression for the magnetization vector becomes much more complicated. The lookup table is extended to a second dimension to account for offresonances, which have to be determined by acquiring an additional ΔB_0 map (see

Section 2.4). In Figure 2.28, the theoretical position of the magnetization vector after the two pulse excitation is depicted. This method is restricted to non-selective excitation, to minimize the influence of B_0 field variations and to allow B_1 mapping over a wide range of ΔB_0.

If the flip angle α is far away from the desired 90°, e.g. in the range of 0° or 180°, the transverse magnetization generated by the second *RF* pulse is very low. This further leads to a very low *SNR* in these regions. To overcome this, an improved version of this method is described in [118] and [117], where the second α pulse is replaced by an adiabatic B_1 insensitive excitation pulse to increase the excitation efficiency.

2.5.1.8 Orthogonal Alpha

A very similar method to the previously describe "phase imaging" is proposed by Chang [48], where also two non-selective excitation pulses, but with equal flip angle α are applied, followed by a *GRE* readout. The first *RF* pulse is applied around the $-x$-axis and the second around the y-axis, such that the phase of the resulting signal depends on the flip angle α. To get rid of other effects influencing the signal phase, a second acquisition is required with reversed order of the *RF* pulses. Using the concept of rotation matrices from Eqs. (A.10) to (A.12) in the Appendix, and considering the T_2^* relaxation with the corresponding exponential E_2^* term at the first two diagonal elements of $\mathbf{E}_2^*$, the resulting magnetization $\overrightarrow{M}_{1,2}$ at the end of the second *RF* pulse for both acquisitions can be described as

$$\overrightarrow{M}_1(\alpha) = \mathbf{R}_y(\alpha)\mathbf{E}_2^*\mathbf{R}_z(\phi)\mathbf{R}_{-x}(\alpha)\overrightarrow{M}_0 = \begin{pmatrix} (1-E_2^*\sin(\phi))\sin(\alpha)\cos(\alpha) \\ E_2^*\cos(\phi)\sin(\alpha) \\ E_2^*\sin(\phi)\sin^2(\alpha)+\cos^2(\alpha) \end{pmatrix}, \quad (2.134)$$

$$\overrightarrow{M}_2(\alpha) = \mathbf{R}_{-x}(\alpha)\mathbf{E}_2^*\mathbf{R}_z(\phi)\mathbf{R}_y(\alpha)\overrightarrow{M}_0 = \begin{pmatrix} E_2^*\cos(\phi)\sin(\alpha) \\ (1+E_2^*\sin(\phi))\sin(\alpha)\cos(\alpha) \\ -E_2^*\sin(\phi)\sin^2(\alpha)+\cos^2(\alpha) \end{pmatrix}. \quad (2.135)$$

Here, ϕ is the offresonance precession angle during the time interval τ, between the center of the two *RF* pulses. E_2^* and ϕ are given as

$$E_2^* = e^{-\frac{-\tau}{T_2^*}}, \qquad \phi = \gamma \Delta B_0 \tau. \quad (2.136)$$

The phase of both signals θ_1 and θ_2 is related by

$$\tan(\theta_1) = \frac{E_2^*\cos(\phi)}{(1-E_2^*\sin(\phi))\cos(\alpha)}, \quad (2.137)$$

$$\tan(\theta_2) = \frac{(1+E_2^*\sin(\phi))\cos(\alpha)}{E_2^*\cos(\phi)}, \quad (2.138)$$

such that their ratio gets proportional to $\cos^2(\alpha)$

$$\frac{\tan(\theta_2)}{\tan(\theta_1)} = \frac{e^{\frac{2\tau}{T_2^*}} - \sin^2(\phi)}{\cos^2(\phi)} \cos^2(\alpha). \tag{2.139}$$

If $\tau \ll T_2^*$, the exponential term in Eq. (2.139) becomes ≈ 1, such that the influence of ϕ cancels out and the flip angle can be calculated with

$$\alpha \approx \arccos\left(\sqrt{\frac{\tan(\theta_2)}{\tan(\theta_1)}}\right). \tag{2.140}$$

The phase accumulation between the second excitation and the echo formation also has to be considered. The basic assumption is that θ_1 and θ_2 are spread symmetrically around $\pi/4$, such that the following correction is applied

$$\theta_1 = \frac{\pi}{4} + \frac{\theta_1' - \theta_2'}{2}, \qquad \theta_2 = \frac{\pi}{4} + \frac{\theta_2' - \theta_1'}{2}, \tag{2.141}$$

for θ_1' and θ_2' being the original phase of first and second acquisition, respectively. To minimize the influence of the T_2^* decay, the time interval τ is tried to keep as short as possible, such that the two *RF* pulses only can be applied non-selective. This restricts this method to pure 3D acquisition over a large volume, as it is the case for "phase imaging" (see Section 2.5.1.7). Furthermore, this sequence is restricted to flip angles $\alpha \leq 60°$, to ensure that the effective flip angle $\alpha_{eff} < 90°$. The advantages of this method are the insensitivity to T_1 and a much lower sensitivity to background field variations as "phase imaging" (see Section 2.5.1.7), so that no B_0 field map is necessary. However, there are two main sources of error: First, there is the influence of T_2^* in Eq. (2.139) leading to an overestimation of α, and second, the assumption that θ_1 and θ_2 are symmetrically around $\pi/4$ in Eq. (2.141). It can be shown for values of $\phi \leq \pi/6$, that this is a quite good approximation with about 5 % error, which corresponds to a resonance offset of $\Delta\omega \approx 2\pi \cdot 85\,\text{Hz}$. A solution for this problem would be a third acquisition with only one *RF* pule to accurately determine θ_1 and θ_2.

2.5.1.9 Hyperbolic Secant

A phase based method to directly determine the B_1^+ magnitude instead of the flip angle α is presented by Lee et al. [172], making use of the phase introduced by two Hyperbolic Secant (HS) pulses. For that purpose, two full-passage *HS* pulses are applied as 90° excitation pulse and a 180° refocusing pulse to form a spin echo. The *HS* pulse is an adiabatic pulse with varying frequency and is defined by its amplitude $B_1(t)$ and frequency variation

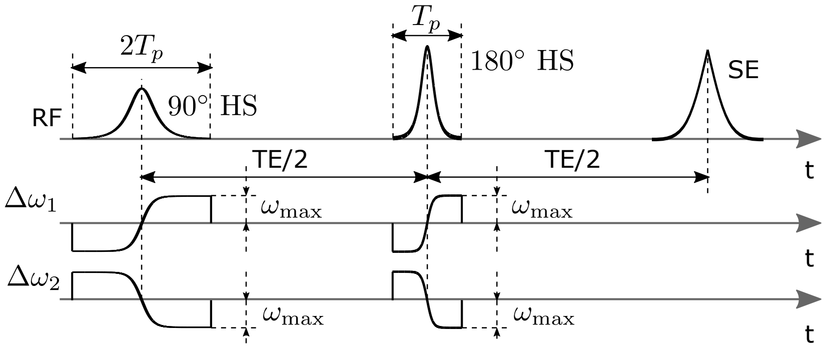

Figure 2.29: Sequence diagram for the hyperbolic secant method, with frequency modulation $\Delta\omega_1$ and $\Delta\omega_2$ for first and second acquisition, respectively.

$\omega_{\text{RF}}(t)$ given as

$$B_1(t) = B_{1,\text{peak}}\text{sech}(\beta t), \tag{2.142}$$

$$\omega_{\text{RF}}(t) = \omega_{\max}\tanh(\beta t). \tag{2.143}$$

Here, $B_{1,\text{peak}}$ is the the maximum B_1^+ magnitude of the pulse and $\omega_{\max}$ is the maximum resonance offset of the frequency modulation, which is equal to half the bandwidth of the pulse. The constant β is a dimensionless truncation factor. There is one condition that has to be fulfilled, the duration of the *HS* excitation pulse has to be twice as long as the duration of the *HS* refocusing pulse, but with the same bandwidth for both (see sequence diagram in Figure 2.29).

This method is based on the B_1 dependent phase created by the *HS* pulse, which is given as the integral over the effective magnetic field ($\omega_{eff}(t) = \gamma B_{eff}(t)$) according to Eq. (2.30) in Section 2.1.4

$$\phi_{\text{HS}} = \pm\int_{-\frac{T_p}{2}}^{\frac{T_p}{2}} \sqrt{(\gamma B_{1,\text{peak}})^2\,\text{sech}^2(\beta t) + (\Delta\omega_0 - \omega_{\max}\tanh(\beta t))^2}\,dt. \tag{2.144}$$

The sign in Eq. (2.144) is positive if the frequency sweep is performed from negative to positive values ($-\omega_{\max} \rightarrow \omega_{\max}$) and it is negative if the frequency is swept in the opposite direction ($\omega_{\max} \rightarrow -\omega_{\max}$). It can be shown that the phase contribution from the frequency sweep can be compensated by the application of both the 90° and the 180° *HS* pulse, such that ϕ_{HS} gets independent of $\Delta\omega_0$ and only depends on $B_{1,\text{peak}}$. As for all other described methods, to remove undesirable phase contributions, two acquisitions are performed with opposite frequency sweep to gain a $B_{1,\text{peak}}$ dependent phase difference $\Delta\phi_{\text{HS}}(B_{1,\text{peak}})$, which monotonically increases with $B_{1,\text{peak}}$. Because the relation between $B_{1,\text{peak}}$ and $\Delta\phi$ is quite complicated, an empirically determined relation was used to determine $B_{1,\text{peak}}$. The relation is gained by acquiring a set of image pairs with different pulse amplitudes and observing the phase difference $\Delta\phi$. This method was shown to be independent of

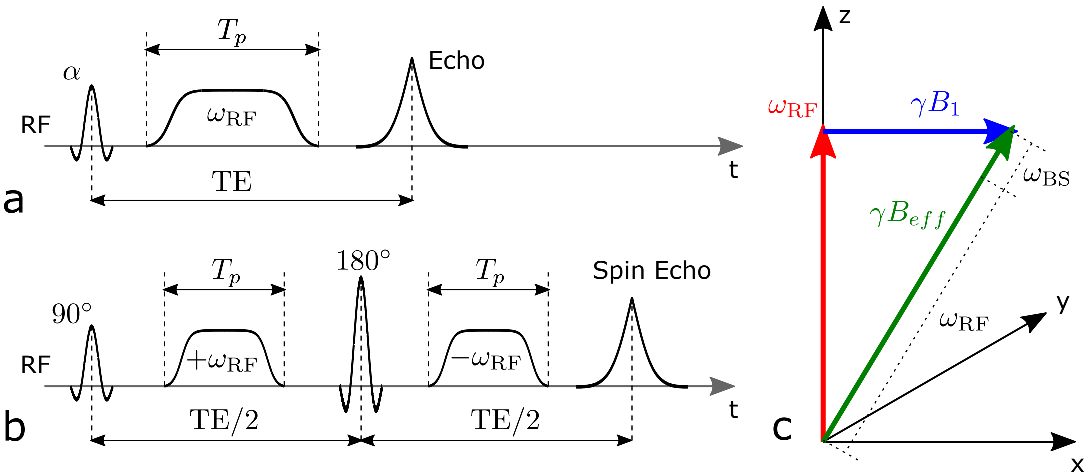

Figure 2.30: Sequence diagram of the BS shift method in two variants, (a) with GRE and (b) with SE readout. In the SE version, the BS pulse is split into one part before and one after refocusing, with opposite sign of the resonance offset ω_{RF}. (c) Visualization of the field configuration during the BS pulse in the rotating frame. The spins rotate with ω_{RF}, whereas the B_1 field stands sill. The frequency shift ω_{BS} is a constant field in the direction of the effective field B_{eff}.

T_1, TR, and insensitive to B_0 variations. Furthermore, it can be applied to a wide range of B_1 amplitudes, such that an application at higher field strength $> 3\,\mathrm{T}$ and different types of coils, volume or surface coils, is possible. Compared to the Bloch-Siegert shift method, it was shown that the sensitivity is better especially for low B_1 magnitudes and the reduced *SAR*. The acquisition time is reported to be around 1 min. This method was further improved by Jordanova et al. [144], performing an optimization of the *HS* pulse parameters in order to increase the sensitivity.

2.5.1.10 Bloch–Siegert Shift Imaging (BS)

The first method which directly measures the B_1^+ field instead of the flip angle α, was proposed by Sacolick et al. [249]. This method, called Bloch-Siegert (BS) shift imaging, utilizes an effect described by Bloch and Siegert [26], where the resonance frequency of a spin ensemble slightly shifts under the presence of an offresonant *RF* field (see Figure 2.30(c)). In the rotating frame, this can be visualized according to the concept of the effective field described in Section 2.1.4 (Eqs. (2.29) and (2.30)). The length of the effective field vector is given by

$$\gamma B_{eff} = \sqrt{\omega_{\mathrm{RF}}^2 + (\gamma B_1)^2} = \omega_{\mathrm{RF}} + \omega_{\mathrm{BS}}, \tag{2.145}$$

where ω_{RF} is the resonance offset of the *RF* field. The change in length of the effective field ω_{BS} (*BS* shift) is described by

$$(\omega_{\mathrm{BS}} + \omega_{\mathrm{RF}})^2 = \omega_{\mathrm{RF}}^2 + (\gamma B_1)^2. \tag{2.146}$$

For large offresonances ($\omega_{\text{RF}} \gg \gamma B_1$), ω_{BS} can be approximated by (neglecting the ω_{BS}^2 term)

$$\omega_{\text{BS}} = \frac{(\gamma B_1)^2}{2\omega_{\text{RF}}}. \tag{2.147}$$

If such an offresonant *RF* pulse (*BS* pulse) is applied in an *MRI* sequence between excitation and readout, an additional phase shift ϕ_{BS} occurs in each voxel depending on the B_1 magnitude

$$\phi_{\text{BS}} = \int_0^{T_p} \omega_{\text{BS}}(t)dt = \int_0^{T_p} \frac{(\gamma B_1(t))^2}{2\omega_{\text{RF}}(t)}dt. \tag{2.148}$$

Two sequence versions (*SE* and *GRE*) are given in Figure 2.30(a) and (b). By using a normalized function for the *RF* pulse, the phase shift ϕ_{BS} only depends on the squared B_1 peak magnitude and a pulse dependent constant K_{BS}

$$\phi_{\text{BS}} = B_{1,\text{peak}}^2 \int_0^{T_p} \frac{\left(\gamma B_{1,\text{norm}}\left(t\right)\right)^2}{2\omega_{\text{RF}}\left(t\right)}dt = B_{1,\text{peak}}^2 \cdot K_{\text{BS}}, \tag{2.149}$$

where K_{BS} depends on the pulse shape $B_{1,\text{norm}}$, the pulse duration T_p, and the resonance offset, which are all known in advance. To separate ϕ_{BS} from other effects influencing the signal's phase, a second acquisition is necessary with negative resonance offset $-\omega_{\text{RF}}$ and identical imaging parameters, leading to a negative phase contribution, such that the *BS* phase can be obtained by

$$\phi_{\text{BS}} = \frac{\angle S_+ - \angle S_-}{2}, \tag{2.150}$$

where S_+ and S_- are the signals with positive and negative resonance offset ω_{RF}, respectively. The peak B_1 magnitude is given by

$$B_{1,\text{peak}} = \sqrt{\frac{\phi_{\text{BS}}}{K_{\text{BS}}}}, \tag{2.151}$$

using Eq. (2.149). Even though, the *BS* shift depends on ΔB_0, it can be shown that the phase difference between both acquisitions is independent on ΔB_0 up to first-order in a Taylor series expansion. The Taylor series expansion for the *BS* shift is given as

$$\omega_{\text{BS}} = \frac{(\gamma B_1)^2}{2(\omega_{\text{RF}} + \Delta\omega_0)} \approx \frac{(\gamma B_1)^2}{2\omega_{\text{RF}}} - \frac{(\gamma B_1)^2 \Delta\omega_0}{2\omega_{\text{RF}}^2} + O(\Delta\omega_0^2), \tag{2.152}$$

where the second term cancels by taking the difference, because of the same sign for both resonance offsets. If $\Delta\omega_0 \ll \omega_{\text{RF}}$, the higher order terms can be neglected. The most important condition for the accuracy of this method is $\omega_{\text{RF}} \gg \gamma B_1$ because of several reasons: first, the approximation in Eqs. (2.146) and (2.147) stays valid, second, the *BS* pulse does not lead to an additional excitation, and third, the influence of ΔB_0 is minimized. On the other hand, according to Eq. (2.148), an increase in ω_{RF} leads to a decreased B_1 sensitivity, such that a compromise between accuracy and sensitivity has to be found. In Sacolick et al. [249], a resonance offset of $\omega_{\mathrm{RF}} = 4\,\mathrm{kHz}$ is suggested using a 8 ms Fermi-shaped *BS* pulse. This resonance offset is shown to be enough that no direct excitation occurs and the error is below $\approx 2.5\,\%$ for $\Delta\omega_0 < 600\,\mathrm{Hz}$. In general, this method is shown to be robust against TR, T_1 relaxation, chemical shift, magnetization transfer, and as already discussed ΔB_0. However, Corbin et al. [58] found out that substantial deviations can occur for low values of TR ($< 40\,\mathrm{ms}$), long T_1 and T_2, combined with interleaved resonance offset acquisition and a lower resonance offset of the *BS* pulse (see later).

The main limitation of the *BS* method in-vivo is the *SAR* constraint, limiting the minimum possible TR. To reach a sufficient B_1 sensitivity, a high magnitude and a long duration is required for the *BS* pulse, leading to an onresonant equivalent flip angle of several hundred degree, leading to quite high *SAR* values. In the initial publication [249], a *GRE* and a *SE* readout were proposed, such that the application of a *BS* pulse is necessary for every k-space line, making the *SAR* problem most severe. To overcome the *SAR* limitation and to decrease the acquisition time, several combinations of the *BS* shift with faster read out trajectories were proposed, e.g. the combination with a *TSE* readout [8, 248], *EPI* [71, 250] and spiral trajectories [152, 250]. Another approach was presented in [9], where many excitation pulses for different slices were placed before a refocusing pulse and the *BS* encoding, to subsequently acquire a separate echo for each excited slice to reduce the *SAR*. It was further shown that the *BS* shift can be encoded by a *STEAM* preparation, similar to the *DREAM* sequence (see Section 2.5.1.6), followed by a fast low-angle *GRE* readout [219]. Further improvements were proposed concerning the optimization of the *BS* pulse to increase the B_1 sensitivity and to decrease *SAR* [137, 153, 154], and also the simultaneous acquisition of a ΔB_0 map, by acquiring a second gradient echo after the *BS* encoding [72]. The field map is calculated according to the equations given in Section 2.4.

It is shown in this thesis that in general interleaved resonance offset acquisition is more robust against phase instabilities during the acquisition (see Section 5.1), so that it is recommended as the method of choice. However, the findings in a recent work presented by Corbin et al. [58] indicate that under certain conditions the steady-state can be disturbed by this interleaved acquisition, leading to an unequal phase offset in both acquisitions, which does not cancel when taking the phase difference. To account for this effect, also a correction strategy is proposed in [58] based on a multi-echo *GRE* sequence and a General Linear Model (GLM). For this purpose, the sequence is modified, such that 2 echos are acquired before and 6 echos after the *BS* encoding pulse, which leads to 16 acquired echos in total for both resonance offsets. The *GLM* is used to model several individual effects which influence the signal phase at each of the 16 acquisitions and to separate them from the quantity of interest, the B_1^+ dependent *BS* phase ϕ_{BS}. These are: main field variations ΔB_0, differences in the influence of eddy currents for odd and even echos during the bipolar readouts ϕ_{eddy}, different phase offsets in the positive and negative *BS* encodings (ϕ_{offset^+} and ϕ_{offset^-}, respectively), and phase effects of same sign arising by the *BS* encoding pulse and the crusher gradients around it $\phi_{sameSign}$. With that the *GLM* is written as

$$\mathbf{S}_\phi(\vec{r}) = \mathbf{G} \cdot \mathbf{a}(\vec{r}), \tag{2.153}$$

where $\mathbf{S}_\phi$ describes the phase of the 16 individual acquisitions and $\mathbf{a}$ is a vector containing the different phase contributions. The system matrix $\mathbf{G}$ describes the contribution of each of the modeled phase effects on the acquired signal and can be separated in positive (left) and negative resonance offset acquisition (right) (see Eq. (2.155)). The dashed line separates the matrix for echos acquired before and after the *BS* encoding pulse and $t_n = \mathrm{TE}_n$ is the echo time at the n^{th} acquisition. $\mathbf{S}_\phi$, $\mathbf{a}$ and $\mathbf{G}$ are given as

$$\mathbf{S}_\phi(\vec{r}) = \begin{pmatrix} \phi_{\mathrm{TE}_1,pos}(\vec{r}) \\ \vdots \\ \phi_{\mathrm{TE}_8,pos}(\vec{r}) \\ \phi_{\mathrm{TE}_1,neg}(\vec{r}) \\ \vdots \\ \phi_{\mathrm{TE}_8,neg}(\vec{r}) \end{pmatrix}, \quad \mathbf{a}(\vec{r}) = \begin{pmatrix} \phi_{\mathrm{BS}}(\vec{r}) \\ \gamma \Delta B_0(\vec{r}) \\ \phi_{eddy}(\vec{r}) \\ \phi_{offset^+}(\vec{r}) \\ \phi_{offset^-}(\vec{r}) \\ \phi_{sameSign}(\vec{r}) \end{pmatrix}, \tag{2.154}$$

$$\mathbf{G}^T = \underset{\text{resonance offset}}{\left(\underbrace{\begin{array}{cc:cccccc} 0 & 0 & 1 & 1 & 1 & 1 & 1 & 1 \\ t_1 & t_2 & t_3 & t_4 & t_5 & t_6 & t_7 & t_8 \\ 1 & -1 & 1 & -1 & 1 & -1 & 1 & -1 \\ 1 & 1 & 1 & 1 & 1 & 1 & 1 & 1 \\ 0 & 0 & 0 & 0 & 0 & 0 & 0 & 0 \\ 0 & 0 & 1 & 1 & 1 & 1 & 1 & 1 \end{array}}_{\text{positive}} \middle| \underbrace{\begin{array}{cc:cccccc} 0 & 0 & -1 & -1 & -1 & -1 & -1 & -1 \\ t_1 & t_2 & t_3 & t_4 & t_5 & t_6 & t_7 & t_8 \\ 1 & -1 & 1 & -1 & 1 & -1 & 1 & -1 \\ 0 & 0 & 0 & 0 & 0 & 0 & 0 & 0 \\ 1 & 1 & 1 & 1 & 1 & 1 & 1 & 1 \\ 0 & 0 & 1 & 1 & 1 & 1 & 1 & 1 \end{array}}_{\text{negative}} \right)}. \tag{2.155}$$

The unknown quantities in $\mathbf{a}$ are solved voxel wise by inverting Eq. (2.153) using weighted least squares given as

$$\mathbf{a}(\vec{r}) = \left(\mathbf{G}^T \mathbf{W} \mathbf{G}\right)^{-1} \mathbf{G}^T \mathbf{W} \mathbf{S}_\phi(\vec{r}), \tag{2.156}$$

where $\mathbf{W}$ is a diagonal weighting matrix, with the signal magnitudes on its diagonal.

A further more fundamental improvement was presented by Duan et al. [73], where it was shown that *BS* based B_1^+ mapping can also be performed under the condition $\gamma B_1 > \omega_{\mathrm{RF}}$. This leads to a highly increase of the sensitivity to B_1^+ and with that to a substantial reduction in *SAR*. For that purpose, a more general relation between $B_{1,\mathrm{peak}}$ and the resulting *BS* phase difference $2\phi_{\mathrm{BS}}$ between both acquisitions with positive and negative resonance offsets was derived as

$$\begin{aligned}2\phi_{\mathrm{BS}} = \int_0^{T_p} & (\Delta\omega_0 + \omega_{\mathrm{RF}}(t)) \left(\sqrt{1 + \left(\frac{\gamma B_1(t)}{\Delta\omega_0 + \omega_{\mathrm{RF}}(t)} \right)^2} - 1 \right) \\ & - (\Delta\omega_0 - \omega_{\mathrm{RF}}(t)) \left(\sqrt{1 + \left(\frac{\gamma B_1(t)}{\Delta\omega_0 - \omega_{\mathrm{RF}}(t)} \right)^2} - 1 \right) dt.\end{aligned} \tag{2.157}$$

Under the condition $|\omega_{\mathrm{RF}}| > |\Delta\omega_0|$ Eq. (2.157) can be further simplified to

$$\begin{aligned}2\phi_{\mathrm{BS}} = \int_0^{T_p} \omega_{\mathrm{RF}}(t) & \left(\sqrt{\left(1 + \frac{\Delta\omega_0}{\omega_{\mathrm{RF}}(t)}\right)^2 + \left(\frac{\gamma B_1(t)}{\omega_{\mathrm{RF}}(t)}\right)^2} \right. \\ & \left. + \sqrt{\left(1 - \frac{\Delta\omega_0}{\omega_{\mathrm{RF}}(t)}\right)^2 + \left(\frac{\gamma B_1(t)}{\omega_{\mathrm{RF}}(t)}\right)^2} - 2 \right) dt,\end{aligned} \tag{2.158}$$

which is solved numerically. The B_0 dependence is compensated by the simultaneous acquisition of a B_0 map [72], which is plugged into Eq. (2.158). Furthermore, the sequence is modified such that an additional crusher gradient is applied around the *BS* pulse to dephase any direct excitation. This modifications allow the acquisition of a *BS* based B_1^+ map with a resonance offset of $\omega_{\mathrm{RF}} = 2\pi \cdot 500\,\mathrm{Hz}$ with a *RMSE* of 0.57 % compared to a reference acquisition with a resonance offset of $\omega_{\mathrm{RF}} = 2\pi \cdot 8\,\mathrm{kHz}$.

Another improvement of this method was presented by Weingärtner et al. [318], where it is utilized for cardiac B_1^+ mapping. The acquisition is performed in the diastolic phase using a segmented *GRE* readout. The acquisition of the positive and negative resonance offset was performed in an interleaved fashion to increase robustness against breathing motion. The interleaved acquisition was further shown to be robust against phase drifts during the acquisition time [176].

2.5.2 Mapping the Phase of the B_1^+ Field

It is necessary to know the spatial distribution of the B_1^+ phase, to determine the phase offset of each channel in B_1 shimming (see Section 2.3.6). Furthermore, the B_1^+ phase distribution carries information about the conductivity distribution $\sigma(\vec{r})$ in the tissue under investigation, which is utilized in *EPT* [309] to determine $\sigma(\vec{r})$.

2.5.2.1 Absolute Phase of the B_1^+ Field

For the reconstruction of $\sigma(\vec{r})$ in *EPT*, the absolute B_1^+ phase has to be determined, whereas for B_1 shimming the relative phase difference between all transmit channels is sufficient. The determination of the absolute B_1^+ phase is very challenging and is only possible under certain assumptions. The phase of the *MRI* signal ϕ_s can be separated into a B_1 dependent component, the transceive phase $\phi_{Tx/Rx}$, and a B_1 independent component, which depends on ΔB_0 and time dependent eddy current effects $B_{\text{eddy}}(t)$ as

$$\phi_s(\vec{r}) = \phi_{Tx/Rx}(\vec{r}) + \gamma \left(\Delta B_0(\vec{r})\text{TE} + \int_0^{\text{TE}} B_{\text{eddy}}(\vec{r}, t) dt \right). \tag{2.159}$$

The transceive phase $\phi_{Tx/Rx}$ consists of a component from the transmit field ϕ_{Tx} and one of the receive field ϕ_{Rx} (see Section 2.3.5), where ϕ_{Tx} should be determined. In [309], a method was proposed assuming

$$\phi_{Tx} = \phi_{Rx}, \tag{2.160}$$

such that they can be separated. This assumption is valid under certain conditions, e.g. for “a dielectrically homogeneous lossy cylinder using quadrature excitation and reception with the same coil” [309]. Furthermore, it could be shown by van Lier et al. [309] that Eq. (2.160) is also a very good approximation in the human head for quadrature excitation and reception with the same coil. The acquisition can be simply performed with a *GRE* sequence, where the influence of ΔB_0 can be determined by acquiring two echos at different TE, as described in Section 2.4. The phase contribution from eddy current effects ϕ_{eddy} can be determined by an additional acquisition with different gradient polarity. With that ϕ_{Tx} is given by

$$\phi_{Tx}(\vec{r}) = \frac{\phi_s((\vec{r}) - \gamma \Delta B_0(\vec{r})\text{TE} - \phi_{\text{eddy}}}{2}. \tag{2.161}$$

2.5.2.2 Relative Phase of the $\mathbf{B}_1^+$ Field between Transmit Channels

Mapping the relative phase between several transmit channels is based on the simple idea to perform a *GRE* acquisition S_n, where only one of them is used for excitation. This acquisition has to be repeated for each of the N_{Tx} transmit channels. For receive, the same coil combination has to be used for all acquisitions. This can be a separate receive coil array or all of the transmit channels if they are used in receive/transmit mode. If all other acquisition parameters stay unchanged, the relative phase ϕ_n of channel n is simply given as the phase difference to an arbitrary chosen reference channel n_{ref}

$$\phi_n(\vec{r}) = \angle S_{N_{\text{ref}}} - \angle S_n \qquad \forall n \neq n_{\text{ref}}. \tag{2.162}$$

The problem of this approach is that local transmit coils usually have also a very local excitation profiles (B_1^+ magnitude), such that the applied flip angle decays rapidly with the distance to the coil. This leads to a quite inhomogeneous *SNR*, with very low signal in a very large area of the image. To overcome this problem, usually a different strategy is applied, where all except one transmit channels are used for excitation. For this purpose, a method for simultaneous mapping of magnitude and phase of the B_1^+ field, in combination with the *BS* approach (see Section 2.5.1.10), was proposed by Zhao et al. [336]. The combined complex B_1 field $\overline{B}_{1_m}^+$ of all active channels with combined phase $\overline{\phi}_m$ can be written as a linear combination of the individual B_1 fields generated by each channel $B_{1_n}^+$ with individual phase ϕ_n

$$\overline{B}_{1_m}^+(\vec{r})e^{i\overline{\phi}_m(\vec{r})} = \sum_{n=1}^{N_{Tx}} \alpha_{m,n} B_{1_n}^+(\vec{r})e^{i\phi_n(\vec{r})}. \tag{2.163}$$

The weighting factor $\alpha_{m,n}$ is one, if channel n contributes to measurement m and zero otherwise ($\alpha_{m,n} = 1 \; \forall \; n \neq m$ and $\alpha_{n,n} = 0$), called the “all-but-one” scheme. The B_1 magnitude of each channel combination $\overline{B}_{1_m}^+$ is determined through a *BS* measurement with positive $S_{+,m}$ and negative $S_{-,m}$ resonance offset acquisition, as described in Section 2.5.1.10. The resulting *BS* phase ϕ_{BS_m} is of course different for each channel combination, so that $\overline{\phi}_m^*$ can be determined from the positive (or negative) resonance offset acquisition corrected by the channel combination dependent ϕ_{BS_m}

$$\overline{\phi}_m^*(\vec{r}) = \frac{\angle S_{\pm,m}(\vec{r})}{e^{\pm i\phi_{\mathrm{BS}_m}(\vec{r})}} = \overline{\phi}_m(\vec{r}) + \phi_b^*(\vec{r}). \tag{2.164}$$

$\overline{\phi}_m^*$ consists of the combined B_1 phase $\overline{\phi}_m$ and an unknown channel independent background phase ϕ_b^*. B_1 magnitude $B_{1_n}^+$ and phase ϕ_n of each individual channel can be determined by solving the following linear set of equations

$$\begin{bmatrix} B_{1_1}^+(\vec{r})e^{i\phi_1^*(\vec{r})} \\ \vdots \\ B_{1_{N_{Tx}}}^+(\vec{r})e^{i\phi_{N_{Tx}}^*(\vec{r})} \end{bmatrix} = \mathbf{A}_\alpha^{-1} \begin{bmatrix} \overline{B}_{1_1}^+(\vec{r})e^{i\overline{\phi}_1^*(\vec{r})} \\ \vdots \\ \overline{B}_{1_{N_{Tx}}}^+(\vec{r})e^{i\overline{\phi}_{N_{Tx}}^*(\vec{r})} \end{bmatrix}, \tag{2.165}$$

where the system matrix $\mathbf{A}_\alpha$ is determined by the weighting factors α

$$\mathbf{A}_\alpha = \begin{bmatrix} \alpha_{1,1} & \cdots & \alpha_{1,N_{Tx}} \\ \vdots & \ddots & \vdots \\ \alpha_{N_{Tx},1} & \cdots & \alpha_{N_{Tx},N_{Tx}} \end{bmatrix}. \tag{2.166}$$

The resulting phase ϕ_n^* again has a contribution of an unknown background phase ϕ_b given as

$$\phi_n^*(\vec{r}) = \phi_n(\vec{r}) + \phi_b(\vec{r}). \tag{2.167}$$

By utilizing Eq. (2.162), the B_1 phase of each transmit channel ϕ_n can be determined relatively, up to an additional rotation by ϕ_b. A very detailed description of how to determine the phase of the transmit field B_1^+ and the receive field B_1^- and how to separate into several phase contributions is given by van de Moortele et al. [305].

3

Basic Principles of MR-Image Reconstruction

> Life can only be understood backwards; but it must be lived forwards.
>
> *Søren Kierkegaard*

Contents

3.1 Accelerated MR Data Acquisition and Parallel Imaging 86
3.2 Image Reconstruction as an Optimization Problem – Variational Methods 92
3.3 Variational Methods in Field Mapping 109

The major drawback of Magnetic Resonance Imaging (MRI) is the long acquisition time, because of the time consuming sequential data acquisition in k-space (see Section 2.1.7). In this section, some methods are shown to accelerate the data acquisition, and how to reconstruct artifact free images from data sampled beyond the Nyquist rate, called undersampling. These methods are based on Parallel Imaging (PI), which can be applied in image space, i.e., Sensitivity Encoding (SENSE) [234], or in k-space Generalized Autocalibrating Partial Parallel Acquisition (GRAPPA) [99]. Moreover, the formulation of the Magnetic Resonance (MR) image reconstruction problem as minimization problem is introduced, and how the application of regularization functionals can be beneficial to stabilize the solution or to include prior knowledge about the image structure to enforce a certain behavior in the final solution. These kind of methods are summarized under the term variational methods. For this purpose, the *MR* forward and backward operators are introduced, mapping from image to data space and back from data to image space, respectively. For these kind of methods, the knowledge of the coil sensitivity profiles is necessary, so that some method are introduced to estimate them out of the undersampled data. Furthermore, a suitable similarity measure and a simple regularization functional is derived from a statistical point of view, and more complex regularization functionals are described based on their specific behavior. Also, some strategies to solve these minimization problems are introduced based on a specific example.

3.1 Accelerated MR Data Acquisition and Parallel Imaging

In this section, the general aspects of accelerated *MR* data acquisition are described, as well as the concepts of classical *PI* in image space and k-space. At the end of this section, the voxel wise unfolding on the basis of the corresponding receive coil sensitivity profiles is described, known as *SENSE*.

3.1.1 General

The discrete acquisition in k-space and the relations between the Field of View (FOV), the image resolution Δx and Δy, k-space resolution Δk_x and Δk_y, and the maximum acquired frequency in k-space $k_{x,max}$ and $k_{y,max}$ are describe in detail in Section 2.1.7.2. According to Shannon's and Nyquist's sampling theorem [223, 263, 264], for a given *FOV* and resolution, a minimum amount of sampling points have to be acquired to guarantee an artifact free solution. In the frequency encoding direction (here k_x), it is technically no problem to fulfill this condition, because the necessary sampling interval Δt (see Eq. (2.65)) of the Analog to Digital Converter (ADC) is reached easily with today's available hardware. To acquire the necessary amount of data points in the phase encoding direction (here k_y), the imaging experiment has to be repeated by the number of phase encoding lines N_{k_y} with a contrast specific waiting time in between, the Repetition Time (TR). To establish a certain contrast, the *TR* can be in the order of seconds, which is the reason for the major limitation of *MRI*. For 3D acquisition the situation gets even more severe, because of the additional phase encoding direction (here k_z), so that the acquisition time increases by a factor of N_{k_z}, which is the number of data points in the second phase encoding direction. Especially for field mapping, the acquisition time is very crucial, because it is usually applied as preparation scan without any diagnostic information.

To reduce the acquisition time, one tries to keep the number of data points in both phase encoding directions as low as possible. Classically, this can be achieved by placing the phase encoding into the direction of the smaller geometric extension of the object and to reduce the *FOV* accordingly, which is called rectangular *FOV*. According to Eq. (2.66), if FOV_y is reduced, Δk_y increases by the same factor and the resolution Δy as well as $k_{y,max}$ stay unchanged. Another possibility is to reduce the resolution in phase encoding direction, which is equivalent to increase Δy. In k-space Δk_y stays unchanged, but the maximum acquired spatial frequency $k_{y,max}$ is reduced (see Eq. (2.66)). The last classical acceleration possibility is to acquire only a part of the k-space (at least half of it), which is called "Partial Fourier", and to recover the remaining part by utilizing symmetry properties of

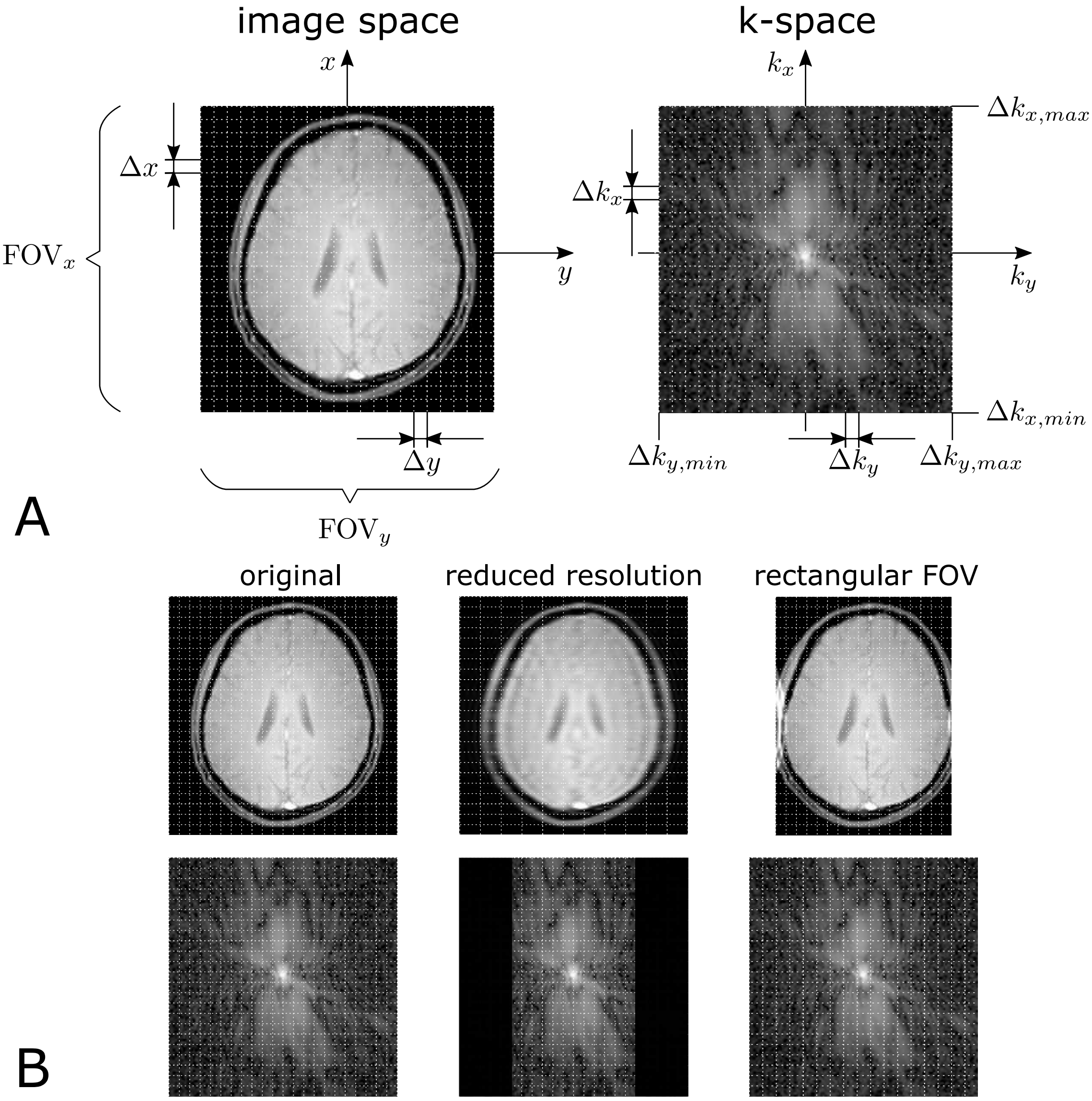

Figure 3.1: (A) Visualization of the connection between k-space and image space in terms of FOV, image resolution Δx and Δy, k-space resolution Δk_x and Δk_y, and the maximum acquired spatial frequency $k_{x,max}$ and $k_{y,max}$. (B) Visualization of the relation if one of the quantities is changes compared to the original acquisition (left column). A reduction of $k_{y,max}$, leads to a reduction of the resolution in y direction (middle column). An increase Δk_y leads to a reduction of the FOV in y direction, known as rectangular FOV (right column).

the Discrete Fourier Transform (DFT) or by using more sophisticated algorithms, such as the Projection Onto Convex Set (POCS) algorithm [51], to compensate for imperfections. In this case neither resolution, nor *FOV* are reduced. These methods still do not violate the Nyquist criterion, so that the image can be reconstructed using the inverse discrete Fourier operator $\mathcal{F}^{-1}$. However, the acceleration potential of these kind of methods is very

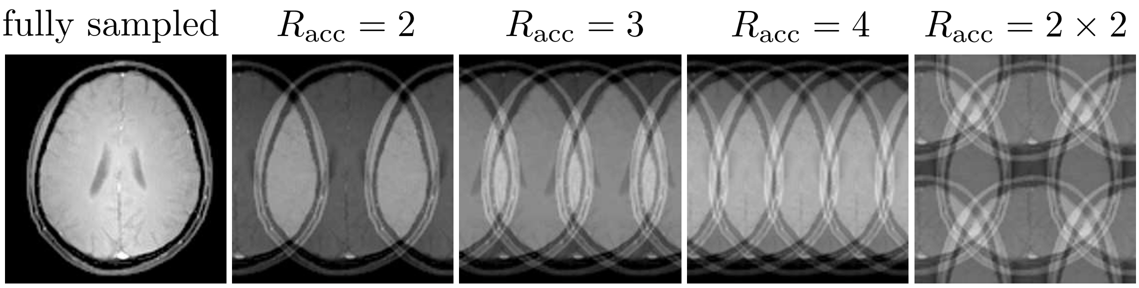

Figure 3.2: Image gained from fully sampled k-space (left) as well as for acceleration in k_y direction with acceleration factors $R_{\mathrm{acc}} = 2$, $R_{\mathrm{acc}} = 3$, and $R_{\mathrm{acc}} = 4$ (2^{nd} to 4^{th} image). The right images shows the effect of acceleration in both directions k_x and k_y, each by the factor of two.

low and except "Partial Fourier" either resolution or *FOV* is reduced. Figure 3.1 shows the general relation between k-space and image space in terms of *FOV*, image resolution Δx and Δy, k-space resolution Δk_x and Δk_y, and the maximum acquired spatial frequency $k_{x,max}$ and $k_{y,max}$ as well as the concepts of reduced resolution and rectangular *FOV*.

3.1.2 Parallel Imaging

To further accelerate the *MR* data acquisition, the only possibility is to reduce the number of sampling points in phase encoding direction below the Nyquist limit. In the Cartesian case, this can be done by acquiring only every m^{th} k-space line in phase encoding direction, so that the acceleration factor R_{acc} is equal to m. According to Eq. (2.66), the k-space resolution Δk_y is increased by the factor m, leading to a reduction of the *FOV* in phase encoding direction by the same factor. This reduced *FOV* is not sufficient to represent the entire object and due to the periodicity of the *DFT*, the periodic repetitions of the image start to overlap. This effect is called back-folding or aliasing, which is visualized for different R_{acc} in Figure 3.2. Such aliased images can be unfolded without reduction in neither resolution nor *FOV* by methods of *PI*, but additional information is necessary. With the transition from using volume coils to nowadays used local phased array surface coils for receive, *PI* became possible. The term "parallel" in *PI* originates from the parallel signal reception in several receive coils. As already described in Section 2.3 (especially referring to Figure 2.20), such surface coils exhibit a very localized B_1 field distributions and, according to the principle of reciprocity, also very localized receive sensitivities $B_1^-(\vec{r})$. According to Eq. (2.44), the signal s_n in each receive coil is not only proportional to the transverse magnetization $M_\perp$, but also to the receive field $B_{1,n}^-(\vec{r})$ of each coil. If these coil sensitivity distributions are known, this information can be used in *PI* methods to unfold the image. Unfortunately, $B_{1,n}^-(\vec{r})$ does not only depend on the coil geometry, but also on the coil load, so that it changes from patient to patient (see Section 2.3). To determine $B_{1,n}^-(\vec{r})$, two different methods are possible: First, it can be determined by a low resolution reference scan before the actual acquisition, or second, by acquiring additional lines in the center of k-space according to the Nyquist rate during the actual

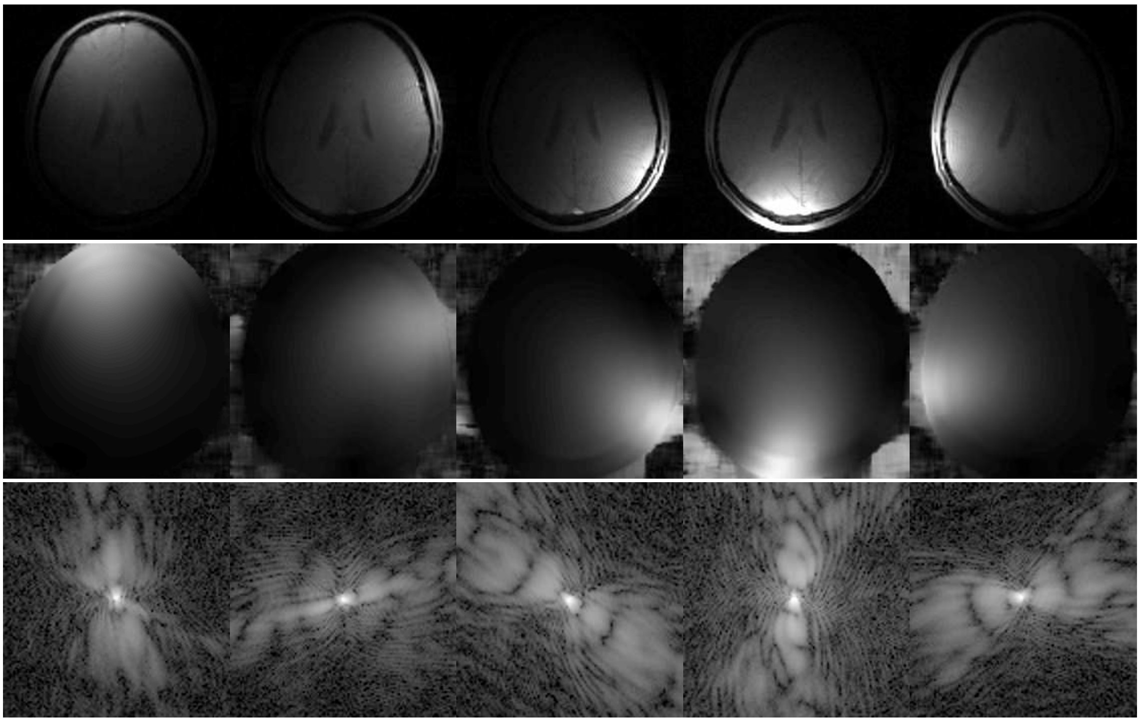

Figure 3.3: Coil images (1^{st} row), normalized receive coil sensitivities $C_n(\vec{r})$ (2^{nd} row), and k-space data of each receive coil (3^{rd} row). Data was acquired on a healthy volunteer using a 64-channel head coil at 3 T, where 5 exemplary channels are shown. The receive coil sensitivity maps are estimated using the algorithm proposed by Walsh et al. [311]. The k-space data is shown in logarithmic scale.

image acquisition, to estimate the sensitivity profiles. These additional lines are usually called Auto Calibration Lines (ACLs). The reference scan method has the advantage that the determined sensitivity profiles can be used for several following scans, but any motion inbetween leads to a mismatch between image and B_1^- distribution. The *ACL* estimation is more robust against motion, so that it is commonly used for coil sensitivity estimation, where some estimation methods are described in Section 3.2.7. Most of these commonly used methods are only able to determine a normalized sensitivity profile instead of the absolute B_1^-, which is sufficient for image reconstruction purposes, so that the normalized sensitivity profiles of each coil are denoted as C_n in the following part of this thesis. In Figure 3.3, the coil images, the receive coil sensitivity profiles C_n, and the acquired k-space data of 5 exemplary receive coils are shown from a data set acquired with a 64-channel head coil at 3 T. In theory, the maximum achievable acceleration factor $R_{\text{acc,max}}$ is determined by the number of available receive coils N_c. In practice, the achievable acceleration factor is much lower, because the information gained from the different receive coils is not linearly independent and the underlying reconstruction problem becomes ill-posed. In clinical practice, reasonable values for the acceleration factor in 2D imaging are $R_{\text{acc}} = 2$ or $R_{\text{acc}} = 3$. In 3D applications, R_{acc} can be chosen slightly higher if the undersampling is split up into both phase encoding directions. The highest efficiency can be reached, if the undersampling in k_y is shifted in each k_z step according to Breuer et al. [41], known as Controlled aliasing in volumetric parallel imaging (CAIPIRINHA). If the acceleration factor is set too high, this can lead to either residual artifacts or a spatially varying massive noise amplification, especially in central regions of the image where most receive coils contribute approximately equal to the total signal in the aliased voxel. To describe this effect, a noise amplification measure $g(\vec{r}) \geq 1$ was introduced in [234], derived from the coil geometry, so that it is called “geometry factor” or simply “g-factor”. The resulting Signal-to-Noise Ratio (SNR) in *PI* reconstruction is given as

$$\mathrm{SNR}_{\mathrm{PI}}(\vec{r}) = \frac{\mathrm{SNR}_{\mathrm{full}}(\vec{r})}{\sqrt{R_{\mathrm{acc}}}\, g(\vec{r})}. \tag{3.1}$$

Noise in *PI* is a very extensive topic, especially g-factor map calculation, so that the interested reader is referred to [1, 42] for further information.

Over the years, many *PI* methods were proposed, which can be split up into image space based and k-space based methods. The first k-space based method was presented by Sodickson and Manning [273], called Simultaneous Acquisition of Spatial Harmonics (SMASH), which is the basis for all other following k-space methods. The most prominent and widely used one is the *GRAPPA* method proposed by Griswold et al. [99]. K-space methods do not require an explicit knowledge of the receive sensitivity profiles. These methods are based on shift invariant convolution kernels, where the missing data points in k-space for one coil are generated as a linear combination of the acquired data points around the missing one from all receive coils. The weighting factors (values of the convolution kernel) are estimated from the fully sampled *ACLs* in the center of k-space, assuming the shift invariance of the convolution kernel. This method was further extended by Lustig and Pauli [196], so that the weighting factors are estimated from the whole acquired k-space data by a least squares fit called iterative Self-consistent Parallel Imaging Reconstruction (SPIRiT). Once, each k-space point is calculated, the image can be reconstructed by applying the discrete inverse Fourier operator $\mathcal{F}^{-1}$. In contrast to that, in image space based methods, the aliased image is calculated by the application of $\mathcal{F}^{-1}$ to the undersampled k-space and the unfolding is performed in image space, requiring the explicit knowledge of the receive sensitivity profiles. The most prominent and widely used image space method is *SENSE* proposed by Pruessmann et al. [234], based on the idea from Ra and Rim [235]. In general, k-space based methods are more robust, because no receive sensitivity profiles have to be estimated, but in image space based methods, the incorporation of image priors is much easier (see Section 3.2). However, there is a strong connection between image and k-space based methods, indicated by the fact that the convolution kernel approach in k-space (*GRAPPA*) has an equivalent counterpart by a multiplication in image space. Similarly, the multiplication of receive sensitivity profiles in image space (*SENSE*), see Section 3.2.3, has an equivalent counterpart in a convolution in

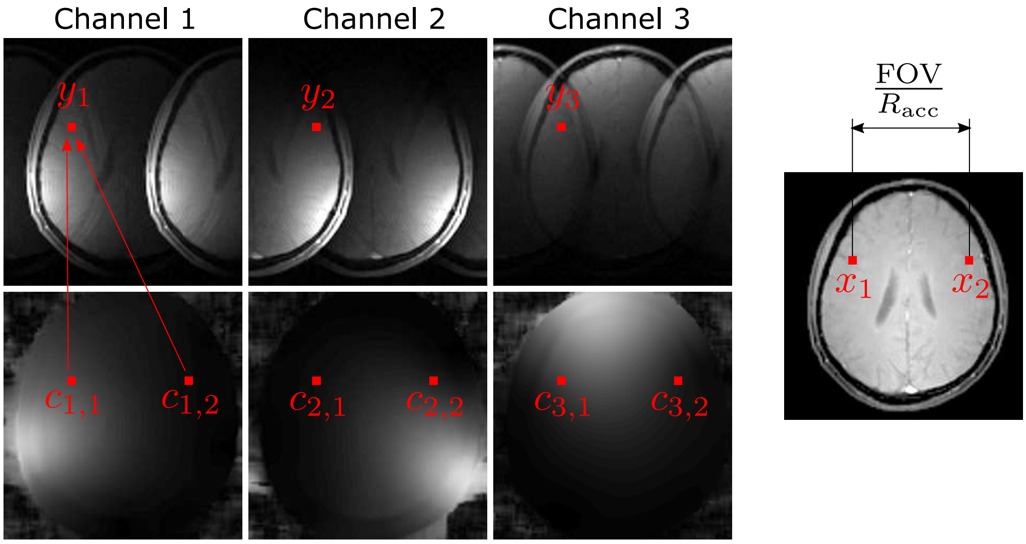

Figure 3.4: The principle of SENSE is visualized for 3 receive channels and an accelearation factor of $R_{\text{acc}} = 2$. The aliased voxel value y_n is composed as the weighted sum of the unaliased voxel values x_1 and x_2 ($\frac{\text{FOV}}{R_{\text{acc}}}$ apart), weighted with the corresponding receive sensitivity $c_{n,1}$ and $c_{n,2}$, respectively.

k-space. Indeed, it was shown mathematically by Uecker et al. [301] that both approaches are equivalent and the receive profiles can be calculated as dominant eigenvectors of the calibration kernel in k-space. Furthermore, this method can be used for the estimation of receive coil sensitivity profiles (see 3.2.7). A more detailed description of *PI* is out of scope of this thesis, so that the interested reader is referred to [24, 299], where a detailed comparison of the different methods is given. The reconstruction methods described in this thesis are based on the idea of *SENSE*, so that the voxel wise unfolding approach is exemplarily described in the following section (Section 3.1.2.1).

3.1.2.1 Sensitivity Encoding (SENSE)

SENSE is based on the idea that the signal in each voxel $y_n(\vec{r})$ of the aliased image of coil $n \in [1, N_c]$ can be represented as the sum of the unaliased image voxel signals $x_i(\vec{r}_i)$, which are separated by $\text{FOV}/R_{\text{acc}}$ in image space ($i \in [1, R_{\text{acc}}]$), weighted with the corresponding receive sensitivity profile $C_n(\vec{r}_i)$. This principle is visualized in Figure 3.4 and can be described as

$$\begin{bmatrix} y_1 \\ \vdots \\ y_{N_c} \end{bmatrix} = \begin{bmatrix} C_{1,1} & \cdots & C_{1,R_{\text{acc}}} \\ \vdots & \ddots & \vdots \\ C_{N_c,1} & \cdots & C_{N_c,R_{\text{acc}}} \end{bmatrix} \cdot \begin{bmatrix} x_1 \\ \vdots \\ x_{R_{\text{acc}}} \end{bmatrix}, \tag{3.2}$$

or

$$\mathbf{y} = \mathbf{C}\mathbf{x}. \tag{3.3}$$

Because of $N_c \geq R_{\mathrm{acc}}$, the unaliased voxel values x_i can be determined out of Eqs. (3.2) and (3.3) using the weighted least squares solution in every voxel

$$\mathbf{x} = \left(\mathbf{C}^H \boldsymbol{\Psi}^{-1} \mathbf{C}\right)^{-1} \mathbf{C}^H \boldsymbol{\Psi}^{-1} \mathbf{y}, \tag{3.4}$$

where as weighting matrix the inverse of the noise correlation matrix $\boldsymbol{\Psi}$ from Eq. (2.51) is used. Furthermore, a regularized version of Eq. (3.4) is possible, to stabilize the solution of the in general ill-posed inverse problem. The solution is then given as

$$\mathbf{x} = \left(\mathbf{C}^H \boldsymbol{\Psi}^{-1} \mathbf{C} + \lambda \mathbf{I}\right)^{-1} \mathbf{C}^H \boldsymbol{\Psi}^{-1} \mathbf{y}, \tag{3.5}$$

where λ is a regularization parameter and $\mathbf{I}$ the identity matrix. This is equivalent to the well known Tikhonov regularization initially proposed in [293] (see Section 3.2.4.1).

3.2 Image Reconstruction as an Optimization Problem – Variational Methods

The solution for the voxel wise image unfolding problem given in Section 3.1.2.1, based on [234], has two main drawbacks: first, this voxel by voxel inversion is tailored to the special case of regular Cartesian undersampling. Irregular Cartesian undersampling or non Cartesian trajectories cannot be tackled, because the point spread function and with that the aliasing artifacts become also irregular. Second, the more important restriction for this thesis, the application of image priors to incorporate prior knowledge of the image structure cannot be incorporated. For that purpose, the image reconstruction problem is written as an inverse problem, where the unknown parameters are the values of the image's voxels which has to be reconstructed, so that the whole image is reconstructed by the solution of a global optimization problem. In this section, all necessary ingredients to perform such a reconstruction are described. These are, the formulation of the *MR* reconstruction problem as minimization problem and the derivation of a suitable similarity measure for the data fidelity term from a probabilistic point of view. For the iterative solution of these kind of problems, a proper forward and backward operator has to be constructed, mapping from image to data space and vice versa. To stabilize the solution and to incorporate prior knowledge of spatial structure of the image, proper regularization functionals are introduced with their mathematical description and spatial properties. Different algorithms to solve the inverse problem of reconstruction are considered for differentiable and non-differentiable functionals, as well as the ability to reach a global optimal solution (the convexity of the problem) are discussed. This section ends with a description of different methods to determine the receive coil sensitivity profiles and a short overview over some existing methods and their underlying ideas.

3.2.1 The inverse Problem in MRI

Mathematically, the *MR* data acquisition can be written in its general form as

$$d = A(u) + \nu, \tag{3.6}$$

where the generated data $d \in \mathbb{C}^{N_{k_x} \times N_{k_y} \times N_{k_z} \times N_c}$ is given by applying a certain operator $A : \mathbb{C}^{N_x \times N_y \times N_z} \mapsto \mathbb{C}^{N_{k_x} \times N_{k_y} \times N_{k_z} \times N_c}$ to the unknown parameters $u \in \mathbb{C}^{N_x \times N_y \times N_z}$. Here, the operator A describes the measurement procedure and the parameters u describe the unknown image. Furthermore, the data d is corrupted by some additional random noise $\nu \in \mathbb{C}^{N_{k_x} \times N_{k_y} \times N_{k_z} \times N_c}$. Here, N_{k_x}, N_{k_y}, and N_{k_z} are the sampled data points in readout (k_x) and both phase encoding directions (k_y and k_z), respectively, which are not necessarily equal to the number of voxels in image space N_x, N_y, and N_z. N_c is the number of receive channels. The goal is now to find an inverse operator $A^{-1} : \mathbb{C}^{N_{k_x} \times N_{k_y} \times N_{k_z} \times N_c} \mapsto \mathbb{C}^{N_x \times N_y \times N_z}$, to gain the reconstructed image from the measured data. In the fully sampled Cartesian case ($N_x = N_{k_x}$, $N_y = N_{k_y}$, and $N_z = N_{k_z}$), the problem is fully determined, hence, the number of unknowns and the number of measurements are equal, so that the inverse operator is simply the discrete inverse Fourier operator ($A^{-1} = \mathcal{F}^{-1}$). In case of undersampling, the inverse problem of recovering u from d, in Eq. (3.6), gets ill-posed in many practical cases, because of measurement errors due to hardware imperfections, the incomplete data and low *SNR*. According to Hadamard [106], the solution of an ill-posed inverse problem might not exist, it might not be unique, and it might change drastically for small variations in the data (low stability). Because of that, the inverse operator A^{-1} cannot be calculated explicitly, so that the problem is usually written as the minimization of a cost function $J(u)$ given as

$$\hat{u} = \arg\min_u J(u) = \arg\min_u \mathcal{D}\left\{A(u), d\right\} + \lambda \mathcal{R}\left\{u\right\}. \tag{3.7}$$

This cost function consists of two terms, a data fidelity term and a regularization term. The data fidelity term measures the similarity between the reconstructed image and the measured data by a certain distance measure $\mathcal{D}$, and the regularization term $\mathcal{R}$ is responsible for stabilizing the solution or the incorporation of prior knowledge to enforce certain image properties as smoothness or edges. At the end, the reconstruction result $\hat{u}$ is the image minimizing the distance between acquired and calculated data under the applied constraint $\mathcal{R}$. This kind of reconstruction problems are referred to as variational calculus or variational methods. The regularization parameter λ balances between data fidelity and regularization. Wrong selection of λ can lead to overregularization (e.g. oversmoothing) if λ is chosen too high, or insufficient noise suppression or residual artifacts if λ is chosen too low. Usually, the regularization parameter is multiplied to the regularization term. However, the location of the minimum does not change if the cost function is multiplied by a constant (i.e., $\frac{1}{\lambda}$), so that it is equivalent to utilize a new regularization parameter $\tilde{\lambda} = \frac{1}{\lambda}$ which is multiplied to the data fidelity term. The following derivations in this thesis are performed for this case. The data fidelity term depends on the noise statistics in the data (see Section 3.2.2) and the regularization describes the image properties, where different kind of functionals are possible, some important are described in Section 3.2.4.

3.2.2 Probabilistic Point of View

From a probabilistic point of view, image reconstruction is searching for the image u, having the highest probability to describe the given data d. For that purpose, u is treated as a random variable and its conditional probability $p(u|d)$ depending on the observation, the measured data d, can be expressed using the Bayes rule

$$p(u|d) = \frac{p(d|u)p(u)}{p(d)}. \tag{3.8}$$

Here $p(d)$ can be seen as constant scaling factor, $p(d|u)$ is the probability that the given data describes the possible solution u, the so called likelihood, and $p(u)$ is the prior probability of u being a valid solution. According to Section 2.1.6, the noise in *MR* data originates from a Gaussian distribution, so that the likelihood can be written as a multivariate Gaussian distribution of the difference between acquired data and calculated data using the forward model. This distribution has a mean of zero and is given as

$$p(d|u) = e^{-[A(u)-d]^H \boldsymbol{\Psi}^{-1}[A(u)-d]}, \tag{3.9}$$

where $\boldsymbol{\Psi}$ is the noise correlation matrix defined in Eq. (2.51). The optimal data fidelity term $\mathcal{D}$ in Eq. (3.7) for the given noise statistic comes out of the maximum likelihood for u, such that the probability in Eq. (3.9) is maximized. Maximizing $p(d|u)$ is equivalent to minimizing the negative exponent in Eq. (3.9), stated as

$$\hat{u}_{\text{ML}} = \frac{1}{2} \arg\max_u p(d|u) = \frac{1}{2} \arg\min_u \left[A(u) - d\right]^H \boldsymbol{\Psi}^{-1} \left[A(u) - d\right]. \tag{3.10}$$

The inverse noise correlation matrix $\boldsymbol{\Psi}^{-1}$ can be set to identity, or incorporated in the forward operator A by using the Cholesky decomposition, as described by Pruessmann et al. [233], so that the data fidelity term $\mathcal{D}$ reduces to the L_2-norm of $A(u) - d$. The optimization problem for the maximum likelihood solution $\hat{u}_{\text{ML}}$ can then be written as

$$\hat{u}_{\text{ML}} = \arg\min_u \frac{1}{2} \|A(u) - d\|_2^2. \tag{3.11}$$

If A can be represented as linear operator $\mathbf{A}$, which is the case for the *MR* operator (see Section 3.2.3), the solution is given by the so called pseudo inverse

$$\hat{u}_{\text{ML}} = (\mathbf{A}^H\mathbf{A})^{-1}\mathbf{A}^H d. \tag{3.12}$$

By maximizing the a posterior probability from Eq. (3.8), a prior probability $p(u)$ has to be defined. In [293], a function of the form

$$p(u) = e^{-\lambda\|u\|_2^2} \tag{3.13}$$

is proposed to stabilize the solution of ill-posed inverse problems, in particular giving a higher probability to lower solution values, because outliers are penalized. With that, the solution for the a posterior probability is given by combining Eqs. (3.9) and (3.13) and the maximum a posterior solution $\hat{u}_{\text{MAP}}$ can be written as

$$\hat{u}_{\text{MAP}} = \arg\max_u p(u|d) = \arg\min_u \frac{1}{2}\|A(u) - d\|_2^2 + \frac{\lambda}{2}\|u\|_2^2, \tag{3.14}$$

giving one possible regularization functional $\mathcal{R}$ for Eq. (3.7). If A can be represented as linear operator the solution is given as

$$\hat{u}_{\text{MAP}} = (\mathbf{A}^H\mathbf{A} + \lambda\mathbf{I})^{-1}\mathbf{A}^H d, \tag{3.15}$$

which is the solution for the well known Tikhonov regularization. Furthermore, the L_2 norm $\|\cdot\|_2$ in the previous equations and in the more general the L_p norm is defined in Appendix A.2.2.

3.2.3 The MR Forward/Backward Operator

According to Eqs. (2.43) and (2.63), the *MRI* signal in each receive coil s_n is given as the Fourier integral over the transverse magnetization $M_\perp(x, y, z)$ during sampling. Each receive coil has its dedicated receive field $B_{1,n}^-(x, y, z)$, describing the sensitivity of coil n to a spin precessing at spatial location (x, y, z) (see Section 2.3.1). With that and the extension to 3D encoding, the signal equation is given as

$$s_n(k_x, k_y, k_z) = \int\int\int_V B_{1,n}^-(x, y, z) M_\perp(x, y, z) e^{-ik_x x} e^{-ik_y y} e^{-ik_z z} dxdydz, \tag{3.16}$$

where V is the measurement volume. After discretization the signal equation writes as

$$\begin{aligned} s_n(l_x\Delta k_x, l_y\Delta k_y, l_z\Delta k_z) = \mathcal{F}\left\{B_{1,n}^-(m_x\Delta x, m_y\Delta y, m_z\Delta z) M_\perp(m_x\Delta x, m_y\Delta y, m_z\Delta z)\right\} = \\ \sum_{m_x=1}^{N_x}\sum_{m_y=1}^{N_y}\sum_{m_z=1}^{N_z} B_{1,n}^-(m_x\Delta x, m_y\Delta y, m_z\Delta z) M_\perp(m_x\Delta x, m_y\Delta y, m_z\Delta z) \\ e^{-il_x\Delta k_x m_x\Delta x} e^{-il_y\Delta k_y m_y\Delta y} e^{-il_z\Delta k_z m_z\Delta z} \Delta x\Delta y\Delta z, \end{aligned} \tag{3.17}$$

where $B_{1,n}^-(x, y, z)$ is approximated by the normalized sensitivity profiles $C_n(x, y, z)$ (see Section 3.2.7). The triple sum in Eq. (3.17) reduces to the discrete Fourier operator $\mathcal{F}$, and the *MR* image u is proportional to the spatially sampled transverse magnetization $M_\perp(x, y, z)$ during sampling, according to Eq. (2.66). With that, the *MR* forward operator $A : \mathbb{C}^{N_x \times N_y \times N_z} \mapsto \mathbb{C}^{N_{kx} \times N_{ky} \times N_{kz} \times N_c}$ in Eq. (3.6) can be written as

$$A(u) = \begin{pmatrix} P \odot \mathcal{F}\{C_1 \odot u\} \\ \vdots \\ P \odot \mathcal{F}\{C_{N_c} \odot u\} \end{pmatrix}, \tag{3.18}$$

where P is the applied undersampling pattern in k-space and the operator $\odot$ is the point wise multiplication. This concept can be easily extended to arbitrary k-space trajectories by replacing $\mathcal{F}$ with the Non-Uniform Fast Fourier Transform (NUFFT) operator described by Fessler and Sutton [79]. The *NUFFT* operator basically extends $\mathcal{F}$ by a gridding of the non-uniform trajectory to a Cartesian grid and accounting for varying sampling densities in k-space by a density compensation function. However, further consideration of non Cartesian trajectories is out of scope of this thesis.

To numerically solve the reconstruction problem, usually iterative methods are applied (see Section 3.2.5), which require the definition of a backward operator $A^H : \mathbb{C}^{N_{kx} \times N_{ky} \times N_{kz} \times N_c} \mapsto \mathbb{C}^{N_x \times N_y \times N_z}$, mapping from k-space to image space. The adjoint backward operator A^H to A in Eq. (3.18) can be expressed as

$$A^H(d) = \sum_{n=1}^{N_c} \overline{C}_n \odot \mathcal{F}^{-1}\{P \odot d_n\}, \tag{3.19}$$

where $\overline{C}_n$ is the complex conjugate of the receive sensitivity profile and d_n is the data of coil n. To achieve convergence in the iterative solution, forward and backward operators have to be adjoint to each other. Two operators are adjoint if

$$\left\langle A(\tilde{u}), \tilde{d} \right\rangle = \left\langle \tilde{u}, A^H(\tilde{d}) \right\rangle \tag{3.20}$$

is satisfied, where $\tilde{u} \in \mathbb{C}^{N_x \times N_y \times N_z}$ is a randomly chosen element in image space and $\tilde{d} \in \mathbb{C}^{N_{kx} \times N_{ky} \times N_{kz} \times N_c}$ is a randomly chosen element in data space.

Furthermore, it is important to note that the forward and backward operators A and A^H defined in Eqs. (3.18) and (3.19) are linear operators, because the Fourier transform is a linear operation and the rest are point wise multiplications. The Fourier operator $\mathcal{F}$ can be represented as a transformation matrix, so that A and A^H can be as well. For that purpose, u and d have to be written as vectors so that $u \in \mathbb{C}^{N_x N_y N_z}$ and $d \in \mathbb{C}^{N_{kx} N_{ky} N_{kz} N_c}$. However, the size of these matrices get very large, so that they are never built up explicitly; in practice only the definitions in Eqs. (3.18) and (3.19) are used. The *MR* forward and backward operators defined here are based on their initial definition given by Pruessmann et al. [233].

3.2.4 Incorporation of Prior Knowledge – Regularization

As described in Section 3.2.1, the *MR* reconstruction problem is an ill-posed inverse problem, but the solution can be stabilized by incorporating a regularization functional into the minimization ($\mathcal{R}(u)$ in Eq. (3.7)). Furthermore, a proper selection of $\mathcal{R}(u)$ can also incorporate prior knowledge about the underlying image structure by enforcing certain properties. Regularization can also be seen as restricting the solution space to valid or preferred solutions. In this section, a selection of some important regularization functionals is given.

3.2.4.1 Tikhonov Regularization

As already introduced in Section 3.2.2, the method proposed by Tikhonov [293] is widely used to stabilize ill-posed inverse problems. The functional is defined as the squared L_2 norm of the inverse problem's parameters, the value of each voxel in the image u. The regularization functional $\mathcal{R}(u)$ is defined as

$$\mathcal{R}(u) = \frac{1}{2}\|u\|_2^2 = \frac{1}{2}\sum_{m_x=1}^{N_x}\sum_{m_y=1}^{N_y}\sum_{m_z=1}^{N_z}|u_{m_x,m_y,m_z}|^2, \tag{3.21}$$

where m_x, m_y, and m_z are the spatial indices in x, y, and z direction, respectively. This functional leads to a penalization of outliers, so that low magnitude solutions are preferred. This leads to a stabilization of the solution as already indicated for the matrix inversion for the voxel wise solution of the *SENSE* problem (see Eq. (3.5) in Section 3.1.2.1). However, with this functional, no additional prior information about the spatial structure of the underlying image can be incorporated. For this purpose, the functional can be extended by a gradient operator, leading to the H_1 regularization.

3.2.4.2 H$_1$ – Regularization

To introduce some spatial regularity, a spatial operator has to be included into the regularization functional. For this purpose, the discrete gradient operator ∇_{xyz}^{+} can be used, which is defined using forward differences, see Eq. (A.29) in the Appendix. For the numerical solution, the corresponding transpose operator ∇_{xyz}^{T-} is needed, which is defined by finite backward differences (see Eq. (A.30)). By taking the L_2 norm of the image gradient, the regularization functional $\mathcal{R}(u)$ can be written as

$$\mathcal{R}(u) = \frac{1}{2}\|\nabla_{xyz}^{+}u\|_2^2 = \frac{1}{2}\sum_{m_x=1}^{N_x}\sum_{m_y=1}^{N_y}\sum_{m_z=1}^{N_z}\sum_{j=1}^{3}\left|\left(\nabla_{xyz}^{+}u\right)_{m_x,m_y,m_z,j}\right|^2, \tag{3.22}$$

where the inner sum, with index $j = [1,3]$, goes over the three gradient directions in each voxel. According to Savage and Chen [251], this regularization functional is known as

H_1 regularization. With the H_1 regularization strong gradients in the image are penalized, which leads to noise suppression and a blurring of sharp edges, so that continuous and smoothly varying image structures are enforced. According to Section 2.3.3, this corresponds exactly to the spatial behavior of the B_1 field distribution. Therefore, this regularization functional is perfectly suited as image prior for the B_1 field reconstruction out of undersampled data.

3.2.4.3 Total Variation (TV)

The Total Variation (TV) functional was first introduced by Rudin et al. [247] as image prior for the purpose of image denoising. The *TV* functional is defined as the L_1 norm of the magnitude of the spatial gradient in each voxel of the image. The magnitude of the gradient is given as its Euclidean length (L_2 norm). This combination of L_1 and L_2 norm is indicated by $\|\cdot\|_{2,1}$. In the 3D case, the *TV* functional is given as

$$\mathcal{R}(u) = \mathrm{TV}(u) = \|\nabla^+_{xyz} u\|_{2,1} = \sum_{m_x=1}^{N_x} \sum_{m_y=1}^{N_y} \sum_{m_z=1}^{N_z} \sqrt{\sum_{j=1}^{3} \left| \left(\nabla^+_{xyz} u \right)_{m_x,m_y,m_z,j} \right|^2}, \tag{3.23}$$

where ∇^+_{xyz} is the discrete gradient operator from Eq. (A.29). The reason for the name is that the *TV* functional measures the "total variation" or the "total gradient" in the image. Because of that, a sharp transition from a certain image value a to another value b causes the same cost as a smooth transition from a to b, so that data driven edges are preserved. In practice, the comparable large costs of noise in smoothly varying regions in the image leads to an enhancement of piecewise constant structures. For the reconstruction of *MR* images, the *TV* functional leads to an unnatural (comic like) appearance of the image and blocky artifacts (staircasing effect) in smoothly varying regions of the image.

3.2.4.4 Total Generalized Variation (TGV)

To improve the properties of the *TV* functional, the Total Generalized Variation (TGV) functional was proposed by Bredies et al. [38] in its most general form. It was shown in [33, 35] that the second order formulation TGV^2_α of the *TGV* functional is a suitable image prior for the solution of ill-posed inverse problems in image processing. The second order TGV^2_α functional is given as a minimization problem as follows

$$\mathcal{R}(u) = \mathrm{TGV}^2_\alpha(u) = \min_v \alpha_1 \|\nabla^+_{xyz} u - v\|_{2,1} + \alpha_0 \|\mathcal{E}v\|_{2,1}, \tag{3.24}$$

with the symmetrized derivative $\mathcal{E}$ defined as

$$\mathcal{E}v = \frac{1}{2} \left(\nabla^-_{xyz} v^T + \left(\nabla^-_{xyz} v^T \right)^T \right). \tag{3.25}$$

∇^-_{xyz} is the discrete gradient operator using backward differences, defined in Eq. (A.31) in the Appendix, where also a more detailed definition of $\mathcal{E}$ is given in Eq. (A.32). Because of the incorporation of higher order derivatives, in this case the second order, the spatial property of piecewise smoothness is enforced by the *TGV* regularization functional. The formulation as minimization problem is an elegant way, allowing to balance between first and second order derivative over the parameter $\alpha = (\alpha_0, \alpha_1)$. *TGV* was first utilized for the purpose of *MR* image reconstruction by Knoll et al. [159]. Furthermore, it was shown that the application of *TGV* regularization leads to a massive gain in reconstruction quality, especially the reconstructed images appear much more naturally without staircasing artifacts. According to Knoll et al. [159], the behavior of the *TGV* regularization can be explained intuitively as follows: If v is locally selected to be approximately the image gradient $v \approx \nabla^+_{xyz}u$, the first term in Eq. (3.24) is approximately zero, so that the second order derivative is penalized. This is usually the case in smooth regions. If v is locally selected to be $v \approx 0$, the second term in Eq. (3.24) is approximately zero, so that the L_1 norm of the image gradient gets penalized, similar to the *TV* behavior. This is usually the case around edges. With that, the behavior of the regularization functional is adapted locally depending on the image content. The parameter $\alpha = (\alpha_0, \alpha_1)$ can be seen as constant which does not have to be tuned. According to Bredies and Holler [37], the ratio α_0/α_1 is fixed to $\alpha_0/\alpha_1 = \sqrt{2}$ in the 2D and $\alpha_0/\alpha_1 = \sqrt{3}$ in the 3D case, which was found to be a robust choice for *MR* image reconstruction. It is further worth to mention, the first order *TGV* functional (TGV^1_α) is equivalent to the *TV* formulation, so that *TGV* can be seen as extension of *TV*. Furthermore, the applicability of *TGV* regularization in other *MRI* applications was demonstrated for diffusion-tensor imaging [304], quantitative-susceptibility mapping [166], joint *MR*-Positron Emission Tomography (PET) reconstruction [162], and in Arterial Spin Labeling (ASL) [279, 280].

3.2.5 Numerical Solution

Even though, the *MR* forward and backward operators defined in Section 3.2.3 are linear and can be expressed as simple transformation matrices, a direct inversion is in general not feasible, because of the huge size of the matrix. Considering the example of a Cartesian 3D acquisition with a matrix size of $N_x \times N_y \times N_z = 256 \times 256 \times 64$ and a 32-channel receive coil ($N_c = 32$), the matrix size of A would be $N_xN_yN_zN_c \times N_xN_yN_z \approx 1.34 \cdot 10^8 \times 4.19 \cdot 10^6$. Using a 64 bit double representation, the required memory only for storing the forward operator would be $\approx$ 4500 TB, so that a direct solution is not possible.

Therefore, iterative solutions are required to solve the reconstruction problem. If the cost function to be minimized is differentiable, as it is the case for Tikhonov and H_1 regularization functionals (see Sections 3.2.4.1 and 3.2.4.2), the problem can be solved by gradient based methods such as “steepest descent” and Conjugate Gradient (CG) (see Section 3.2.5.1). The L_2 data fidelity term is always differentiable. Because of the L_1 norm in the definition of *TV* and *TGV* regularization (see Sections 3.2.4.3 and 3.2.4.4), these functionals are non-differentiable around zero. Therefore, gradient based methods cannot be applied. To solve these kind of problems, a special kind of minimization algorithm was developed, which is called the primal dual algorithm, proposed by Chambolle and Pock [46]. The basic idea of this algorithm is outlined in Section 3.2.5.2.

3.2.5.1 Gradient based Minimization – Steepest Descend and Conjugate Gradient

Gradient based optimization algorithms try to find the minimum of a cost function $J(u)$, defined as a point where the optimality condition $\nabla_u J(u) = 0$ is fulfilled, by iteratively converging to the solution from a randomly chosen starting point u_0. For this purpose, a search direction p_k and a step size κ_k have to be calculated in each iteration step k to update the solution u_k as

$$u_{k+1} = u_k + \kappa_k p_k. \tag{3.26}$$

Steepest Descend: The most natural approach is to define the search direction p_k as the steepest descend, which is given as the negative gradient of the cost function $J(u_k)$ in iteration step k as

$$p_k = -\nabla_u J(u_k), \tag{3.27}$$

where ∇_u is the analytic gradient operator with respect to the model parameters, i.e., the intensity value in each voxel of the image u, which is defined in Eq. (A.35) in the Appendix. If $J(u)$ is convex (see Section 3.2.6), the initialization u_0 can be chosen arbitrarily, a suitable choice would be to initialize u with zeros ($u_0 = 0$). The choice of the step size is very crucial in this algorithm. Choosing κ too small will result in a poor convergence in the beginning and choosing κ too large will lead to jumping back and forth around the actual solution at the end of the optimization. Therefore, the step size κ should be updated in every iteration step as

$$\kappa_k = \arg\min_{\kappa_k} J(u_k + \kappa_k p_k). \tag{3.28}$$

The update step is exemplarily shown for the *MR* image reconstruction problem with H_1-regularization given as

$$u_{k+1} = u_k + \kappa_k \underbrace{\left(A^H\left(A(u_k) - d\right) + \lambda \nabla_{xyz}^{+T} \nabla_{xyz}^{+} u_k\right)}_{p_k}. \tag{3.29}$$

The optimized step size κ_k is given as

$$\kappa_k = \frac{p_k^H p_k}{p_k^H A^H(A(p_k)) + \lambda p_k^H \nabla_{xyz}^{+T} \nabla_{xyz}^{+} p_k}. \tag{3.30}$$

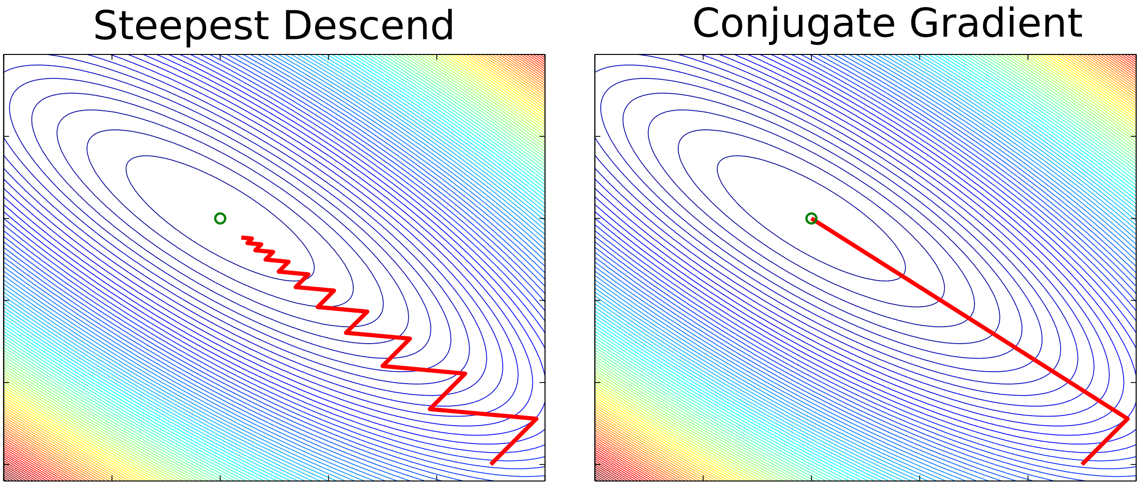

Figure 3.5: Comparison of the convergence rate of steepest descent (left) and CG (right) on an arbitrary 2D problem. After 20 iterations, the steepest descent is still far away from the solution indicated with the green circle, whereas the CG converges to the optimal solution after the second iteration. The red line denotes the progress of the solution in both cases.

Nevertheless, to use the negative gradient of $J(u_k)$ as search direction turns out to be a bad choice, because of the poor convergence rate in the general case.

Conjugate Gradient (CG): To overcome this problem, a much better strategy to determine the search direction p_k was proposed by Hestenes and Stiefel [125], known as the *CG*-method. The *CG* algorithm can be applied to problems of the form

$$\mathbf{D}x = z \quad \text{or} \quad \mathbf{D}x - z = 0, \tag{3.31}$$

where D is a symmetric and positive semi-definite matrix. The *MR* forward operator (in matrix form) does not fulfill this condition, so that the optimization problem from Eq. (3.11) has to be rewritten as

$$\min_u \frac{1}{2}\|A(u) - d\|_2^2 \quad \Longrightarrow \mathbf{A}^H\mathbf{A}u - \mathbf{A}^H d = \nabla_u J(u) \overset{!}{=} -g, \tag{3.32}$$

where

$$\mathbf{D} = \mathbf{A}^H\mathbf{A}, \quad \text{and} \quad z = \mathbf{A}^H d. \tag{3.33}$$

To determine the search direction p_k in each iteration step k, the system matrix $\mathbf{A}$ and all previous search directions p_i $\forall i < k$ are taken into account, so that

$$\langle p_i, \mathbf{D}p_j\rangle \overset{!}{=} 0 \quad \text{for} \quad i \neq j \tag{3.34}$$

is fulfilled (D-orthogonality). Under this condition, the search direction p_k is given as

$$p_k = g_k + \frac{g_k^H g_k}{g_{k-1}^H g_{k-1}} p_{k-1}, \quad \text{with} \quad p_0 = g_0 \tag{3.35}$$

where g_k is the negative gradient in iteration k (see Eq. (3.32)). The update step is equal to the steepest descend method, as shown in Eq. (3.26). The step size optimization yields

$$\kappa_k = \frac{p_k^H g_k}{p_k^H \mathbf{A}^H \mathbf{A} p_k} = \frac{p_k^H g_k}{p_k^H \mathbf{D} p_k}. \tag{3.36}$$

It can be shown that the *CG* algorithm converges to the exact solution after N iterations for linear problems, where N is the number of unknowns in the problem. The difference in convergence rate is shown in Figure 3.6, where the convergence rate of both algorithms is evaluated on an arbitrary 2D problem. For the *MR* reconstruction problem, the number of unknowns is still too large ($4.19 \cdot 10^6$), so that a convergence to the exact solution is not possible in an acceptable amount of time. In practice, a sufficient convergence can be usually reached after ≈ 1000 iterations. The *CG* solution for the *MR* reconstruction problem with H_1 regularization is exemplarily shown, which is given as

$$\hat{u} = \arg\min_u J(u) = \arg\min_u \frac{\lambda}{2} \|A(u) - d\|_2^2 + \frac{1}{2} \|\nabla_{xyz}^{+} u\|_2^2. \tag{3.37}$$

The gradient can be calculated as

$$\nabla_u J(u) = \lambda \mathbf{A}^H (\mathbf{A}u - d) + \nabla_{xyz}^{+T} \nabla_{xyz}^{+} u = 0 = -g, \tag{3.38}$$

so that the problem can be written in terms of $\mathbf{D}$ and z, given as

$$\underbrace{\left(\lambda \mathbf{A}^H \mathbf{A} + \nabla_{xyz}^{+T} \nabla_{xyz}^{+}\right)}_{\mathbf{D}} u = \underbrace{\lambda \mathbf{A}^H d}_{z}. \tag{3.39}$$

3.2.5.2 Primal Dual

As described in Sections 3.2.4.3 and 3.2.4.4, the regularization functionals *TV* and *TGV* are based on the L_1 norm. Because of the non-differentiability of the L_1 norm, gradient based method cannot be used to solve the optimization problem. For that purpose, several solution strategies were proposed, as the Fast Iterative Shrinkage and Thresholding Algorithm (FISTA) [12] based on a proximal gradient method. However, the most accurate and efficient one was proposed by the seminal work of Chambolle and Pock [46], known as “Primal-Dual” algorithm. With this algorithm, a solution of the following class of optimization problems can be calculated

$$\min_x F(Kx) + G(x). \tag{3.40}$$

This problem can be rewritten into a saddle-point problem in terms of the primal variable x and the dual variable y by using the convex conjugate or Fenchel duality as

$$\min_x \max_y \langle Kx, y\rangle - F^*(y) + G(x), \tag{3.41}$$

where K is an arbitrary linear operator and $G : \mathbb{C}^N \mapsto \mathbb{R}^+$ and $F : \mathbb{C}^N \mapsto \mathbb{R}^+$ are convex functionals and F^* is the convex conjugate of F. According to [46], the problem can be solved using the following algorithm:

$$\begin{aligned}
&\tau, \sigma > 0;\ \tau\sigma\|K\|_2 < 1;\ \theta \in [0,1];\ \text{initialize: } x_0 \in X,\ y_0 \in Y,\ \bar{x}_0 = x_0\\
&\text{update } x_n, y_n, \bar{x}_n;\ n \geq 0\\
&\begin{cases}
y_{n+1} = \left(I + \sigma\partial F^*\right)^{-1}\left(y_n + \sigma K\bar{x}_n\right)\\
x_{n+1} = \left(I + \tau\partial G\right)^{-1}\left(x_n + \tau K^H y_{n+1}\right)\\
\bar{x}_{n+1} = x_{n+1} + \theta\left(x_{n+1} + x_n\right)
\end{cases}
\end{aligned} \tag{3.42}$$

Here, $(I + \sigma\partial F^*)^{-1}$ and $(I + \tau\partial G)^{-1}$ are the proximal mapping operators (or simply prox operator) for F^* and G, respectively, σ and τ are the step sizes for the primal and dual update, respectively, and K^H is the Hermitian adjoint operator to K. The definition of convex conjugate and proximal mapping is given in the Appendix (Eqs. (A.37) and (A.49)).

Exemplarily, the primal dual solution for the *MR* reconstruction problem with second order *TGV* regularization is shown in the following paragraph. In the primal form, the optimization problem with the two primal variables u and v is written as

$$\begin{aligned}
\hat{u} = \arg\min_u J(u) = \arg\min_u \frac{\lambda}{2}\|A(u) - d\|_2^2 + \mathrm{TGV}_\alpha^2(u) =\\
\arg\min_{u,v} \frac{\lambda}{2}\|A(u) - d\|_2^2 + \alpha_1\|\nabla_{xyz}^+ u - v\|_1 + \alpha_0\|\mathcal{E}v\|_1.
\end{aligned} \tag{3.43}$$

First, the minimization problem from Eq. (3.43), with the primal variables u and v, has to be dualized according to Eq. (A.37), so that the saddle point problem in the primal dual formulation writes as

$$\begin{aligned}
\min_{u,v}\max_{p,q,r} \left\langle \nabla_{xyz}^+ u - v, p\right\rangle - \mathcal{I}_{\alpha_1\|\cdot\|_\infty\leq 1}(p) + \langle\mathcal{E}v, q\rangle - \mathcal{I}_{\alpha_0\|\cdot\|_\infty\leq 1}(q) +\\
\langle A(u) - d, r\rangle - \frac{1}{2\lambda}\|r\|_2^2,
\end{aligned} \tag{3.44}$$

where p and q are the dual variables to u and v, respectively and $\mathcal{I}_C$ is the convex indicator function defined as

$$\mathcal{I}_C(x) = \begin{cases} 0, & \text{if} \quad x \in C\\ \infty, & \text{if} \quad x \notin C \end{cases} \tag{3.45}$$

The variable r is the dual variable to the data fidelity term $\|A(u) - d\|_2^2$. The dualization of the data fidelity term is not absolutely necessary, the proximal operator could be applied directly, but this would require the solution of a linear set of equations, leading to a high computational effort in each primal dual iteration. The dualization circumvents this step and leads to a more efficient solution. The convex conjugate for the L_1 and the L_2 norm as well as all necessary relation to derive Eq. (3.44) from Eq. (3.43) are defined in Appendix A.2.6. Based on the solution strategy from Eq. (3.42), a solution algorithm for the optimization problem defined in Eq. (3.44) can be developed, as denoted in Algorithm 1, with the proximal mapping operators $\mathrm{prox}_{p,q,r}$ for the dual variables p, q, r given as

$$\mathrm{prox}_p(\tilde{p})_{m_x,m_y,m_z} = \frac{\tilde{p}_{m_x,m_y,m_z}}{\max\left(1, \frac{|\tilde{p}_{m_x,m_y,m_z}|}{\alpha_1}\right)}, \tag{3.46}$$

$$\mathrm{prox}_q(\tilde{q})_{m_x,m_y,m_z} = \frac{\tilde{q}_{m_x,m_y,m_z}}{\max\left(1, \frac{|\tilde{q}_{m_x,m_y,m_z}|}{\alpha_0}\right)}, \tag{3.47}$$

$$\mathrm{prox}_r(\tilde{r}) = \frac{\tilde{r}}{1+\frac{\sigma}{\lambda}}. \tag{3.48}$$

To measure the degree of convergence, a modified primal-dual gap (introduced by Bredies and Holler [36]) is used, which is written for the given reconstruction problem with the primal variables $x = (u, v)$ and the dual variables $y = (p, q, r)$ as

$$\begin{aligned}\mathcal{G}(x_k, y_k) = \frac{\lambda}{2}\|A(u_k) - d\|_2^2 + \alpha_1\|\nabla_{xyz}^{+} u_k - v_k\|_{2,1} + \alpha_0\|\mathcal{E} v_k\|_{2,1} + \frac{1}{2\lambda}\|r_k\|_2^2 + \\ \sum_{m_x=1}^{N_x}\sum_{m_y=1}^{N_y}\sum_{m_z=1}^{N_z}\left|\left(\nabla_{xyz}^{+T} p_k + A^H(r_k)\right)_{m_x,m_y,m_z}\right| + \left|\left(p_k + \mathcal{E}^T q_k\right)_{m_x,m_y,m_z}\right|.\end{aligned} \tag{3.49}$$

Algorithm 1 Primal–Dual algorithm for the MR image reconstruction with second order TGV regularization (TGV_α^2) based on Knoll et al. [159].

```
Require: Measurement data: $d$, Operators: $A$, $\nabla_{xyz}^{+}$, $\nabla_{xyz}^{+T}$, $\mathcal{E}$, $\mathcal{E}^T$
  Initialize: $u_0 \leftarrow 0$, $\bar{u}_0 \leftarrow 0$, $v_0 \leftarrow 0$, $\bar{v}_0 \leftarrow 0$, $p_0 \leftarrow 0$, $q_0 \leftarrow 0$, $r_0 \leftarrow 0$
  Choose: $\sigma > 0$, $\tau > 0$
  repeat
    Dual update:
    $p_k \leftarrow \mathrm{prox}_p\left(p_{k-1} + \sigma\left(\nabla_{xyz}^{+}\bar{u}_{k-1} - \bar{v}_{k-1}\right)\right)$
    $q_k \leftarrow \mathrm{prox}_q\left(q_{k-1} + \sigma\mathcal{E}\bar{v}_{k-1}\right)$
    $r_k \leftarrow \mathrm{prox}_r\left(r_{k-1} + \sigma\left(A(\bar{u}_{k-1}) - d\right)\right)$

    Primal update:
    $u_k \leftarrow u_{k-1} - \tau\left(\nabla_{xyz}^{+T}p_k + A^H(r_k)\right)$
    $\bar{u}_k \leftarrow 2u_k - u_{k-1}$
    $v_k \leftarrow v_{k-1} + \tau\left(p_k + \mathcal{E}^T q_k\right)$
    $\bar{v}_k \leftarrow 2v_k - v_{k-1}$
  until convergence of $u$: $\mathcal{G} <$ threshold or $k = k_{\max}$
  return $u_k$
```

3.2.6 Convexity

The convexity of the cost function $J(u)$, which has to be minimized, is a very important property to guarantee that a global optimal solution can be found. A function $J(u)$ is convex if the condition

$$J\left(\lambda u + (1-\lambda)\,v\right) \leq \lambda J(u) + (1-\lambda)J(v) \quad \forall u, v \in \mathrm{C} \quad \lambda \in [0,1] \tag{3.50}$$

is fulfilled [11]. The convexity condition ensures that a found optimal solution, fulfilling the optimality condition $\nabla_u J(u) = 0$, is the only one so that it is the global optimum. If the condition in Eq. (3.50) is not fulfilled, there can be an infinite number of points fulfilling $\nabla_u J(u) = 0$, so that nothing is known about the global optimality. In practice, the Hessian matrix defined in Eq. (A.36), can be used as indicator for convexity. If the Hessian is positive semi-definite, the cost function is convex. For the *MR* image reconstruction problem, the Hessian for the data fidelity term can be calculated as

$$\nabla_u^2\left(\|\mathbf{A}u - d\|_2^2\right) = \mathbf{A}^H\mathbf{A}, \tag{3.51}$$

which is a positive semi-definite matrix. Also, for the regularization functionals defined in Sections 3.2.4.1 to 3.2.4.4 it can be shown that they are all convex. For the primal dual algorithm, convexity is also very important, because it is only defined for convex problems.

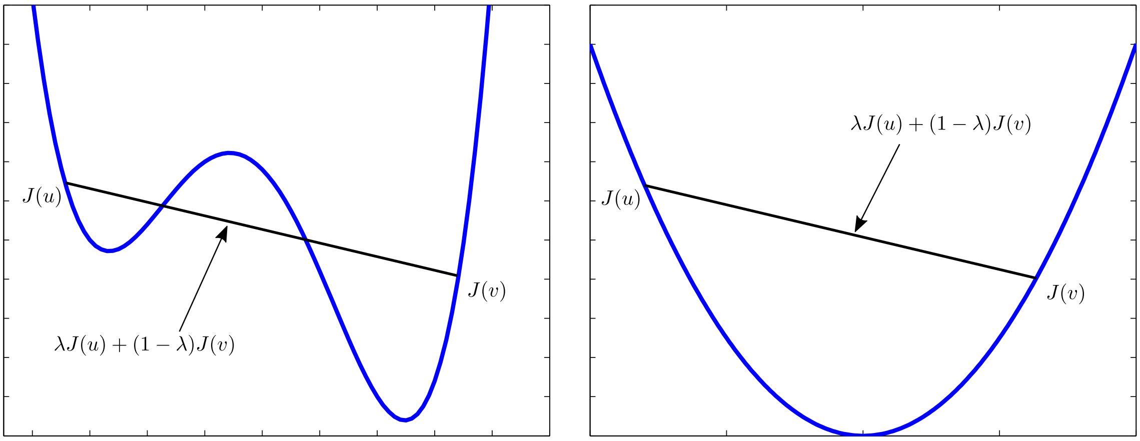

Figure 3.6: The property of convexity is shown on a 1D example. (Left) Example of a non-convex function, where the condition of Eq. (3.50) is not fulfilled. (Right) Example of a convex function, where the condition of Eq. (3.50) is fulfilled for all values of u, v and λ.

3.2.7 Determination of Receive Coil Sensitivity Profiles

For *SENSE* based reconstruction algorithms, the explicit knowledge of the receive coil sensitivity maps $C_n(\vec{r})$ is required, to generate the forward and backward operators (see Section 3.2.3). In general, there exist two different strategies to determine the receive coil sensitivity profiles: first, this can be done by a low resolution reference scan acquired with both, the actual phased array receive coil and the whole body birdcage volume coil. The birdcage coil is assumed to have a very homogeneous receive sensitivity, so that the morphological structure of the investigated object cancels out by applying a point wise division between the image of each receive coil $S_n(\vec{r})$ and the birdcage reference image $S_{ref}(\vec{r})$. With that the sensitivity profile $C_n(\vec{r})$ of each coil can be expressed as

$$C_n(\vec{r}) = \frac{S_n(\vec{r})}{S_{ref}(\vec{r})}. \tag{3.52}$$

In general, the sensitivity profiles determined with this method are very accurate, but the additional reference scan prolongs the acquisition time. Much more important, this methods is very sensitive to motion occurring between the reference scan and the actual image acquisition, which leads to a mismatch between the sensitivity profiles and the actual image acquisition and with that to wrong forward and backward operators. These coil sensitivity errors propagate to the reconstructed image and can lead to severe artifacts. Therefore, in image reconstruction, the receive coil sensitivities are usually determined out of the measurement data itself, which is the second strategy. Therefore, a certain number of k-space lines are acquired at Nyquist rate around the k-space center (typically 16-24), which are called *ACLs*. Because the B_1 field is smooth and continuously varying in space, it only consists of low spatial frequencies (see Section 2.3.3), so that this low resolution approach is justified.

To determine the receive coil sensitivity profiles out of the *ACLs*, several algorithms were proposed. A complete review would be out of scope of this thesis, but the most important methods should be briefly introduced. One of the first methods to determine receive sensitivity profiles out of *ACLs* was proposed by Walsh et al. [311], for the adaptive combination of multiple phased array coil images. The receive sensitivity profiles are determined by a matched filter approach to maximize the local *SNR*. For this purpose, both the signal and the noise are treated as stochastic processes, the signal as desired and the noise as undesired one. It can be shown that the weighting factors in each voxel are given as the eigenvector of $\mathbf{\Psi}_n^{-1}\mathbf{\Psi}_s$ with the corresponding maximum eigenvalue. Here, $\mathbf{\Psi}_n$ is the noise correlation matrix defined in Section 2.1.6 and $\mathbf{\Psi}_s$ is the voxel wise signal correlation matrix determined out of a patch around each voxel. If the patch size is large enough to remove the influence of spin density variations, the determined weighting factors are a good approximation of the corresponding coil sensitivity map. The phase of the coil sensitivity map in each channel is normalized by using the one with the maximum intensity, so that only the relative phase can be determined. This method delivers robust coil sensitivity estimates even at low *SNR*. For a low number of *ACLs*, blocky artifacts can occur because of the patch based approach. Another important method, already mentioned in Section 3.1.2, is known as ESPIRiT and was presented by Uecker et al. [301]. Here, the whole sensitivity map for each channel is determined as the dominant eigenvector (corresponding to the greatest eigenvalue) of the calibration kernel in k-space, showing the strong connection of k-space and image space based *PI* methods. This method delivers much more smooth and natural appearing coil sensitivity profiles, but sometimes lead to errors in low *SNR* regions.

Also, some methods based on variational modeling were proposed. Uecker et al. [300] proposed a non-linear inversion by jointly reconstructing receive coil sensitivities C_n and the underlying image u out of undersampled data. Because of the high number of unknowns, this under-determined problem gets highly ill-posed. The solution of this method is based on Iteratively Regularized Gauss Newton (IRGN) framework, where in each iteration the linearized subproblem is solved to calculate an update step. To stabilize the solution, a Tikhonov regularization is applied to the update step, and a smoothness constraint is applied to the sensitivity maps C_n. With this method, the coil sensitivity profiles are rather a side product. The *IRGN* method was further improved in Knoll et al. [160], by the application of L_1 based regularization functionals as *TV* and *TGV* to reach a better noise and artifact suppression. A further method based on variational modeling was proposed by Schlögl et al. [254], especially for the coil sensitivity estimation from dynamic data. Here again, a *TGV* prior is used as regularization for the magnetization and a H_1 regularization for the receive sensitivity in magnitude and phase.

As described by Griswold et al. [100], the coil sensitivity maps have to be normalized, which is inherently done in available implementations of the above described methods as

$$C_{n,norm}(\vec{r}) = \frac{C_n(\vec{r})}{\sqrt{\sum_{i=1}^{N_c} |C_i(\vec{r})|^2}}, \tag{3.53}$$

so that the reconstructed image has a nearly homogeneous sensitivity distribution and to ensure the operator adjointness.

3.2.8 Iterative Image Reconstruction and Compressed Sensing

Based on the ideas described previously, several methods were proposed to reconstruct *MR* images from undersampled data. The first reconstruction approach introducing these basic ideas was presented by Pruessmann et al. [233], known as *CG*-*SENSE*, as an extension of the *SENSE* technique to arbitrary k-space trajectories. In this work, the *CG* algorithm was used to iteratively solve the reconstruction problem, combined with a Tikhonov regularization to stabilize the solution. Furthermore, the concept of *MR* forward and backward operators was introduced in this work. The next step in image reconstruction was introduced by the seminal work of Lustig et al. [194], known as Compressed Sensing (CS). The concept of *CS* comes from the signal theoretic point of view [69], dealing with the question how to describe a given signal in a sparse representation to reduce the necessary amount of sampling points. From image compression it is known that natural images exhibit a huge amount of redundancy, so that the necessary amount of information to represent the image can be massively reduced by applying a sparsity transform. It was shown by Lustig et al. [194] that the same concept can be used to drastically reduce the necessary data points in k-space to reconstruct a diagnostic useful image. Three ingredients are necessary to achieve this: first, incoherent undersampling, second, a sparsity transform, and third, an iterative solution to balance between data fidelity and the sparsity requirement. For incoherent undersampling, non-Cartesian trajectories [28] or incoherent Cartesian undersampling, which is most efficient for 3D acquisitions, can be applied. Incoherent undersampling ensures that the occurring undersampling artifacts appear like noise and that they are evenly spread over the whole image in the sparsity domain. As sparsity transform, the Discrete Cosinus Transforms (DCT), the wavelet transform [63] and the *TV* functional (see Section 3.2.4.3) were proposed by Lustig et al. [194]. Because the *TV* functional only delivers high values at image edges, it can be seen as sparsity transform as well. The reconstruction problem in [194] was written as an optimization problem which can be solved using the *CG* algorithm. For a detailed overview over *CS* based methods in *MR* image reconstruction, the interested reader is referred to the following review articles [126, 195].

The application of L_1 based image priors started with the work from Block et al.[28], where a *TV* functional was applied to stabilize the image reconstruction from undersampled radial data. A similar regularization approach using Bregman iterations was proposed by Liu et al. [187]. As already mentioned in Section 3.2.7, the nonlinear inversion of the *MR* image reconstruction problem was proposed by Uecker et al. [300], where both the receive coil sensitivity profiles and the image are jointly reconstructed by solving a non-linear optimization problem. This was introduced, to incorporate the whole available information for image and coil sensitivities, yielding more accurate sensitivity maps and therefore a better reconstruction results. This method was improved by incorporating L_1 image priors, in particular *TV* and *TGV* by Knoll et al. [160]. The *TGV* functional was introduced for *MR* image reconstruction by Knoll et al. [159] and a variant for dynamic image reconstruction was presented by Schlögl et al. [255], known as Infimal Convolution Total Generalized Variation (ICTGV), leading to a further improvement of the reconstruction quality.

3.3 Variational Methods in Field Mapping

For field mapping, variational methods are often used to apply a smoothness constraint on the field map, to enforce its physical behavior and to suppress outliers. For example, a regularized approach to estimate magnitude and phase of the B_1^+ field in a parallel transmit (pTX) setting was introduced by Funai et al. [83], based on the idea of the Double Angle Method (DAM) but extended to an arbitrary number of acquired flip angles N_α. The cost function is formulated in terms of the three unknown quantities: the underlying magnetization image $\mathbf{M}$, the normalized magnitude $\mathbf{B}_{1_n}^{+,norm}$ and the phase $\mathbf{\Phi}_n$ of the B_1^+ field, given as

$$\begin{aligned} J(\mathbf{M}, \mathbf{B}_1^{+,norm}, \mathbf{\Phi}) = \frac{1}{2} \sum_{n=1}^{N_{Tx}} \sum_{j=1}^{N_\alpha} \sum_{q=1}^{N_x N_y N_z} & \left| S_{n,j,q} - M_q e^{i\phi_{n,q}} \sin\left(\alpha_j B_{1_{n,q}}^{+,norm}\right) \right|^2 \\ & + \frac{\lambda_1}{2} \left\| \nabla_{xyz}^{+T} \nabla_{xyz}^{+} \mathbf{B}_{1_n}^{+,norm} \right\|_2^2 + \frac{\lambda_2}{2} \left\| \nabla_{xyz}^{+T} \nabla_{xyz}^{+} \mathbf{\Phi}_n \right\|_2^2 , \end{aligned} \tag{3.54}$$

where N_{Tx} is the number of transmit channels and $S_{n,j,q}$ is the acquired signal of voxel q, for flip angle j, and using transmit channel n. Magnitude and phase for each transmit channel are separately regularized by the L_2 norm of its second order spatial derivative and λ_1 and λ_2 are their regularization parameters, respectively. This problem is solved by performing a gradient based update step for $\mathbf{B}_{1_n}^{+,norm}$ and $\mathbf{\Phi}_n$ in each iteration, whereas a solution for $\mathbf{M}$ can be obtained analytically with assumed constant $\mathbf{B}_{1_n}^{+,norm}$ and $\mathbf{\Phi}_n$ in each iteration. The non-convexity of this optimization problem is tackled by a proper initialization by using the solution of the standard *DAM*. Zhao et al. [336] presented a quite similar approach for B_1^+ magnitude and phase mapping based on the Bloch-Siegert (BS) method. As a regularization functional, the H_1 functional was used applied to the complex B_1^+ field estimate instead of separately to magnitude and phase. Another formulation of this problem was proposed by Sun et al. [288]. The approach from Funai et al. [83] was also applied to B_0 mapping in [84] and [80], where the data fidelity term in the cost function was adapted properly to take the B_0 model into account, leading to an optimization problem similar to Eq. (2.101). As regularization functional, also the second order spatial derivative was used. In these methods, variational modeling is used to stabilized the solution in low *SNR* regions, but without acceleration.

Undersampling was also investigated for B_1^+ mapping, i.e., an accelerated version for *BS* based B_1^+ mapping was introduced by Sharma et al. [265], but without using an image prior. For the reconstruction of the undersampled data, a modified *SPIRiT* approach (presented by Lustig et al. [196]) was used. *SPIRiT* is more or less an extended version of *GRAPPA*, where the missing data points in k-space for each receive coil are obtained as weighted sum of its neighbors of all available receive coils. The basic idea of the method of Sharma et al. is to incorporate the information of both *BS* acquisitions obtained with each of the N_{Tx} transmit channels into the *SPIRiT* framework. These additional acquisitions (both *BS* encodings for each transmit channel) are treated as “additional receive coils” for the reconstruction. Moreover, the *BS* acquisitions for each transmit channel have to be performed sequentially, so that different k-space positions can be acquired for each. With that, the determination of the convolution kernel is improved, referred to as “joint staggered” approach in [265]. This method already performs very well, acceleration factors of about 30 can be achieved without sacrificing accuracy, but further improvement can be expected by directly applying a smoothness constraint to the reconstructed B_1^+ field.

4

Applications

> In the end, it's not the years in your life that count. It's the life in your years.
>
> *Abraham Lincoln*

Contents

4.1 Chemical Shift Imaging (Water/Fat Separation) 112
4.2 Quantitative MRI 134

Several applications in Magnetic Resonance Imaging (MRI) have very high requirements on the field homogeneity, or require a certain correction on the basis of field mapping. According to Section 2.2.3.2, strong geometric distortions can occur due to a deviation of the expected k-space trajectory caused by B_0 field variations. This is most severe for sequences with long readout trajectories, as it is the case for Echo Planar Imaging (EPI) based sequences or spiral readouts. If the field distribution is known, this effect can be corrected, i.e., in image space as proposed by Jezzard and Balaban [139]. In Quantitative Susceptibility Mapping (QSM), it is tried to map the tissue specific susceptibility variation, where field mapping techniques are used. Here, the main challenge is to separate the field variations caused by the susceptibility distribution of the tissue, from the macroscopic background filed variations. In a subsequent step, the underlying susceptibility distribution is obtained by a deconvolution operation on the field map. A possible solution for this problem, based on variational modeling, was proposed by Langkammer et al. [166]. Also, for a method called Chemical Exchange Saturation Transfer (CEST), where metabolic information is obtained from the saturation of the magnetization at certain frequency bands, field mapping is essential. First, a deviation in B_0 leads to a shift of the saturation band to a wrong position, and second, the degree of saturation depends on the actual

B_1^+ magnitude at a certain location, which has to be taken into account for quantitative evaluations. A more detailed analysis is given by Kim et al. [156]. Also, for spectroscopy, a high degree of B_0 homogeneity in the voxel of interest is necessary, because the line width is directly proportional to ΔB_0 inside the voxel, leading to a decrease in spectral resolution. Here, a retrospective correction is not possible, so that the requirement on accurate B_0 shimming is very high. According to Sections 2.2.5 and 2.3.6, B_0 as well as B_1 shimming require the exact knowledge of the underlying field distribution, so that field mapping is an essential part of these procedures. Two selected applications are covered in more detail in this section, these are chemical shift imaging, in particular water/fat separation, and the correction for B_1^+ field induced modeling errors in quantitative *MRI* models.

4.1 Chemical Shift Imaging (Water/Fat Separation)

In this section several aspects concerning fat/water separation are considered. First, the physical background is described, especially the origin of the chemical shift and its effect on the Magnetic Resonance (MR) signal. Second, some mathematical models to describe the signal behavior are introduced, and at the end, several methods to separate the fat and water signal are described.

4.1.1 Physical Principles of Water/Fat Separation

According to Section 2.1.1, the *MRI* signal originates from the ^{1}H nucleus in the hydrogen atom, which occurs in different chemical environments in typical biological tissue. Chemically, the hydrogen atom can be bound to macro-molecules, lipids (fat-molecules) or water molecules. Hydrogen nuclei that are bound to macro-molecules cannot be measured directly with classical *MRI* techniques, because of the instantaneous dephasing with a T_2 time in the order of a few µs. They can only be measured indirectly by an offresonant saturation and measuring the subsequent decrease in the directly measurable signal, which is known as Magnetization Transfer (MT). The direct contribution to the measurable *MRI* signal is therefore restricted to hydrogen atoms from two different chemical species, fat and water. In fat, hydrogen is mainly bound to carbon atoms, which exhibit a much lower electronegativity than oxygen, which is the binding counterpart in the water molecule. The orbiting electrons shield the external magnetic field, “seen” by the nucleus, to a certain degree. The higher electronegativity of the oxygen shifts the center of the “electron cloud” away from the hydrogen slightly closer to the oxygen. Hence, the shielding effect decreases for ^{1}H nuclei in water. In fat, the ^{1}H nuclei experiences a higher shielding effect, because the “electron cloud” is more evenly shared between the hydrogen and the carbon atom. Because of the higher shielding, the hydrogen atoms in fat exhibit a slightly lower resonance frequency than those bound in water molecules. This difference in resonance frequency $\Delta\omega_F$ is known as chemical shift and can be used to separate the fat from the

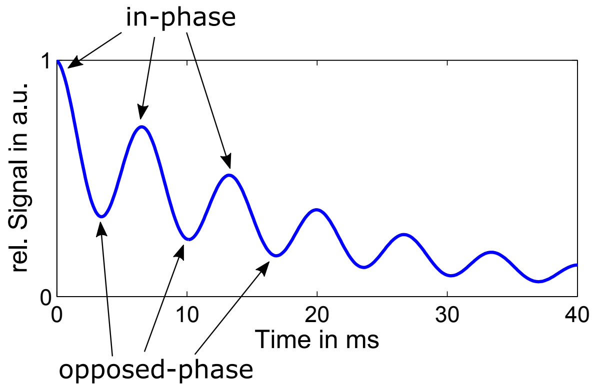

Figure 4.1: FID signal in a voxel containing fat and water, with the system frequency synchronized to water. The signal is simulated for a fat fraction of 30 % and a common T_2^* relaxation time constant of $T_2^* = 20\,\mathrm{ms}$ at a field strength of 1 T.

water signal. The relative shift in resonance frequency between fat and water depends on the specific dominant fat molecule in a certain tissue, but is in average $\approx 3.5\,\mathrm{ppm}$ [199]. The absolute value depends on the field strength, resulting in $\Delta\omega_F \approx 2\pi \cdot 220\,\mathrm{Hz}$ at 1.5 T or $\Delta\omega_F \approx 2\pi \cdot 440\,\mathrm{Hz}$ at 3 T. This frequency difference has two effects on the voxel signal: first, it leads to a periodical signal variation with the frequency $\Delta\omega_F$ in the demodulated signal additionally to the signal decay due to dephasing. This is because the fat and water signal add up constructively if they are in-phase and destructively if they have opposed phase. The time interval ΔT_F between signal maximum and minimum is given by

$$\Delta T_F = \frac{\pi}{\Delta\omega_F}. \tag{4.1}$$

This effect is visualized by a simulation in Figure 4.1. The second effect is a spatial misalignment of the fat signal in frequency encoding direction, because the chemical shift overlays with the frequency encoding gradient during readout, similar to the effect causing geometric distortions due to ΔB_0 field variations, described in Section 2.2.3.2. According to Eq. (2.67), the shift distance Δx_F between fat and water is determined by the readout bandwidth Δf_{BW} and is given as

$$\Delta x_F = \frac{N_x \Delta\omega_F}{2\pi\Delta f_{\mathrm{BW}}} \Delta x, \tag{4.2}$$

where Δx is the voxel size and N_x is the number of voxels in readout direction. Therefore, a higher readout bandwidth reduces the fat/water shift, but leads to a decrease in Signal-to-Noise Ratio (SNR). If the readout bandwidth per voxel is larger than the chemical shift ($2\pi\Delta f_{\mathrm{BW}}/N_x > \Delta\omega_F$), the misalignment is below the voxel size and can be neglected in this case.

In many clinically relevant applications, the fat signal dominates, whereas the water signal is of primary interest. Especially, structures around fatty tissue are often difficult to

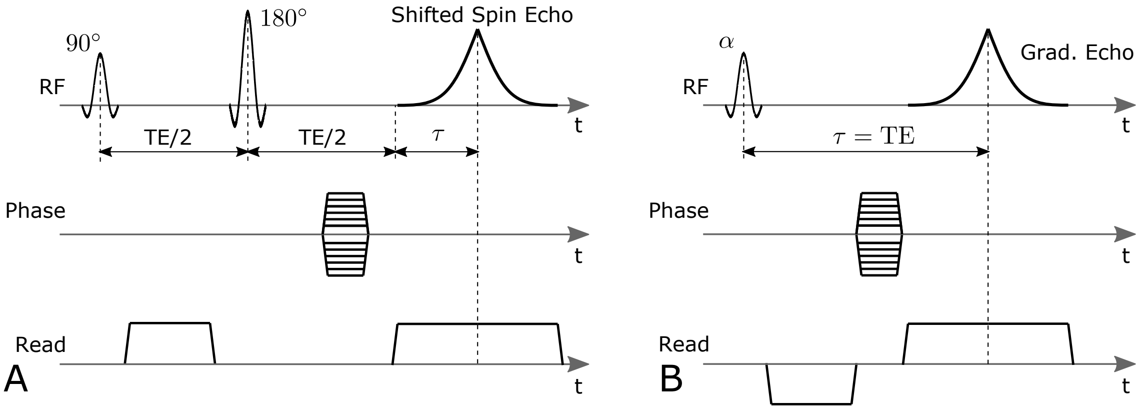

Figure 4.2: MR sequences used to encode the fat water shift as spin echo based (A) and gradient echo based version (B).

diagnose, because of a chemical shift artifact, resulting in an overlay of fat and water signal. Therefore, it is tried to suppress the fat signal, either by the application of spectral selective Radio Frequency (RF) pulses or an inversion preparation pulse. The spectral selective *RF* pulses can be either used to selectively excite the water compartment or to selectively saturate the fat compartment with a 90° pulse followed by a spoiler gradient. However, this approach is highly sensitive to B_0 field variations, especially if $\gamma|\Delta B_0| > \Delta\omega_F/2$ and also B_1 field variations can lead to incomplete fat saturation, due to a deviation of the desired 90° flip angle. The inversion preparation makes use of the much lower T_1 in fat ($T_{1,F} \approx 300\,\mathrm{ms}$) compared to most water dominant tissues, so that the excitation takes place during the zero crossing of the fat signal. This approach is insensitive to variations in B_0 and also to B_1 for an adiabatic inversion. However, this approach also saturates other tissues having similar T_1 and partially saturates the water signal, leading to a decrease in *SNR*. Instead of suppressing the fat signal, it might be more beneficial to separate both signals to get individual fat and water images, which also adds diagnostic relevant information, i.e., for the diagnosis of bone marrow or liver diseases. Furthermore, also the quantitative analysis of the fat content in a specific tissue gets possible, which can be used as a biomarker to quantify the state or the progress of a certain disease. For this purpose, several methods to separate fat and water signal were developed over the years, where a brief overview is given in Section 4.1.3, based on the signal model derived in Section 4.1.2.

4.1.2 Signal Model and Fat Quantification

In the simplest case, the *MR* signal in the presence of water and fat can be modeled as two spectral lines, with a spectral distance of $\Delta\omega_F$ (chemical shift), where the system frequency ω is synchronized to the frequency of water ω_W ($\omega = \omega_W$) and the frequency of fat is given as $\omega_F = \omega_W - \Delta\omega_F$. With that the signal $S(t)$ at time t after excitation writes as

$$S(t) = S_W e^{-j(\omega_W-\omega)t} + S_F e^{-j(\omega_F-\omega)t} = S_W + S_F e^{j\Delta\omega_F t}, \tag{4.3}$$

Peak Nr. (m)	Chemical Group	Spectral Position ppm	Spectral Position of Combined Peak ppm	Chemical Shift $\Delta\omega_{F,m}$ at 3 T Hz
1	-C**H**=C**H**- -C**H**-O-CO-	5.29 5.19	5.3	-77
Water	$\mathbf{H}_2$O	4.70	4.7	0
2	-C$\mathbf{H}_2$-O-CO-	4.20	4.2	64
3	-CH=CH-C$\mathbf{H}_2$-CH=CH-	2.75	2.75	249
4	-CO-C$\mathbf{H}_2$-CH$_2$- -C$\mathbf{H}_2$-CH=CH-C$\mathbf{H}_2$-	2.24 2.02	2.1	332
5	-CO-CH$_2$-C$\mathbf{H}_2$- -(C$\mathbf{H}_2$)$_n$-	1.60 1.30	1.3	434
6	-(CH$_2$)$_n$-C$\mathbf{H}_3$	0.90	0.9	485

Table 4.1: Here, the spectral position of the signal from a ^{1}H nucleus bound to a specific chemical group in the fat molecule (shown in bold). For those peaks lying too close together, the spectral position of the combined peak is given, as well as the resonance offset in Hz for each of the 6 main peaks relative to water at 3 T. The peaks are numerated by the peak number m. The values are out of Hamilton et al. [108].

where S_W and S_F are the signal components from the water and fat compartment, respectively, proportional to their individual spin densities ρ_W and ρ_F. Even assuming perfect shimming, the signal is further influenced by static field variations ΔB_0 induced by susceptibility variations between different tissues especially between air and tissue (see Section 2.2.2). This effect has also to be considered, as well as the influence of T_2^* decay, where usually the relaxation rate $R_2^* = \frac{1}{T_2^*}$ is used. After spatial encoding, the signal of a voxel located at point $\vec{r}$ in space after the evolution time τ is given as

$$S\left(\vec{r}, \tau\right) = \left(S_W(\vec{r}) + S_F(\vec{r}) e^{j\Delta\omega_F \tau}\right) e^{j(\gamma\Delta B_0(\vec{r})\tau + \phi_0(\vec{r}))} e^{-R_2^*(\vec{r})\tau}, \tag{4.4}$$

with ϕ_0 is the initial time independent phase shift known as trancieve phase (see Section 2.5.2.1). The T_2^* decay is often neglected by setting $R_2^* = 0$. The definition of the evolving time τ depends on the sequence and is defined as the time difference between the time point where fat and water are in-phase and the center of the acquired echo. In a Spin Echo (SE) sequence, τ is defined as the time difference between the *SE*, determined by the 90° and 180° *RF* pulses, and the center of the readout gradient. This can be done, because the chemical shift induced phase difference between fat and water is refocused at the time of the *SE*. In Gradient Recalled Echo (GRE) sequences, τ is simply the echo time. The timing for fat/water sensitive sequences is depicted in Figure 4.2. The phase shift between the water and the fat signal at time τ is given as $\Theta = \Delta\omega_F \tau$.

	Peak Nr. (m)	Spectral Position ppm	Chemical Shift $\Delta\omega_{F,m}$ at 3 T Hz	Fitted Area α_m %	T_1 ms	T_2 ms
Liver	1	5.3	-77	4.7	–	–
	2	4.2	64	3.9	–	–
	3	2.75	249	0.6	–	51
	4	2.1	332	12	–	52
	5	1.3	434	70	–	62
	6	0.9	485	8.8	–	83
Bone Marrow	1	5.3	-77	4.16	–	–
	2	4.2	64	–	–	–
	3	2.75	249	1.64	600 ± 30	59 ± 3
	4	2.1	332	16.13	430 ± 20	51 ± 3
	5	1.3	434	69.38	550 ± 30	69 ± 4
	6	0.9	485	8.69	1160 ± 40	74 ± 6
Subcutaneous Fat	1	5.3	-77	4.19	–	–
	2	4.2	64	–	–	–
	3	2.75	249	1.53	580 ± 30	58 ± 3
	4	2.1	332	16.14	400 ± 25	47 ± 3
	5	1.3	434	69.89	530 ± 40	63 ± 5
	6	0.9	485	8.25	1080 ± 50	67 ± 8

Table 4.2: Spectral position and the resonance offset in Hz relative to water at 3 T as well as the relative contribution α_m in % for the 6 main contributing fat components in three types of tissue: Liver, bone marrow and subcutaneous fat. For some peaks also their T_1 and T_2 relaxation time constants are given. The liver values are out of Hamilton et al. [108] and the values for bone marrow and subcutaneous fat are from Ren et al. [243], where the relaxation time constants are determined at 7 T.

The single peak model fits very well for the signal from the simple water molecule, whereas the fat molecule is much more complex. Moreover, the resonance frequency depends on the position in the molecule and its direct neighbors. In Figure 4.3 (A), a typical fat molecule is shown, where 9 different chemical groups with different resonance frequencies are identified. Figure 4.3 (B) and (C) shows a simulated and a measured fat spectrum, respectively. The main contribution originates from the CH_2 elements in the fatty acid chains ($\approx 70\,\%$) exhibiting the commonly used chemical shift of 3.5 ppm. Even though this effect is known for a long time, it was first introduced to fat water separation in [334], with a modified signal model given as

$$S\left(\vec{r},\tau\right) = \left(S_W(\vec{r}) + S_F(\vec{r}) \sum_{m=1}^{N_F} \alpha_m e^{j\Delta\omega_{F,m}\tau}\right) e^{j(\gamma\Delta B_0(\vec{r})\tau + \phi_0(\vec{r}))} e^{-R_2^*(\vec{r})\tau}, \tag{4.5}$$

with

$$\sum_{m=1}^{N_F} \alpha_m = 1, \tag{4.6}$$

where α_m is the relative contribution of one of the different spectral components of the fat signal. N_F is the number of modeled fat peaks. If each α_m is known, the calculation effort does not increase, because the complex phasor $e^{j\Delta\omega_F\tau}$ in Eq. (4.4) is replaced by a precalculated sum of complex phasors. According to Yu et al. [334], the spectral position of each individual fat peak can be seen as constant, but their contribution α_m can vary for different types of fatty tissue. For the determination of α_m two variant are possible: the first method is a spectroscopic measurement with water suppression, where a Lorentzian function is fitted centered around the position of the maximum of each fat peak. α_m is then determined as the area under the fitted curve. The second possibility is a calibration measure, as proposed by Yu et al. [334], where 16 echos were acquired. The separation of the 7 different components (one water and 6 fat peaks) was performed by using an extended version of the Iterative Decomposition of water and fat with Echo Asymmetry and Least squares estimation (IDEAL) algorithm. The contributions α_m are then determined as the average over a region with fat dominant voxels. It was shown that this recalibration of the fat model leads to an increase in accuracy over predetermined values for α_m. However, the improvement is so low that most studies use predefined values from literature.

Referring to 4.3, some values for the different fat peaks are given in Tables 4.1 and 4.2. 9 different signal components can be identified in total, but some of them are so close together or their contribution is so low that a discrimination is not purposeful. Usually, 6 different signal components are distinguished. In Table 4.1, the spectral position of the 9 identified chemical groups in the fat molecule are given as well as the position of the usually used combined peak for components lying closely together. Moreover, the resonance offset in Hz for 3 T is given as well. In Table 4.2, the relative contributions α_m for these 6 main peaks in liver, bone marrow and subcutaneous fat are given as well as T_1 and T_2 relaxation time constants for some of the peaks, if available. The values are out of [108, 241, 243], where also more details are given according this topic.

This signal model is sufficient for the separation of both signal contributions, but it is not sufficient for the quantification of fat. The fat signal fraction η_s is usually defined as

$$\eta_s = \frac{\rho_F}{\rho_F + \rho_W}. \tag{4.7}$$

However, after separation, only the water and fat signal components S_W and S_F can be obtained, which are proportional to their individual spin densities ρ_W and ρ_F, but also depend on other influences. For example, it is well known that water and fat have completely different T_1 time constants, so that the magnetization of both components has different relaxation states at the following excitation. If a *GRE* sequence is used, the signal components S_W and S_F follow the steady state equation (see Eq. (4.41)) with their specific

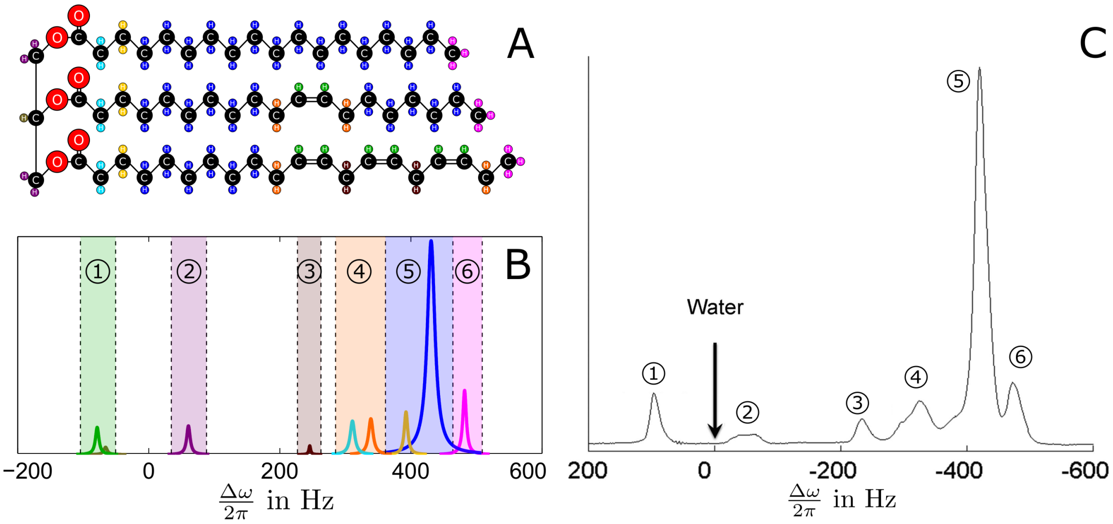

Figure 4.3: (A) Typical structure of a fat molecule with 9 different identified chemical groups, where the hydrogen atom can be bound to. In each configuration, the ^{1}H nucleus experiences a different shielding, resulting in slightly different Larmor frequencies. In (B), a simulated spectrum is shown for each of the 9 identified chemical groups in (A), where the color of the group corresponds to the color of the peak. In practice not all of this peaks can be resolved in-vivo, so that some are grouped together, leading to 6 resolvable peaks. The simulation is based on a Lorentzian line shape for each peak, using the values reported for liver tissue in Table 4.2. (C) A measured fat spectrum in vegetable oil at 3 T is shown. The 6 dominant peaks in (B) are marked with the corresponding number and the position of the water peak is also indicated. The measured spectrum is a modified version from Reeder and Sirlin [241].

T_1 relaxation time constants, $T_{1,W}$ and $T_{1,F}$, respectively. This influence is considered by Liu et al. [188], where also a compensation approach is proposed, based on a dual flip angle acquisition, similar to the ideas of the Variable Flip Angle (VFA) approach for T_1 mapping [65]. Also the R_2^* effect has to be considered. It was shown by Yu et al. [331] that the additional estimation of R_2^* leads to an improved separation accuracy, but this is still not sufficient for quantification. It was shown by Chebrolu et al. [50] and Bydder et al. [45] that the estimation of separate relaxation rates for both components, $R_{2,W}^*$ and $R_{2,F}^*$, leads to a massive improvement in fat quantification accuracy. In general, also different relaxation rates are possible for each fat peak, as reported in Table 4.2, so that the complete signal model can be written as

$$S\left(\tau\right) = \left(S_W(T_{1,W})e^{-R_{2,W}^*\tau} + S_F(T_{1,F})\sum_{m=1}^{N_F}\alpha_m e^{j\Delta\omega_{F,m}\tau}e^{-R_{2,F,m}^*\tau}\right)e^{j(\gamma\Delta B_0\tau+\phi_0)}. \quad (4.8)$$

For the reason of simplicity, the $\vec{r}$ dependency is skipped. The individual relaxation rates of the different fat peaks, $R_{2,F,m}^*$, are usually not determined, because of the ill-posedness of the problem. Noise and the low contribution of some of the peaks will not allow a reliable quantification. A detailed comparison between different fat/water signal models was given by Hernando et al. [124]. Even when everything is corrected perfectly, the fat fraction is given in terms of spin densities, whereas usually the fat volume or the fat mass fraction is of interest. It was described by Reeder et al. [236], how to obtain these these quantities out of the fat signal fraction.

4.1.3 Methods for Water/Fat Signal Separation

The separation of the fat and water signal can be done spectroscopically, where a very long acquisition time is necessary to reach a reasonable spatial resolution, or by a semi spectroscopic approach as proposed by Sepponen et al. [260]. In this method, a certain number of 2D k-space data sets with different, but equally spaced evolution times τ (Eq. (4.4)) are acquired, which are fed into a 3D Fourier transform, where the spectral component is resolved in the third dimension, with a resolution reciprocal to the echo spacing $\Delta\tau$. For the separation of fat and water, there are only two components with known spectrum which have to be resolved, image space methods are preferable, because of the much higher spatial resolution and the shorter acquisition time. Most of the currently available state of the art methods are based on the simple idea proposed in the seminal work of Dixon [67], therefore, they are referred to as Dixon methods. In the following, the initially proposed two-point Dixon method is described as well as several improvements which were developed over the years making this technique practically applicable.

4.1.3.1 Initially proposed Two-Point Dixon

The basic idea of the initially proposed two-point Dixon method [67] in its simplest form is to choose τ in Eq. (4.4) according to Eq. (4.1), so that one image is acquired at the maximum and one in the minimum of the oscillating decay, as shown in Figure 4.1. At the maximum, the fat and water signal components are in-phase ($\Theta = 0°$) and at the minimum they are maximal out of phase ($\Theta = 180°$). According to 4.4, the in-phase signal S_{in} and the opposed phase signal S_{out} are given as

$$
\begin{aligned}
S_{in}(\vec{r}) &= S_W(\vec{r}) + S_F(\vec{r}), &(4.9)\\
S_{out}(\vec{r}) &= S_W(\vec{r}) - S_F(\vec{r}), &(4.10)
\end{aligned}
$$

where ΔB_0 effects and R_2^* decay are neglected ($\Delta B_0 = 0$, $\phi_0 = 0$ and $R_2^* = 0$). The signal components of water and fat S_W and S_F can be resolved as

$$
\begin{aligned}
S_W(\vec{r}) &= \frac{1}{2}\left|S_{in}(\vec{r}) + S_{out}(\vec{r})\right|, &(4.11)\\
S_F(\vec{r}) &= \frac{1}{2}\left|S_{in}(\vec{r}) - S_{out}(\vec{r})\right|. &(4.12)
\end{aligned}
$$

In this form, the Dixon method suffers from the same problem as the spectral selective fat saturation, because the influence of ΔB_0 is neglected. Referring to Section 2.2, even under perfect conditions having a well shimmed main field, the remaining field inhomogeneity over the Field of View (FOV) can be easily in the range of the chemical shift or above, due to susceptibility variations especially between air and tissue. This leads to incomplete fat/water separation, leading to additional intensity variations in fat and water image according to the underlying field variation. If $\gamma|\Delta B_0| > \Delta\omega_F/2$, fat is assumed to be water and vice versa, which is called fat/water swap. Even though, a *SE* sequence was used in [67], which is less sensitive to variations in ΔB_0 than a *GRE* sequence, severe artifacts can be observed. In this form, fat/water separation cannot be applied in clinical practice, nevertheless, today's available state of the art methods are still based on this simple idea. The main challenge in Dixon based fat/water separation is to gain a valid estimate for ΔB_0. If this is established, the separation of the signal components is a simple task.

Over more than three decades, many methods were proposed to solve this ill-posed inverse problem, by either modifications in data acquisition, post-processing or both, to get more robust results. In Chapter 6, an approach based on variational modeling, by applying a Total Generalized Variation (TGV) prior is presented. Although, huge improvements could be reached, a global optimal solutions still does not exist, so that it is still an open research topic. Some of these improvements are reviewed briefly in the following.

4.1.3.2 Three-Point / Multi-Point Dixon Methods

The first improvements were done by acquiring more data points to get additional information about the main field variations. In Yeung and Kormos [328] for example, the initially proposed acquisition of two separate *SEs* [67] was extended by adding a second refocusing pulse each, so that four echos are acquired in total. In the first Multiple Spin Echo (MSE) acquisition, the evolution time in Figure 4.2 (A) is set to zero ($\tau = 0$) and in the second *MSE* acquisition, both echos are shifted, so that the evolution times τ_1 and τ_2 in Figure 4.2(A) fulfills the condition $\tau_2 = 2\tau_1$. Out of this, ΔB_0 can be estimated, but also the current orientation of the transverse $\overrightarrow{M}_\perp$ in the second acquisition, to determine if unwrapping is necessary. With that, the maximum resolvable ΔB_0 can be increased by a factor of two. To further extend the applicability of this method, an improvement was presented in Szumowski et al. [291] by the application of a 2D region growing phase unwrapping algorithm dedicated to Dixon based fat/water separation [292]. A similar approach was presented by Szumowsiu and Plewes [290], where phase cycling of the excitation pulse (0° and 180°) in combination with a dedicated timing scheme was applied to gain more information about the underlying field inhomogeneity. First and second echo of a single *SE* sequence are shifted by ΔT_F with respect to each other, but in both cases fat and water magnetization have an arbitrary orientation in the transverse plane. By using four acquisitions with the same scheme, also T_2^* compensation in the fat component can be reached. A further improvement was presented by Williams et al. [321], where a four echo *MSE* sequence was utilized to acquire the necessary data for ΔB_0 field estimation and the correction of B_1 introduced phase errors, because of multiple refocusing.

Another method, known as the three-point Dixon method, was first introduced by Kim et al. [157] and Lodes et al. [191]. The basic idea of three-point Dixon is to extend the initially proposed in-phase S_0 and opposed phase S_{180} acquisition [67] by and additional opposed phase acquisition, S_{-180}, where the echo is shifted in the opposite direction. According to Eq. (4.4), the signals are given as

$$\begin{aligned} S_0 &= (S_W + S_F)\, e^{j\phi_0}, && (4.13)\\ S_{180} &= (S_W - S_F)\, e^{j(\gamma\Delta B_0\tau+\phi_0)}, && (4.14)\\ S_{-180} &= (S_W - S_F)\, e^{j(-\gamma\Delta B_0\tau+\phi_0)}, && (4.15) \end{aligned}$$

so that the phase shift caused by the field inhomogeneity $\phi_{B_0} = \gamma\Delta B_0\tau$ can be estimated from S_{180} and S_{-180} as

$$\phi_{B_0} = \frac{1}{2}\angle\left(S_{180}\cdot\overline{S}_{-180}\right), \tag{4.16}$$

and ϕ_0 is given as the phase of S_0

$$\phi_0 = \angle S_0. \tag{4.17}$$

The estimates for ϕ_{B_0} and ϕ_0 can be used as a correction, so that S_W and S_F can be estimated according to Dixon [67]. To increase the *SNR* in the fat and water images, the following scheme was proposed by Glover and Schneider [95]

$$\begin{aligned} S_W &= \frac{1}{2}\left(S_0 e^{-j\phi_0} + \cos\left(\angle S_{-180}\cdot e^{j(\phi_{B_0}-\phi_0)}\right)\sqrt{S_{180}\cdot\overline{S}_{-180}}\right), && (4.18)\\ S_F &= \frac{1}{2}\left(S_0 e^{-j\phi_0} - \cos\left(\angle S_{-180}\cdot e^{j(\phi_{B_0}-\phi_0)}\right)\sqrt{S_{180}\cdot\overline{S}_{-180}}\right). && (4.19) \end{aligned}$$

Phase wrapping in ϕ_{B_0} is a serious problem for this method, making phase unwrapping unavoidable. Without phase unwrapping, the resonance offset would be restricted to $\gamma\Delta B_0 \leq \Delta\omega_F/2$. For this purpose, the three-point Dixon method was extended by a phase unwrapping algorithm [95], which is similar to an approach presented by Schneider and Glover [258] for B_0 shimming. More details on phase unwrapping are given in Section 2.4.1 and in a review given by Ma [199].

Glover further extended the three-point Dixon method to arbitrary phase shifts between fat and water and it was shown that an equal spread over the unit circle $\Theta = (0°, 120°, -120°)$ leads to the best *SNR* behavior and also overcomes the problem of signal dropout in voxels with equal fat and water contribution [94]. Furthermore, this method was extended by an additional T_2^* estimate determined out of the Dixon data. It was further shown by Coombs et al. [57] and Skinner and Glover [269] that the three point Dixon acquisitions are redundant and the necessary information for the correction of the ΔB_0 influence can be determined directly out of the two-point Dixon acquisition, as long as $S_W \neq S_F$. However, in this case the solution is given by $S_W = S_F = |S_0|/2$.

The three-point Dixon method was implemented within a Turbo Spin Echo (TSE) sequence [114], and an improved version with more efficient echo spacing was proposed by Ma et al. [200].

Another three-point Dixon algorithm was proposed by Wang et al. [315], where three *GRE* acquisitions are performed with a phase shift between fat and water of $\Theta = (0°, 180°, 360°)$. In *GRE* sequences, the echo at $\Theta = 0°$ cannot be sampled, hence, the first in-phase acquisition already has a phase difference of $\Theta = 360°$, but it can be treated as the $\Theta = 0°$ acquisition, because the necessary information is encoded in the phase difference. Here, a local phase unwrapping approach is proposed, where several phase consistency conditions between the $\Theta = 0°$ and the $\Theta = 360°$ acquisition were proposed, to determine if a phase unwrap is necessary or not. This extends the applicability to field inhomogeneities of $\gamma \Delta B_0 = 3\Delta\omega_F/2$. Furthermore, the applicability to 2D and 3D *GRE* sequences was shown.

Another two-point Dixon approach was presented by Xiang [324], where an in-phase and a partially opposed phase echo is acquired. The partially opposed phase condition ($\Theta < 180°$) enables the possibility to identify the fat and water signals after separation by utilizing a leading or lagging condition similar to the ideas described in Xiang and An [325]. After an initial phase correction and separation of the two signal components, two possible phasor candidates are estimated in each voxel, where phasor refers to the complex phase term associated to the ΔB_0 field variations ($e^{j\gamma\Delta B_0 \tau}$). The phasor selection is iteratively updated voxel by voxel on the basis of a local smoothing condition until no further changes occur.

Based on the ideas of Glover [94], an approach to jointly estimate fat and water images S_F and S_W, the main field inhomogeneity ΔB_0 and the relaxation rates R_2^* and R_2 from one single measurement was proposed by Ma et al. [204]. For this purpose, two monopolar *GRE* trains with an echo spacing of ΔT_F (see Eq. (4.1)) are acquired before and after an 180° refocusing pulse. The echo spacing is adjusted so that fat and water magnetization are alternating between in-phase and opposed phase orientation. It was further shown that this technique is able to determine the specific relaxation rates of both chemical compartment, fat and water, however, the *SNR* is quite poor.

4.1.3.3 Region Growing based Methods

Most of the methods described so far require a phase shift between fat and water of $\Theta = 180°$. In Xiang and An [325], the solution of the three-point Dixon acquisition was generalized to phase shifts $\Theta \neq 180°$. For that purpose, the separation result can be obtained as the solution of a quadratic equation, where only one of the two mathematically possible solutions is physically valid. The solution consists of two unambiguously resolved complex magnetization vectors $M_{\perp 1}$ and $M_{\perp 2}$, corresponding to those of fat and water, but it cannot be unambiguously resolved which one corresponds to which of the two chemical species. It was further shown that this problem can be solved without requiring phase unwrapping, if the phase shift between fat and water is restricted to $\Theta \neq 180°$, using the prior knowledge that fat has to be the leading vector because of its lower precession frequency. Because this approach only works if both components, fat and water, are present in each voxel, additionally a proper post procession was proposed on the basis of the smoothness assumption on the background field. A quantity proportional to the background field can be estimated out of $M_{\perp 1}$ and $M_{\perp 2}$ and the smoothness is enforced by a region growing algorithm, where fat and water are exchanged in the solution so that the voxel under investigation is most similar to its neighborhood. The region growing is performed several times with arbitrary chosen initial seed points and the final solution is that which occurs more often in each voxel. This approach only works if more than 50 % of the initially assigned voxels are correct. This is reached by assigning all "problematic" voxels to be water, because it is more likely in biological tissue to appear. Two acquisition schemes were proposed, the first one is optimal in terms of solution stability and phase error tolerance with $\Theta = (-90°, 90°, 270°)$, and the second one in terms of *SNR* with $\Theta = (0°, 120°, 240°)$.

Another region growing approach using a two-point Dixon *GRE* acquisition was presented by Ma [198], which is based on the spatial gradient of the phase image. After an initial phase correction, the problem is reduced to determining the correct sign of in the opposed phase acquisition, which is done on the basis of the average value in a region around the current seed point from voxels which have been already corrected. To avoid error propagation, most reliable voxels with a low spatial gradient in the signal phase are processed first. The most problematic point is the selection of the initial seed point, which could lead to an error propagation, but no further details were reported. This approach was further applied to a *TSE* acquisition by Ma et al. [201], where both echos (in-phase and opposed phase) are acquired inbetween each 180° refocusing pulse, similar to Gradient and Spin Echo (GRASE). This method was further combined with a Sensitivity Encoding (SENSE) based accelerated acquisition (see Section 3.1.2.1). In Ma et al. [203], this *TSE* approach was further extended to a three-point Dixon acquisition. In Berglund et al. [15], the region growing method from Ma [198] was extended to be applicable to 3D volumes, and an initial seed point selection based on a combination of magnitude weight and a phasor reliability measure was reported. Furthermore, a general solution for three-point Dixon acquisitions with equal echo spacing was presented and applied to whole-body fat/water imaging. The method of Ma [198] was further improved by a multi-resolution approach by Schmidt and Fraser [256], to increase its robustness against noise.

4.1.3.4 Iterative Decomposition and Variants of IDEAL

An alternative approach to solve the fat/water separation problem was presented by Reeder et al. [242], for an arbitrary number of acquisitions with arbitrary fat/water phase shifts Θ_n. An iterative solution of Eq. (4.4) was proposed, which is obtained independently in each voxel. Knowing ΔB_0, Eq. (4.4) gets linear and a voxel wise solution can be obtained in a least squares sense. Therefore, an initial guess for ΔB_0 has to be obtained, here $\Delta B_0 = 0$, to calculate an initial estimate for S_W and S_F. After linearizing Eq. (4.4) using a Taylor series expansion, the error term for all unknowns ΔS_W, ΔS_F, and $\Delta(\Delta B_0)$ can be obtained again by a least squares solution, leading to a new estimate for ΔB_0. This is repeated until a convergence occurs, i.e., the update falls under a certain threshold. As already mentioned, the inversion of Eq. (4.4) is ill-posed, even without noise. This is because of the joint estimation of S_W, S_F, and ΔB_0 and the consequent periodicity, i.e., exchanging S_F and S_W and setting $\gamma \Delta B_0 \tau = \gamma \Delta B_0 \tau + 2\pi$ leads to exactly the same measurement data. According to Yu et al. [332], if an arbitrary number of echos N_S with non-equidistant echo spacing is acquired, the cost function gets aperiodic, but still showing an infinite number of local minima, as shown in Figure 4.4. Therefore, the solution of the iterative algorithm strongly depends on its initialization. If it is initialized too far from the true solution, the algorithm will get stuck in such a local minimum. To improve this behavior, a region growing approach in combination with the iterative solution of Reeder et al. [242] was proposed by Yu et al. [332], where the initial guess for every voxel is calculated by a 2D linear fit, estimated from the already processed surrounding. Here, the crucial point is again the selection of a proper starting point. The selection is performed on a down-sampled low resolution image out of those voxels which have a field map value close to the median of all voxels, which are above a certain magnitude threshold. Out of these voxels, that one closest to the center of the image is selected. It was shown that this combination of iterative solution [242], region growing [332], and a noise optimal selection of the fat/water phase shifts Θ_n, described by Reeder et al. [240] (see Section 4.1.3.5) leads to a substantially improvement to unambiguously resolve the fat and water signal. Usually, this technique is referred to as *IDEAL*.

Several improvements or extension to *IDEAL* were proposed. *IDEAL* was successfully applied to *GRE* acquisitions by Reeder et al. [239], where the influence of ΔB_0 is usually more severe. *IDEAL* was further extended by Yu et al. [331] for the additional estimation of an R_2^* map, out of the multiecho *GRE* acquisition. For this purpose, a "complex" field map $\hat{\psi} = \gamma \Delta B_0 + jR_2^*$ was introduced, so that the same iterative solution of Reeder et al. [240] can be applied. The *IDEAL* method was further combined with a homodyne reconstruction by Reeder et al. [237], to be able to reconstruct partial Fourier data from asymmetric echos, to increase the flexibility of selection different echo spacings. Furthermore, *IDEAL* was also combined with a *GRASE* sequence in Li et al. [183], to decrease acquisition time with integrated eddy current compensation. *IDEAL* was also successfully applied to cardiac imaging also by Reeder et al. [238], using a steady state free precession sequence. To further increase the separation accuracy, the multipeak fat model, from Eq. (4.5), was also included into the *IDEAL* algorithm by Yu et al. [334].

4.1.3.5 General Aspects

Noise Behavior: To describe the noise behavior of the individual fat and water images, the quantity Number of Signal Averages (NSA) was introduced by Glover and Schneider [95] defined as

$$\mathrm{NSA} = \frac{\sigma^2_{W,F}}{\sigma^2_0}, \tag{4.20}$$

where $\sigma^2_{W,F}$ and σ^2_0 are the noise variances of the individual fat/water images and the individual acquisitions, respectively. It was shown that $\mathrm{NSA} = 2.67$ can be achieved for the initially proposed three point Dixon scheme with fat/water shifts of $\Theta = (0°, 180°, -180°)$, which is slightly lower than the theoretical maximum of $\mathrm{NSA} = 3$. In [94], the *NSA* was increased to the theoretical maximum by equally spreading the acquisitions around the unit circle with phase shifts of $\Theta = (0°, 120°, -120°)$. However, it was shown by Pineda et al. [230] that the *NSA* also strongly depends on the fat/water ratio, so that these considerations are only true for voxels only containing either fat or water. For $S_F \approx S_W$, the *NSA* even drops to $\mathrm{NSA} \approx 0$ for acquisition schemes symmetrically around zero. Therefore, an acquisition scheme was introduced by Reeder et al. [240], to maximize the *NSA* independent of the fat/water content, which is given for phase shifts of $\Theta = -30° + k \cdot 180°, 90° + k \cdot 180°, 210° + k \cdot 180°$, where k is an arbitrary integer value. This is also a beneficial result for *GRE* acquisitions, where the $\Theta = 0°$ data point cannot be sampled.

Sequences and Acquisition: The early Dixon based approaches are all based on *SE* sequences because of their higher robustness against background field variations. At the time of the *SE*, a complete refocusing of background field and chemical shift induced dephasing occurs. At this point, a real in-phase acquisition can be performed and the effect of ΔB_0 deviation is restricted to the echo shift time or evolution time τ (see Figure 4.2(A)). However, the use of *GRE* sequences is beneficial, because of the potential of multiecho acquisition and the, in general, lower acquisition times. Most of today's available state of the art methods are based on *GRE* sequences, where its applicability was initially shown by [239, 315]. Furthermore, the applicability to *TSE* was shown in [114, 200, 203, 242] and to steady state free precession in [131, 242]. Also non Cartesian trajectories were investigated and the applicability of spiral [215, 216] and radial trajectories [13] was shown.

4.1.3.6 Recent Developments

Most of the previously described methods are restricted to a specific number of echos with a specific timing (phase shifts Θ_n), giving an analytic solution for this specific configuration. The introduction of *IDEAL* and its variants enabled the possibility to use arbitrary echo times [239, 242], because of the formulation of the signal separation as optimization problem. As for all previously described methods, the solution is still obtained voxel by

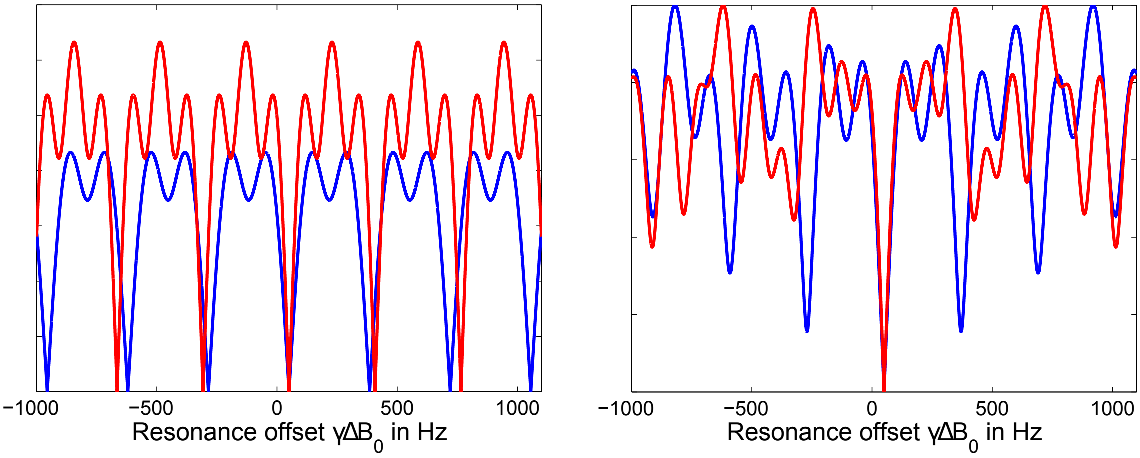

Figure 4.4: (Left) Residuum $\mathtt{R}(\Delta B_{0,q}) = \mathcal{D}_q(\Delta B_{0,q})$ in a single voxel for constant echo spacing $\Delta\tau$. Values are simulated at 3 T with a resonance offset $\gamma\Delta B_0 = 2\pi \cdot 50\,\text{Hz}$ with 3 simulated echos (blue line) with $\tau = [0\,\text{ms}, 3\,\text{ms}, 6\,\text{ms}]$ and with 4 simulated echos (red line) with $\tau = [0\,\text{ms}, 2.8\,\text{ms}, 5.6\,\text{ms}, 8.4\,\text{ms}]$. The cost function is periodic with $\frac{1}{\Delta\tau}$ and the number of local minima in one period depends on the number of acquired echos N_S. (Right) Residuum $\mathtt{R}(\Delta B_{0,q}) = \mathcal{D}_q(\Delta B_{0,q})$ in a single voxel for non-equidistant echo spacing. Values are simulated at 3 T with a resonance offset $\gamma\Delta B_0 = 2\pi \cdot 50\,\text{Hz}$ with $\tau = [0.2\,\text{ms}, 3\,\text{ms}, 6.3\,\text{ms}]$ (blue line) and with $\tau = [1.6\,\text{ms}, 3.1\,\text{ms}, 5.7\,\text{ms}]$ (red line)

voxel, so that the incorporation of global image priors is not possible. However, it is tried to apply some smoothness constraints on the ΔB_0 field distribution, mostly by either a smoothing operation, i.e., a convolution kernel, and subsequent recalculation of fat and water content [242], or by region growing approaches [198, 332]. These region growing approaches are heuristic and depend highly on the initial seed voxel and on the voxel processing order. Iterative methods, as *IDEAL*, suffer from getting stuck in a local minimum and depend highly on the initialization. However, the initialization with a smooth field map, as proposed by Yu et al. [332], does not guarantee neither the convergence to the optimal solution nor the achievement of a smooth field map.

With the introduction of a new method by Hernando et al. [122] in 2008, a change in paradigm takes place, where methods started to develop trying to minimize a global cost function in terms of the whole field map $\mathbf{\Delta B_0}(\vec{r})$ and the whole water and fat images $\mathbf{S}_W(\vec{r})$ and $\mathbf{S}_F(\vec{r})$, respectively, as it is done in variational modeling. Using this formulation, the incorporation of global image priors to enforce certain properties, especially on the field map, gets possible. In the following, the bold notation is used when referring to the whole image or field map ($\mathbf{\Delta B_0}(\vec{r})$, $\mathbf{S}_W(\vec{r})$ and $\mathbf{S}_F(\vec{r})$) and the normal notation ($\Delta B_{0,q}$, $S_{F,q}$ and S_{W_q}) when referring to one value at a certain voxel q. Similar to image reconstruction, the cost function $J(\mathbf{\Delta B_0}(\vec{r}), \mathbf{S}_W(\vec{r}), \mathbf{S}_F(\vec{r}))$ consists of a data fidelity term $\mathcal{D}(\mathbf{\Delta B_0}(\vec{r}), \mathbf{S}_W(\vec{r}), \mathbf{S}_F(\vec{r}))$ and regularization terms for all three unknown quantities $\mathcal{R}_1(\mathbf{\Delta B_0}(\vec{r}))$, $\mathcal{R}_2(\mathbf{S}_W(\vec{r}))$ and $\mathcal{R}_3(\mathbf{S}_F(\vec{r}))$ in general. Skipping the explicit notation of spatial dependency $(\vec{r})$, the cost function in its most general form can be written as

$$J\left(\Delta\mathbf{B_0}, \mathbf{S}_W, \mathbf{S}_F\right) = \mathcal{D}(\Delta\mathbf{B}_0, \mathbf{S}_W, \mathbf{S}_F) + \lambda_1\mathcal{R}_1(\Delta\mathbf{B_0}) + \lambda_2\mathcal{R}_2(\mathbf{S}_W) + \lambda_3\mathcal{R}_3(\mathbf{S}_F), \tag{4.21}$$

where λ_1, λ_2 and λ_3 are regularization parameters balancing between data fidelity and each regularization term. The solution is given as

$$\left(\Delta\hat{\mathbf{B}}_\mathbf{0}, \hat{\mathbf{S}}_W, \hat{\mathbf{S}}_F\right) = \arg\min_{\Delta\mathbf{B_0}, \mathbf{S}_W, \mathbf{S}_F} J\left(\Delta\mathbf{B_0}, \mathbf{S}_W, \mathbf{S}_F\right). \tag{4.22}$$

This optimization problem is highly non-convex and non-linear, making it very hard to solve. Therefore, it has to be simplified to make it mathematically solvable. First of all, it can be shown that the optimization can be decoupled between the estimation of the water/fat images and the field map. The same local minima are obtained in the data fidelity term independent of the actual fat and water concentration. This is known as Variable Projection (VARPRO) and was first introduced by Hernando et al. [122] based on the mathematical foundation in [29, 96]. Furthermore, the regularization of $\mathbf{S}_W$ and $\mathbf{S}_F$ is usually removed, so that the optimization problem can be reduced to one only depending on $\Delta\mathbf{B_0}$, leading to a reduction in dimensions by a factor of three. With that, the optimization problem writes as

$$\Delta\hat{\mathbf{B}}_\mathbf{0} = \arg\min_{\Delta\mathbf{B_0}} \mathcal{D}(\Delta\mathbf{B_0}, \mathbf{S}_W, \mathbf{S}_F) + \lambda\mathcal{R}(\Delta\mathbf{B_0}), \tag{4.23}$$

where $\mathbf{S}_W$ and $\mathbf{S}_F$ in the data fidelity term are treated as constants, as explained later. Having a closer look at the data fidelity term in each voxel, by using the signal model from Eq. (4.4), the signal $S_{n,q} = S_q(\tau_n)$ in each voxel for N_S acquired echos at different evolution times τ_n can be written as

$$\underbrace{\begin{pmatrix} S_{1,q} \\ \vdots \\ S_{N_S,q} \end{pmatrix}}_{\mathbf{S}} = \underbrace{\begin{pmatrix} e^{j\gamma\Delta B_{0,q}\tau_1} & 0 & 0 \\ 0 & \ddots & 0 \\ 0 & 0 & e^{j\gamma\Delta B_{0,q}\tau_{N_S}} \end{pmatrix}}_{\mathbf{T}(\Delta B_{0,q})} \underbrace{\begin{pmatrix} 1 & e^{j\Delta\omega_F\tau_1} \\ \vdots & \vdots \\ 1 & e^{j\Delta\omega_F\tau_{N_S}} \end{pmatrix}}_{\mathbf{K}(\Delta\omega_F)} \underbrace{\begin{pmatrix} S_{W,q} \\ S_{F,q} \end{pmatrix}}_{\mathbf{S}_{W,F,q}}. \tag{4.24}$$

In any state of the optimization, an estimate for $S_{W,q}$ and $S_{F,q}$ can be obtained as the least squares solution of Eq. (4.24), where $\mathbf{S}_q$ is a vector containing the measured signals values at echo times $\tau_1 \dots \tau_{N_S}$ in voxel q and the known chemical shift $\Delta\omega_F$. The solution writes as

$$\mathbf{S}_{W,F,q}(\Delta B_{0,q}) = \left(\mathbf{K}^H\mathbf{K}\right)^{-1}\mathbf{K}^H\left(\mathbf{T}(\Delta B_{0,q})\right)^{-1}\mathbf{S} = \mathbf{K}^\dagger\mathbf{T}(-\Delta B_{0,q})\mathbf{S}_q, \tag{4.25}$$

where $\mathbf{K}^\dagger$ is the pseudo-inverse of $\mathbf{K}$. Because of its form as diagonal matrix having complex exponentials in its diagonal, the inverse of the matrix $\mathbf{T}$ can be simply calculated by using the negative value of $\Delta B_{0,q}$ in each voxel. Using this formalism, $S_{W,q}$ and $S_{F,q}$ can be complex, because $\phi_{0,q}$ is not considered explicitly. According to Section 3.2.2, the L_2 norm is a suitable distance measure for the data fidelity term in the presence of Gaussian noise, which is the case for complex *MR* data, so that the global data fidelity term can be written as

$$\mathcal{D}(\Delta\mathbf{B_0}) = \sum_{q=1}^{N_x N_y N_z} \left\| \left(\mathbf{I} - \mathbf{K}\mathbf{K}^{\dagger}\right) \mathbf{T}(-\Delta B_{0,q})\mathbf{S}_q \right\|_2^2 = \sum_{q=1}^{N_x N_y N_z} \mathtt{R}_q \left(\Delta B_{0,q}\right)^2, \tag{4.26}$$

where $\mathtt{R}_q(\Delta B_{0,q})$ is the residuum for the current instance of $\Delta B_{0,q}$ in voxel q. The deviation here, based on Eq. (4.24), is done for the most simple signal model, the single peak fat model with neglected R_2^*. However, R_2^* and the multipeak model from Eq. (4.5) can be easily incorporated by simple modifications of the matrices $\mathbf{T}$ and $\mathbf{K}$

$$\mathbf{T} = \begin{pmatrix} e^{\left(j\gamma\Delta B_{0,q} - R^*_{2,q}\right)\tau_1} & 0 & 0 \\ 0 & \ddots & 0 \\ 0 & 0 & e^{\left(j\gamma\Delta B_{0,q} - R^*_{2,q}\right)\tau_{N_S}} \end{pmatrix}, \tag{4.27}$$

$$\mathbf{K} = \begin{pmatrix} 1 & \sum_{m=1}^{N_F} \alpha_m e^{j\Delta\omega_{F,m}\tau_1} \\ \vdots & \vdots \\ 1 & \sum_{m=1}^{N_F} \alpha_m e^{j\Delta\omega_{F,m}\tau_{N_S}} \end{pmatrix}. \tag{4.28}$$

Allowing arbitrary, non-equidistant echo spacing, the data fidelity term of the cost function gets non-periodic, so that a global optimum exist. However, this global optimum is still hard to find because of the infinite number of local minima. By restricting the echo spacing to be equally spaced, the data fidelity term of the cost function gets periodic, so that no global optimum exists. This behavior is shown in Figure 4.4. Despite this behavior, most methods are restricted to equidistant echo spacing, because it leads to a mathematically favorable structure, which can be easily solved so that the advantages of equal echo spacing are predominant. Furthermore, it is not restricted to, but usually only three echos are acquired ($N_S = 3$), because it is sufficient to resolve the three unknowns and the noise optimal phase angles between water and fat from Reeder et al. [240] can be applied. With this, Eq. (4.24) can be rewritten as

$$\underbrace{\begin{pmatrix} S_{1,q} \\ S_{2,q} \\ S_{3,q} \end{pmatrix} e^{-j\angle S_{1,q}}}_{\mathbf{S}'_q} = \underbrace{\begin{pmatrix} 1 & 0 & 0 \\ 0 & e^{j\gamma\Delta B_{0,q}\Delta\tau} & 0 \\ 0 & 0 & e^{j\gamma\Delta B_{0,q}2\Delta\tau} \end{pmatrix}}_{\mathbf{T}'(\Delta B_{0,q})} \underbrace{\begin{pmatrix} 1 & e^{j\Delta\omega_F\tau_1} \\ 1 & e^{j\Delta\omega_F\tau_2} \\ 1 & e^{j\Delta\omega_F\tau_3} \end{pmatrix}}_{\mathbf{K}(\Delta\omega_F)} \underbrace{\begin{pmatrix} S_{W,q} \\ S_{F,q} \end{pmatrix}}_{\mathbf{S}_{W,F,q}}, \tag{4.29}$$

where the signals in $\mathbf{S}'_q$ are corrected by the phase of the first echo. With that, the data fidelity term can be rewritten as

$$\mathcal{D}(\Delta\mathbf{B_0}) = \sum_{q=1}^{N_x N_y N_z} \left\| \left(\mathbf{I} - \mathbf{K}\mathbf{K}^\dagger\right) \begin{pmatrix} 1 & 0 & 0 \\ 0 & e^{-j\gamma\Delta B_{0,q}\Delta\tau} & 0 \\ 0 & 0 & e^{-j\gamma\Delta B_{0,q}2\Delta\tau} \end{pmatrix} \mathbf{S}'_q \right\|_2^2 . \tag{4.30}$$

Rearranging everything with

$$\mathbf{M}_q = \left(\mathbf{I} - \mathbf{K}\mathbf{K}^\dagger\right) \begin{pmatrix} S'_{1,q} & 0 & 0 \\ 0 & S'_{2,q} & 0 \\ 0 & 0 & S'_{3,q} \end{pmatrix}, \qquad z_q = e^{j\gamma\Delta B_{0,q}\Delta\tau}, \tag{4.31}$$

the data fidelity term can be written in its most condensed form, which is the basis for the polynomial approach, written as

$$\mathcal{D}(\Delta\mathbf{B_0}) = \sum_{q=1}^{N_x N_y N_z} \left\| \mathbf{M}_q \underbrace{\begin{pmatrix} z_q^0 \\ z_q^{-1} \\ z_q^{-2} \end{pmatrix}}_{\mathbf{z}_q} \right\|_2^2 . \tag{4.32}$$

The data fidelity term of the cost function is non-convex and periodic in $\Delta\omega_0 = \gamma\Delta B_0$ with a periodicity of $\frac{2\pi}{\Delta\tau}$ and has $(N_S - 1)$ local minima in each period (see Figure 4.4), so that gradient based methods would fail solving this problem. One period is often referred to as spectral *FOV*. To solve this kind of problem, all local minima of $\mathcal{D}_q$ in each voxel are determined and periodically extended over an expected range of ΔB_0 variation $(-\Delta\omega_{0,\max} \le \frac{\gamma\Delta B_0}{2\pi} \le \Delta\omega_{0,\max})$, with typical values for $\Delta\omega_{0,\max} = 2\pi \cdot (1000\,\text{Hz to } 2000\,\text{Hz})$. The determination of the local minima of $\mathcal{D}_q$ can be done by a brute force search, which is feasible because of the 1D search direction, but a more elegant and efficient way can be achieved with the formulation in Eq. (4.31). With that, the data fidelity term of each voxel $\mathcal{D}_q$ can be written as a polynomial of degree $2(N_S - 1)$, given as

$$\begin{aligned} \mathcal{D}_q(\Delta B_{0,q}) = \mathbf{z}_q^H \mathbf{M}_q^H \mathbf{M}_q \mathbf{z}_q = \sum_{n=-2(N_S-1)}^{0} \kappa_{n,q} z_q^n = \\ = \sum_{n=-2(N_S-1)}^{0} \kappa_{n,q} \left(e^{j\gamma\Delta B_{0,q}\Delta\tau}\right)^n , \end{aligned} \tag{4.33}$$

with the polynomial coefficients $\kappa_{n,q}$, which can be determined from the diagonals of $\mathbf{M}_q^H\mathbf{M}_q$. The minima are obtained by setting the first derivative with respect to $\Delta B_{0,q}$ to zero, given as

$$\frac{d\mathcal{D}_q(\Delta B_{0,q})}{d\Delta B_{0,q}} = j\gamma\Delta\tau \sum_{n=-2(N_S-1)}^{0} \kappa_{n,q} \left(e^{j\gamma\Delta B_{0,q}\Delta\tau}\right)^n = 0, \tag{4.34}$$

which is equivalent of finding the $2(N_S - 1)$ complex roots of the polynomial. Each complex root corresponds to one of the $2(N_S-1)$ extreme points in each period. The (N_S-1) minima can by found by applying the second derivative or by checking the local neighborhood, with the corresponding field values $\Delta B_{0,q,k}$ with $k \in [0,(N_S-1)]$. This polynomial formalism was first introduced by Doneva et al. [68]. With that the optimization problem reduces to selecting the right local minimum in the range $[-\Delta\omega_{0,\max}, \Delta\omega_{0,\max}]$ and can be written as

$$\Delta\hat{\mathbf{B}}_\mathbf{0} = \arg\min_{\Delta B_{0,q}\in\Omega_q} \sum_{q=1}^{N_xN_yN_z} \left\| \left(\mathbf{I} - \mathbf{K}\mathbf{K}^\dagger\right) \mathbf{T}'(-\Delta B_{0,q})\mathbf{S}'_q \right\|_2^2 + \lambda\mathcal{R}(\Delta\mathbf{B}_\mathbf{0}), \tag{4.35}$$

where Ω_q is defined as the solution space of all local minima of $\mathcal{D}_q$ in each voxel, given as

$$\Omega_q = \left\{ \left|\gamma\Delta B_{0,q,k} + l\frac{2\pi}{\Delta\tau}\right| \leq \Delta\omega_{0,\max} \quad \forall \quad k\in[0,(N_S-1)], \quad l\in(-\infty,\infty) \right\}. \tag{4.36}$$

Even though the solution space can be reduced drastically, the combinatorial complexity is far too high for a brute force search. Therefore, many methods were proposed to solve this problem, which mostly differ in the explicit formulation of $\mathcal{R}$ and the solution strategy.

One of the first methods based on this idea was presented by Hernando et al. [122], where the voxel wise global minimum of the data fidelity term in Eq. (4.26) is obtained by an exhaustive search over one period. This is used as initialization for the subsequent optimization, which is calculated for each voxel q by using an iterated conditional modes algorithm and is given as

$$\Delta B_{0,q}^{new} = \arg\min_{\Delta B_{0,q}} \mathcal{D}(\Delta B_{0,q}^{old}) + \lambda \sum_{j\in\delta_q} w_{q,j}(\Delta B_{0,q}^{old} - \Delta B_{0,j}^{old})^2, \tag{4.37}$$

where $\Delta B_{0,j}^{old}$ is the current field estimate in the neighborhood δ_q of voxel q, which is set to a 5×5 kernel centered at voxel q. $w_{q,j}$ is a weighting factor set to the inverse distance between voxel q and j. This image prior penalizes high differences between the field estimates in the local neighborhood. This step is repeated for each voxel until the L_1 norm of the change in the field map is smaller than a predefined threshold. An improved version of this was presented by Hernando et al. [121, 123] by utilizing the same image prior, but using a global cost function (extending Eq. (4.37) by a sum over all voxels), so that all voxels can be updated simultaneously in each iteration. For this purpose, an update step is calculated on the basis of the local minima in each voxel $\Delta B_0^{old} \rightarrow \Delta B_0^{new}$. The optimization in each voxel is reduced to a binary decision problem, where the algorithm has to decide for each voxel if the update is accepted or not, to minimize the total cost function. This problem has $2^{N_x N_y N_z}$ possible solutions, which can be efficiently solved by a graph cut based algorithm. The local minima in each voxel are determined by an exhaustive search over one period, which is periodically extended to cover a wider range of inhomogeneity. With that a much higher degree of field inhomogeneity can be captured than with the voxel wise solution. In Berglund et al. (2011) [14], an approach based on the same image prior was proposed for a two-point Dixon acquisition and the approach from Hernado et al. [123] was extended to 3D data with joint R_2^* estimation by Berglund et al. (2012) [16].

A completely different approach, based on the ideas described above, was presented by Lu and Hargreaves [192], where the local minima in each voxel are obtained by a golden section search over one period, which is more efficient than the exhaustive search approach. After selecting a suitable starting point, which has to fulfill some criterions, the final field map is calculated by a region growing approach, where the starting voxel serves as initial contour. A voxel value in contour $n+1$ is given by its local minimum (including periodic extensions) closest to the value of the nearest voxel of contour n. For efficient calculation a multi-resolution approach is applied. This is a kind of intermediate method, utilizing the cost function approach, but spatial regularity is incorporated by region growing. Compared to the region growing approach from Yu et al. [332], this method is able to capture a wider range of field inhomogeneity.

Another approach was presented by Jacob and Sutton [136], where the local minima are determined by a polynomial approach similar to that presented here. The total field map is obtained by applying H_1 regularization (see Section 3.2.4.2), meaning selecting those local minima in each voxel, minimizing the H_1 functional. Because of the computational complexity, the solution is obtained by a region merging approach. For that purpose, the field map is subdivided into a certain number of connected regions depending on the current phase. Afterwards, region pairs are merged sequentially, so that the overall cost function is reduced. This is based on the assumption that the same local minimum has to be selected in the connected initial regions. A similar approach was presented by Lu et al. [193], where the image prior introduced in Eq. (4.37) is used to determine locally connected smooth regions as initial estimate. Compared to the method of Jacob and Sutton [136], where only smooth regions falling into the same spectral *FOV* can be determined, this approach is able to determine connected smooth regions over more than one period, so that the number of initial regions can be decreased. Furthermore, a consistency measure was introduced, where two neighboring voxels p and q are considered as consistent if the condition

$$|\Delta B_{0,p} - \Delta B_{0,q}| \leq \max\left(\min_{\Delta B_{0,j} \in \Omega_q} |\Delta B_{0,p} - \Delta B_{0,j}|, \min_{\Delta B_{0,j} \in \Omega_p} |\Delta B_{0,j} - \Delta B_{0,q}| \right) \tag{4.38}$$

is fulfilled. Here, Ω_p and Ω_q are the sets of feasible field map values (local minima) in voxel p and q, respectively. The regions are merged by selecting that local minimum over the whole region, so that the number of inconsistent voxels is minimized along the region boundaries. The advantage of this method is that no explicit smoothness constraint is applied to the field map, only inconsistent voxels along the boundary are penalized.

Fat/water separation was also combined with undersampling by Doneva et al. [68], using the Compressed Sensing (CS) approach described in Section 3.2.8. Here, in addition to the sparsifying transform in S_W and S_F, also a smoothness constrained is applied to the field map in form of the second order spatial derivative. This leads to an optimization problem with data fidelity term and three regularization terms as stated in Eq. (4.21). The data fidelity term has to be extended by the discrete Fourier operator $\mathcal{F}$. This minimization problem is solved by iterative linearization around the current estimate for S_W, S_F and ΔB_0 using a Taylor series expansion. It is solved for the update step utilizing a modified Conjugate Gradient (CG) algorithm. Because this gradient based optimization is prone to stuck in local minima, it relies on a stable initialization for the field map. This initialization can be derived as a low resolution estimate from the Auto Calibration Lines (ACLs) in k-space center or by applying *CS* separately to each of the acquired images. The solution space is further restricted to the local minima of the cost function in each voxel and the initial estimate is obtained by a region growing similar to Lu and Hargreaves [192]. As a final step, the obtained solution is back projected to the acquired k-space samples, such that final solution is given after an additional last iteration step. This approach was further extended by a more sophisticated field map estimation described by Sharma et al. (2012) [266]. For that purpose, the field map estimate is restricted to be in a certain subspace avoiding getting stuck in local minima. During the iteration, this restriction is step-wise relaxed to allow a better solution. This method was further improved by Sharma et al. (2013) [267], with an extension to Parallel Imaging (PI) and the use of B-splines to stabilize the field map estimate. Wiens et al. [320] further extended the *CS* framework by an additional R_2^* estimation. Also a direct k-space formulation was proposed by Honorato et al. [128] to account for phase accumulation during readout.

Tsao and Jiang proposed a hierarchical approach, without an explicit image prior [297]. The global cost function Eq. (4.26) is solved for ΔB_0 for different regions of the image. In the first iteration, the region contains the whole image, so that only one field offset value is calculated. In the subsequent iteration, the image is continuously subdivided into overlapping regions where again one field offset value is calculated for each region. The calculation is initialized with the value obtained in the previous larger region and solved with a gradient free Nelder-Mead algorithm. If the finest level is reached, the field map is smoothed by a convolution kernel and S_W and S_F are calculated according to Eq. (4.25). The main advantage of this method is its computational efficiency.

A completely different approach was presented by Yu et al. (2012) [333]. Here, the separation process is based on the assumption that the multipeak model from Eq. (4.5) fits better in fat dominant voxels than the single peak model from Eq. (4.4), whereas the single peak model leads to a lower residuum Eq. (4.26) (better fit) in water dominant voxels.

Based on these residuals, a normalized fat likelihood map is calculated in the range of $[-1, +1]$, where -1 is the maximum water and $+1$ the maximum fat likelihood. Likelihood values around zero indicate no clear distinction due to noise or partial volume effects. With this distinction, a good first estimate for S_W, S_F and ΔB_0 can be calculated. Starting at the voxel with the maximum likelihood value, a field smoothness map is calculated by a region growing approach, so that the value decreases at every discontinuity. The average field map value in the neighborhood of each voxel weighted by fat likelihood, smoothness map and signal magnitude is calculated. If the actual field map deviation is greater than a certain threshold it has to be recalculated. After a few iterations a valid field map can be obtained. The main advantage of this method is the availability of two independent reliability measures, fat likelihood and field smoothness.

Another promising algorithm was presented by Soliman et al. [276, 277], where the field map estimation is performed by a labeling approach, using the multi-label Potts model known as Max-*IDEAL*. For this purpose, the whole range of expected field variations is discretized using M points $\Delta B_{0,m}$, where $\Delta B_{0,1} = -\Delta B_{0,\max}$ and $\Delta B_{0,M} = \Delta B_{0,\max}$, with i.e., $M = 50$. The labeling procedure assigns every voxel a label $m \in [1, M]$, so that the image is subdivided into M non-overlapping regions $\mathcal{C}_m$. The Potts model is a labeling approach which minimizes the total perimeter of all single-label regions. This constraint implicitly enforces the required smoothness of the field map. The optimal labeling is given as

$$\min_{\{\mathcal{C}_m\}_{m=1}^{M}} \sum_{m=1}^{M} \int_{\mathcal{C}_m} \mathcal{D}(\Delta B_{0,m}, \vec{r}) d\vec{r} + \lambda \sum_{m=1}^{M} |\partial \mathcal{C}_m|, \tag{4.39}$$

where $|\partial \mathcal{C}_m|$ is the perimeter of $\mathcal{C}_m$. This problem is approximated with its convex relaxation, so that a global convergence can be reached. Furthermore, it can be solved efficiently by using the continuous “max flow” approach, which is the dual formulation to the convex relaxation of the model. With that, a very rough initial field estimate can be obtained, which is further refined by applying the gradient based *IDEAL* algorithm, which converges to the closest local minimum of the data fidelity term $\mathcal{D}(\Delta B_0)$. This approach is capable of detecting regions with high change rates in ΔB_0, which is important in regions around air-tissue interfaces.

An improvement of the graph-cut algorithm from Hernando et al. [123] was presented by Cui et al. (2015) [60], known as Globally Optimal Surface Estimation (GOOSE), where the explicit smoothness prior in the initial unconstrained formulation is replaced by constraints on the field map. The constraint in each voxel is defined as

$$\max \left\{ \left| \nabla^{+}_{xyz} \left(\Delta B_0(\vec{r}) \right) \right| \right\} \leq b. \tag{4.40}$$

This formulation leads to a much more efficient graph representation, leading to a graph optimization, which can be solved efficiently using an optimal surface segmentation algorithm. The main advantage of this method is that no iterative approximation is necessary and the convergence to the global optimum of the constraint optimization problem can be guaranteed. This algorithm was further improved by Cui et al. (2018) [59], to decrease the calculation time and to enable the ability to handle non-equidistant voxel sizes. A different improvement of the graph-cut approach is described by Berglund and Skorpil [17], where the graph-cut algorithm is combined with a multi-resolution approach to improve robustness.

In recent years, also classical region growing approaches gained renewed interest. An improved version of the quality guided region growing approach from Ma (2004) [198] was presented by Ma (2016) [202], including an additional segmentation for handling of spatially isolated objects. Cheng et al. proposed a multi-seed approach [52] with self-feeding phasor estimation combined with a multi-resolution region merging approach. The approach presented by Peng et al. [229] relies on the detection of fat/water transition regions by detecting sudden changes in the phasor map. The voxels in transition region are solved by choosing the smoothest phasor combination.

4.2 Quantitative MRI

Besides B_1 shimming (see Section 2.3.6) and Electrical Property Tomography (EPT), a very important application for B_1 mapping is the correction for flip angle variations in signal models used in quantitative MRI (qMRI), especially for the determination of T_1 and T_2 maps. The gold standard methods are the direct sampling of the T_1 recovery by an inversion recovery *SE* with different inversion times or the direct sapling of the T_2 decay by a *MSE* or a single *SE* sequence with different echo times. These methods require full relaxation between subsequent excitations TR $\geq 5T_1$, so that the resulting acquisition times are not clinically acceptable. Commonly used state of the art methods use *GRE* or balanced Steady State Free Precession (bSSFP) based sequences in the steady state [65], known as *VFA*, or during the transient after an inversion pulse [257]. These methods allow repetition times three orders of magnitude less than those necessary for using gold standard methods, bringing the acquisition times into a clinically acceptable range. Combined with acceleration strategies based on model based reconstruction for transient *bSSFP* [177] or for steady state *GRE* approaches [207–209], acquisition times in the order of 1 min for a 3D dataset with full brain coverage and 1 mm isotropic resolution are possible. However, these methods are based on signal models, which depend on the flip angle in a highly nonlinear manner. Even slight B_1 induced flip angle variations can lead to strong deviations in the resulting T_1 or T_2 maps due to error propagation. These errors are modeling errors and therefore they can be corrected if the actual flip angle in a certain voxel is known. Therefore, B_1 mapping is an essential prerequisite for these kind of methods. As an example, a T_1 map gained with the accelerated *VFA* approach from [209] is shown in Figure 4.5 with and without B_1 correction. An over- or underestimation of T_1 values can be observed in regions with high or low B_1 field values in the uncorrected map, whereas homogeneous T_1 values are achieved for a specific tissue with the correction of variations in the B_1 field. Exemplarily, the signal models used by Deoni et al. [65]

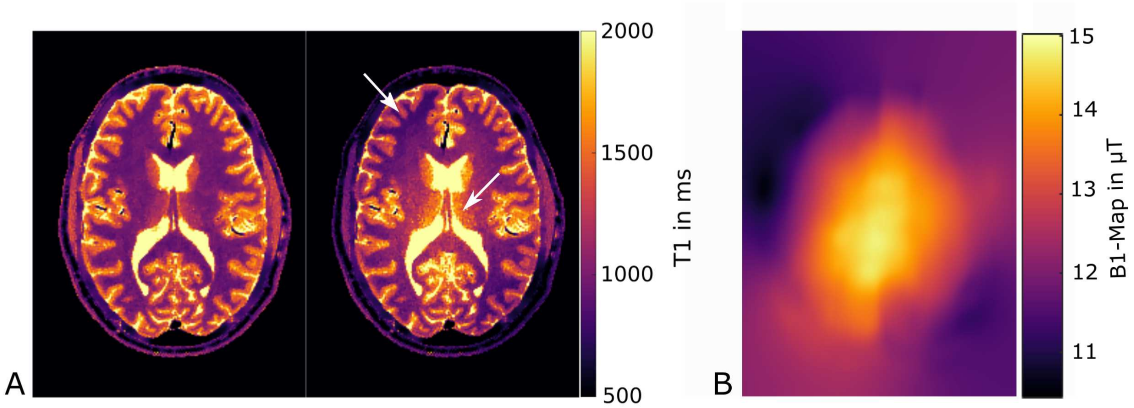

Figure 4.5: (A) T_1 map acquired with the accelerated VFA approach with regularized reconstruction from Maier et al. [209] with (left) and without (right) B_1 correction. A clear overestimation of T_1 in the white matter in the center of the brain and an underestimation in the gray matter of the frontal and prefrontal cortex can be seen (white arrows) in the uncorrected T_1 map. This corresponds well with the areas with high and low B_1 values in (B).

and Schmitt et al. [257] are shown. In [65], the steady-state signal equations for the *GRE* and *bSSFP* are used, where the signals S_{GRE} and S_{bSSFP} are given as

$$S_{\mathrm{GRE}} = M_0 \frac{(1-E_1)\sin(\alpha)}{1-E_1\cos(\alpha)}, \tag{4.41}$$

$$S_{\mathrm{bSSFP}} = M_0 \frac{(1-E_1)\sin(\alpha)}{1-E_1E_2-(E_1-E_2)\cos(\alpha)}, \tag{4.42}$$

with

$$E_{1,2} = e^{-\frac{\mathrm{TR}}{T_{1,2}}}. \tag{4.43}$$

The values for T_1 and T_2 are determined from different acquisitions with different flip angles α. The model used in Schmitt et al. [257] for the inversion recovery *bSSFP* transient is given by

$$T_1 = T_1^* \left[\cos^2\left(\frac{\alpha}{2}\right) + (A\cdot\mathrm{INV}+B)\sin^2\left(\frac{\alpha}{2}\right)\right], \tag{4.44}$$

$$T_2 = T_1^* \left[\sin^2\left(\frac{\alpha}{2}\right) + (A\cdot\mathrm{INV}+B)^{-1}\cos^2\left(\frac{\alpha}{2}\right)\right], \tag{4.45}$$

with

$$A = \frac{2\cos\left(\frac{\alpha}{2}\right)}{1-\cos(\alpha)}, \tag{4.46}$$

$$B = \frac{1+2\cos\left(\frac{\alpha}{2}\right)+\cos(\alpha)}{\cos(\alpha)-1}, \tag{4.47}$$

where T_1^* is the fitted time constant of the acquired transient and INV is the fitted inversion factor. In both cases the signal depends on the flip angle α in a highly non-linear manner.

In general, R_2^* mapping is performed by fitting a mono-exponential decay to a multiecho *GRE* acquisition, which is usually independent of α and B_1. However, it was shown in Söllradl et al. (2019) [274] that the gradient of the local ΔB_0 map highly influences the resulting R_2^* values. In 2D imaging, the effect is most severe in z-direction, because of the in general larger voxel dimensions. The model for correction, which is presented in this work, requires an accurate ΔB_0 map, which can be obtained directly from the acquired data for R_2^* mapping. Moreover, it was shown that also the influence of B_1^+ field variation leads to non-negligible errors for flip angles of $\alpha > 60°$. This is due to the non-linear relation between slice profile and α, influencing the decay rate, so that accurate B_1-mapping is required. In Söllradl et al. (2020) [275], a strategy is presented to compensate these effects to a certain degree, nevertheless B_1-mapping is still required.

5

Bloch–Siegert based B_1^+ Mapping

> A life spent making mistakes is not only more honorable, but more useful than a life spent doing nothing.
>
> *George Bernard Shaw*

This chapter is based on the following publication and proceedings:

- A. Lesch, A. Petrovic, and R. Stollberger. Robust implementation of 3D Bloch Siegert B1 mapping. In *Proceedings of the 23rd Annual Meeting of ISMRM, Toronto, Ontario, Canada*, page 2381, 2015
- A. Lesch, M. Schlögl, M. Holler, K. Bredies, and R. Stollberger. Ultrafast 3D Bloch–Siegert B_1^+-mapping using variational modeling. *Magnetic Resonance in Medicine*, 81(2):881–892, 2019. `doi:10.1002/mrm.27434`
- A. Lesch, C. S. Aigner, S. Spann, M. Schlögl, and R. Stollberger. 3D Bloch-Siegert EPI B_1^+-mapping. In *Proceedings of the 27th Annual Meeting of ISMRM, Montreal, Quebec, Canada*, page 926, 2019
- A. Lesch, C. S. Aigner, and R. Stollberger. Highly accelerated 3D Bloch Siegert B_1^+ mapping at 7T. In *Proceedings of the 28th Annual Meeting of ISMRM, Virtual Meeting*, page 662, 2020

Contents

5.1 Robust Implementation of 3D Bloch-Siegert B_1^+ Mapping . . . 140
5.2 Highly accelerated 3D Bloch-Siegert B_1^+ Mapping 143
5.3 3D Bloch-Siegert EPI B_1^+ Mapping 163
5.4 Highly accelerated 3D Bloch Siegert B_1^+ Mapping at 7T 167

As already mentioned in this thesis, highly accurate B_1^+ mapping is very important at high and ultra high field strength ($B_0 \geq 3\,\mathrm{T}$) for several applications, as B_1 shimming (see Section 2.3.6), the correction of flip angle dependent models in quantitative MRI (qMRI) (see Section 4.2), Electrical Property Tomography (EPT), or Chemical Exchange Saturation Transfer (CEST). For this purpose, many methods were proposed over the years, where the most important are reviewed in Section 2.5, with their own disadvantages and limitations. Some widespread limitations are: their T_1 dependency (Double Angle Method (DAM), "Stimulated Echo – Spin Echo Imaging", Saturated Turbo FLASH (satTFL)) and to a lower degree for Actual Flip Angle Imaging (AFI) and Dual Refocusing Echo Acquisition Mode (DREAM), leading to either long acquisition times or inaccurate B_1 maps; the influence of non-ideal slice profiles (*DAM*, "Stimulated Echo – Spin Echo Imaging", *satTFL*, *AFI* and *DREAM*); the validity of the model equation is restricted to the first echo (central k-space line) (*satTFL* and *DREAM*); the restriction to a certain flip angle range limits their potential application to a certain degree of inhomogeneity (*DAM*, "Stimulated Echo – Spin Echo Imaging", *satTFL*, *AFI*, *DREAM*, "180° Signal Null", "Phase Imaging", and "Orthogonal Alpha"); their sensitivity to main field variations ΔB_0 ("Phase imaging", "Orthogonal Alpha" and to a lower degree "Bloch-Siegert (BS) Shift Imaging"); a high Specific Absorption Rate (SAR) deposition (Hyperbolic Secant (HS), "180° Signal Null", and "*BS* Shift Imaging"). Furthermore, nearly all discussed methods suffer from quite long acquisition times. The only exception is *DREAM*, where acquisition times in the order of $< 20\,\mathrm{s}$ for whole brain coverage are possible. However, the main limitations of *DREAM* are the restriction to flip angles $\alpha < 90°$, because of the ambiguity of the arctan function; slice profile effects and resulting modeling errors for flip angles $\alpha > 60°$; and the invalidity of the model for all echos after the first one, limiting the resolution of the field map to very low values, typical matrix sizes of 38×64 are reported.

Moreover, only two of the methods described in Section 2.5 are able to directly measure the B_1^+ field instead of the flip angle α, which is advantageous for some applications such as *CEST* or B_1 shimming. These are the *HS* method and the method of "*BS* Shift Imaging". Even though, the *HS* method exhibits lower *SAR* values, the *BS* method is preferable, because there exists a clear physical relationship between the B_1^+ magnitude and the measured phase shift ϕ_{BS}; whereas for the *HS* method only an empirical relation exists, which has to be calibrated to the transmit chain of the Radio Frequency (RF) system. This is the reason, why the "*BS* Shift Imaging" method was chosen to be used as the basis for B_1^+

mapping throughout this thesis. The *BS* method is already quite fast, because it is widely independent of T_1 so that low Repetition Times (TRs) are possible. However, in practice, the minimum possible *TR* is restricted by the *SAR* constraint, because of the high energy deposition of the *BS* encoding pulse. Here, a compromise between Signal-to-Noise Ratio (SNR) and acquisition time has to be made. Practically, acquisition times in the order of 20 s for a 2D single slice acquisition are possible. Nevertheless, for 3D volume acquisitions, the acquisition time easily rises into the order of many minutes, which is unacceptable for a preparation scan without any diagnostic information so that acceleration is needed. In general, there are two possibilities to accelerate the data acquisition.

First, imaging strategies were proposed to acquire more data after one *BS* encoding pulse using faster readout strategies such as Turbo Spin Echo (TSE) [248], an Echo Planar Imaging (EPI) based readout [71, 250] or spiral trajectories [152, 250]. These approaches have, however, its own challenges at high and ultra high field strength. The second acceleration strategy is to acquire less Cartesian encodings, usually termed undersampling, and recover the missing information within the reconstruction using concepts of Parallel Imaging (PI) and Compressed Sensing (CS). Such an approach was proposed by Sharma et al. [265] using a modified iterative Self-consistent Parallel Imaging Reconstruction (SPIRiT) reconstruction [196], that yields acceleration factors of about 30 without sacrificing accuracy. This method already performs very well, but further improvement can be expected by directly applying a smoothness constraint to the reconstructed B_1^+ field. In Zhao et al. [336] a H_1 regularization was applied to improve the B_1^+ field estimation especially in low signal regions in a parallel transmit (pTX) setting out of fully sampled *BS* data. In the case of undersampling this has not been done so far.

The main contribution of this thesis is to apply variational methods, to obtain highly accurate B_1^+ maps out of highly undersampled data. For this purpose, a preliminary work is described in Section 5.1, where a robust data acquisition scheme for *BS* based B_1^+ mapping is investigated, to reduce the sensitivity against phase variations during the data acquisition. In Section 5.2, the reconstruction algorithm to obtain accurate B_1^+ field maps from highly undersampled data is described. Specific sampling patterns typically play an important role for the reconstruction of morphological images from subsampled data [161]. Therefore, the influence of different undersampling patterns on the accuracy of the reconstructed B_1^+ maps is investigated as well. In Section 5.3, the combination of undersampling and *EPI* readout is considered, and in Section 5.4, the application of the proposed reconstruction is investigated under the conditions of a main field strength of 7 T with respect to accuracy and acceleration potential.

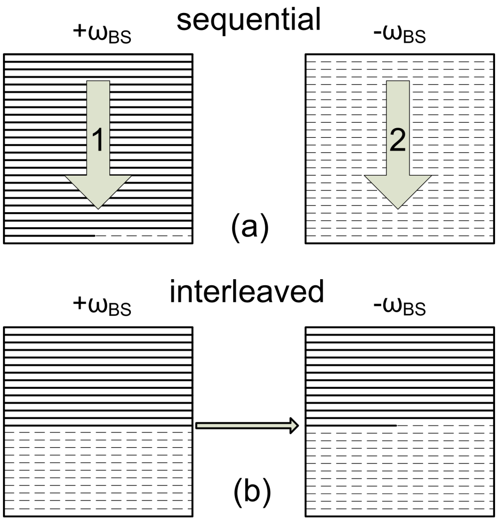

Figure 5.1: (a) Sequential sampling scheme: all k-space lines of the positive resonance offset acquisition $+\omega_{\mathrm{BS}}$ are acquired before the negative resonance offset acquisition $-\omega_{\mathrm{BS}}$ starts. (b) Interleaved sampling scheme: After a certain acquired k-space line in the $+\omega_{\mathrm{BS}}$ data set, the same line is acquired in the $-\omega_{\mathrm{BS}}$ data set, leading to an increased robustness against phase errors.

5.1 Robust Implementation of 3D Bloch-Siegert B_1^+ Mapping

To suppress influences on the signal phase arising from ΔB_0, chemical shift or excitation, the data has to be acquired with positive and negative resonance offset $\pm\omega_{\mathrm{BS}}$ of the *BS* pulse. The difference of those two phase images is proportional to $B_{1,\mathrm{peak}}^2$ (see Eq. (2.149)). In the conventional implementation, these acquisitions are performed sequentially, whereas in this work the advantage of an interleaved acquisition pattern is exploited. The different acquisition schemes are visualized in Figure 5.1.

5.1.1 Methods

All measurements were performed on a clinical Siemens Magnetom Skyra 3 T system (Siemens, Erlangen, Germany). The *BS* method was implemented by adding an offresonant Gaussian shaped *BS* pulse with a duration of 10 ms, a calibration constant K_{BS} of 53.4 rad G^{-2} and scaled to an onresonant equivalent flip angle of 1000° into a Gradient Recalled Echo (GRE) sequence. The offresonance frequency to encode the *BS* shift was set to 4 kHz and −4 kHz, respectively. The phase drift was measured over 6 h at the end of three regular measurement days with different preloads of the scanner using the sequence described above. The B_1^+ maps were acquired with a Field of View (FOV) of 250 mm, a matrix size of 128 × 76, a TE of 13.4 ms and a TR of 150 ms which is near the lower limit due to *SAR* restrictions. The 3D B_1^+ maps were acquired in a slab with 16 phase encoded slices with a thickness of 5 mm, using both sequential and interleaved acquisition. The

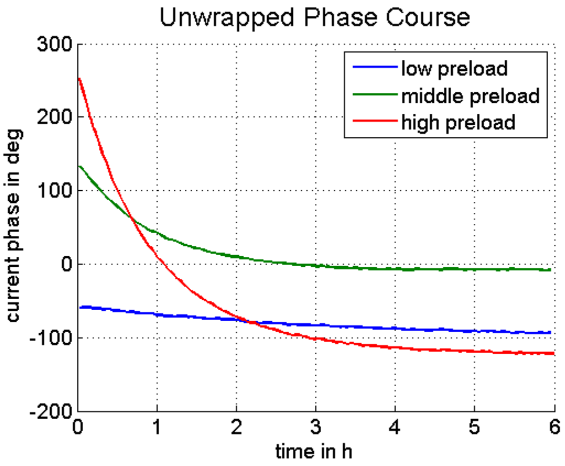

Figure 5.2: Unwrapped phase drift measured at the end of 3 regular measurement days over a time period of 6 h.

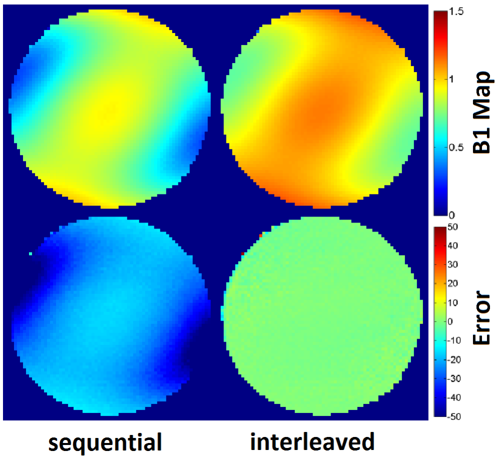

Figure 5.3: Comparison between BS based B_1^+ maps obtained with sequential (left) and interleaved (right) acquisition as central slice of a 3D data set containing 16 slices measured on a cylindrical water phantom. The error maps $\epsilon(\vec{r})$ are given in % with respect to the DAM reference.

reference was measured using the *DAM* [286], with a TR $> 5T_{1,\mathrm{max}}$. To enable a direct comparison to the reference measurement, the B_1^+ maps were normalized such that the nominal applied flip angle appears at one. The error maps $\epsilon(\vec{r})$ show the deviation of a specific B_1^+ map compared to the reference measurement in %.

5.1.2 Results

In Figure 5.2, the phase variation is shown over 6 h for three different scanner preloads. The changing rate is different but the phase stabilizes and reaches a steady state after about 3 to 4 h independent of the initial slope. Figure 5.3 shows a comparison between the calculated B_1^+ maps (center slice) of two 3D scans acquired with sequential (left) and

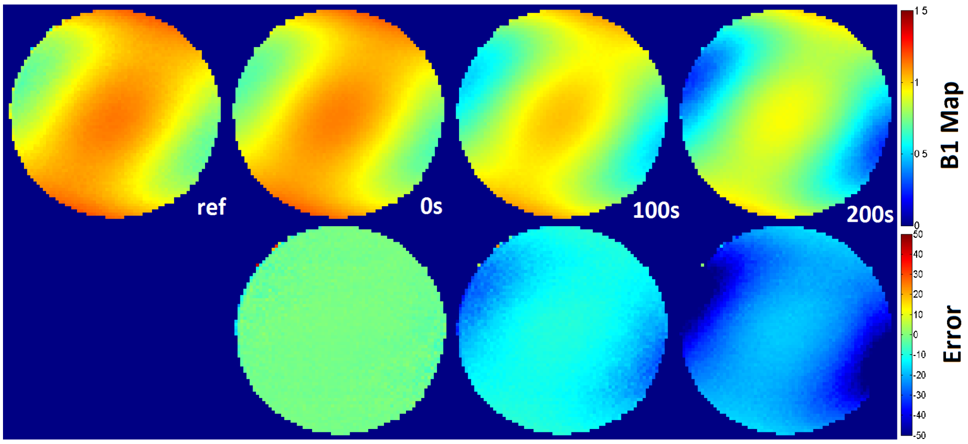

Figure 5.4: DAM reference scan and 2D BS B_1^+ maps acquired with different delays (Δt = 0, 100 and 200 s) between positive and negative offresonance BS encoding using sequential acquisition and the deviation with respect to the reference scan $\epsilon(\vec{r})$ in %.

interleaved acquisition (right) and the corresponding error maps $\epsilon(\vec{r})$, in comparison to the reference scan shown in Figure 5.4 (top left). Figure 5.4 further shows several 2D *BS* acquisitions with increasing delay between both *BS* encodings using sequential acquisition with the corresponding error maps.

5.1.3 Discussion

The resonance frequency is not stable within the scanner and behaves like an exponential decay. We assume that thermal effects within the hardware are the reason for that. Extending the sequential *BS* acquisition to 3D for, i.e. 16 slices, there is a time difference of more than 3 minutes between both *BS* encoding steps. If the resonance frequency drifts within that time with a decay rate of the most severe measured case, indicated by the red line in Figure 5.2, the additional phase accumulation leads to a substantial error in the acquired B_1^+ map, as shown in Figure 5.3. Even if the drift lies within the hardware specifications (0.1 ppm/h) an error of about 15 to 20 % occurs. We found that an interleaved acquisition scheme is capable to suppress those phase effects. A comparison between *DAM* reference and the achieved results shows that the error is lower than 2 % over the whole *FOV* for the interleaved acquisition, whereas the error for the sequential case varies from 17 % to more than 50 %, depending on the absolute value of B_1^+ (Figure 5.3). Because of the square root dependency between phase and RF-field, the error increases in low B_1^+ field regions. To show that only the phase drift is responsible for the quantification error, some sequential 2D acquisitions with different delays between both *BS* encodings are shown in Figure 5.4. The error increases substantially with increasing delay. The delay of 200 s is about the time required for the acquisition of the 16 slices in the 3D case and the errors are in the same range. In an actual 2D scan, this effect is negligible due to the comparable low acquisition time.

5.1.4 Conclusion

We showed that the phase drift within the scanner is responsible for substantial errors occurring in the *BS* based B_1^+ mapping in 3D. Furthermore, an interleaved acquisition scheme is effective to suppress this influence on *BS* based B_1^+ mapping and makes the measurement robust and independent from the thermal preload of the system.

5.2 Highly accelerated 3D Bloch-Siegert B$_1^+$ Mapping

With the goal to allow single breath hold 3D B_1^+ mapping, a highly accelerated method is proposed, based on the efficient reconstruction of subsampled *BS* data, using a variational two-step regularization strategy. This tailored regularization reflects the prior knowledge of piecewise smoothness on the underlying morphological image and the prior knowledge of spatial smoothness on the B_1^+ field. This allows us to exploit shared information present in the measured data. The evaluation of the resulting algorithm is carried out with retrospectively and prospectively accelerated in-vivo measurements against fully sampled *BS* data. Furthermore, an abdominal in-vivo acquisition with full liver coverage during a single breath hold is demonstrated.

5.2.1 Theory

5.2.1.1 Bloch-Siegert Approach for B$_1^+$ Mapping

By applying an *RF*-field with arbitrary resonance-offset ω_{RF}, a slight shift in resonance frequency can be observed in any Nuclear Magnetic Resonance (NMR) experiment [26]. This effect depends on the *RF*-magnitude and was exploited by Sacolick et al. [249] to map the spatial varying B_1^+ field, by applying an offresonant *RF*-pulse (*BS*-pulse) between excitation and readout in an arbitrary Magnetic Resonance Imaging (MRI) sequence, causing a B_1^+ dependent phase shift ϕ_{BS} in each voxel. Under the assumption $\omega_{\text{RF}} \gg \gamma B_1$ [249], this additional phase shift only depends on the spatially varying squared B_1^+ peak-magnitude $B_{1,\text{peak}}^2$ and a pulse shape dependent constant K_{BS}. The factor K_{BS} can be computed as a function of the normalized *BS* pulse shape $B_{1,\text{norm}}(t)$ with duration T_p, the resonance-offset ω_{RF} and the gyro-magnetic ratio γ, leading to the following equation for the phase shift ϕ_{BS}

$$\phi_{\text{BS}} = B_{1,\text{peak}}^2 \int_0^{T_p} \frac{(\gamma B_{1,\text{norm}}(t))^2}{2\omega_{\text{RF}}(t)} dt = B_{1,\text{peak}}^2 \cdot K_{\text{BS}}. \tag{5.1}$$

To separate the phase shift ϕ_{BS} from other effects influencing the signal phase, such as ΔB_0 field inhomogeneities, receiver coils or excitation, a reference measurement is required, which is typically performed as an acquisition with the negative resonance-offset $-\omega_{\text{RF}}$ to increase the *SNR* in the final B_1^+ map. The signals of these two acquisitions, S_+ for positive and S_- for the negative resonance offset, are proportional to the magnitude of the transverse magnetization $M_\perp$, the background phase ϕ_0 and the desired *BS* phase ϕ_{BS}, given as

$$S_+ \propto |M_\perp| e^{j(\phi_0+\phi_{\mathrm{BS}})}, \tag{5.2}$$

$$S_- \propto |M_\perp| e^{j(\phi_0-\phi_{\mathrm{BS}})}. \tag{5.3}$$

The B_1^+ map is given as the peak value of the applied *BS* pulse $B_{1,\mathrm{peak}}$. It can be calculated easily out of these two measurements in the fully sampled case by a complex division of the independently reconstructed images, S_+ and S_-, by reformulation of Eq. (5.1) under the assumption of temporally constant ϕ_0 as

$$B_{1,\mathrm{peak}} = \sqrt{\frac{\angle\left(I_+/I_-\right)}{2K_{\mathrm{BS}}}} = \sqrt{\frac{\phi_{\mathrm{BS}}}{K_{\mathrm{BS}}}}. \tag{5.4}$$

5.2.1.2 Variational BS Reconstruction from highly subsampled Data

The proposed approach to accelerate the B_1^+ mapping is to employ a tailored undersampling of Fourier data combined with variational image reconstruction. The two measurements with positive and negative resonance offset, as described above, yield undersampled Fourier data d_+ and d_-, corresponding to the two images $S_+ \simeq |M_\perp| e^{j(\phi_0+\phi_{\mathrm{BS}})}$ and $S_- \simeq |M_\perp| e^{j(\phi_0-\phi_{\mathrm{BS}})}$, respectively. Our goal is to obtain the phase shift ϕ_{BS} from these measurements. Due to undersampling, however, it is not possible to separate this phase shift from the magnetization $|M_\perp|$ and the background phase ϕ_0 directly in the measured k-space data. To overcome this, we use a variational approach to recover the three unkonwn quantities from the undersampled Fourier data. To this aim, a direct approach would be to seek for morphological data $p \simeq |M_\perp| e^{j\phi_0}$ and phase shift data $q \simeq e^{j\phi_{\mathrm{BS}}}$, with $|q| = 1$ given as solutions of the minimization problem

$$\min_{\substack{p,q\\|q|=1}} \frac{\lambda_1}{2}\|A_+\left(p \odot q\right) - d_+\|_2^2 + \frac{\lambda_2}{2}\|A_-\left(p \odot \overline{q}\right) - d_-\|_2^2 + \mathcal{R}_1(p) + \mathcal{R}_2(q). \tag{5.5}$$

Here, the first two terms match the pointwise products $p \odot q \simeq |M_\perp| e^{j(\phi_0+\phi_{\mathrm{BS}})}$ and $p \odot \overline{q} \simeq |M_\perp| e^{j(\phi_0-\phi_{\mathrm{BS}})}$, with $\overline{q}$ being the complex conjugate of q, to the corresponding acquired data d_+ and d_-, respectively. The last two terms employ a regularization of the morphological data p and the phase shift data q. The regularization parameters λ_1 and λ_2 control the influence of the data fidelity terms on the whole cost function in comparison to the regularization terms weighted identically with one. Their choice depends on the noise-level and image resolution. The data fidelity terms are defined as squared L^2-norm of the difference between the Magnetic Resonance (MR) forward calculation and the acquired data, due to the Gaussian distributed noise with zero mean in the measured data (see Section 3.2.2). The *MR* forward operators $A_+(u)$ and $A_-(u)$ are given according to Section 3.2.3, as the point wise multiplication with the precalculated receiver coil sensitivity maps C_n, the discrete Fourier operator $\mathcal{F}$, and the undersampling patterns P_+ and P_- for each of the two acquisitions as

$$A_+(u) = \begin{pmatrix} P_+ \odot \mathcal{F}\{C_1 \odot u\} \\ \vdots \\ P_+ \odot \mathcal{F}\{C_{N_c} \odot u\} \end{pmatrix}, \quad A_-(u) = \begin{pmatrix} P_- \odot \mathcal{F}\{C_1 \odot u\} \\ \vdots \\ P_- \odot \mathcal{F}\{C_{N_c} \odot u\} \end{pmatrix}. \tag{5.6}$$

The different operators account for the in general different undersampling patterns for positive and negative resonance offset acquisition. Although, Eq. (5.5) is a rather natural approach for the problem under consideration, it comprises the solution of a non-convex optimization problem, also when using convex regularization terms $\mathcal{R}_1$ and $\mathcal{R}_2$. In particular, even if we would drop the non-convex constraint $|q| = 1$, due to the mappings $(p, q) \mapsto p \odot q$ and $(p, q) \mapsto p \odot \overline{q}$, the data fidelity terms are still non-convex. As a result, one can generally not expect to obtain a globally optimal solution of Eq. (5.5).

To overcome the non-convexity, we reformulate Eq. (5.5) using a change of variables, where we define $u = p \odot q$ and $v = \overline{q}^2$. With these new variables, the data fidelity term in Eq. (5.5) reads as

$$(u, v) \mapsto \frac{\lambda_1}{2}\|A_+(u) - d_+\|_2^2 + \frac{\lambda_2}{2}\|A_-(u \odot v) - d_-\|_2^2. \tag{5.7}$$

We see that the variable v only appears in the second term. Now adding two regularization terms for u and v, instead of the ones on p and q as in Eq. (5.5), would still yield a non-convex problem which in particular comprises two data fidelities for u. However, if we drop the second data fidelity for u (which corresponds to using less measurements), the minimization problem for u decouples from the terms involving the variable v. This allows to separately first solve a convex variational problem for $u = p \odot q \simeq |M_\perp| e^{j(\phi_0 + \phi_{\mathrm{BS}})}$ and afterwards, having u fixed, a second convex variational problem for $v = \overline{q}^2 \simeq e^{-j2\phi_{\mathrm{BS}}}$, where we drop the non-convex constraint $|q| = 1$ to obtain convexity. The phase shift ϕ_{BS} can be obtained directly from the optimizer $\hat{v}$. The first step is realized by solving the convex minimization problem

$$\hat{u} = \arg\min_u \frac{\lambda_1}{2}\|A_+(u) - d_+\|_2^2 + \mathrm{TGV}_\alpha^2(u), \tag{5.8}$$

where we employ the second order Total Generalized Variation (TGV) functional [38] for the regularization of the unknown u, which contains morphological information that is modulated by a smooth phase shift. The functional TGV_α^2 is known to be a suitable image prior for morphological *MR* images since it enforces piecewise smooth solutions, which is exactly the behavior of *MR* images with edges at tissue boundaries and modulated excitation and receiver inhomogeneities. For more details according definition and properties, the reader is referred to Section 3.2.4.4. The second step of obtaining the phase information is realized via the solution of the convex optimization problem

$$\hat{v} = \arg\min_{v} \frac{\lambda_2}{2} \|A_{-}(\hat{u} \odot v) - d_{-}\|_2^2 + \frac{1}{2} \|\nabla_{xyz}^{+} v\|_2^2. \tag{5.9}$$

Here, the unknown v corresponds to the B_1^+ field, which is known to be spatially smooth, and hence the squared L_2 norm of the image gradient is used for regularization (H_1 regularization, for more details see Section 3.2.4.2). Overall, this yields to a variational two-step reconstruction method that comprises the sequential solution of two convex optimization problems, such that the optimizer $\hat{v} \approx e^{-j2\phi_{\mathrm{BS}}}$ of the second optimization problem exhibits a phase equal to the doubled *BS* phase ϕ_{BS} without morphological structure. With that, the B_1^+ magnitude is given as

$$B_{1,\mathrm{peak}} = \sqrt{\frac{-\angle \hat{v}}{2K_{\mathrm{BS}}}}. \tag{5.10}$$

5.2.2 Methods

5.2.2.1 Implementation

Numerical Solution:
The optimization problem in Eq. (5.8) of the proposed variational two-step algorithm belongs to the class of non-smooth convex optimization problems that can be solved efficiently with the primal-dual splitting algorithm [46], where an explicit solution strategy is described in Section 3.2.5.2 based on the considerations given by Knoll et al.[159]. The optimization problem in the second step (Eq. (5.9)) is a smooth and convex problem that can be solved using the well known Conjugate Gradient (CG) algorithm [125] on the normal equations, where a solution is described in Section 3.2.5.1.

Reconstruction framework:
The overall reconstruction framework was implemented in MATLAB (MathWorks, Inc., Natick, MA). To reduce the calculation time, the iterative optimization for Eqs. (5.8) and (5.9) were implemented in C++/CUDA (NVIDIA Corporation, Santa Clara, CA) using a modified version of an open-source Graphics Processing Unit (GPU) library (AGILE)[1] [82] and a reconstruction library (AVIONIC)[2] [255]. The source code of the reference implementation of this method is available on GitHub[3]. Receiver coil sensitivities were estimated from the fully sampled k-space data using the method proposed by Walsh et al. [311], that was also used for coil combination to calculate the fully sampled reference and the zero padded low resolution estimates from the multi-coil measurements. We further note that data normalization was carried out with respect to the maximum of a Hamming-filtered low resolution estimate from the positive *BS* dataset similar to [302].

---

[1] https://github.com/IMTtugraz/AGILE

[2] https://github.com/IMTtugraz/AVIONIC

[3] https://github.com/IMTtugraz/BSReconFramework

5.2.2.2 Validation and parameter optimization

To assess the practical applicability of the developed algorithm, different in-vivo investigations from healthy volunteers with retrospective and prospective undersampling have been performed.

In-vivo Measurements:

All in-vivo measurements were gained from 5 male healthy volunteers in the age between 28 and 33 with the approval of the responsible ethics committee on a Skyra 3T system (Siemens, Erlangen, Germany). To measure the *BS* shift, a *GRE* sequence was modified by adding an offresonant Gaussian shaped *RF* pulse between excitation and readout as stated in [249] with a duration $T_p = 10\,\text{ms}$, an offresonance frequency $\omega_{\text{RF}} = 2\pi \cdot 4\,\text{kHz}$, and an on-resonant equivalent flip angle $\alpha_{\text{BS}} = 1000°$, leading to a pulse constant $K_{\text{BS}} = 53.4\,\text{rad/G}^2$. Measurement data was acquired using a 20-channel head/neck receive coil (Siemens, Erlangen, Germany) and the birdcage body coil for transmit. The acquired in-vivo 3D brain datasets have a matrix size of $128 \times 128 \times 32$ as in [265], a squared *FOV* with 230 mm, a resolution of 2 mm in slice direction and a slice oversampling of 25 %. Echo Time (TE) and *TR* were set to minimal values of TE = 13.5 ms TR = 95 ms, respectively, and an excitation flip angle of $\alpha = 25°$ was used which corresponds to the mean Ernst-angle in gray and white matter. The minimal *TE* is restricted by the length of the *BS* pulse and the *TR* by the *SAR* constraint. The acquisition parameters for the liver and the knee dataset were adjusted to a matrix size of $128 \times 128 \times 44$ and $128 \times 128 \times 52$, a *FOV* of 220 mm and 150 mm and a resolution in slice direction of 3.2 mm and 2.5 mm, respectively.

Error evaluation:

The reconstructed B_1^+ maps, $B_{1,\text{rec}}$, were validated against a reference map $B_{1,\text{ref}}$, which is a fully sampled dataset. The error maps ϵ are defined as

$$\epsilon(\vec{r}) = \frac{|B_{1,\text{ref}}(\vec{r}) - B_{1,\text{rec}}(\vec{r})|}{B_{1,\text{nom}}}, \tag{5.11}$$

with a normalization to the desired B_1^+ magnitude $B_{1,\text{nom}}$ necessary to achieve the nominal flip angle α_{BS}. This error measure is proportional to the correction error in many quantitative *MRI* models. Each result is further evaluated as Mean Absolute Error (MAE), the median Absolute Error (medAE) and the 99 % quantile $q_{99\%}$ over a certain Region Of Interest (ROI) covering the whole brain inside the cranial bone structure. For the evaluation of random undersampling patterns, all three error measures are given as average over 10 independent trials. The reconstruction results are compared to the fully sampled reference and a low resolution estimate, which is obtained as zero padded inverse Fast Fourier Transform (FFT), with subsequent coil combination for both measurements using [311] and Eq. (5.4). Furthermore, results are evaluated by an error histogram.

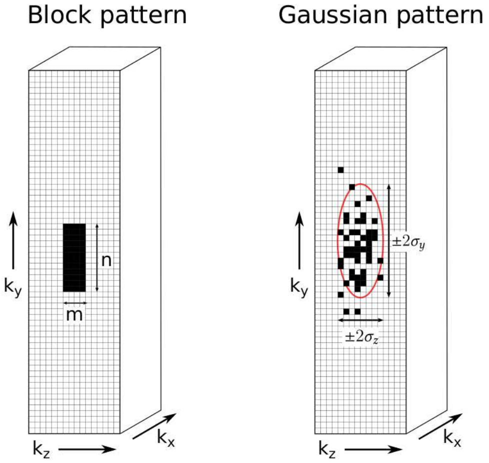

Figure 5.5: Schematic representation of the block pattern and the irregular pattern with Gaussian density function. For the block pattern a rectangular region in k-space center with a predefined number of $n \times m$ Cartesian encodings in k_y and k_z, respectively is used. The irregular pattern with Gaussian density function is defined by the standard deviation σ_y and σ_z in both phase encoding directions. Here the $\pm 2\sigma_{y,z}$ area is shown in red. The sampling pattern is gained by selecting a random number of Cartesian encodings according to the probability density function. The readout direction is k_x in all cases.

Tuning of the Regularization Parameters:

In the proposed approach, two regularization parameters λ_1 and λ_2 need to be tuned, in order to achieve optimal results. For that purpose, first, a grid search was performed for one particular measured dataset and undersampling pattern. Those led to the minimum *MAE* were fixed for all further experiments. The found values are $\lambda_{1,opt} = 64$ and $\lambda_{2,opt} = 5.0 \cdot 10^{-4}$.

Undersampling Patterns:

The in-vivo data was retrospectively subsampled from the fully sampled reference k-space data. Initially, we used a rectangular region in k-space center (block pattern) as undersampling pattern which is defined by a fixed number of $n \times m$ Cartesian encodings in k_y and k_z phase encoding direction. Results with this type of pattern were already shown in [178]. The block sampling strategy was used, because the B_1^+ dependent information is mostly encoded with low spatial frequency information. However, in compressed sensing image reconstruction, it is common to use irregular undersampling patterns, to fulfill the incoherence condition. Therefore, randomized sampling schemes as proposed in the seminal work of Lustig et al. [194] were investigated. Therein, random samples are generated according to polynomial density kernels around the k-space center. In order to generate more densely sampled patterns, we also substituted the polynomial kernels with Gaussian density kernels. Block and Gaussian patters are schematically visualized in Figure 5.5. The benefit of random sampling was explored firstly, for only the positive and secondly for both, positive and negative, *BS* pulse encoding as described in [179]. The random pattern described in [194] is defined by the parameter p, which is the polynomial degree used in the density function. A higher p-value means that the sampling points are spread more uniformly over the whole k-space. The Gaussian density pattern is described by its standard deviation σ_y and σ_z in both phase encoding directions. The effect of such patterns with different distribution parameters and a fixed acceleration factor R_{acc} were evaluated against the fully sampled reference. For the acquisition of prospectively subsampled data the sequence was modified, such that only an adjustable number of Cartesian encodings are acquired in k-space center in both phase encoding directions.

5.2.3 Results

Figure 5.6 shows results of the proposed variational reconstruction method on retrospectively subsampled measurement data in the brain for different block sizes. The results are compared to the fully sampled reference and a low resolution estimate with the same amount of data. The B_1^+ maps gained by zero padding (low resolution) are highly corrupted with artifacts, especially in low signal regions where dominant phase jumps are likely to occur. In contrast to that the variational reconstruction method yields artifact free results in very good accordance to the fully sampled reference for block sizes with 10×6 and 12×4 encodings and even for a block size of 4×4 the error is bounded to comparable low values. In Table 5.1, *MAE*, *medAE* and $q_{99\%}$ values for different block sizes are summarized for both methods. All three error measures show a substantial improvement for our variational reconstruction approach compared to results gained from low resolution data for all cases.

Figure 5.7 displays error histograms for the low resolution estimate and the proposed variational reconstruction method to visualize the error distribution inside the described *ROI*. The histograms are shown for a retrospectively subsampled dataset with block sizes of 4×4, 10×6, and 12×4 encodings in the k-space center. The error histograms for the proposed variational reconstruction are much narrower for all block sizes as compared to zero padded results. Using the proposed variational reconstruction method about 1.4 %, 1.7 % and 11 % of all voxels exceed a defined error limit of 2.5 % for pattern sizes of 12×4, 10×6, and 4×4 compared to 16 %, 23 % and 55 % using zero padding.

Figure 5.8 shows the *MAE* value for different block sizes as a function of the regularization parameters λ_1 and λ_2. The error stays stable over a wide range, reflecting the algorithm's robustness to non-optimally tuned regularization parameters. Furthermore, for those sampling patterns where the block size has a similar ratio of both phase encoding directions as the imaging matrix (i.e., 12×4 and 10×4 encodings in k-space center) a lower sensibility with respect to changes in λ_1 and λ_2 can be observed.

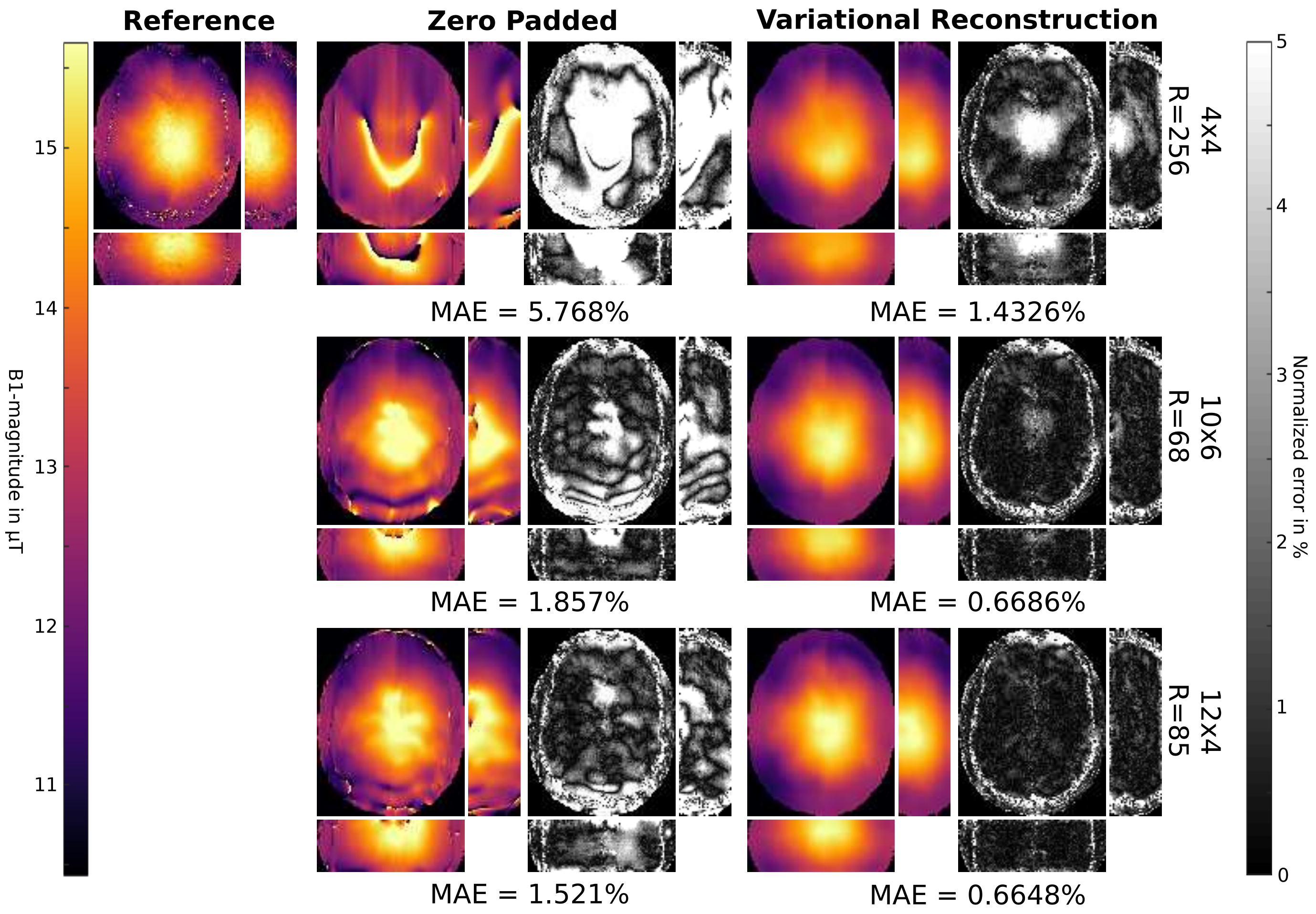

Figure 5.6: *Retrospectively subsampled:* B_1^+ map in µT for fully sampled reference, low resolution estimate and the result of the proposed variational reconstruction method for a retrospectively subsampled dataset in the brain of a healthy volunteer for a block size of 4×4, 10×6 and 12×4 encodings in the k-space center. The results are shown as central slice of the 3D-dataset in transverse, sagittal and coronal orientation. The right part of each column shows the error map $\epsilon(\vec{r})$ for the corresponding result as normalized error in percent of the desired B_1^+ peak-magnitude. The MAE is given as the mean of the error map over the whole 3D-brain inside the cranial bone structure for each case.

Figure 5.9 shows results for the variational reconstruction method for different irregular undersampling patterns. Pattern combinations that irregularly sample higher frequency information in the *TGV* part, P_+, while only densely sampling the k-space center in the H_1 part, P_-, (patterns 1 and 2) did not improve the reconstruction quality but lead to an increase in error, especially if the distribution favors sampling higher spatial frequencies. Using two different irregular sampling patterns with the same distribution parameters in both parts of the reconstruction also introduces artifacts. Increased reconstruction quality is achievable, when the same irregular pattern is used in both reconstruction steps as it is done in cases 4 to 7, where the error decreases the more sampling is concentrated around the k-space center. The highest concentration is achieved using a Gaussian density function (pattern 6) which yielded the highest B_1^+ accuracy. Furthermore, the Gaussian density function allows even higher acceleration with only slight increase in error (pattern 7). Compared to the best block-sampling pattern (12×4 encodings in Figure 5.6) a slight improvement in error with equal acceleration rate R_{acc} can be observed, nevertheless, for the acquisition of prospectively subsampled data block-sampling was used to keep the acquisition protocol simple. Figure 5.10 and 5.12 show results obtained with the proposed variational reconstruction approach from prospectively subsampled brain, knee and liver datasets from different healthy volunteers. For the brain and knee dataset we further provide an additional fully sampled dataset as reference. For the liver dataset, it is not feasible to obtain a fully sampled reference due to breath hold limitations such that an overlay of the B_1^+ field on a morphological scan is provided. To further show the improvement of the proposed method over zero padding, Figure 5.12 also provides zero padded results of the liver dataset for comparison. Zero padded results for brain and knee dataset are further shown in Figure 5.11. For brain and knee dataset the results of our variational reconstruction are in high agreement with the fully sampled reference, whereas the knee dataset shows a slight corruption due to high blood flow in the leg artery that leads to phase errors. The effect is much more prominent in the reference than in the final results of the proposed method. For the abdominal dataset in Figure 5.12 some minor heart-motion related artifacts outside the liver tissue are visible.

In contrast to the results shown in Figures 5.6 and 5.9, where the receive coil sensitivity maps C_n are estimated out of fully sampled data, Figure 5.13 shows reconstruction results obtained with sensitivity maps estimated from the undersampled dataset. For medium pattern sizes, only a slight decrease in accuracy can be observed, due to error propagation from imperfect coil sensitivity estimation. The corresponding error values for *MAE*, *medAE*, and $q_{99\%}$ are given in Table 5.2 in the right column group. For example, the average error for a pattern size of 12×4 increased from 0.665 %, with perfect coil sensitivities, to 1.059 % with realistic estimates. However, for the very small pattern size of 4×4, the reconstruction breaks down completely, because the coil sensitivity estimation fail with such a low amount of data, whereas by using perfect coils sensitivity maps the error is bound to very low values for the available amount of data.

Moreover, Table 5.2 shows a comparison of the error values obtained with globally opti-

pattern	R_{acc}	**Zero Padded** MAE in %	medAE in %	$q_{99\%}$ in %	**Variational Reconstruction** MAE in %	medAE in %	$q_{99\%}$ in %
4 × **4**	256.0	5.768	3.124	46.726	1.433	1.062	6.518
6 × **4**	170.7	3.834	2.529	21.843	0.938	0.700	4.220
6 × **6**	113.8	3.534	2.452	18.810	0.846	0.637	3.748
8 × **4**	128.0	2.956	1.973	17.881	0.812	0.622	3.350
8 × **6**	85.3	2.699	1.824	16.811	0.747	0.564	3.216
8 × **8**	64.0	2.681	1.799	17.651	0.728	0.549	3.121
10 × **4**	102.4	2.049	1.482	9.154	0.731	0.558	3.084
10 × **6**	68.3	1.857	1.366	8.187	0.669	0.505	2.891
12 × **4**	85.3	1.521	1.139	6.779	0.665	0.512	2.799
12 × **6**	56.9	1.416	1.039	6.511	0.609	0.463	2.593
12 × **12**	28.4	1.321	0.968	5.672	0.573	0.437	2.417

Table 5.1: *Retrospectively subsampled:* MAE, medAE and $q_{99\%}$ inside the described ROI for different block sizes in percent of the desired B_1^+ peak-magnitude and the corresponding acceleration factor R. The values are given for the low resolution estimate and the result of the proposed variational reconstruction method.

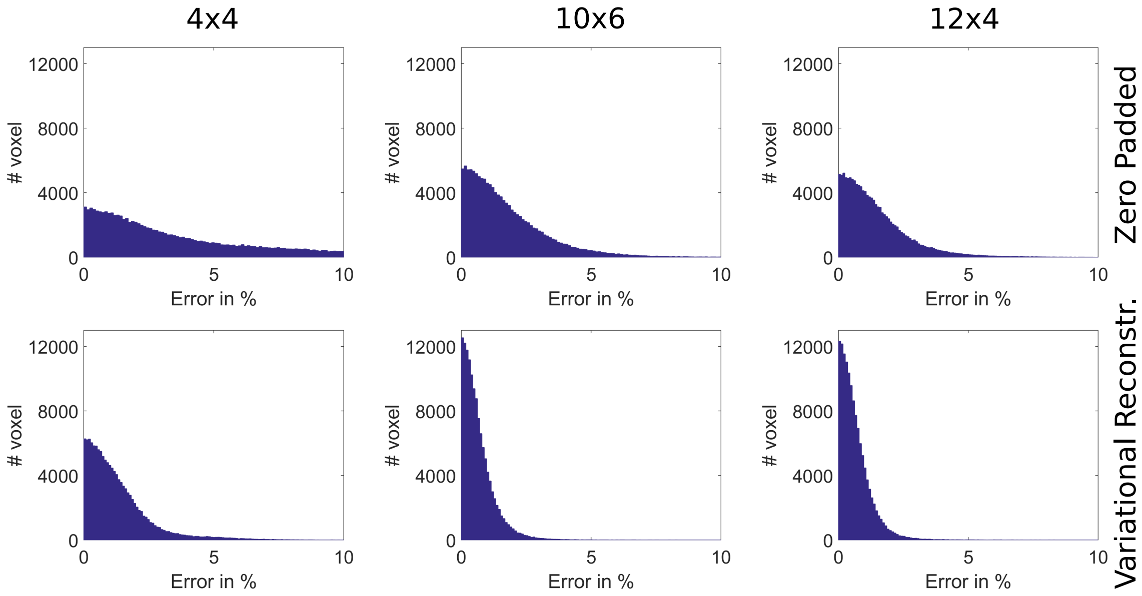

Figure 5.7: *Retrospectively subsampled:* Error histogram for the retrospectively subsampled dataset compared to the fully sampled reference in percent of the desired B_1^+ peak-magnitude for block sizes of 4 × 4, 10 × 6 and 12 × 4 encodings in the k-space center. The error histograms are shown for zero padded low resolution estimate and the result of our proposed variational reconstruction method.

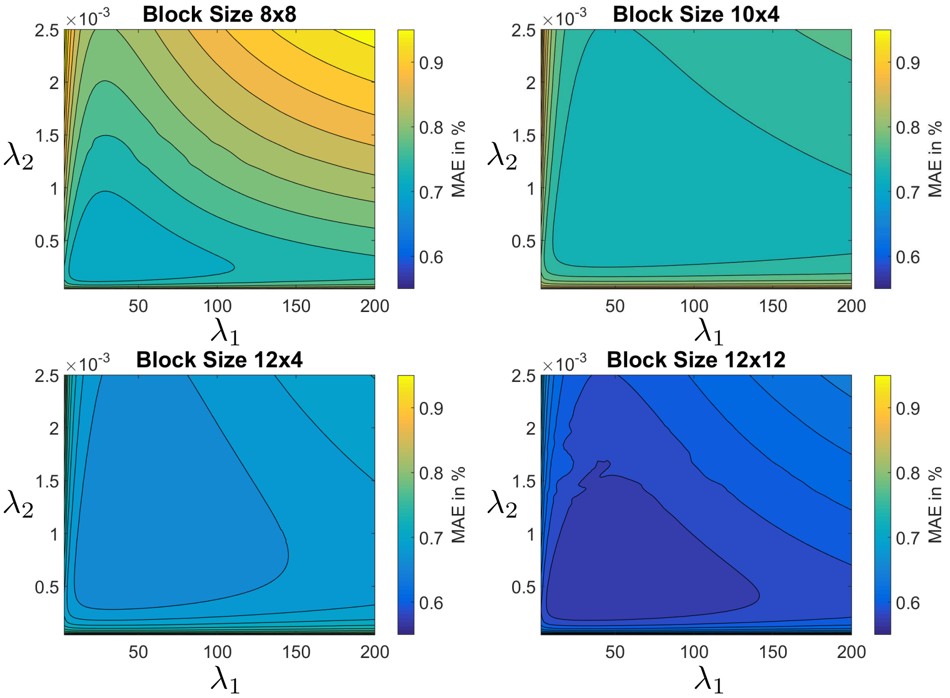

Figure 5.8: MAE inside the described ROI as a function of both regularization parameters λ_1 and λ_2 for different block sizes (8×8, 10×4, 12×4 and 12×12 encodings in k-space center) in percent of the desired B_1^+ peak-magnitude. For this evaluation the retrospective subsampled brain dataset shown in Figure 5.6 was used.

mized and fixed regularization parameters for all pattern sizes, compared to regularization parameters which are optimized individually for each pattern. This result again shows the robustness against mistuned regularization parameters. The improvements achieved by individual readjustments are very low ($< 0.1\,\%$) for all error measures.

To give a better insight of how the algorithm works, the intermediate results after the *TGV* reconstruction as well as the magnitude of the H_1 part are shown in Figure 5.14 for 4 different slices of a 3D dataset for an undersampling patter of size 12×4. The phase of the H_1 result is proportional to the square of the B_1^+ peak magnitude. The results of the *TGV* reconstruction are of poor quality, which is obvious for this low amount of available data, it leads to a stabilization of the phase, so that stable B_1^+ maps can be obtained in the second step. The magnitude of the H_1 result is shown in a range between 0.9 and 1.1, indicating that its deviation from the desired value of 1 is very low, even without an explicit requirement during the optimization.

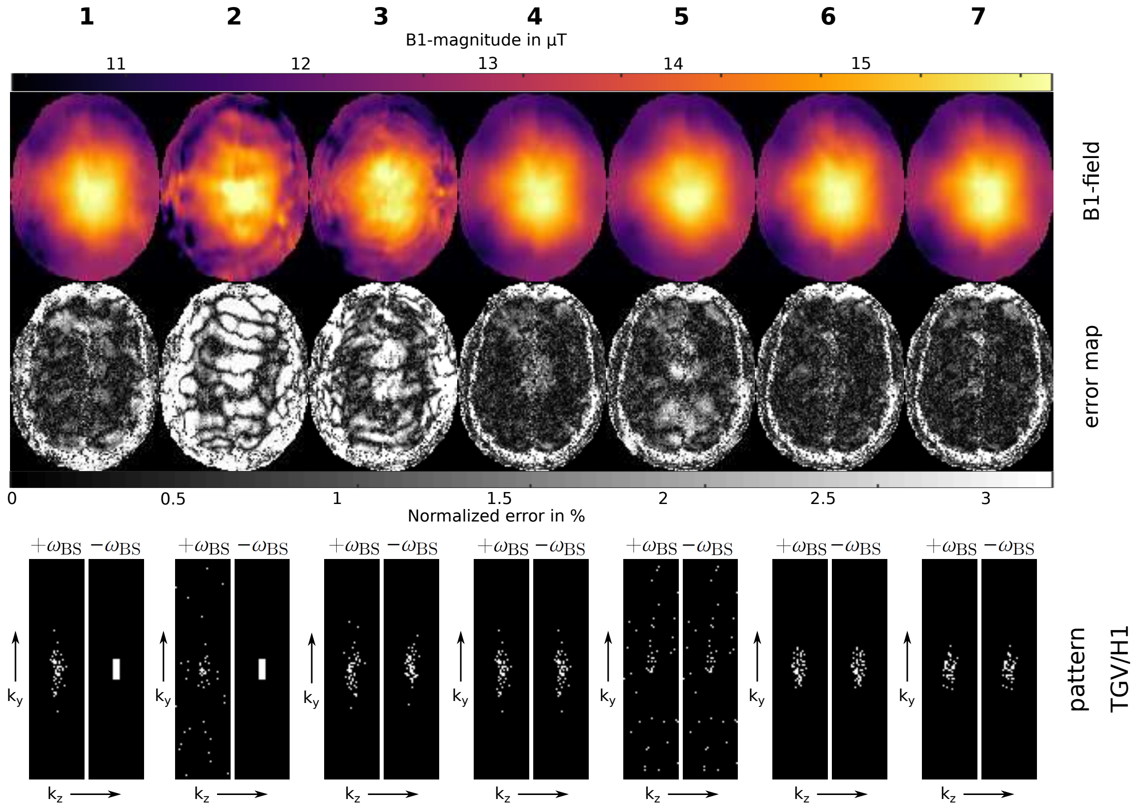

85.3	85.3	85.3	85.3	85.3	**85.3**	102.4	R
0.8677%	2.2886%	1.4605%	0.6660%	0.8970%	**0.6553%**	0.6670%	MAE
0.6860%	1.7487%	1.1526%	0.5125%	0.6942%	**0.5050%**	0.5342%	medAE
3.3526%	9.4783%	5.6145%	2.7579%	3.5117%	**2.7020%**	2.8694%	$q_{99\%}$

Figure 5.9: *Retrospectively subsampled:* First row: Reconstruction results of the proposed variational reconstruction method in µT using different undersampling patterns. Second row: Corresponding error maps as normalized error in percent of the desired B_1^+ peak-magnitude $\epsilon(\vec{r})$ (Reference see Figure 5.6). Third row: Combinations of undersampling patterns for the first step P_+ (TGV,$+\omega_{\text{BS}}$, left pattern) and the second step P_- (H_1,$-\omega_{\text{BS}}$, right pattern) were investigated as follows: Case 1 and 2: 12×4 block-pattern in k-space center in H1-part and a variable density pattern out of [194] in TGV-part with $p = 14.4$ and $p = 25$ respectively. Case 3: Different instances of this pattern with $p = 14.4$ in both parts. Case 4 and 5: The same instances of this pattern with $p = 14.4$ and $p = 25$ respectively. Cases 6 and 7: Pattern with Gaussian density function with $\sigma_y = 5$ and $\sigma_z = 2$, in case 7 with a higher acceleration factor. For each case the achieved acceleration R, the MAE, the medAE and the $q_{99\%}$ quantile inside the described ROI are given in percent of the desired B_1^+ peak-magnitude as mean over 10 trails with different realizations out of the described probability distribution.

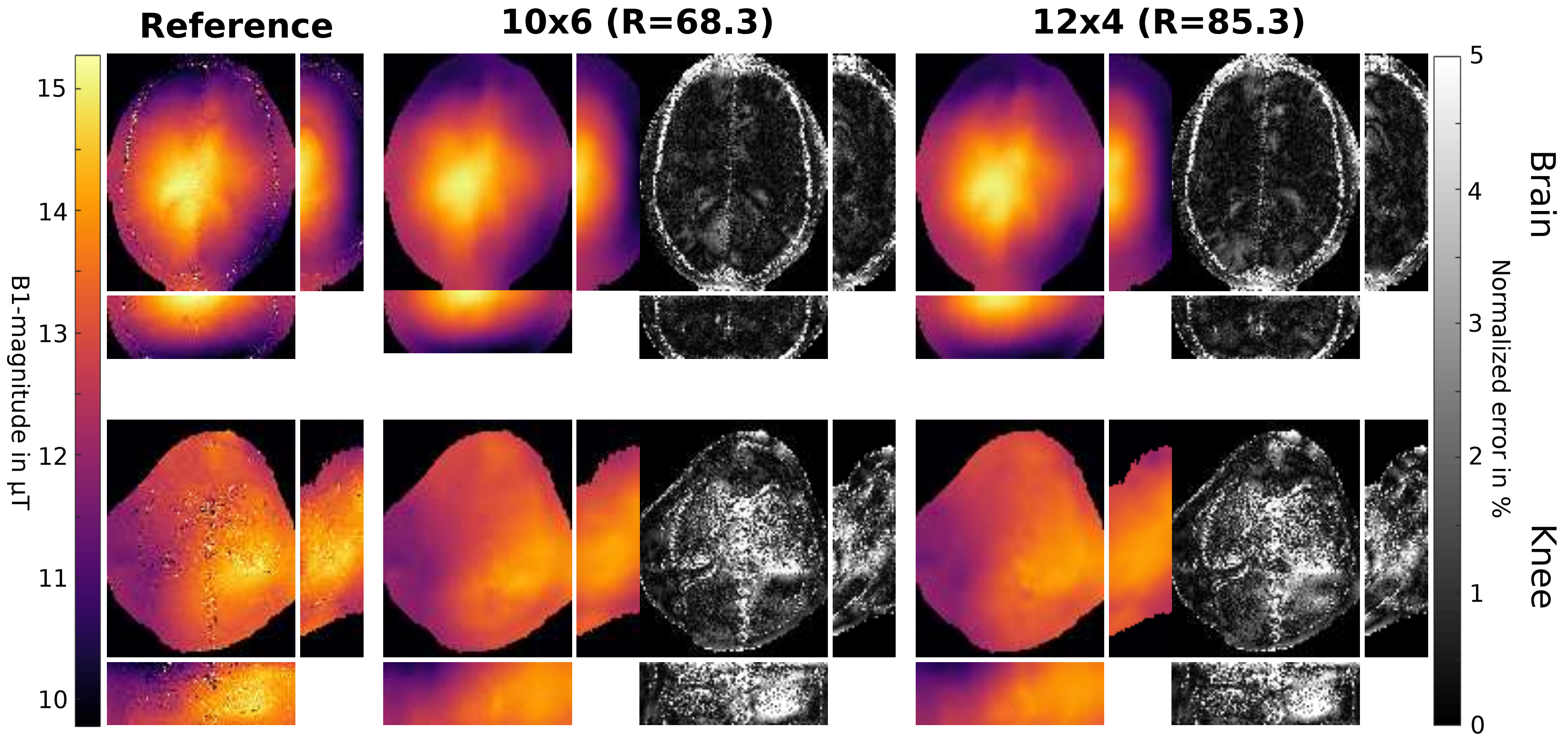

Figure 5.10: *Prospectively subsampled:* B_1^+ map in µT for fully sampled reference and the result of our proposed variational reconstruction method with 10×6 and 12×4 encodings in the k-space center and the corresponding error map $\epsilon(\vec{r})$ in percent of the desired B_1^+ peak-magnitude from prospectively subsampled data. The B_1^+ maps are shown for a brain and knee dataset from two different healthy volunteers. All results are shown in a transverse, coronal and sagittal orientation.

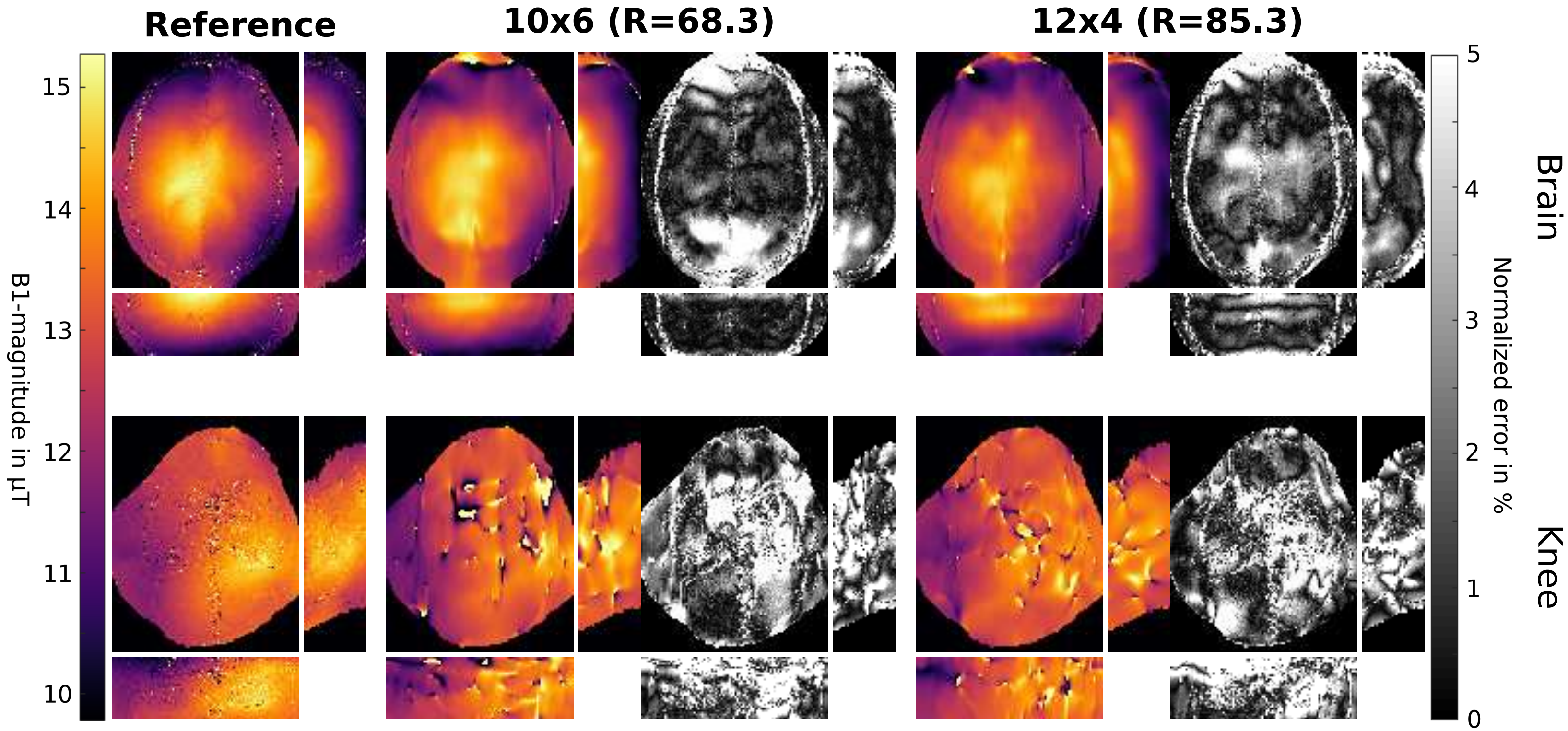

Figure 5.11: *Prospectively subsampled:* B_1^+ map in µT for fully sampled reference and the **zero padded results** with 10×6 and 12×4 encodings in the k-space center and the corresponding error map $\epsilon(\vec{r})$ in percent of the desired B_1^+ peak-magnitude from prospectively subsampled data. The B_1^+ maps are shown for a brain and knee dataset from two different healthy volunteers. All results are shown in a transverse, coronal and sagittal orientation.

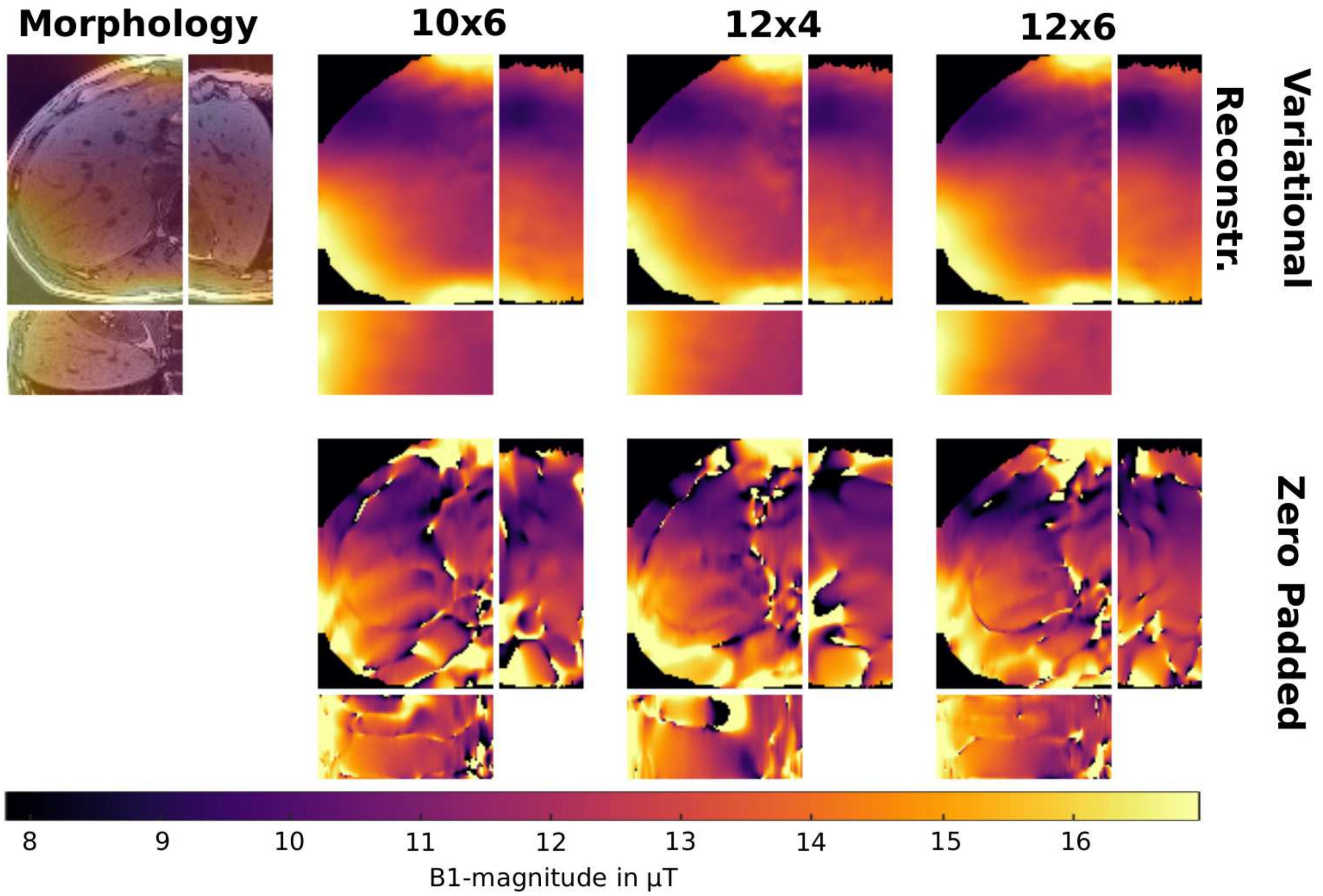

Figure 5.12: *Prospectively subsampled:* B_1^+ map in µT as result of our proposed variational reconstruction method with 10×6, 12×4 and 12×6 encodings in the k-space center in the liver of a healthy volunteer. These results are compared to those gained with zero padding using the same amount of data. The datasets were measured prospectively subsampled and acquired in a single breath hold. Due to the lack of a reference in the liver dataset, the reconstructed B_1^+ map (10×6 encodings) is also shown as an overlay to a morphological scan to show the underlying morphological structure. All results are shown in a transverse, coronal and sagittal orientation.

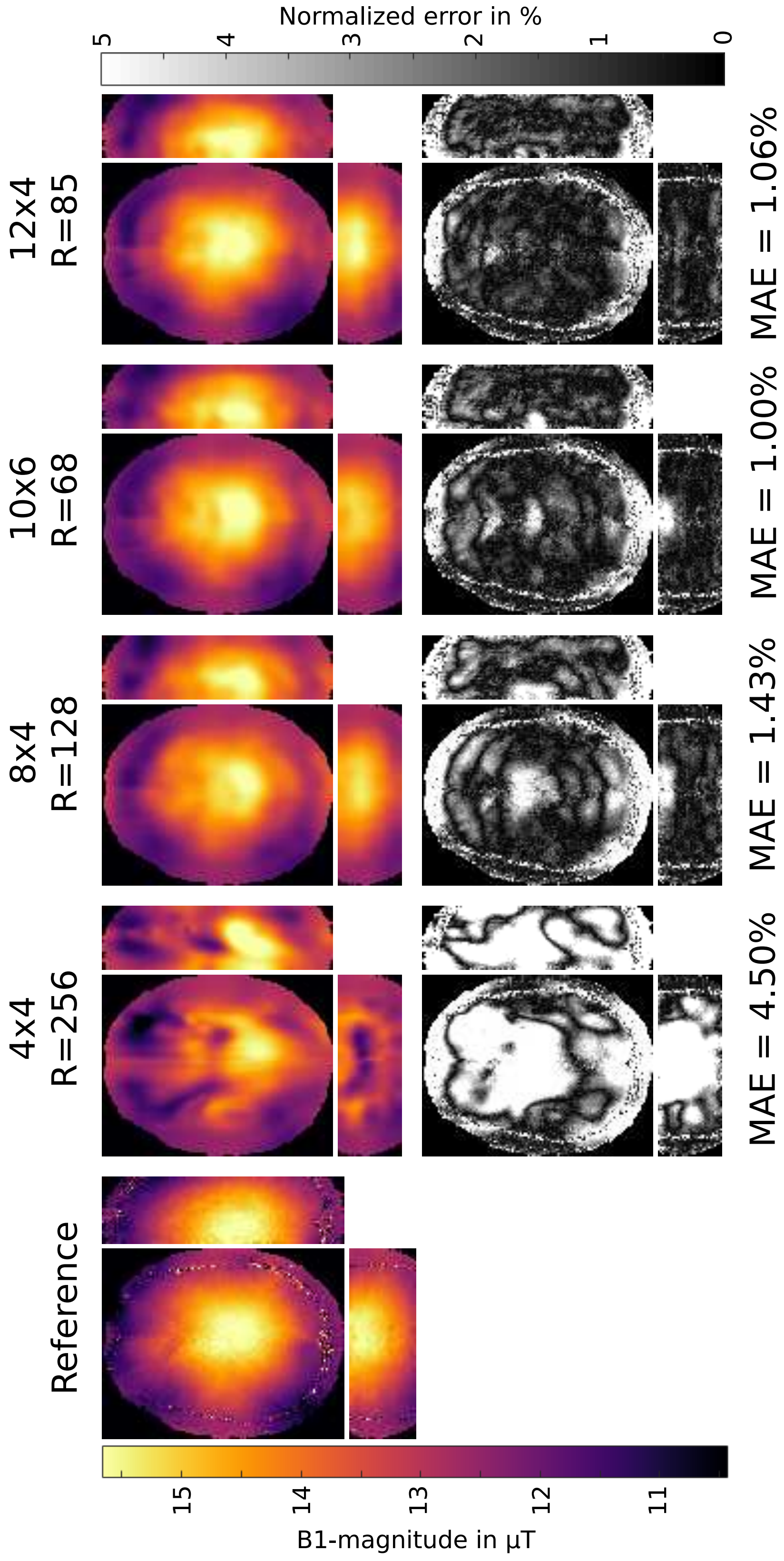

Figure 5.13: *Retrospectively subsampled:* B_1^+ map in µT for fully sampled reference and the result of our proposed variational reconstruction method with 4×4, 8×4, 10×6 and 12×4 encodings in the k-space center and the corresponding error map $\epsilon(\vec{r})$ in percent of the desired B_1^+ peak-magnitude from retrospectively subsampled data. The receive coil sensitivity maps C_n used for the reconstruction are estimated directly from the undersampled data. All results are shown in a transverse, coronal and sagittal orientation.

		individually optimized regularization parameters			**globaly optimized regularization parameters**			**coil sensitivities from undersampled data**		
pattern	R_{acc}	MAE in %	medAE in %	$q_{99\%}$ in %	MAE in %	medAE in %	$q_{99\%}$ in %	MAE in %	medAE in %	$q_{99\%}$ in %
4 × 4	256.0	1.304	0.996	5.897	1.433	1.062	6.518	4.498	3.377	22.031
6 × 4	170.7	0.918	0.695	4.058	0.938	0.700	4.220	2.723	1.862	14.079
6 × 6	113.8	0.839	0.637	3.685	0.846	0.637	3.747	2.436	1.651	13.143
8 × 4	128.0	0.799	0.618	3.242	0.812	0.622	3.350	1.429	1.129	5.590
8 × 6	85.3	0.730	0.553	3.079	0.747	0.564	3.216	1.229	0.902	5.265
8 × 8	64.0	0.710	0.539	2.996	0.728	0.549	3.120	1.153	0.859	4.925
10 × 4	102.4	0.727	0.559	3.028	0.731	0.558	3.084	1.175	0.944	4.268
10 × 6	68.3	0.667	0.506	2.854	0.669	0.504	2.891	1.002	0.777	4.044
12 × 4	85.3	0.658	0.509	2.722	0.665	0.512	2.799	1.059	0.855	3.863
12 × 6	56.9	0.607	0.462	2.562	0.609	0.463	2.593	0.876	0.673	3.545
12 × 12	28.4	0.572	0.436	2.404	0.573	0.437	2.417	0.784	0.577	3.467

Table 5.2: The error measures MAE, medAE, and $q_{99\%}$ are given for reconstruction results obtained with the proposed variational reconstruction approach for different conditions and different undersampling pattern sizes with respect to the fully sampled reference. In the fist column group the error measures are given for individually optimized regularization parameters for each pattern size, giving the best achievable result. The second column group shows the error measures for globally optimized and fixed regularization parameters for each pattern size, as it is done for all other reported results. The third and last column group shows the error measures for reconstruction results obtained with receive coil sensitivity profiles estimated directly from the undersampled data, to give a more realistic scenario.

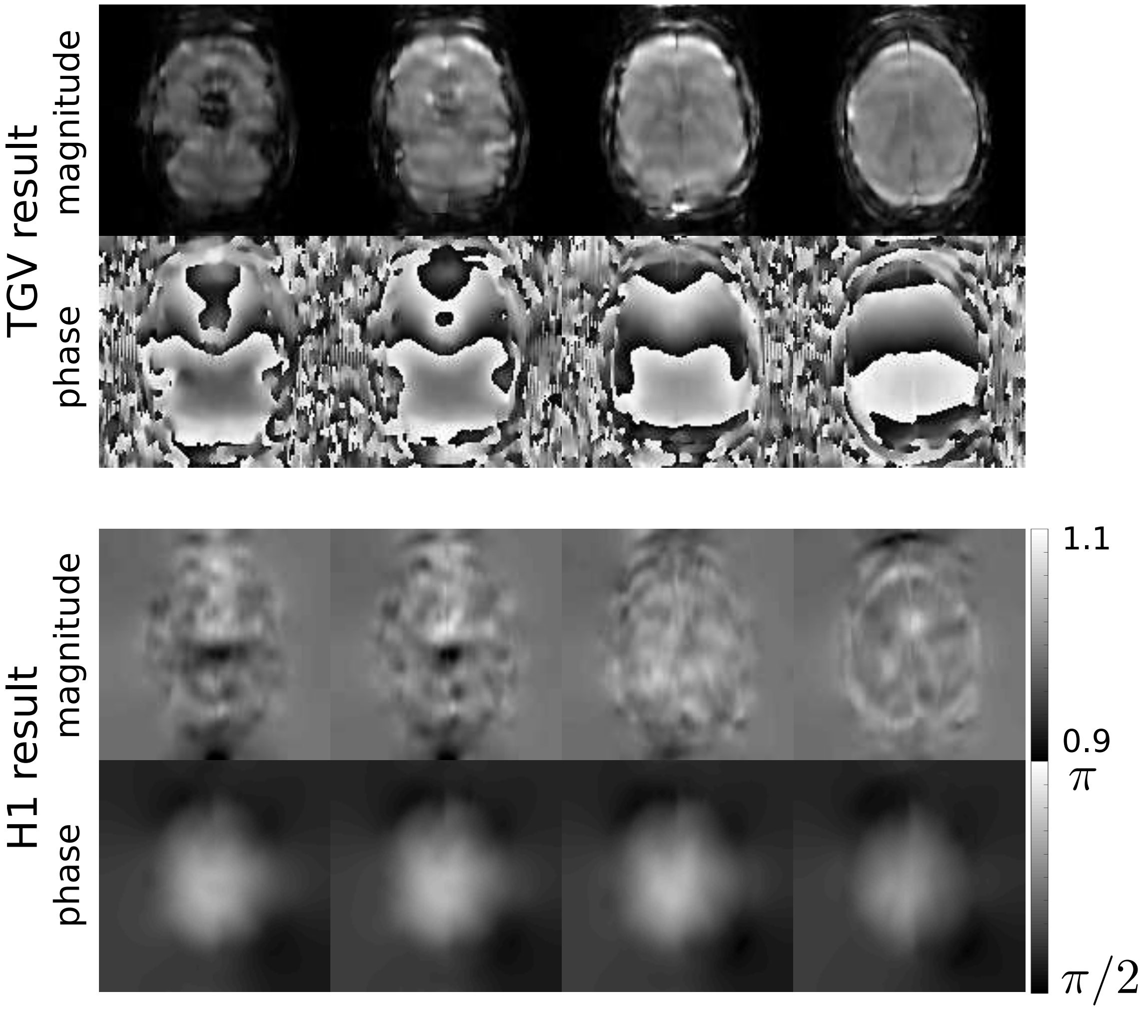

Figure 5.14: Intermediate reconstruction results given as magnitude and phase after the first step, the TGV part ($\hat{u}$ in Eq. (5.8)), and after the second step, the H_1 part of the reconstruciton ($\hat{v}$ ind Eq. (5.9)) for a block pattern size of 12×4. The results of the TGV reconstruction are of poor quality, which is obvious for this very low amount of data. However, the phase can be stabilized by the TGV regularization, so that high quality B_1^+ maps can be obtained. The phase of the H_1 part is basically the final result, except a square root and a scaling operation, whereas the magnitude is more interesting here. The magnitude of $\hat{v}$ is scaled between 0.9 and 1.1, hence, it deviates only slightly from the desired value of 1 (see Eq. (5.5)), even though the optimization was not explicitly restricted to that.

5.2.4 Discussion

In this work we presented a variational two-step approach to reconstruct the B_1^+ field from highly subsampled *BS* data. Different undersampling strategies were investigated on the basis that the spatially smooth B_1^+ field information mostly relies on low spatial frequencies in the k-space center. In the initial hypothesis, we assumed that it might be advantageous to sample a broader distribution of spatial frequencies for the reconstruction of the *TGV* regularized part, S_+, to better characterize the morphological basis. The performed undersampling experiments, however, showed that it is more important to sample a dense k-space center region for both *BS* acquisitions and to encode in both measurements the identical k-space lines. This behavior can be probably explained that undersampling artifacts depend on the specific encoding pattern and their suppression is more effective for similar occurrence in both parts of the reconstruction. It could be shown that two different instances of a random pattern with the same distribution parameters exhibit substantially more artifacts in the final B_1^+ map compared to the reconstruction results using the identical encoding pattern. The investigation of the error for different distributed sampling patterns showed a flat minimum for a compact sampling in the k-space center. The retrospective undersampling study (see Figure 5.6) suggest that a compact sampling with a block-pattern of similar ratio as the imaging matrix yields nearly as good results as with Gaussian distributed dense sampling (see Figure 5.9) in terms of accuracy and achievable acceleration. Thus, the block sampling approach was implemented for in-vivo measurements to simplify the acquisition protocol.

In contrast to this work, the authors in [265] used the *SPIRiT* method [196] to perform a joint reconstruction with staggered pattern, the acceleration potential was only investigated on top of a fixed number (20 × 20, 32 × 32) of auto calibration lines in a multi-transmit system, which reduces the effective acceleration. Since the proposed algorithm also includes the principles of parallel imaging, it relies on the precomputation of receiver coil sensitivities. For high acceleration factors this translates to an increased error when the highly subsampled *BS* data is used for estimation (see Figure 5.13). It is then recommended to either use prescan calibration data or a concurrently measured dataset after the *BS* calibration scan for sensitivity profile estimation. However, it could be also shown that for moderate pattern sizes (e.g.. 12 × 4), the introduced error is lower than 0.3 % in average (see Table 5.2). This is usually lower than other errors introduced by the measurement or modeling assumptions, influencing the final B_1^+ map. All other presented results are reconstructed using coil sensitivity maps estimated out of fully sampled data (assuming "perfect" sensitivity profiles), so that the performance of the reconstruction algorithm can be investigated without the influence of imperfection in the coil sensitivity estimation. The application of the proposed method to *pTX* data and different k-space trajectories is straight forward and will be subject to future research. A question which may arises is the ability to capture very localized B_1^+ field variations occurring for parallel transmit coils or at higher field strength. To give an idea of the behavior, the experiment in Figure 5.15 shows the B_1^+ map in a phantom placed very close to the elements of a small-animal birdcage coil. Near these elements very localized B_1^+ field inhomogeneities occur which can be captured quite well with the proposed method. Nevertheless, depending on a specific coil configuration, a detailed examination of the undersampling pattern would be necessary, which might lead to larger block sizes.

The investigation concerning the dependency of the reconstruction quality on the model

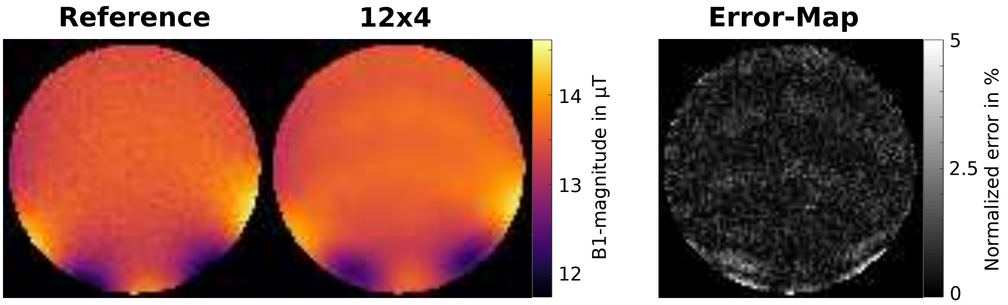

Figure 5.15: *Prospectively subsampled:* B_1^+ map in µT for fully sampled reference and the proposed variational reconstruction method measured with a block size of 12×4. The measurement was performed with a TX/RX small-animal birdcage coil with an inner diameter of 4 cm. The cylindrical agar phantom was placed very close to the elements of the birdcage, leading to localized B_1^+ field variations similar as in a parallel transmit setting. The measurement was performed using a FOV of 40 mm and a flip angle $\alpha = 12°$. To achieve optimal reconstruction results for this special case the regularization parameters have to be retuned, leading to the following values: $\lambda_1 = 5$, $\lambda_2 = 16 \cdot 10^{-4}$

parameters λ_1 and λ_2 showed that these are fairly stable over a wide range and across different pattern sizes for a given *SNR* scenario. Since the *SNR* is usually only altered slightly, it is possible to achieve robust reconstruction results without additional tuning. Even though, if the regularization parameters are tuned for each pattern size individually, the achieved improvement is $< 0.1\,\%$ for every error measure (see Table 5.2), indicating the robustness of the algorithm against slightly mistuned regularization parameters and their independence of different pattern sizes. *GPU* powered reconstruction on a NVIDIA Geforce Titan Xp *GPU* takes about 30 s for the complete 3D measurement.

General limitations of the *BS* method are phase drifts or phases fluctuations between positive and negative *BS* encoding. Although the used interleaved acquisition scheme [176] makes the method more robust against phase drifts, phase fluctuations may still be an issue within regions with fast and pulsatile phase changes such as large arteries. In Figure 5.12 this becomes visible, e.g. in the right part of the liver dataset due to heart motion or in Figure 5.10 within the knee dataset due to blood flow in the leg artery. Since the proposed method enforces smoothness on the B_1^+ field, the error due to local disturbances is effectively suppressed and interpolated based on the local neighborhood in the resulting B_1^+ map (see knee dataset in Figure 5.10). In Figures 5.6 and 5.10, the described interpolation effect leads to an alleged increased error in the cranial bone structure where the fully sampled reference exhibits low signal leading to an uncertainty in the reference map. Therefore, this region was excluded from the error analysis.

In this work, we also performed an investigation about the feasible acceleration potential for 3D acquisitions and the expectable error in the B_1^+ field with respect to the fully sampled reference. For all investigated regions, receiving array coils with 20 to 32 active coils were used. For these applications acceleration factors from 80 to 100 were achieved that reduces the acquisition time into the range of 10 s to 12 s for the whole 3D dataset.

From retrospective undersampling experiments mean errors below 1 % and maximal errors below 4 % were observed for the investigated setting and used acceleration factors. Further acceleration is achievable for a higher number of independent receiver coils or by sacrificing accuracy.

Similar acquisition times for whole brain coverage are still possible by a combination of *BS* based B_1^+ mapping with spiral readouts and optimized *BS* pulses (12 s) [152, 250] or below 40 s combined with an *EPI* readout [71]. However, these methods are prone to artifacts in particular at high and ultrahigh field strength. Nevertheless, the combination of the proposed method with such trajectories is straight forward and further acceleration can be expected. For regions that allow a long readout train 3D single shot acquisition might be feasible. However, in this work we focused on the robust implementation of accelerated *BS* mapping for widely available Cartesian imaging. In a recent work [318], a method is described, where interleaved acquisition and Electrocardiography (ECG) triggering are combined in a proper way to acquire cardiac B_1^+ maps. By a combination of this approach and the proposed method a 3D cardiac B_1^+ map in a few heart beats seems possible.

5.2.5 Conclusions

A new highly accelerated 3D B_1^+ mapping method based on the *BS* shift and reconstruction by variational modeling was introduced. The method is able to reconstruct 3D B_1^+ maps from parallel acquired Cartesian encodings within a typical breath-hold period of a patient by using acceleration factors of up to 100. With Cartesian encoding, the method is stable even at very high field strength. The reconstruction errors were estimated from retrospective undersampling experiments and were found to be below 1 % in mean and 4 % in maximum.

5.3 3D Bloch-Siegert EPI B_1^+ Mapping

The results achieved with the reconstruction algorithm presented in the previous section (Section 5.2) are already impressive in terms of accuracy and acceleration. There, the data acquisition was performed on the basis of a quite robust *GRE* sequence. In this section, the combination of the reconstruction algorithm with a faster acquisition trajectories, i.e. the *EPI* sequence (see Section 2.1.8.3), and the feasibility of a two shot acquisition for a 3D volume is exploited.

5.3.1 Methods

A 3D *EPI* Spin Echo (SE) sequence with segmented acquisition in slice encoding direction with an echo train length of 128 was implemented using the open source sequence development tool known as Pulseq [170]. Figure 5.16 depicts the main sequence elements and their timing. We used a slab selective excitation pulse with an flip angle of $\alpha = 25°$ and a non-selective rectangular refocusing pulse together with symmetric

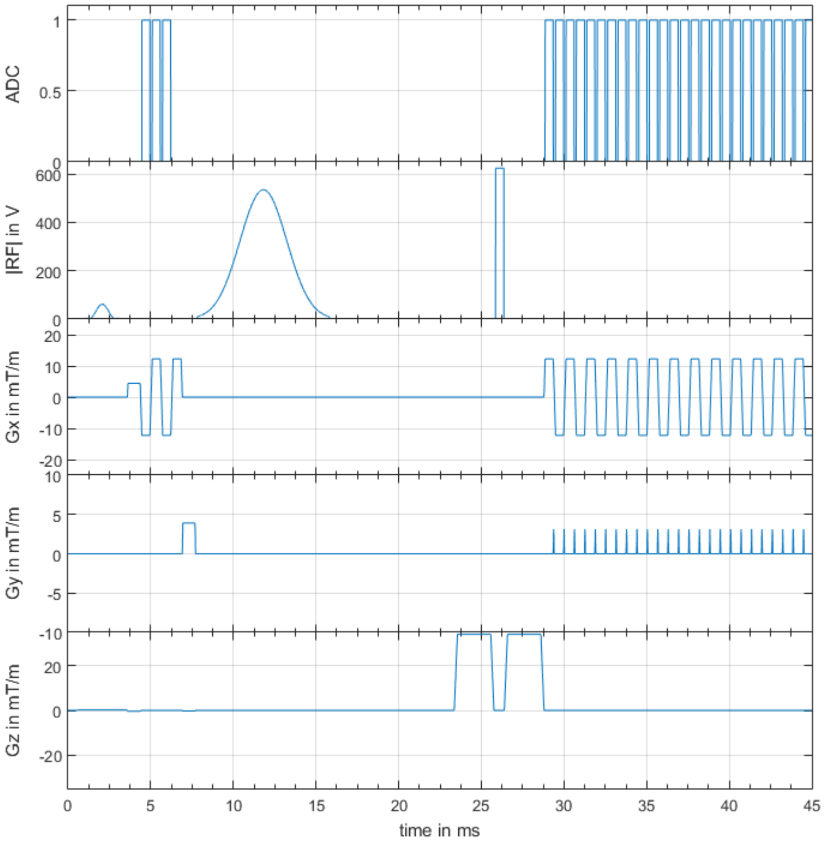

Figure 5.16: Sequence Diagram for the BS EPI SE sequence. Three reference lines are acquired after excitation for N/2 EPI ghost correction followed by the offresonant BS pulse. After the 2nd crusher gradient of the non-selective refocusing the EPI readout starts.

crusher gradients. An offresonant *BS* pulse with a duration $T_p = 8\,\text{ms}$, a resonance offset $\Delta\omega_{\text{RF}} = 4\,\text{kHz}$, and an onresonant equivalent flip angle $\alpha_{\text{BS}} = 1000°$ leading to a pulse constant $K_{\text{BS}} = 35.7\,\text{rad}\,\text{G}^{-2}$ was inserted between the excitation and refocusing pulse. With this sequence we acquired a 3D dataset of a cylindrical water phantom on a 3 T *MR* system (Skyra, Siemens, Erlangen, Germany). The following imaging parameters were used, leading to a total acquisition time of $T_{\text{aq}} = 22\,\text{s}$: FOV $= 250\,\text{mm}$, a matrix size of $128 \times 128 \times 32$, 37.5 % slice oversampling, readout bandwidth of 2041 Hz/pix, TR $= 250\,\text{ms}$, TE $= 105\,\text{ms}$ and a resolution of 5 mm in slice direction.

The variational reconstruction algorithm for undersampled *BS* measurements and consists of a two-step procedure. Both steps are defined by solving an optimization problem. In the first step a *TGV* regularization term [38, 159], which enforces piece wise smooth solutions, is applied to reconstruct the magnitude and phase of the underlying image. In the second step a smoothness constraint is applied to stabilize the spatial smoothness of

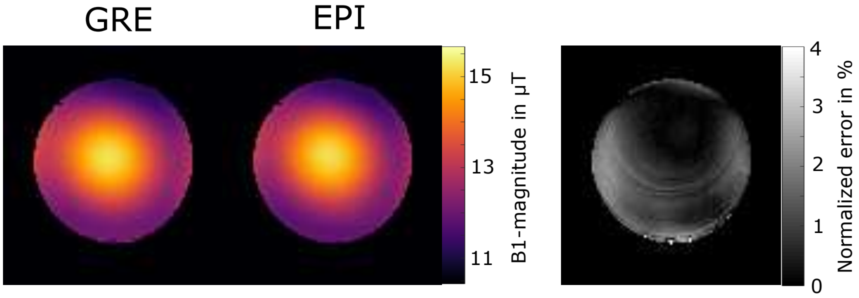

Figure 5.17: One representative B_1^+ map in µT from fully sampled data acquired with GRE and EPI. The normalized difference map between the GRE and EPI acquisition on the right side shows the good accordance between this two approaches.

the underlying B_{1+} field defined as follows (for further details we refer to Section 5.2):

$$\hat{u} = \arg\min_{u} \frac{\lambda_1}{2} \|d_+ - A_+(u)\|_2^2 + \mathrm{TGV}_\alpha^2(u) \tag{5.12}$$

$$\hat{v} = \arg\min_{v} \frac{\lambda_2}{2} \|d_- - A_-(\hat{u} \odot v)\|_2^2 + \|\nabla_{xyz}^+ v\|_2^2 = e^{-j2\phi_{\mathrm{BS}}} \tag{5.13}$$

Here, d_+ and d_- are the acquired undersampled k-space data for positive and negative resonance offset acquisition, respectively, and $A_+(u)$ and $A_-(u)$ are the are the *MR* forward operators according to Eq. (5.6). The regularization parameters λ_1 and λ_2 where chosen as follows: $\lambda_1 = 64$ and $\lambda_2 = 15 \cdot 10^{-4}$. To investigate the potential of the proposed method for a two shot acquisition, the fully sampled data set was retrospectively under-sampled using block sampling patterns of different sizes, summarized in Table 5.3. For the evaluation the *MAE* compared to the fully sampled reference, its median *medAE* and its 99 % quantile $q_{99\%}$ were used. Additionally, a fully sampled *BS* 3D dataset with the *GRE* based acquisition was used as reference ($T_{\mathrm{aq}} = 15\,\mathrm{min}$).

5.3.2 Results

In Figure 5.17, a comparison between *EPI* and *GRE* acquisition is shown, where only very small deviations can be observed. Figure 5.17 shows the results gained with our variational reconstruction method from under-sampled 3D *EPI SE* data compared to a zero padded low resolution estimate. The dedicated reconstruction method lead generally to lower errors in comparison to the full sampled reference measurement. Even for the very small kernel size of 6 × 4 encodings, good results could be achieved with the *EPI* acquisition for the phantom. The lager k-space block with 10 × 4 and 12 × 6 should certainly work in-vivo and can be typically implemented as a single shot. A summary of all investigated under-sampling patterns is given in Table 5.3 showing a reduction of all error measures.

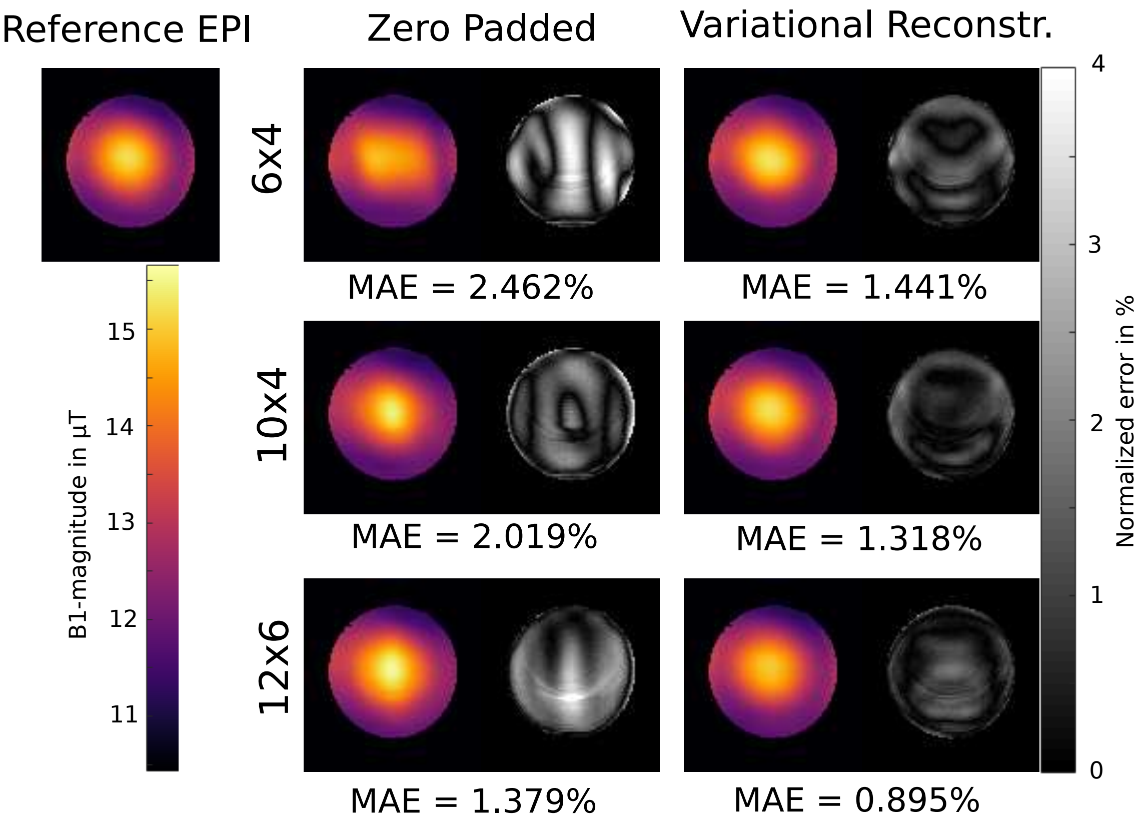

Figure 5.18: B_1^+ map in µT for fully sampled reference, zero padded low resolution estimate and the result of the variational reconstruction algorithm for a retrospectively subsampled dataset in a cylindrical water phantom for block sizes of 6 × 4, 10 × 4 and 12 × 6 encoding in k-space center. One representative slice of a 3D-dataset is shown. The right part of each column shows the error map $\epsilon(\vec{r})$ for the corresponding result as normalized error in percent of the desired B_1^+ magnitude. The MAE is given as the mean of the error map over a certain ROI inside the cylinder.

5.3.3 Discussion and Conclusion

With the proposed strategy we could show that similar acceleration factors are achievable with *EPI* as stated in Section 5.2, where a much more robust *GRE* readout was used. In the performed measurement, we used an echo train length for the *EPI* readout of 128, which means that even for the large block pattern size of 14×8 encodings in k-space center the echo train length would be shorter, showing the feasibility that the goal of a two shot acquisition (two different *BS* pulses) of the whole 3D volume is more than feasible. The challenge for the *EPI* based measurement consists in the influence of B_0 inhomgenities and chemical shift effects. But in all situation where other *EPI* based measurements are possible (diffusion, perfusion) the 3D *EPI* based B_1^+ mapping should also be applicable. With only two *BS* pulses the *SAR* is reduced to a minimal fraction.

pattern	R_{acc}	**ZeroPadded**			**Variational Reconstruction**		
		MAE in %	medAE in %	$q_{99\%}$ in %	MAE in %	medAE in %	$q_{99\%}$ in %
6 × 4	170.7	2.462	2.007	8.570	1.441	0.898	7.181
8 × 4	128.0	2.070	1.565	8.672	1.364	0.840	6.963
10 × 4	102.4	2.019	1.426	9.262	1.318	0.770	6.985
10 × 6	68.3	1.437	0.922	7.063	0.925	0.625	4.429
12 × 4	85.3	1.970	1.347	9.475	1.314	0.782	6.930
12 × 6	56.9	1.379	0.854	7.045	0.895	0.596	4.342
14 × 8	36.6	1.110	0.885	4.480	0.844	0.636	3.283
16 × 10	25.6	0.916	0.670	4.423	0.838	0.636	3.822

Table 5.3: MAE, medAE and $q_{99\%}$ inside a certain ROI for different block sizes in percent of the desired B_1^+ magnitude and the corresponding acceleration factor R_{acc}. The values are given for the zero padded low resolution estimate and the results of the variational reconstruction algorithm.

5.4 Highly accelerated 3D Bloch Siegert B_1^+ Mapping at 7T

Fast and accurate B_1^+ mapping is a very important prerequisite at high and Ultrahigh Field (UHF) for various applications. However, at *UHF* 3D *BS* B_1^+ mapping is in particular limited by high energy deposition of multiple offresonant *RF* pulses resulting in unacceptable long acquisition times. To overcome this problem, the reconstruction algorithm presented in Section 5.2 was applied to 7 T data, acquired with a *GRE* based sequence. The much more pronounced spatial *RF* field variations and energy deposition at 7 T makes an investigation according the performance and accuracy of the reconstruction algorithm necessary. In this section, the performance of the proposed *BS* based B_1^+ mapping technique is investigated for phantom and in-vivo data at 7 T.

5.4.1 Theory and Methods

The variational reconstruction algorithm consists of a two-step procedure, defined by solving two optimization problems. In the first step a *TGV* regularization term [38, 159] (see Section 3.2.4.4), enforcing piece wise smooth solutions, is applied to reconstruct the magnitude and phase of the underlying image. In the second step a smoothness constraint is applied to enforce the spatial smoothness of the underlying B_1^+ field defined as follows:

$$\hat{u} = \arg\min_{u} \frac{\lambda_1}{2} \|d_+ - A_+\left(u\right)\|_2^2 + \mathrm{TGV}_\alpha^2\left(u\right) \tag{5.14}$$

$$\hat{v} = \arg\min_{v} \frac{\lambda_2}{2} \|d_- - A_-\left(\hat{u} \odot v\right)\|_2^2 + \|\nabla^+_{xyz} v\|_2^2 = e^{-j2\phi_{\mathrm{BS}}} \tag{5.15}$$

A spherical phantom and three healthy subjects were scanned on a 7 T system (Magnetom, Siemens, Erlangen, Germany) with a 1Tx32Rx head coil (Nova Medical, Wilmington,

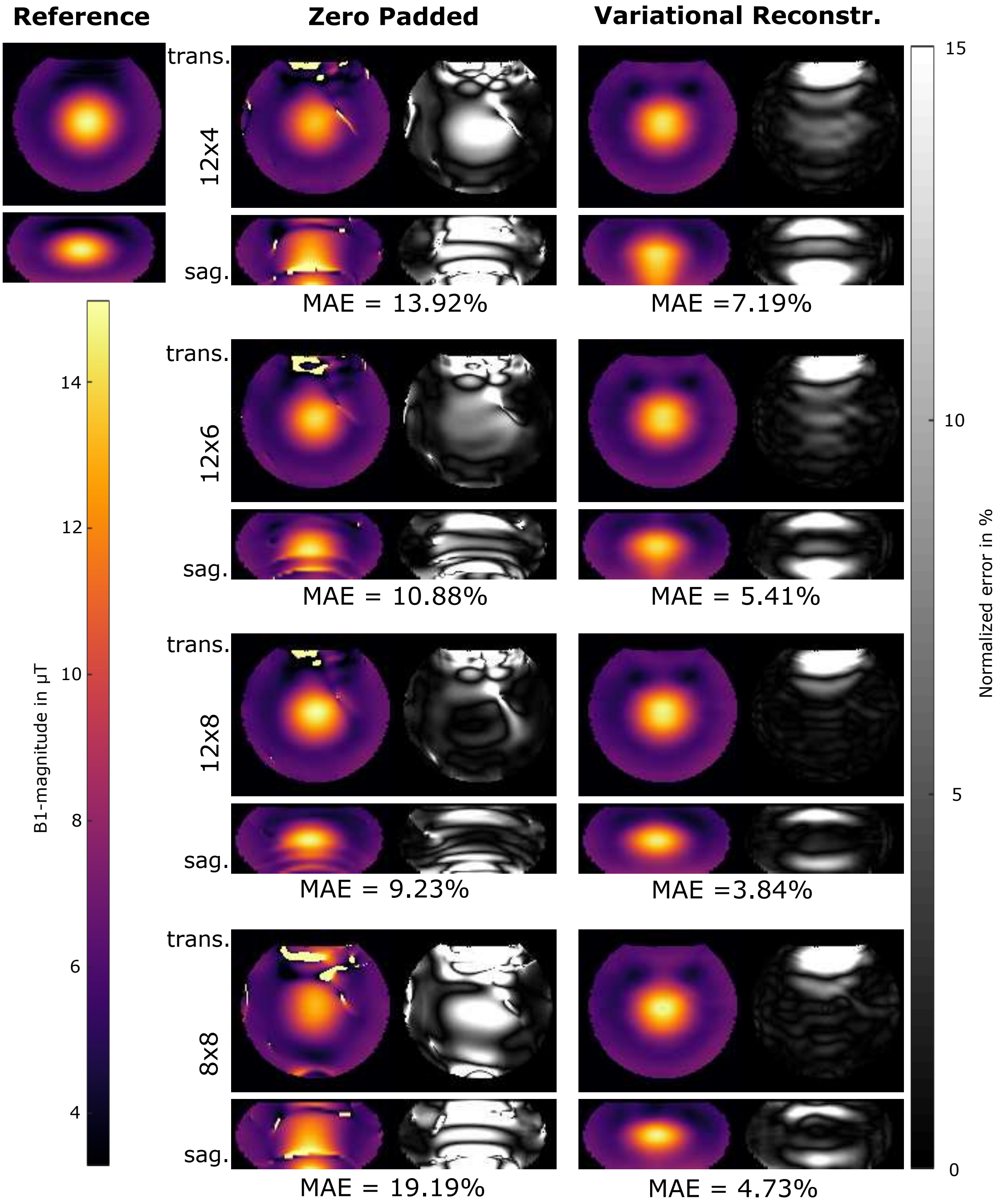

Figure 5.19: B_1^+ map in μT for fully sampled reference, low resolution estimate and the result of the proposed variational reconstruction algorithm for a retrospectively subsampled dataset in a spherical phantom for a block pattern with size of 12×4, 12×6, 12×8, and 8×8. The results are shown as a transversal and a sagittal slice through the 3D dataset. The right part of each column shows the error map $\epsilon(\vec{r})$ for the corresponding result as normalized error in percent of the desired B_1^+ peak magnitude. The MAE is given as the mean of the error map over the whole phantom.

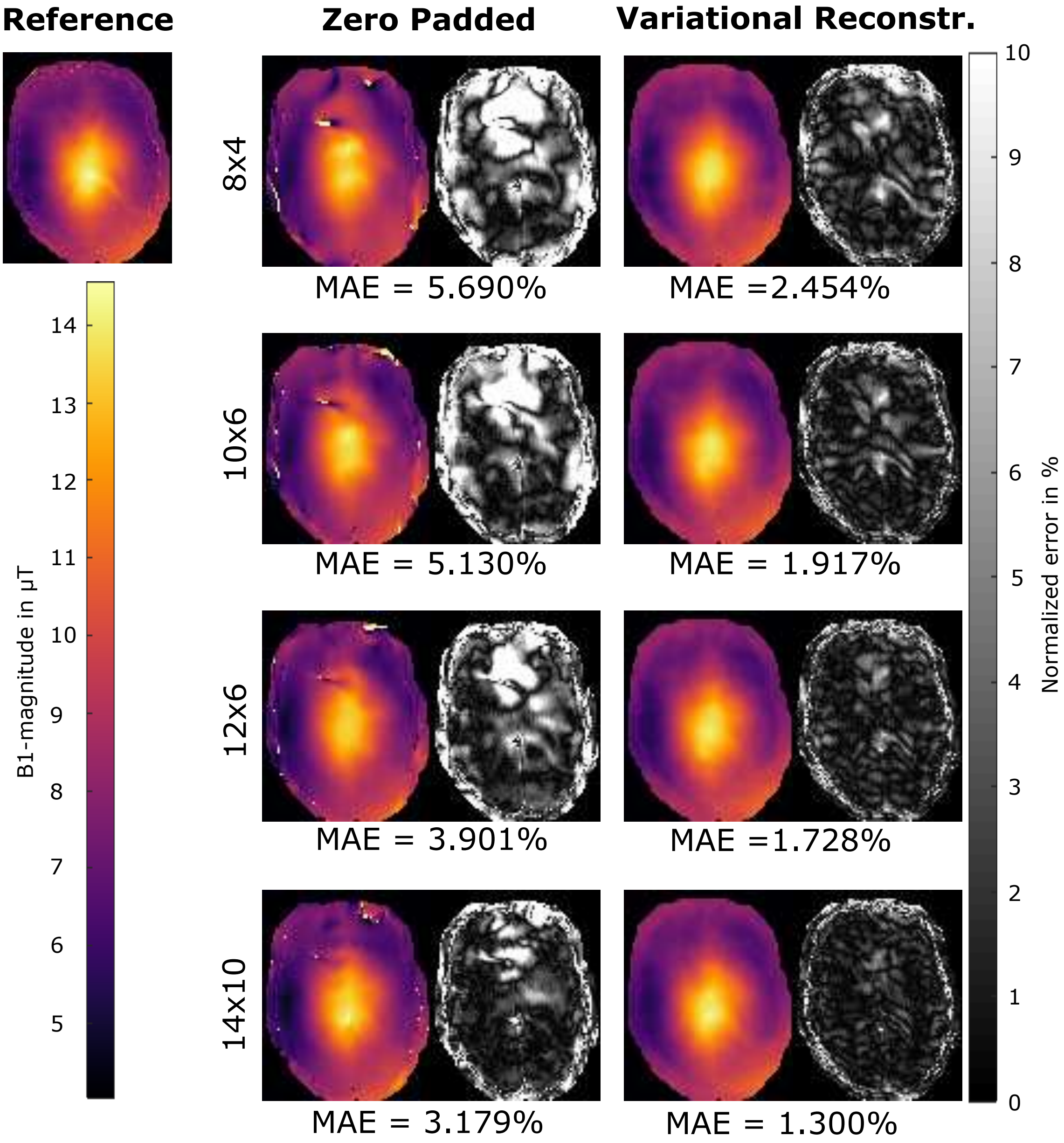

Figure 5.20: B_1^+ map in µT for fully sampled reference, low resolution estimate and the result of the proposed variational reconstruction algorithm for a retrospectively subsampled dataset in the brain of a healthy volunteer for different block patterns with a size of 8×4, 10×6, 12×6, and 14×10. The results are shown as the central slice of a 3D dataset. The right part of each column shows the error map $\epsilon(\vec{r})$ for the corresponding result as normalized error in percent of the desired B_1^+ peak magnitude. The MAE is given as the mean of the error map over the whole brain inside the cranial bone structure for each case.

USA) according to a local IRB approved protocol. The following scan parameters were used to acquire the phantom data: FOV $= 200 \times 200\,\text{mm}$, a slab thickness of 150 mm, an acquisition matrix of $128 \times 128 \times 30$, $T_p = 10\,\text{ms}$, $\alpha_{\text{BS}} = 1000°$, $\omega_{\text{RF}} = 2\pi \cdot 5\,\text{kHz}$. The

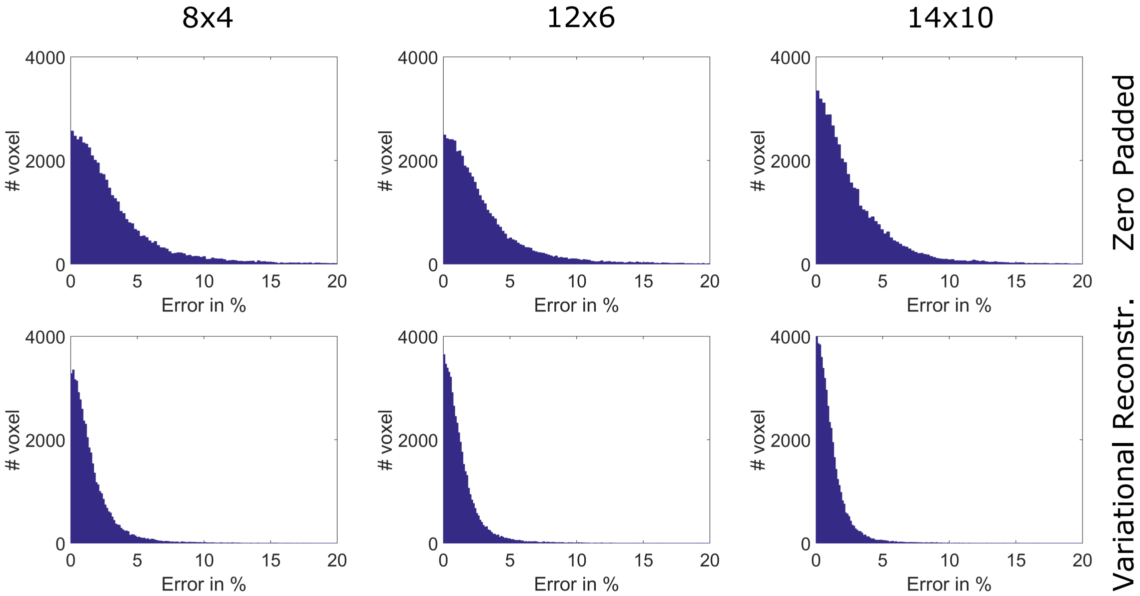

Figure 5.21: Error histogram for the retrospectively subsampled in-vivo dataset acquired at 7 T compared to the fully sampled reference in percent of the desired B_1^+ peak magnitude for different block patterns with size of 8 × 4, 12 × 6 and 14 × 10 encodings in the k-space center. The error histograms are shown for zero padded low resolution estimate and the result of our proposed variational reconstruction algorithm.

in-vivo dataset was acquired using: FOV = 256 × 192 mm, a slab thickness of 80 mm, an acquisition matrix of $128 \times 96 \times 16$, TR = 160 ms, TE = 15 ms and 25 % slice oversampling. A Fermi shaped *BS* pulse with duration of $T_p = 7\,\text{ms}$, an on-resonant equivalent flip angle of $\alpha_{BS} = 600°$, and a resonance offset of $\omega_{\text{RF}} = 2\pi \cdot 4\,\text{kHz}$ leading to a pulse constant $K_{\text{BS}} = 70.93\,\text{rad}\,\text{G}^{-2}$ was used. The regularization parameters λ_1 and λ_2 were adjusted doing a parameter sweep to $\lambda_1 = 10$ and $\lambda_2 = 1.2 \cdot 10^{-2}$.

Data were retrospectively subsampled using a block pattern with different sizes, where only $n \times m$ lines in k-space center were acquired as described in Section 5.2. The reconstruction results were compared to a fully sampled reference and for each result an error map $\epsilon(\vec{r})$ with respect to the fully sampled reference is shown. Each result was further evaluated by *MAE*, median value *medAE* and the 90 % quantile $q_{90\%}$ over a *ROI* inside the subject's brain.

5.4.2 Results and Discussion

Figure 5.19 (phantom) and Figure 5.20 (in-vivo) show the reconstructed 3D B_1^+ maps after zero filling and the proposed variational reconstruction approach for 4 different pattern sizes together with a fully sampled reference. The difference map and the *MAE* indicate substantial improvement of the proposed method compared to zero filling in both cases. The limitation of this method can be seen in the sagittal plane of Figure 5.19 (12 × 4

		Zero Padding			Variational Reconstruction		
pattern	R_{acc}	MAE in %	medAE in %	$q_{90\%}$ in %	MAE in %	medAE in %	$q_{90\%}$ in %
16 × 12	10.0	3.03	1.97	6.37	1.13	0.81	2.41
14 × 10	13.7	3.18	2.08	6.75	1.30	0.93	2.78
12 × 8	20.0	3.46	2.29	7.32	1.54	1.09	3.34
12 × 6	26.7	3.90	2.68	8.27	1.73	1.22	3.75
12 × 4	40.0	4.91	3.44	10.82	2.06	1.40	4.59
10 × 6	32.0	5.13	3.58	11.19	1.92	1.37	4.15
10 × 4	48.0	5.13	3.58	11.19	2.22	1.54	4.93
8 × 8	30.0	5.69	3.77	12.04	1.97	1.42	4.28
8 × 6	40.0	5.69	3.77	12.04	2.16	1.55	4.74
8 × 4	60.0	5.69	3.77	12.04	2.45	1.72	5.47
6 × 6	53.3	6.85	4.35	14.41	2.51	1.80	5.49
6 × 4	80.0	6.85	4.35	14.41	2.89	2.02	6.44
4 × 4	120.0	8.35	5.78	16.54	3.38	2.52	7.32

Table 5.4: MAE, medAE and $q_{90\%}$ inside the cranial bone structure of the in-vivo dataset acquired at 7 T using different block sizes in percent of the desired B_1^+ peak magnitude. The values are given for the zero padded low resolution estimate and the result of the proposed variational reconstruction algorithm.

pattern) where the B_1 hotspot in the center of the phantom is blurred out in z-direction as a result of insufficient k-space data. Interestingly, for a block size of 12 × 6 we observe slight blurring only in the phantom data. Even though, for the pattern size of 8 × 8 only 1.7 % of the k-space data was used, the average error stays below 5 %. Table 5.4 lists the *MAE*, *medAE* and the 90 % quantile for a range of under-sampling pattern sizes and the resulting acceleration factor R_{acc} for the in-vivo measurements. With the pattern size of 10 × 6 (about 2 % of the fully-sampled data) we can reach an average error below 2 % over the whole *FOV* in a scan time of about 45 s with the given TR at 7 T. Figure 5.21 shows the error histograms over the whole brain region inside the cortical bone structure for three pattern sizes for zero padding and the variational reconstruction results. The narrowing in the histograms for the results obtained with the variational reconstruction clearly demonstrates the increased accuracy. Compared to the results at 3 T, reported in Section 5.2, the mean error increased for all pattern sizes from below 1 % at 3 T to about 2 % for medium pattern sizes. For smaller pattern sizes the error increases drastically, indicating that the more pronounced field variations at 7 T cannot be resolved any more. This is further supported by an increase of the optimal regularization parameter λ_2 by more than an order of magnitude from $5 \cdot 10^{-4}$ to $1.1 \cdot 10^{-2}$, indicating that more data weighting is necessary to resolve the field variations.

Figure 5.22 shows reconstruction results for the block pattern sizes of 12 × 6 and 14 × 10 on three different subjects as three slices of the 3D dataset each. The error maps indicate that the previously reported accuracy can be achieved over wide areas through all investigated subjects, however, especially in subject 3, an increased error around the nasal cavities and the ear channel can be observed, indicated by the red arrows. However, a slight non-naturally appearing artifact (white arrow) can be observed in the fully sampled reference as well (first row of each subject). Due to the higher influence of ΔB_0 variations at 7 T, resulting in a faster signal decay, the reference is can be prone to artifacts in these areas. It can be expected that the influence of such errors is reduced in the regularized reconstruction results, even though in the case of undersampling. The corresponding error values (*MAE*, *medAE*, and $q_{90\%}$) are given in Table 5.5.

Compared to 3 T, as expected, these very low acquisition times are not possible at 7 T. Here, a certain compromise between accuracy and acquisition time has to be made, depending on the requirements of the application. Even though, the *RF* energy deposition increases heavily, a minimum acquisition time in the order of 45 s to 1 min is possible.

5.4.3 Conclusion

In this study we successfully applied the proposed algorithm on 7 T phantom and in-vivo data. The mean error was reduced for both in-vivo and phantom measurements compared to zero padding which allows the acquisition of accurate 3D B_1^+-maps in about 45 s.

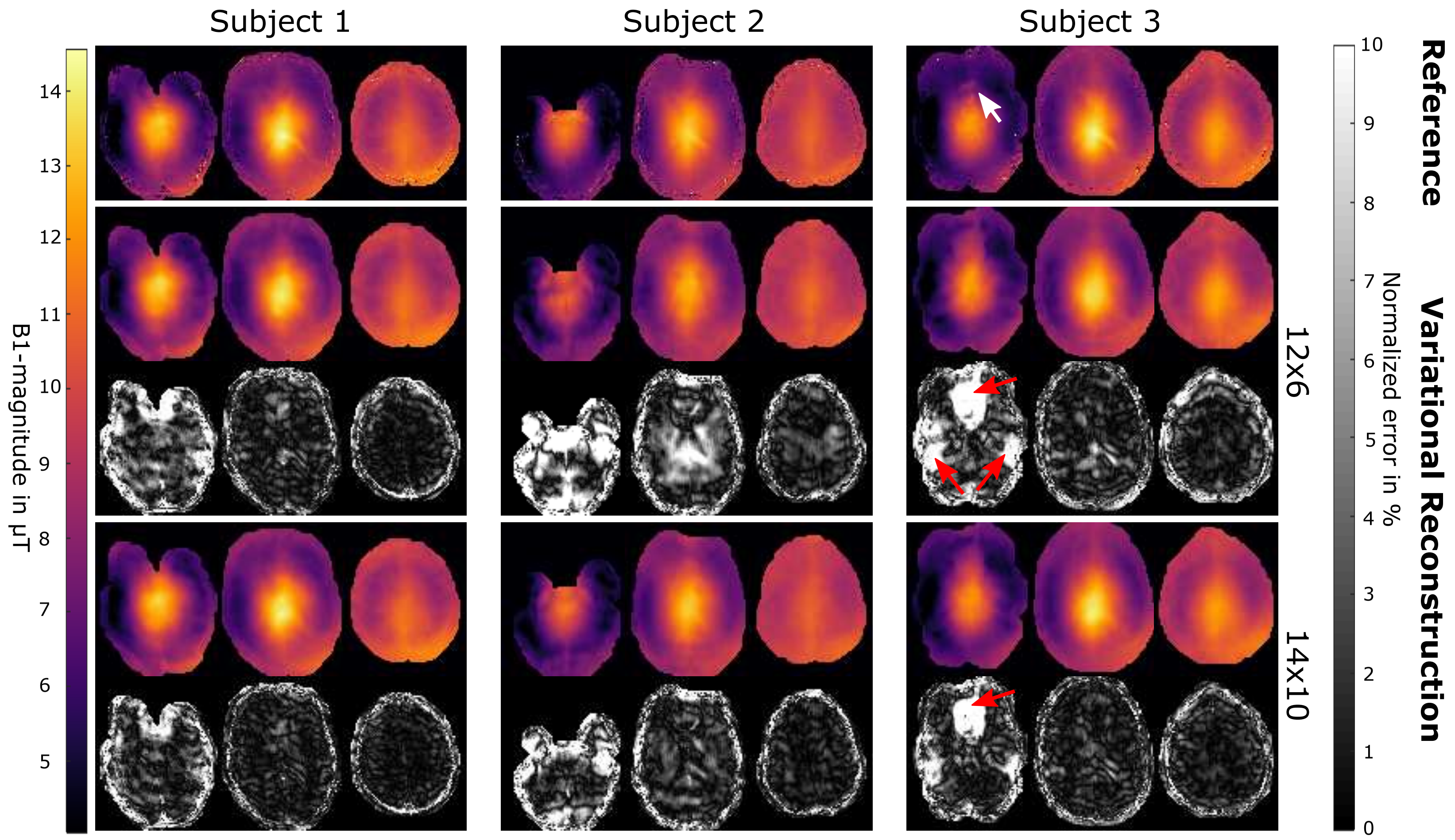

Figure 5.22: B_1^+ map in µT for fully sampled reference and the result of the proposed variational reconstruction algorithm for a retrospectively subsampled dataset in the brain of three healthy volunteers using the block patterns a size of 12×6, and 14×10. The results are shown in three different slices of each 3D dataset. The lower part of each row are the error maps $\epsilon(\vec{r})$ for the corresponding result as normalized error in percent of the desired B_1^+ peak magnitude, with respect to the reference.

	Subject 1			**Subject 2**			**Subject 3**		
patterns	MAE in %	medAE in %	$q_{90\%}$ in %	MAE in %	medAE in %	$q_{90\%}$ in %	MAE in %	medAE in %	$q_{90\%}$ in %
16 × 12	1.13	0.81	2.41	1.14	0.92	2.34	1.61	1.04	3.28
14 × 10	1.30	0.93	2.78	1.49	1.20	3.08	1.88	1.21	3.73
12 × 8	1.54	1.09	3.34	2.20	1.74	4.59	2.21	1.38	4.50
12 × 6	1.73	1.22	3.75	2.61	2.01	5.57	2.76	1.74	5.78
12 × 4	2.06	1.40	4.59	2.96	2.22	6.27	3.50	2.23	7.60
10 × 6	1.92	1.37	4.15	2.73	2.07	5.93	2.90	1.83	6.31
10 × 4	2.22	1.54	4.93	3.09	2.30	6.82	3.63	2.33	8.04
8 × 8	1.97	1.42	4.28	2.49	1.97	5.34	2.67	1.70	5.63
8 × 6	2.16	1.55	4.74	2.95	2.29	6.37	3.23	2.06	7.02
8 × 4	2.45	1.72	5.47	3.24	2.37	7.33	3.94	2.55	8.83
6 × 6	2.51	1.80	5.49	3.01	2.33	6.39	3.72	2.34	8.34
6 × 4	2.89	2.02	6.44	3.64	2.84	7.76	4.33	2.85	9.71
4 × 4	3.38	2.52	7.32	4.54	3.56	9.43	4.71	3.41	10.47

Table 5.5: MAE, medAE and $q_{90\%}$ inside the cranial bone structure three different subjects acquired at 7 T using different block sizes in percent of the desired B_1^+ peak magnitude.

6

Chemical Shift based Fat-Water Separation using a Variational Approach for B_0 Correction

If at first you don't succeed,
try, try again.

W. E. Hickson

This chapter is based on the proceeding presented on the ISMRM 2016:

- A. Lesch, K. Bredies, C. Diwoky, and R. Stollberger. Chemical shift based fat-water separation using a variational approach for B0-field correction. In *Proceedings of the 24th Annual Meeting of ISMRM, Singapore*, volume 24, page 1875, 2016

Contents

6.1 Theory and Methods 176
6.2 Results 181
6.3 Discussion 183

In many clinical applications, it is tried to suppress the in general hyperintense fat signal to enable the diagnosis in some regions. The efficiency of fat suppression suffers from ΔB_0 variations and small T_1 values of water dominant tissue (in the range of fat), so that partial saturation effects in the surrounding tissue may occur. An alternative is the separation of both signal components with the additional benefit that a fat fraction map can be calculated out of both signal, which can serve as biomarker for several diseases. Most of the today available state of the art methods are based on the seminal work from Dixon [67], where the main challenge is to provide an accurate ΔB_0 field map. Over the years, many methods were proposed based on this idea, trying to reduce the influence of

ΔB_0 on the separation result. Most of them use heuristic approaches as region growing based on quality measures, in combination with phase unwrapping and a smoothness constraint. Good solutions are available with their specific advantages and disadvantages, but a fundamental solution still does not exist, because of the strong non-convexity and non-linearity of the problem. The basics of fat water separation, different signal models, and a review over existing Dixon based methods is given in Section 4.1.

In this section, a new approach for the fat/water signal separation problem is presented, by using variational methods. This approach uses a Total Generalized Variation (TGV) based regularization functional to stabilize the solution of the field map. Referring to Sections 2.2.2.2 and 2.2.4, the B_0 field is only smooth inside a homogeneous tissue, discontinuities can occur along tissue boundaries oriented parallel to the main field direction. This fact is often neglected, which could lead to errors around tissue boundaries. This drawback can be overcome by the use of the *TGV* functional (see 3.2.4.4). Furthermore, ΔB_0 is obtained as the global optimal solution of a convex optimization problem, with respect to the *TGV* constraint, enforcing piecewise smooth solutions, which does not depend on the initial seed voxel or the processing order. Nevertheless, it cannot be guaranteed that the obtained global optimal solution is the correct one.

6.1 Theory and Methods

The fat signal is modeled by utilizing the multi-peak fat model according to Eq. (4.5). With that, the signal $S_q(\tau_n)$ at echo time τ_n in a voxel q can be described as

$$S_q(\tau_n) = \left(S_{W,q} + S_{F,q} \sum_{m=1}^{N_F} \alpha_m e^{j\Delta\omega_{F,m}\tau_n} \right) e^{j\gamma\Delta B_{0,q}\tau_n} e^{-R^*_{2,q}\tau_n}, \tag{6.1}$$

where $S_{W,q}$ is the water signal contribution, $S_{F,q}$ is the fat signal contribution, and $\Delta B_{0,q}$ is the main field inhomogeneity in voxel q. γ is the gyromagnetic ratio and $R^*_{2,q}$ is the reciprocal of the transverse relaxation time constant T_2^* in voxel q. The parameters of the multi-peak fat signal model are $\Delta\omega_{F,m}$, which is the chemical shift of peak m and α_m is its normalized signal contribution $\left(\sum_{m=1}^{N_F} \alpha_m = 1\right)$. The values are taken from the ISMRM fat water challenge 2012[1](see Table 6.1), where $N_F = 6$ fat peaks are modeled. More details according the fat signal model are given in Section 4.1.2.

To solve the fat/water separation problem, we propose a 3-step procedure: First, a rough estimate for $R^*_{2,q}$ is calculated by a linear fit on

$$\log |S_q(\tau_n)| = -R^*_{2,q}\tau_n + c_q \tag{6.2}$$

in each voxel, where c_q is an arbitrary constant. According to Soliman et al. [276], a rough estimate for T_2^* is usually sufficient to obtain accurate fat/water separation results. In the

---

[1] http://challenge.ismrm.org/node/8

Peak Nr. (m)	Chemical Shift $\Delta\omega_{F,m}$ in ppm	Relative Signal Contribution α_m in %
1	0.8996	8.7
2	1.2996	69.3
3	2.0997	12.8
4	2.7598	0.4
5	4.3100	3.9
6	5.3001	4.8

Table 6.1: Used values for the parameters in the fat signal model from Eq. (6.1). The values are from the ISMRM fat water challenge 2012.

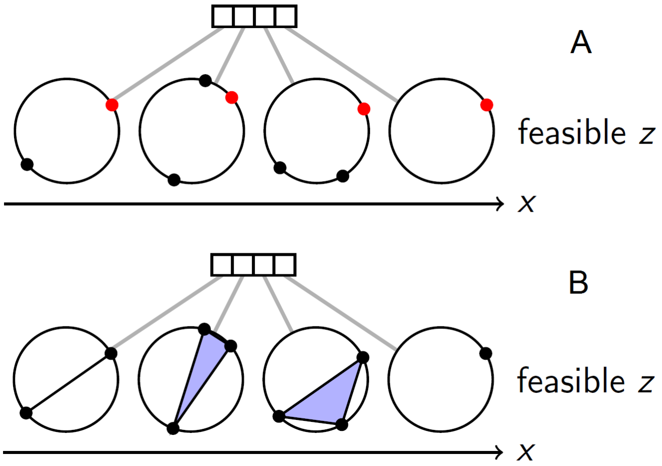

Figure 6.1: (A) The solution space is restricted to local minima of $\mathtt{R}_q(z)$ in each voxel. (B) Convex relaxation: Solution space is extended to all possible solutions inside the unit circle connecting the local minima, leading to the convex relaxation of the problem with the relaxed residual $\mathtt{R}_{\text{relax}}$.

second step, a piecewise smooth solution for $\Delta B_{0,q}$ is calculated. A constant echo spacing $\Delta\tau$ is required, so that the echo times τ_n are given as

$$\tau_n = \tau_1 + (n-1)\Delta\tau, \tag{6.3}$$

where τ_1 can be selected arbitrary, and $R^*_{2,q}$ is taken out of the linear fit in the first step, the squares residual $\mathtt{R}^2_q(\Delta B_{0,q})$ in each voxel q can be defined as

$$\mathtt{R}^2_q(\Delta B_{0,q}) = \min_{S_{W,q},S_{F,q}} \sum_{n=1}^{N_S} \left(S_{n,q} - \left(S_{W,q} + S_{F,q} \sum_{m=1}^{N_F} \alpha_m e^{j\Delta\omega_{F,m}\tau_n} \right) e^{j\gamma\Delta B_{0,q}\tau_n} e^{-R^*_{2,q}\tau_n} \right)^2 . \tag{6.4}$$

Here, $S_{n,q} = S_q(\tau_n)$ is the voxel signal acquired at τ_n and N_S is the number of acquired echos. The minimization problem with respect to $S_{W,q}$ and $S_{F,q}$ is linear and can be solved in the least squares sense, using the pseudo-inverse of the system matrix and treating $\Delta B_{0,q}$ as constant. Using the definitions in Eqs. (4.24) to (4.26), the residuum can be rewritten as

$$\mathtt{R}_q^2(\Delta B_{0,q}) = \left\| \left(\mathbf{I} - \mathbf{K}\mathbf{K}^\dagger \right) \mathbf{T}(-\Delta B_{0,q}, -R_{2,q}^*)\mathbf{S}_q \right\|_2^2 . \tag{6.5}$$

Here, $\mathbf{S}_q$ is a vector containing the acquired complex signals in each voxel for all echo times, $\mathbf{K}$ is the matrix considering the fat model (see Eq. (4.27)), $\mathbf{K}^\dagger$ is the pseudo-inverse of $\mathbf{K}$, $\mathbf{T}(-\Delta B_{0,q}, -R_{2,q}^*)$ is the diagonal matrix considering the field offset ΔB_0 and R_2^* decay (see Eq. (4.28)) and $\mathbf{I}$ is the identity matrix. Using the definitions in Eqs. (4.29) to (4.31) and

$$z_q = e^{j\gamma \Delta B_{0,q} \Delta\tau}, \tag{6.6}$$

the residuum in each voxel can be written as a trigonometric polynomial in z or z^{-1}. According to Eqs. (4.32) and (4.33), the residuum for an arbitrary number of echos writes as

$$\mathtt{R}_q^2\left(\Delta B_{0,q}\right) \rightarrow \mathtt{R}_q^2\left(z_q\right) = \left\| \mathbf{M}_q \begin{pmatrix} z_q^0 \\ \vdots \\ z_q^{-n} \\ \vdots \\ z_q^{N_S-1} \end{pmatrix} \right\|_2^2 , \tag{6.7}$$

leading to a polynomial of order $2(N_S - 1)$ in z^{-1}, where the matrix $\mathbf{M}_q$ combines all ΔB_0 independent terms of the residuum. All local minima of this polynomial in each voxel can be determined efficiently by polynomial root finding, and because of their finite number, also the global one which serves as initial estimate for the $\Delta B_0(\vec{r})$ map. Furthermore, the residual is periodic with $\frac{2\pi}{\Delta\tau}$ and has $(N_S - 1)$ local minim in this period. This formulation was first described in [68] for the case of three echoes, while our proposed solution is able to deal with an arbitrary number of echoes. A detailed derivation of this formalism is given in Section 4.1.3.6.

Due to artifacts and noise, the global minimizer is not always the correct solution, which can lead to fat water swaps. The given problem is now reformulated into a variational problem extended by a regularization term $\mathcal{R}(\Delta\mathbf{B_0})$. Here, a second order *TGV* functional is applied ($\mathcal{R}(\Delta\mathbf{B_0}) = \mathrm{TGV}_\alpha^2\left(\mathbf{z}\right)$), which was introduced by Bredies et al. [38], enforcing piecewise smoothness (for more details see Section 3.2.4.4). With that, in the continuous case, the optimization problem can be written as

$$\begin{aligned} \hat{z}(\vec{r}) = \arg\min_{z} \int_\Omega \mathtt{R}^2\left(\vec{r}, z\left(\vec{r}\right)\right) d\vec{r} + \lambda\, \mathrm{TGV}_\alpha^2\left(z(\vec{r})\right), \\ \text{s.t. } z(\vec{r}) \text{ is local minimum of } \mathtt{R}(\vec{r}), \end{aligned} \tag{6.8}$$

where Ω is the measurement domain (sensitive volume of the receive coils). For discrete

Nr.	Anatomy	N_{TE}	$\text{TE}_{\min}$ in ms	$\text{TE}_{\max}$ in ms	Matrix Size	Sli.	B_0 in T	Scale ΔB_0 map in Hz
1	Knee	6	1.4	9.2	192 × 192	4	3	−303 to 303 Hz
2	Head/Neck	8	1.2	10.6	225 × 227	2	3	−500 to 500 Hz
3	Foot	5	1.4	10.6	256 × 256	2	3	−647 to 647 Hz
4	Knee	6	1.4	9.7	192 × 192	4	3	−303 to 303 Hz
5	Calves	4	1.6	18.8	122 × 242	5	1.5	−500 to 500 Hz
6	Thigh	5	1.6	13.1	122 × 244	5	1.5	−175 to 175 Hz
7	Foot	6	1.9	17.4	250 × 175	5	1.5	−500 to 500 Hz
8	Liver	5	1.4	12.6	224 × 248	3	1.5	−700 to 700 Hz
9	Brain	6	1.7	15.4	251 × 201	3	3	−700 to 700 Hz
10	Wrist	5	1.3	7.2	192 × 192	4	3	−340 to 340 Hz
11	Liver	6	1.2	11.2	256 × 256	5	1.5	−250 to 250 Hz
12	Liver	4	1.7	11.0	157 × 257	3	1.5	−163 to 163 Hz
13	Thigh	4	1.2	4.2	256 × 131	4	3	−510 to 510 Hz
14	Head/Neck	4	1.4	8.3	256 × 256	4	1.5	−500 to 500 Hz
15	Breast	4	2.9	12.5	256 × 55	5	1.5	−700 to 700 Hz
16	Spine	5	2.9	15.7	160 × 208	3	1.5	−156 to 156 Hz
17	Shoulder	3	2.9	9.3	101 × 101	4	1.5	−500 to 500 Hz

Table 6.2: Parameters for of the datasets served as test cases for the ISMRM fat water challenge 2012 and the used scaling of the ΔB_0 map in terms of frequency to show the achieved results in Figures 6.5, 6.6 and 6.9.

voxels, the optimization problem writes as

$$\begin{gathered}\hat{\mathbf{z}} = \arg\min_{\mathbf{z}} \sum_{q=1}^{N_x N_y N_z} \mathtt{R}_q^2\left(z_q\right) + \lambda\, \mathrm{TGV}_\alpha^2\left(\mathbf{z}\right), \\ \text{s.t. } z_q \text{ is local minimum of } \mathtt{R}_q,\end{gathered} \tag{6.9}$$

where $\mathbf{z}$ is a vector containing all z_q for all voxels. Interpreting Eq. (6.9) means that the sum over all residuals is minimized, which are restricted to the local minima of each polynomial on the unit circle, under the condition of the *TGV* constraint. The overall goal is to select the local minimum in each voxel, which gives the globally best estimate, as illustrated in Figure 6.1 A. Because of the combinatorial complexity, a direct solution is not feasible. Therefore, the convex relaxation of the problem is solved, where the solution space of each residuum $\mathtt{R}_q$ is extended to its convex hull, i.e., all solutions inbetween (inside the unit circle), which is visualized in Figure 6.1 B, according to Bredies et al. [39]. With that, the optimization problem writes as

$$\hat{\mathbf{z}} = \arg\min_{\mathbf{z}} \sum_{q=1}^{N_x N_y N_z} \mathtt{R}_{q,\text{relax}}^2\left(z_q\right) + \lambda\, \mathrm{TGV}_\alpha^2\left(\mathbf{z}\right). \tag{6.10}$$

This problem can be easily solved using the primal dual algorithm described by Chambolle and Pock [46]. The obtained solution is then back-projected to the nearest local minimum on the unit circle. To improve the final result, the solution of Eq. (6.10) is repeated several times, called outer iterations. At the beginning a solution with a high value of λ is calculated, leading to a strong regularization. This is repeated several times, where the regularization parameter λ is reduced in each step by a certain factor. The solution of the previous step serves as initial estimate for the next one. Usually four repetitions are performed. Finally, in the third and last step the signal equation is solved using a least square fit to determine $S_{W,q}$ and $S_{F,q}$ in each voxel, according to Eq. (4.25). Without considering individual T_1 or R_2^* values for the fat and water components, the fat signal fraction η_s writes as

$$\eta_s = \frac{S_F}{S_F + S_W}. \tag{6.11}$$

This method was evaluated on all 17 available datasets of the ISMRM fat/water challenge 2012[1], containing different acquisitions with different echo times, echo spacings, and field strength, as well as a variety of different anatomies throughout the human body. The most important parameters for each of the 17 datasets are given in Table 6.2. The results for the fat fraction obtained with the proposed algorithm η_s are compared to 11 different state of the art algorithms using the ISMRM fat/water challenge datasets, where their score values are taken from several publications, see Tables 6.3 and 6.4. For each dataset, a score value $\mathcal{S}$ is calculated on the basis of the provided fat fraction reference $\eta_{s,\mathrm{ref}}$ and a provided mask $\mathcal{M}$ to avoid the influence of background voxels. The sore value is calculated by

$$\mathcal{S} = \frac{\displaystyle\sum_{q=1}^{N_x N_y N_z} |\eta_{s,q} - \eta_{s,q,\mathrm{ref}}| \cdot \mathcal{M}_q < 0.1}{\displaystyle\sum_{q=1}^{N_x N_y N_z} \mathcal{M}_q} \cdot 10000, \tag{6.12}$$

counting the voxels in which the absolute difference between the calculated fat fraction $\eta_{s,q}$ and the reference fat fraction $\eta_{s,q,\mathrm{ref}}$ is less than 10 % within $\mathcal{M}$, normalized to the number of voxels inside the mask $\mathcal{M}$. With that, the maximum score value is 10000, meaning that all voxels within $\mathcal{M}$ deviate less than 10 % to the reference. Additionally, a noise analysis is performed, where complex valued Gaussian noise with a standard deviation σ of 2 %, 5 %, 10 % and 20 % of the mean magnitude within the mask $\mathcal{M}$ is added to the measurement data.

Moreover, the algorithm was also applied to a measured dataset, acquired on a 3 T Skyra system (Siemens, Erlangen Germany) with 4 equally spaced echos using a 2D Gradient Recalled Echo (GRE) sequence. The acquisition was performed with the following sequence parameters: FOV = 300 mm, a slice thickness of 3 mm, TR = 100 ms, $\alpha = 25°$,

---

[1] http://challenge.ismrm.org/node/8

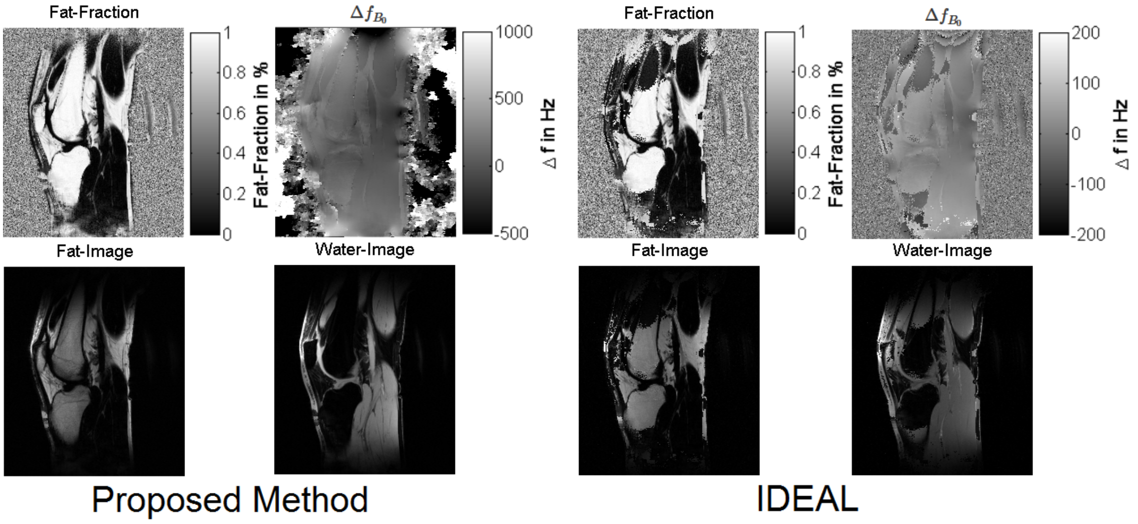

Figure 6.2: Fat fraction, frequency offset due to ΔB_0 inhomogeneity (Δf_{B_0}), fat and water image are shown for the acquired dataset with $\Delta TE = 3.32\,\text{ms}$ obtained using the proposed method and the IDEAL implementation.

a matrix size of 256×256, $\tau_1 = \text{TE}_1 = 1.86\,\text{ms}$, and $\Delta\tau = \Delta\text{TE} = 3.32\,\text{ms}$. The results are compared to an Iterative Decomposition of water and fat with Echo Asymmetry and Least squares estimation (IDEAL) implementation according to [331].

6.2 Results

Figure 6.2 shows fat fraction, field map, fat and water image of the acquired dataset, using the proposed method in comparison to that achieved with the *IDEAL* implementation. Figures 6.3 and 6.4 show the same quantities for dataset 7 and 8 of the ISMRM fat-water-challenge 2012[1], respectively. Compared to the results obtained with *IDEAL*, the proposed algorithm lead to massively improved results.

Tables 6.3 and 6.4 show the achieved scoring values obtained with the proposed method for all datasets of the ISMRM fat water challenge 2012[1] without additional noise and with additional noise levels of 2 %, 5 %, 10 % and 20 % of the mean magnitude within $\mathcal{M}$. The score for the proposed *TGV* regularized results (without noise) and the maximum score achieved with the 11 state of the art reference methods are given in bold for comparison. In Table 6.4 also a mean score value over all 17 datasets is given for each method. Figures 6.5 and 6.6 show the provided fat fraction maps $\eta_{s,\text{ref}}(\vec{r})$ for all challenge datasets (first row) compared to those obtained with the proposed *TGV* regularized method (second row). Results obtained with the proposed *TGV* algorithm are in very good accordance to the reference, visual differences are only observable in datasets 12 (left and right shoulder) and 14 (back part of the stomach). In the third row, the achieved field maps are illustrated for

---

[1] http://challenge.ismrm.org/node/8

each dataset, where their scalings are given in Table 6.2. For some datasets, the field map had to be unwrapped for visualization, which was performed by a seed point algorithm proposed by Ghiglia and Pritt [92]. The last two rows show the corresponding fat and water images.

In Figures 6.7 and 6.8, the obtained results for the noise analysis are shown for each challenge dataset with noise levels of 2 %, 5 %, 10 % and 20 % compared to the provided reference. Until a noise level of 5 %, nearly no changes can be observed in all datasets. For a noise level of 10 %, a few single voxels are swapped, but still a good separation accuracy can be achieved, whereas for a noise level 20 %, strong artefacts occur effecting larger regions especially with lower signal magnitude. Obviously, a similar behavior can be observed for the obtained field maps depicted, in Figure 6.9, where until 10 % noise level stable field maps can be obtained, whereas the noise influence becomes dominant in some regions at a noise level of 20 %.

Figure 6.10 shows a boxplot evaluation for the noise analysis, giving the median, 25 % and 75 % quantile of the deviation between achieved fat fraction with the proposed *TGV* algorithm at different noise levels and the provided reference for all voxels within $\mathcal{M}$ over all datasets. The whisker is parametrized, so that approximately 99 % of all considered voxels lie within. The ≈ 1 % outliers are not shown. Up to a noise level of 5 %, the median is very close to zero and the whisker is below 10 % up to a noise level of 2 %. The increasing influence of noise for a noise level of 20 %, can be seen here as well with a median of about 8 % and the whisker ranging to nearly 70 % deviation.

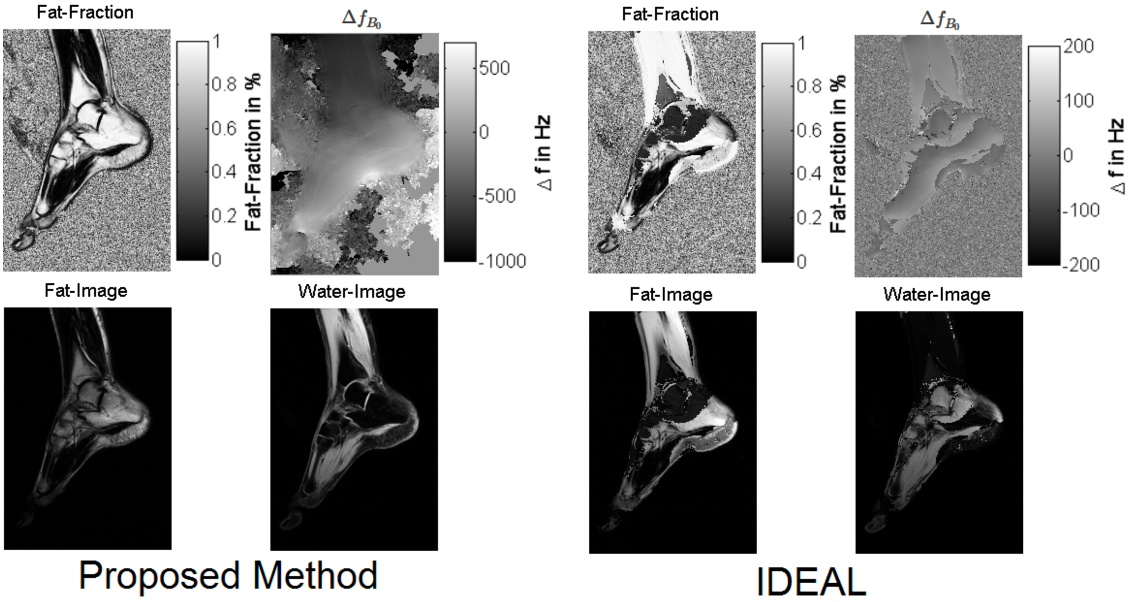

Figure 6.3: Fat fraction, frequency offset due to ΔB_0 inhomogeneity (Δf_{B_0}), fat and water image are shown for dataset 7 of the ISMRM fat/water challenge 2012 obtained using the proposed method and the IDEAL implementation.

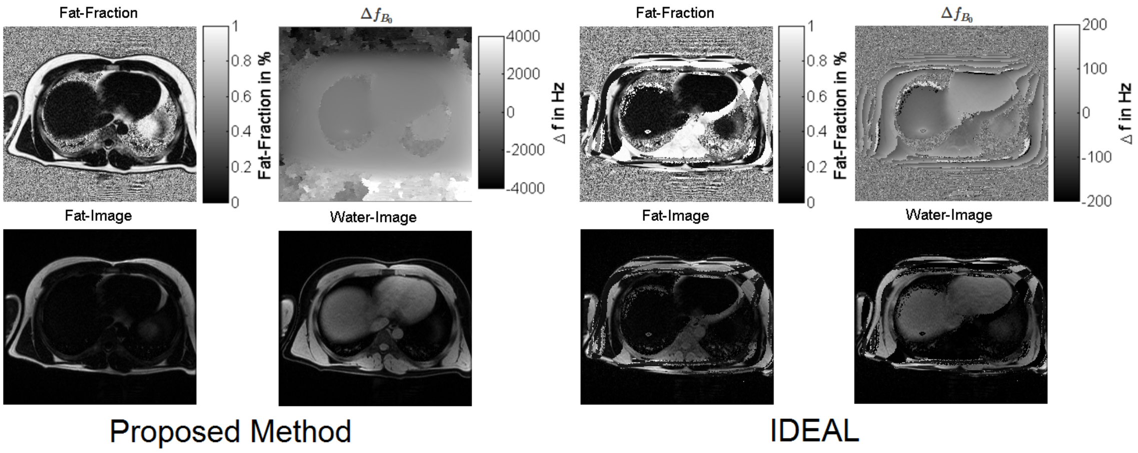

Figure 6.4: Fat fraction, frequency offset due to B_0 inhomogeneity (Δf_{B_0}), fat and water image are shown for tdataset 8 of the ISMRM fat/water challenge 2012 obtained using the proposed method and the IDEAL implementation.

6.3 Discussion

The separation accuracy is considerably improved compared to *IDEAL*, where the results are corrupted by wide fat/water swaps, rendering the result as unusable. The same can be seen on the challenge results, especially dataset 8, see Figure 6.4, where *IDEAL* produces fat/water swaps nearly periodically over the whole Field of View (FOV), which is completely removed with the proposed method. Also the ΔB_0 field is estimated incorrectly in wide areas in all shown datasets using *IDEAL*, which is the reason for the described fat/water swaps.

Although, a few algorithms perform slightly better, the values in Tables 6.3 and 6.4 indicate that the proposed *TGV* regularized algorithm can compete with all current stat of the art algorithms based on the scoring results using the ISMRM fat water challenge datasets[1]. In total, 5 method performed better than the proposed one, but with only marginal improvements. mR-GOOSE and R-GOOSE are counted as one, because these are two variants of the same algorithm presented in the same publication [59], also the achieved scores are nearly identical. Furthermore, it has to be mentioned that a variant of this algorithm was developed for the ISMRM fat water challenge in 2012 (and presented at the annual meeting of 2016 [175]), where the 3rd rank could be achieved in the final ranking, only beaten by GOOSE [60] and the winner approach presented by Smith et al. [271]. Meanwhile, of course, more recent methods were proposed which slightly outperform the proposed *TGV* approach. However, an average score of 9905 was reached, meaning that 99.05 % of all voxels over all datasets were classified correctly. Compared to that, the method performing best reaches a score of 9959 which is only an improvement of 0.5 %. Furthermore, it has to be mentioned that for most datasets, our result comes very close to

---

[1] http://challenge.ismrm.org/node/8

the best achieved score: 9982 vs. 9984 for dataset 1 or 9991 vs. 9992 for dataset 7, only to mention two examples. For dataset 6 the maximum score can be reached as well as for dataset 8 and 9 where the maximum score of 10000 was reached. A better score was only prevented by two datasets (12 and 14), where fat water swaps can be detected visually (see Figure 6.6). Also under the presence of noise, the good performance can be maintained. For a noise level of up to 5 % the achieved score is still above the lower 5 methods in the ranking of Table 6.4 and for a noise level of to 10 %, still more than 85 % of all voxels can be classified correctly. The scoring results can be also confirmed by visual inspection of the obtained results in Figures 6.5 to 6.9 and the boxplot given in Figure 6.10.

To sum up, we could show the capability of this method to deal with huge ΔB_0 inhomogeneities and its ability to avoid fat/water swaps. Also the robustness of this method against noise could be shown, leading to still accurate fat fraction and ΔB_0 maps up to a noise level of 10 %. Furthermore, this method is able to consider small susceptibility changes and the corresponding discontinuity in the ΔB_0 field along tissue boundaries oriented parallel to the main field orientation.

		1	2	3	4	5	6	7	8	9	10	11	12
TGV	no noise	**9982**	**9962**	**9668**	**9990**	**9999**	**9991**	**9991**	**10000**	**10000**	**9972**	**9976**	**9578**
	2 % noise	9972	9948	9640	9981	9500	9939	9977	9998	10000	9969	9973	9540
	5 % noise	9846	9805	9461	9880	8657	9470	9853	9847	9926	9913	9826	9133
	10 % noise	9228	8928	8768	9229	6521	7607	9260	8757	7865	9621	8799	7322
	20 % noise	7272	6480	6748	6865	3714	4356	7299	6115	3533	8318	6401	4277
Multi-scale graph-cut3) [17]		9976	9973	–	**9995**	9972	9986	9990	9994	**10000**	9973	**9991**	9671
mR-GOOSE2) [59]		**9984**	**9983**	9612	9989	**10000**	9987	9991	**10000**	**10000**	**9988**	9979	**9775**
R-GOOSE2) [59]		9983	9981	9595	9990	9999	9979	9991	9995	**10000**	9973	9961	9763
Winner of the ISMRM fat water challenge 20124) [271]		9983	9982	9555	9991	**10000**	9989	**9992**	9998	**10000**	9971	9941	9652
Self-feeding phasor estimation4) [52]		9970	9944	**9710**	9980	9847	9983	9951	9992	9989	9965	9955	9697
GOOSE1) [60]		**9984**	9981	9650	9987	9994	9988	9990	9994	9997	9972	9975	9558
Graph-cut1) [123]		9946	6829	9597	9971	9100	9988	9536	8158	9178	9968	**9991**	8128
Safest-first region growing1) [15]		9137	4536	–	9652	2647	9927	8792	9923	4894	9303	9960	5171
Hierarchical IDEAL1) [297]		9749	5638	4201	9807	6347	9955	4603	6414	5899	9379	9914	5123
IDEAL with Region growing4) [332]		9621	5664	7042	9789	3108	9944	2463	2053	2704	9316	9884	5115
Golden section search4) [192]		9319	5251	6716	8884	3206	9776	5323	2987	6550	8259	9603	4428

Table 6.3: Scoring values $\mathcal{S}$ according to Eq. (6.12) for the datasets 1–12 of the ISMRM fat water challenge of 2012 for the results obtained with the proposed TGV regularized algorithm, without and with an additional noise level of 2 %, 5 %, 10 % and 20 % of the mean magnitude value within the provided mask $\mathcal{M}(\vec{r})$. The maximum score is 10000 indicating that every voxel of the obtained fat fraction map lies within an error bound of $< 10\,\%$ of the provided reference. The scoring values are compared to those of 11 state of the art algorithms, where reference implementations are available in the ISMRM fat water toolbox. The maximum scoring value for each dataset as well as that for the TGV result are printed in bold for easier comparison. The values for the comparison methods are from: 1)[60]; 2)[59]; 3)[17]; 4)[52]

		13	14	15	16	17	Mean
TGV	no noise	**9990**	**9478**	**9984**	**9957**	**9872**	**9905**
	2 % noise	9986	9444	9944	9888	9788	9852
	5 % noise	9824	9355	9731	9618	9462	9624
	10 % noise	8776	8040	9038	8917	8556	8540
	20 % noise	6407	4875	7148	7320	6588	6094
Multi-scale graph-cut3) [17]		9999	**9989**	9984	9961	9887	**9959**
mR-GOOSE2) [59]		**10000**	9972	9969	**9967**	**9893**	9946
R-GOOSE2) [59]		**10000**	9971	9952	9957	9875	9939
Winner of the ISMRM fat water challenge 20124) [271]		9998	**9989**	**9985**	9957	9840	9931
Self-feeding phasor estimation4) [52]		9985	9985	**9985**	9959	9884	9928
GOOSE1) [60]		9991	9987	9915	9913	9880	9927
Graph-cut1) [123]		9418	8771	8179	9884	9464	9183
Safest-first region growing1) [15]		9923	9988	9873	9602	9643	8311
Hierarchical IDEAL1) [297]		9041	1786	5867	8544	6252	6972
IDEAL with Region growing4) [332]		9972	2145	3960	9337	7190	6430
Golden section search4) [192]		8994	6164	4341	8098	5410	6665

Table 6.4: Scoring values $\mathcal{S}$ according to Eq. (6.12) for the datasets 13–17 of the ISMRM fat water challenge of 2012 and a mean value over all datasets (see Table 6.3) for the results obtained with the proposed TGV regularized algorithm, without and with an additional noise level of 2 %, 5 %, 10 % and 20 % of the mean magnitude value within the provided mask $\mathcal{M}(\vec{r})$. The maximum score is 10000 indicating that every voxel of the obtained fat fraction map lies within an error bound of $< 10\,\%$ of the provided reference. The scoring values are compared to those of 11 state of the art algorithms, where reference implementations are available in the ISMRM fat water toolbox. The maximum scoring value for each dataset as well as that for the TGV result are printed in bold for easier comparison. The values for the comparison methods are from: 1)[60]; 2)[59]; 3)[17]; 4)[52]

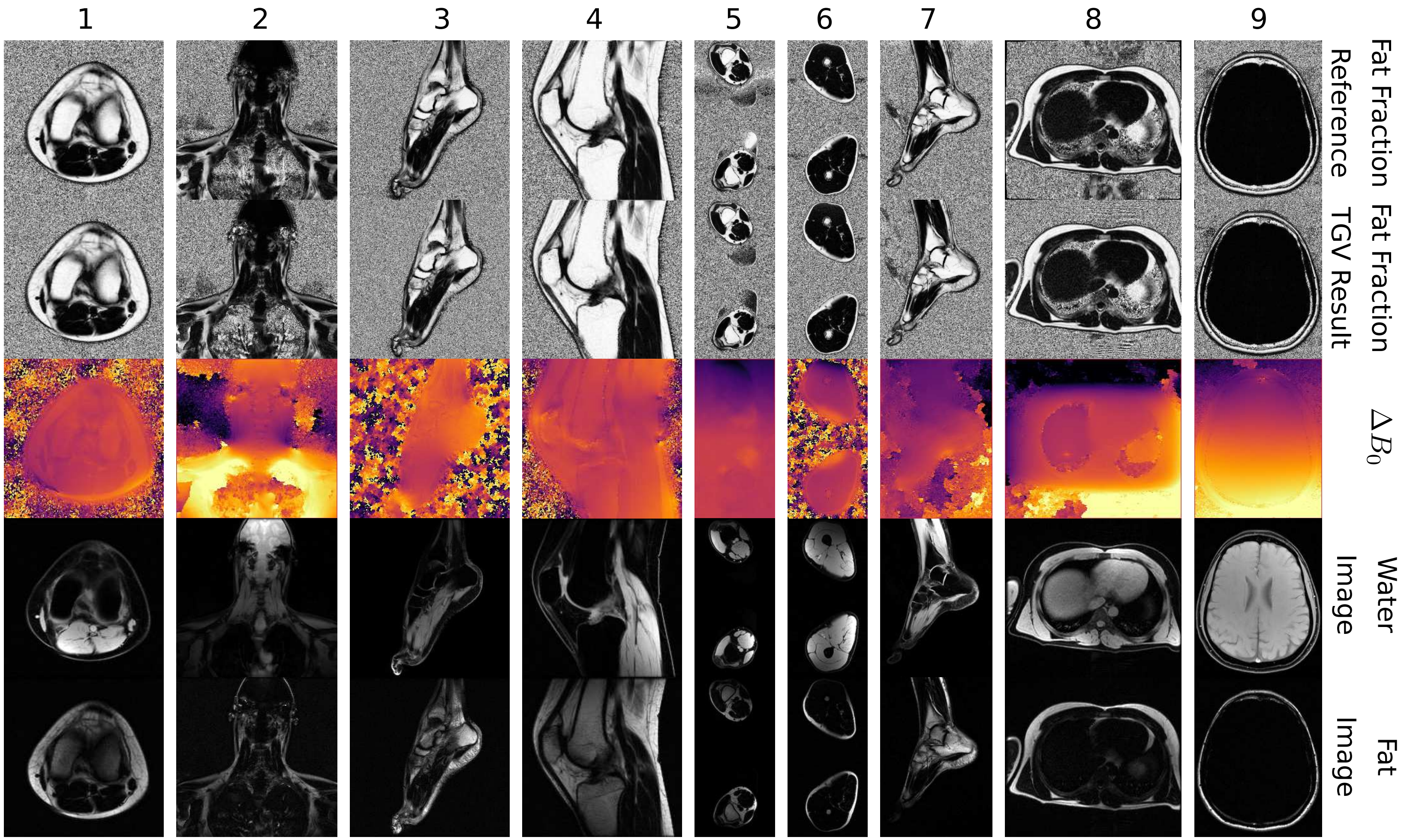

Figure 6.5: Provided reference fat fraction maps $\eta_{s,\mathrm{ref}}(\vec{r})$ and the obtained fat fraction maps $\eta_s(\vec{r})$ with the proposed TGV regularized algorithm, as well as the corresponding field maps, $\Delta B_0(\vec{r})$, and the fat and water images $S_F(\vec{r})$ and $S_W(\vec{r})$, respectively, for the datasets 1–9 of the ISMRM fat water challenge of 2012. Some of the field maps are unwrapped using an algorithm proposed by Ghiglia and Pritt [92]. The scaling of the ΔB_0 map is given in Table 6.2.

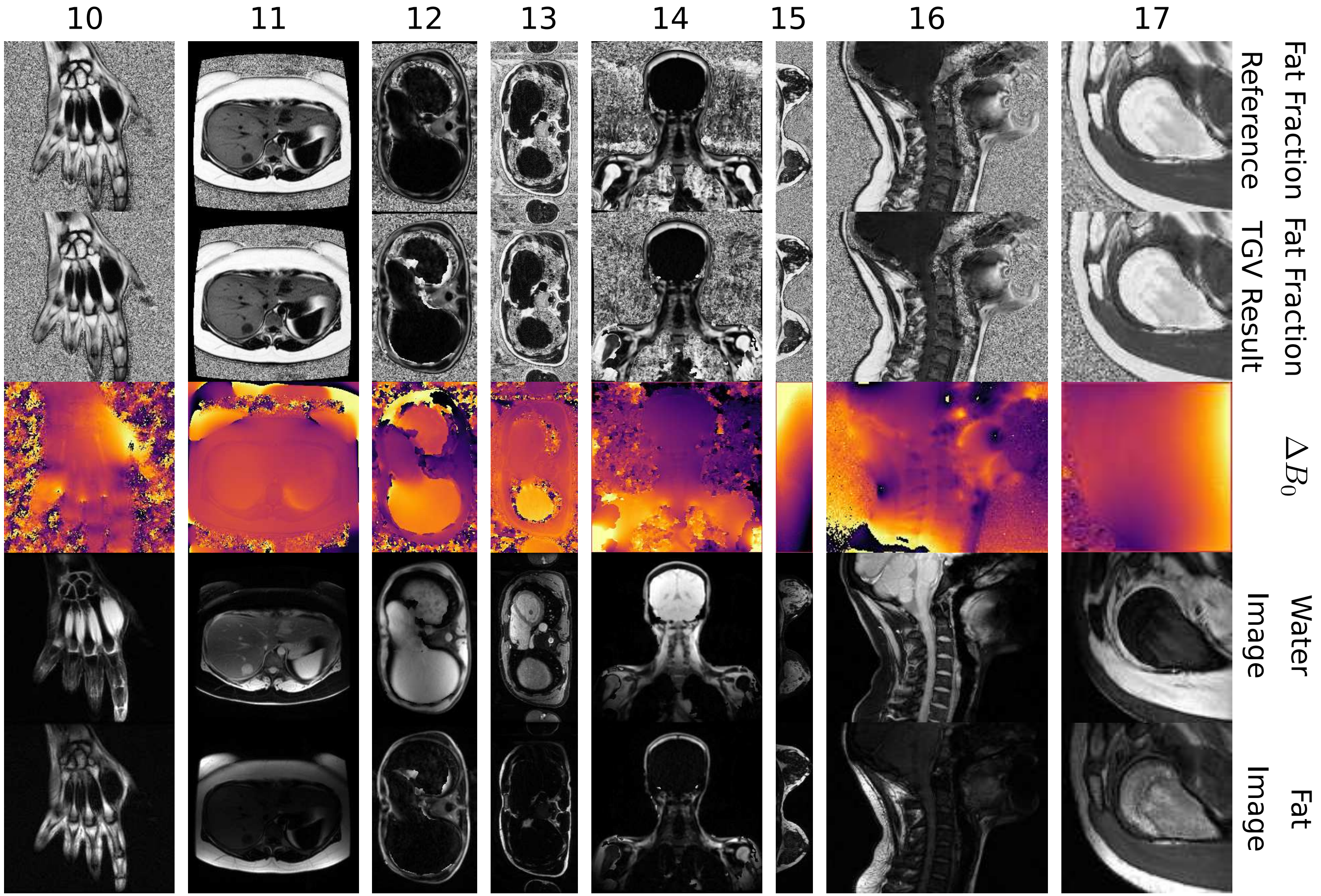

Figure 6.6: Provided reference fat fraction maps $\eta_{s,\text{ref}}(\vec{r})$ and the obtained fat fraction maps $\eta_s(\vec{r})$ with the proposed TGV regularized algorithm, as well as the corresponding field maps, $\Delta B_0(\vec{r})$, and the fat and water images $S_F(\vec{r})$ and $S_W(\vec{r})$, respectively, for the datasets 10–17 of the ISMRM fat water challenge of 2012. Some of the field maps are unwrapped using an algorithm proposed by Ghiglia and Pritt [92]. The scaling of the ΔB_0 map is given in Table 6.2.

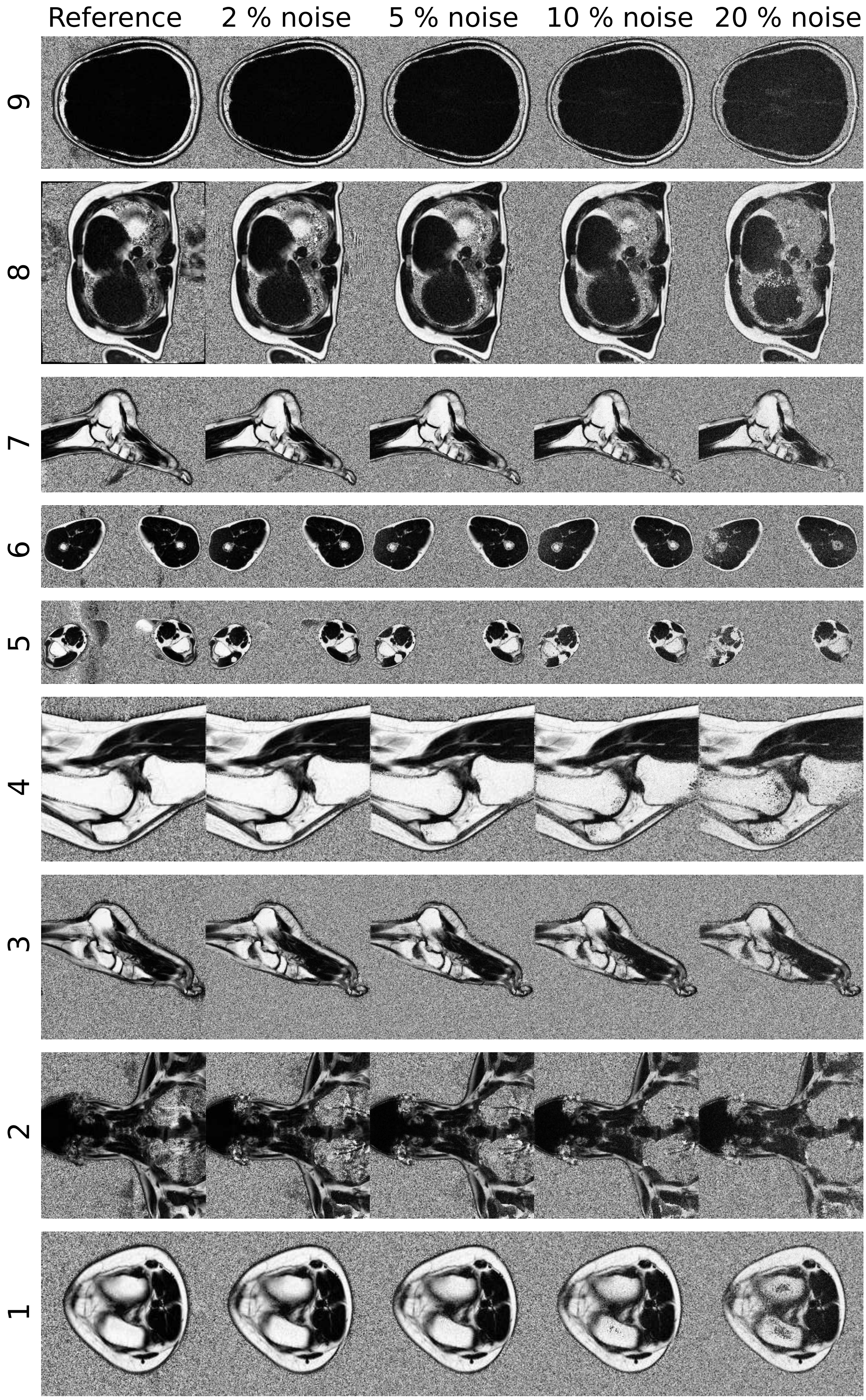

Figure 6.7: Provided reference fat fraction maps $\eta_{s,\mathrm{ref}}(\vec{r})$ and the obtained fat fraction maps $\eta(\vec{r})$ with the proposed TGV regularized algorithm for different levels of additive complex Gaussian noise for the datasets 1–9 of the ISMRM fat water challenge of 2012. The noise is generated with a standard deviation of 2 %, 5 %, 10 % and 20 % of the mean image magnitude within the provided mask $\mathcal{M}(\vec{r})$.

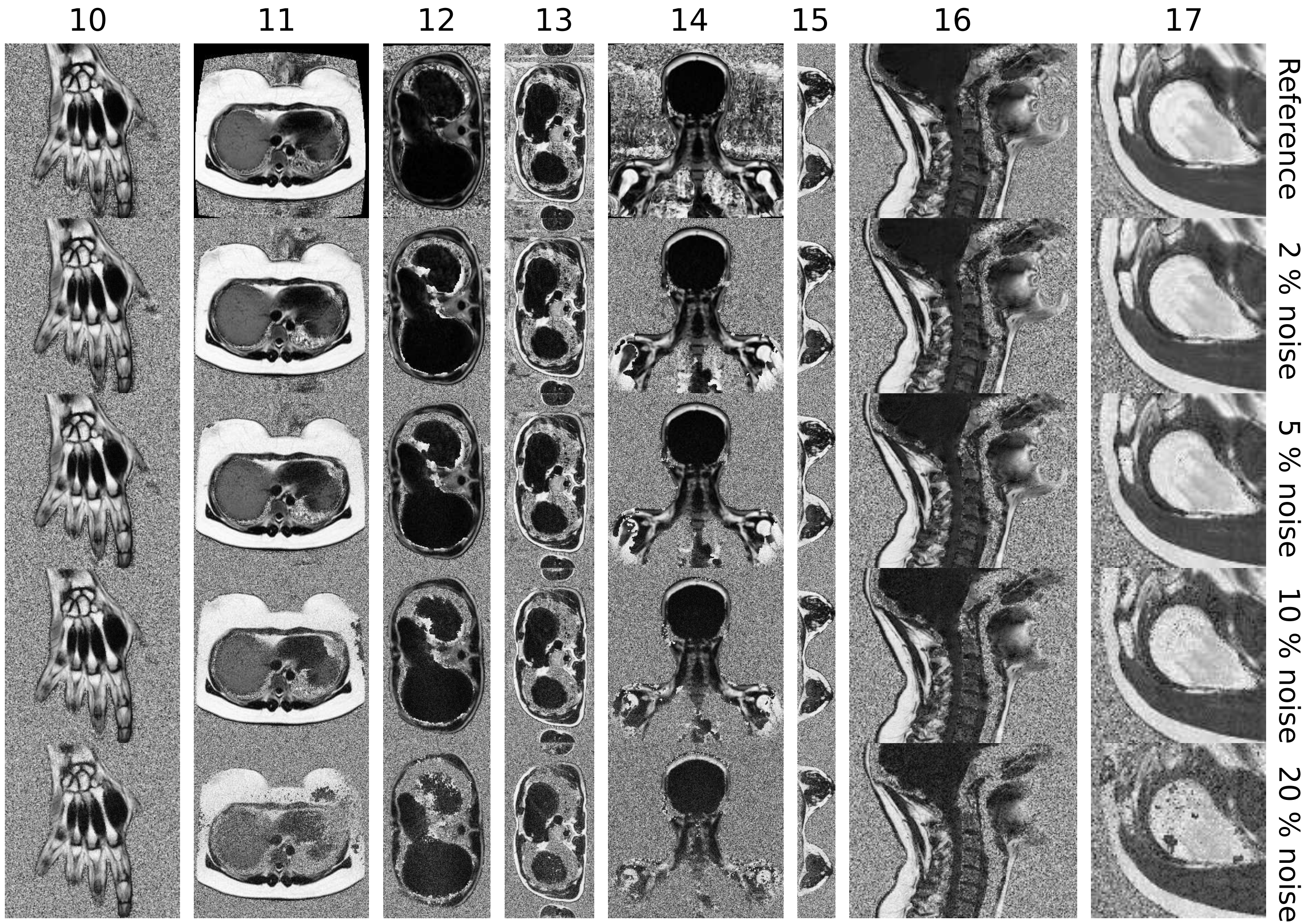

Figure 6.8: Provided reference fat fraction maps $\eta_{s,\mathrm{ref}}(\vec{r})$ and the obtained fat fraction maps $\eta_s(\vec{r})$ with the proposed TGV regularized algorithm for different levels of additive complex Gaussian noise for the datasets 10–17 of the ISMRM fat water challenge of 2012. The noise is generated with a standard deviation of 2 %, 5 %, 10 % and 20 % of the mean image magnitude within the provided mask $\mathcal{M}(\vec{r})$.

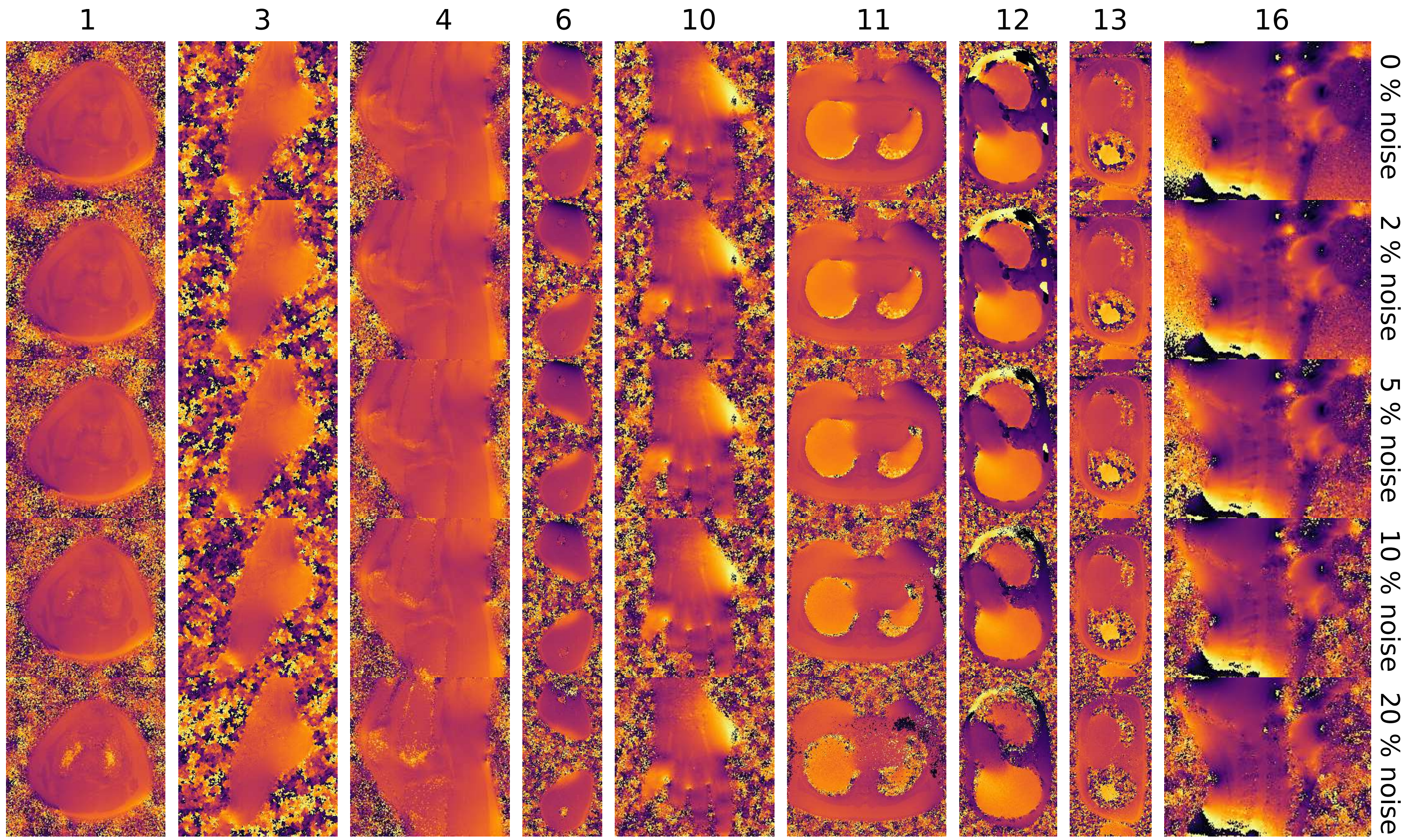

Figure 6.9: $\Delta B_0(\vec{r})$ maps obtained with the proposed TGV regularized algorithm for different levels of additive complex Gaussian noise for the datasets (1,3,4,6,10,11,12,13 and 16) of the ISMRM fat water challenge of 2012. The noise is generated with a standard deviation of 2 %, 5 %, 10 % and 20 % of the mean image magnitude within the provided mask $\mathcal{M}(\vec{r})$. The scaling of the ΔB_0 map is given in Table 6.2.

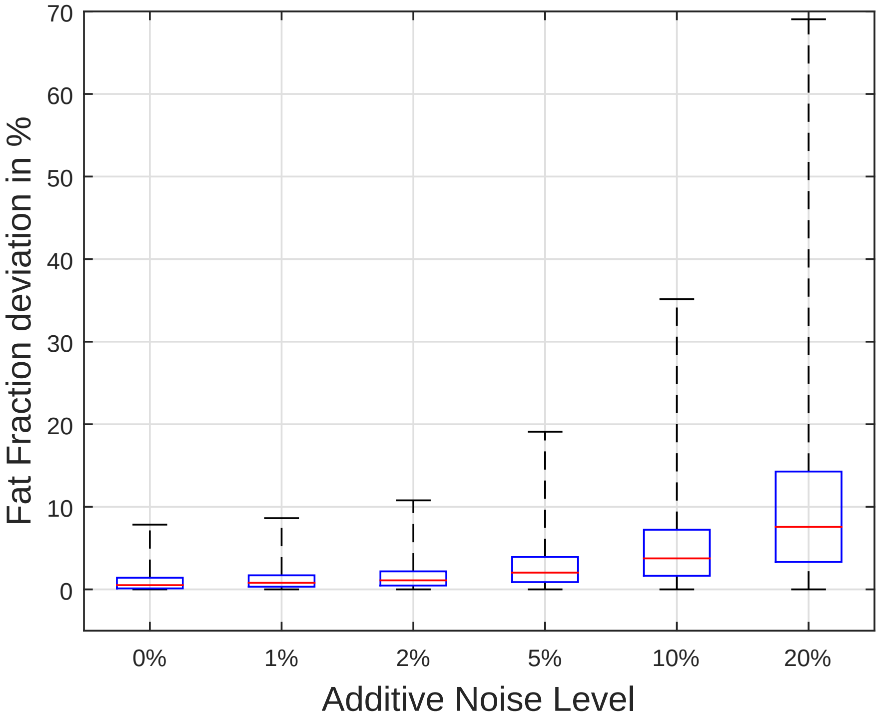

Figure 6.10: *Noise Analysis:* Box-plot of the fat fraction deviation within the provided mask $\mathcal{M}(\vec{r})$ of the results obtained with the proposed TGV regularized algorithm compared to the provided reference, without noise and with 5 different levels of additive Gaussian noise using all datasets provided by the ISMRM fat water challenge of 2012. The noise is generated with a standard deviation of 2 %, 5 %, 10 % and 20 % of the mean image magnitude within the provided mask $\mathcal{M}(\vec{r})$. The boxplot shows the median deviation (red line), the 25 % and 75 % quantile (blue box), and the whiskers are parameterized so that about 1 % of the pixel values lie outside, classified as outliers. The outliers are not shown.

7

Summary, Conclusion and Outlook

If at first you don't succeed,
try, try again.

W. E. Hickson

Contents

7.1 Highly accelerated $\mathbf{B_1^+}$ Mapping 193
7.2 Chemical Shift based Fat-Water Separation 195
7.3 Conclusion and Outlook 196

The goal of this thesis was to develop certain regularization strategies applied to field mapping applications in Magnetic Resonance Imaging (MRI). The main focus of this thesis lies on the reconstruction of highly accurate B_1^+ maps from highly undersampled data. The second aspect in this thesis is the determination of highly accurate B_0 maps to solve the ill-posed inverse problem of the separation from fat and water signal contributions (chemical shift imaging).

7.1 Highly accelerated $\mathbf{B_1^+}$ Mapping

All considerations for B_1^+ mapping are based on the Bloch-Siegert (BS) shift imaging approach. The fundamental advantage of this method is its ability to directly determine the B_1^+ field instead of the flip angle α in most of the other commonly used methods. The B_1^+ magnitude information is encoded in the signal phase, making this approach insensitive to T_1 relaxation effects, and it was further shown to be quite insensitive to ΔB_0 variations. Furthermore, also a ΔB_0 compensated approach was presented. The main disadvantage of this method is the high energy deposition, restricting the minimum possible Repetition Time (TR) due to patient safety Specific Absorption Rate (SAR) constraints. This aspect is less severe, if only a low number of data points need to be acquired. Time independent phase effects can be easily removed by the acquisition of two images with opposite resonance offsets and considering the phase difference. However, in a prework it could be shown that the background phase is not necessarily stable, due to hardware drifts. These phase drift during the acquisition time of a 3D dataset can lead to substantial deviations in the final B_1^+ map. Deviations in the range between 17 % to 50 % are reported. It was shown that an interleaved acquisition of positive and negative resonance offset is much more stable against these effect and the deviations could be compensated completely.

For the reconstruction of B_1^+ maps from highly undersampled data, a two-step regularization approach was presented. For this purpose, the reconstruction problem was written as an optimization problem so that the contribution from the underlying image and the B_1^+ dependent *BS* phase can be separated. Depending on their known spatial behavior, a dedicated regularization can be applied. With a change of variables, the optimization for both unknown quantities can be decoupled so that they can be solved independently. For the underlying image, a second order Total Generalized Variation (TGV) and for the *BS* phase a H_1 regularization functional was applied. The second order *TGV* functional is known to enforce piecewise smooth solutions, representing the behavior of Magnetic Resonance (MR) images, and the H_1 functional which consists of the squared L_2 norm of the image gradients leads to spatial smooth solutions, which is exactly the behavior of the B_1^+ field. With that, highly accurate 3D B_1^+ maps covering the whole brain with an average deviation of < 1 % to the fully sampled reference can be acquired within 15 s to 20 s, so that a single breath hold acquisition is possible. This can be established without using any low bandwidth acquisitions as Echo Planar Imaging (EPI) or spirals, making the acquisition very sensitive to ΔB_0 variations and gradient imperfections. Nominally, on the basis of a matrix size of $128 \times 128 \times 32$, this corresponds to an acceleration factor R_{acc} in the range of 85 to 100.

Because of its spatial structure, the B_1^+ field relies on very low spatial frequencies. However, no fundamental investigation was available, exploring the practical limits of how much data is necessary to reconstruct an accurate B_1^+ map. In this thesis it was shown that only a few phase encoding steps are necessary in k-space center, i.e., 12×4, to reconstruct B_1^+ maps with an average deviation of < 1 % to the fully sampled reference. It could be argued that this kind of undersampling is equivalent to a low resolution estimate obtained by zero padding. Under perfect condition, indeed, zero padding leads to similar results, which was confirmed by simulations (results are not shown). However, under practical conditions, the zero padding results suffer from severe artifacts, due to phase instabilities arising from coil combination, phase singularities, and undefined phase values in regions with low magnitude, making regularization necessary. Furthermore, it was shown that random undersampling pattern with Gaussian density functions concentrated around the k-space center lead to similar (slightly better) results, if the same instance of a certain undersampling patter is used for both acquisitions. To keep the acquisition protocol simple, all further considerations focus on the described dense block pattern with a certain number of acquisitions in k-space center. For both cases, it was shown that additionally sampling higher spatial frequencies in k-space does not improve the final reconstructed B_1^+ map.

Calculation time is usually an issue for the application of variational methods, because of the iterative solution of the optimization problems. However, in this case, efficient Graphics Processing Unit (GPU) implementations of the primal dual algorithm to solve the *TGV* part, the Conjugate Gradient (CG) algorithm to solve the H_1 part and for the finite difference operations are used, so that a solution for the whole 3D volume can be obtained in $\approx 30\,\mathrm{s}$ on a NVIDIA Geforce Titan Xp *GPU*. With that, the reconstructed B_1^+ map is available during the time necessary for a subsequent *MR* acquisition, which is sufficient for clinical applicability.

When going to 7 T, a slight increase in the average error can be observed compared to the results obtained at 3 T, i.e., the Mean Absolute Error (MAE) increases from $\approx 0.7\,\%$ to $\approx 2\,\%$ for a pattern size of 12×4 in-vivo. For the results of the phantom dataset, a strong smearing out effect of the B_1^+ hot-spot in the center of the phantom can be observed for this small pattern size. This behavior can be expected, due to the much more rapid transitions in the B_1^+ field at 7 T. In general, at 7 T, a compromise between low acquisition time and high accuracy has to be made. At 3 T, very accurate results are possible with a pattern size of 12×4, whereas at 7 T an increase to 12×8 or 14×8 is suggested. Here, the application of irregular undersampling patterns might be beneficial. However, the more severe limitation regarding acquisition time is the nearly 4-times increase in *TR*, so that a single breath-hold acquisition is still not possible at 7 T. However, 3D B_1^+ maps with an average error of $< 2\,\%$ with respect to the fully sampled reference are possible in about 45 s to 60 s for full brain coverage.

For very special applications, a combination of the proposed reconstruction algorithm with an *EPI* readout was investigated, with the goal of a two shot acquisition. The general feasibility could be shown, but it was only possible to apply an *EPI* readout along one phase encoding direction. As soon as the *EPI* readout was combined in both phase encoding directions, no stable signals could be obtained. It is assumed that unsufficient eddy current compensation is responsible for that.

7.2 Chemical Shift based Fat-Water Separation

The application of variational methods could also be shown to be beneficial to obtain accurate B_0 estimates for the purpose fat/water signal separation. Based on the evaluation on the datasets provided for the ISMRM fat water challenge in 2012, an average score of 9905 could be reached. This means that 99.05 % of all voxels over 17 datasets with a magnitude above a certain threshold where classified correctly. Most of the uncorrectly assigned voxels are single voxels inside noisy regions. Only in the results of two datasets visually detectable fat/water swaps could be observed. The good performance also holds under the presence of noise. For an additional noise level of 5 % in the data, the correct classification rate is still 96.24 % and 85.4 % for 10 %. What is very important to note, the reduction in classification rate is cause by single voxels. The noise does not introduce additional fat/water swaps over wide areas, so that the resulting visual image quality is still very high. In total, 5 algorithms performed better than the proposed one. However, the best achieved score is 9959, meaning that the correct classification rate could only slightly be increased by 0.5 %. Also the calculation time is in an acceptable range with < 6 min for all evaluated datasets using a partial *GPU* implementation. The proposed *TGV* regularized algorithm was shown to be able to substantially reduce the appearance of fat/water swaps compared to the reference Iterative Decomposition of water and fat with Echo Asymmetry and Least squares estimation (IDEAL) implementation and that it is able to compete with other more recent state of the art algorithms.

7.3 Conclusion and Outlook

With the application of variational methods, the acquisition time for 3D *BS* based B_1^+ maps can be reduced from the order of minutes in the fully sampled case into 15 s to 20 s at 3 T with an average deviation of $< 1\,\%$ to the fully sampled reference, allowing single breath hold acquisitions. At 7 T, the acceleration potential is slightly reduced, due to the steeper spatial variations in the B_1^+ field. The increase in acquisition time mostly results from the nearly 4 times increased *TR*. However, the application of variational methods is also beneficial to obtain highly accurate B_1^+ maps at 7 T, with acquisition times in the order of 45 s to 60 s. To further improve this method, the model can be extended for the estimation of an additional B_0 map without increasing the acquisition time, similar to [72]. In the case of Gradient Recalled Echo (GRE) acquisition, this can be easily achieved by the acquisition of one or more additional echos. For the reconstruction, the regularization has to be extended to be able to deal with phase wraps, a simple H_1 regularization is not sufficient. In a next step the General Linear Model (GLM) proposed by Corbin et al. [58] should be incorporated into the reconstruction as a future goal, to be able to obtain also information about the eddy current influence and phase offsets besides B_1^+ and ΔB_0. This would require to properly adapt the optimization problems and to add new regularization terms for the additional quantities. Moreover, a kind of joint regularization might be necessary to solve this problem.

The application of variational methods is also shown to be beneficial for the application of fat/water separation to obtain a highly accurate ΔB_0 estimate. The proposed *TGV* regularized algorithm is able to obtain robust fat/water separation results over a wide range of anatomies, in case of strong ΔB_0 variations and with moderate to high values of noise. On the basis of the score of the ISMRM fat water challenge in 2012, the proposed algorithm performed as one of the best at the time of its development and is still able to compete with other more recently proposed state of the art algorithms. To further improve this method, a combination with undersampling might be possible as it is done in Doneva et al. [68], however, making the ill-posedness of this problem more severe. The rough T_2^* map estimate obtained in the first step (not shown) is highly affected by noise. To reduce this effect, the application of a second regularization term for T_2^* might be beneficial. However, a joint solution of ΔB_0 and T_2^* is mathematical not trivial because of the special form of this problem (periodicity in ΔB_0). A much easier way would be to alternately optimize ΔB_0 and T_2^*, by setting the other one constant. However, the calculation time for this iterative approximation might increase.

At the moment, methods based on machine learning lead to very promising results in various fields, including *MR* image reconstruction [109, 110]. The application of these kind of methods may also lead to further improvements to achieve highly accurate field maps in *MRI*. However, fundamental stability problems were recently reported for machine learning based methods to solve inverse problems, which is not the case for solutions obtained with variational methods [4, 97].

A
Appendix I

A.1 Spherical Harmonics

Spherical harmonics are a set of functions, typically described in spherical polar coordinates, which are defined on the surface of a sphere. These functions form a complete orthonormal solution basis for the Laplace differential equation $\nabla^2 X = 0$ such that any field fulfilling the Laplace equation can be described as a sum of spherical harmonic functions with order $l = [0, \infty)$ and degree $m = [-l, l]$. The spherical polar coordinates are defined by the radius r, the polar angle $\vartheta = [0, \pi]$ and the azimuthal angle $\varphi = [0, 2\pi]$. A_{lm} is a weighting factor describing the contribution of each basis function $X_l^m(\vartheta, \varphi)$ to the total field distribution $X(r, \vartheta, \varphi)$ as

$$X(r, \vartheta, \varphi) = \sum_{l=0}^{\infty} \sum_{m=-l}^{l} A_{lm} r^l X_l^m(\vartheta, \varphi). \tag{A.1}$$

They are further a set of Eigen-functions of the angular part of the Laplace operator, which can be seen if the Laplace operator is written in spherical polar coordinates, where the Eigenvalue equation is written as

$$\left(\frac{\partial^2}{\partial \vartheta^2} + \frac{\cos\vartheta}{\sin\vartheta} \frac{\partial}{\partial \vartheta} + \frac{1}{\sin^2\vartheta} \frac{\partial^2}{\partial \varphi^2} \right) X_l^m(\vartheta, \varphi) = -l(l+1) X_l^m(\vartheta, \varphi). \tag{A.2}$$

A solution for this problem is given by

$$X_l^m(\vartheta, \varphi) = \frac{1}{\sqrt{2\pi}} \sqrt{\frac{2l+1}{2} \frac{(l-m)!}{(l+m)!}} P_l^m\left(\cos(\vartheta)\right) e^{jm\varphi}, \tag{A.3}$$

with the corresponding Legendre polynomials $P_l^m(z)$ defined by

$$P_l^m(z) = \frac{(-1)^m}{2^l l!} \left(1 - z^2\right)^{\frac{m}{2}} \frac{\partial^{l+m}}{\partial z^{l+m}} \left(z^2 - 1\right)^l. \tag{A.4}$$

A more easy way to calculate the Legendre polynomials in most cases is given by

$$P_l(z) = \frac{1}{2^l} \sum_{k=0}^{\lfloor l/2 \rfloor} (-1)^k \frac{(2l-2k)!}{k!(l-k)!(l-2k)!} z^{l-2k} \tag{A.5}$$

and

$$P_l^m(z) = (1-z^2)^{\frac{|m|}{2}} \left(\frac{\partial}{\partial z} \right)^{|m|} P_l(z). \tag{A.6}$$

The description here is based on [116]. Expressions for the spherical harmonic functions up to 3$^{\text{rd}}$ order are given in Table A.1 in spherical and Cartesian coordinates. The relation between spherical and Cartesian coordinates is given as

$$\begin{aligned} x &= r\sin(\vartheta)\cos(\varphi) = r\sin(\vartheta)\Re(e^{i\varphi}), \\ y &= r\sin(\vartheta)\sin(\varphi) = r\sin(\vartheta)\Im(e^{i\varphi}), \\ z &= r\cos(\vartheta). \end{aligned} \tag{A.7}$$

In spherical coordinates the basis function $X_l^m(r,\vartheta,\varphi)$ is always the complex conjugate of $X_l^{-m}(r,\vartheta,\varphi)$ ($X_l^m(r,\vartheta,\varphi) = \bar{X}_l^{-m}(r,\vartheta,\varphi)$). The Cartesian basis functions $X_l^m(x,y,z)$ are given as

$$X_l^{-m}(x,y,z) = \frac{1}{2}\Re(X_l^m(r,\vartheta,\varphi)) + \Re(X_l^{-m}(r,\vartheta,\varphi)), \tag{A.8}$$

$$X_l^m(x,y,z) = \frac{1}{2}\Im(X_l^m(r,\vartheta,\varphi)) - \Im(X_l^{-m}(r,\vartheta,\varphi)). \tag{A.9}$$

A graphical representation of the spherical harmonic basis functions in spherical polar coordinates for up to 3$^{\text{rd}}$ order is given in Figure A.1, where the function value is plotted on the surface of a sphere with $r = 1$. Figure A.2 shows the function value for the spherical harmonic basis functions as a cross section in Cartesian coordinates with their corresponding common name for up to 3$^{\text{rd}}$ order.

$X_l^m(r,\vartheta,\varphi)$		$l=0$	$l=1$	$l=2$	$l=3$
$m=-3$	*Sph.*				$\frac{\sqrt{35}}{2\sqrt{16\pi}} r^3 \sin^3\vartheta e^{-j3\varphi}$
	Cart.				$\frac{\sqrt{35}}{2\sqrt{16\pi}} \left(x^3 - 3xy^2\right)$
$m=-2$	*Sph.*			$\sqrt{\frac{15}{32\pi}} r^2 \sin^2\vartheta e^{-j2\varphi}$	$\sqrt{\frac{105}{32\pi}} r^3 \sin^2\vartheta \cos\vartheta e^{-j2\varphi}$
	Cart.			$\sqrt{\frac{15}{32\pi}} \left(x^2 - y^2\right)$	$\sqrt{\frac{105}{32\pi}} z \left(x^2 - y^2\right)$
$m=-1$	*Sph.*		$\frac{\sqrt{3}}{2\sqrt{2\pi}} r \sin\vartheta e^{-j\varphi}$	$\sqrt{\frac{15}{8\pi}} r^2 \sin\vartheta \cos\vartheta e^{-j\varphi}$	$\frac{\sqrt{7}}{8\sqrt{\pi}} r^3 \sin\vartheta \left(5\cos^2\vartheta - 1\right) e^{-j\varphi}$
	Cart.		$\frac{\sqrt{3}}{2\sqrt{2\pi}} x$	$\sqrt{\frac{15}{8\pi}} zx$	$\frac{\sqrt{7}}{8\sqrt{\pi}} x \left(5z^2 - r^2\right)$
$m=0$	*Sph.*	$\frac{1}{2\sqrt{\pi}}$	$\frac{\sqrt{3}}{2\sqrt{\pi}} r \cos\vartheta$	$\frac{\sqrt{5}}{4\sqrt{\pi}} r^2 \left(3\cos^2\vartheta - 1\right)$	$\frac{\sqrt{7}}{4\sqrt{\pi}} r^3 \left(5\cos^3\vartheta - 3\cos\vartheta\right)$
	Cart.	$\frac{1}{2\sqrt{\pi}}$	$\frac{\sqrt{3}}{2\sqrt{\pi}} z$	$\frac{\sqrt{5}}{4\sqrt{\pi}} \left(3z^2 - r^2\right)$	$\frac{\sqrt{7}}{4\sqrt{\pi}} r^3 \left(5z^3 - 3zr^2\right)$
$m=1$	*Sph.*		$\frac{\sqrt{3}}{2\sqrt{2\pi}} r \sin\vartheta e^{j\varphi}$	$\sqrt{\frac{15}{8\pi}} r^2 \sin\vartheta \cos\vartheta e^{j\varphi}$	$\frac{\sqrt{7}}{8\sqrt{\pi}} r^3 \sin\vartheta \left(5\cos^2\vartheta - 1\right) e^{j\varphi}$
	Cart.		$\frac{\sqrt{3}}{2\sqrt{2\pi}} y$	$\sqrt{\frac{15}{8\pi}} zy$	$\frac{\sqrt{7}}{8\sqrt{\pi}} y \left(5z^2 - r^2\right)$
$m=2$	*Sph.*			$\sqrt{\frac{15}{32\pi}} r^2 \sin^2\vartheta e^{j2\varphi}$	$\sqrt{\frac{105}{32\pi}} r^3 \sin^2\vartheta \cos\vartheta e^{j2\varphi}$
	Cart.			$\sqrt{\frac{15}{32\pi}} 2xy$	$\sqrt{\frac{105}{32\pi}} 2xyz$
$m=3$	*Sph.*				$\frac{\sqrt{35}}{2\sqrt{16\pi}} r^3 \sin^3\vartheta e^{j3\varphi}$
	Cart.				$\frac{\sqrt{35}}{2\sqrt{16\pi}} \left(3x^2y - y^3\right)$

Table A.1: Expressions for spherical harmonics functions given in Cartesian and spherical polar coordinates up to 3rd order according to [116] and [323, Ch.4].

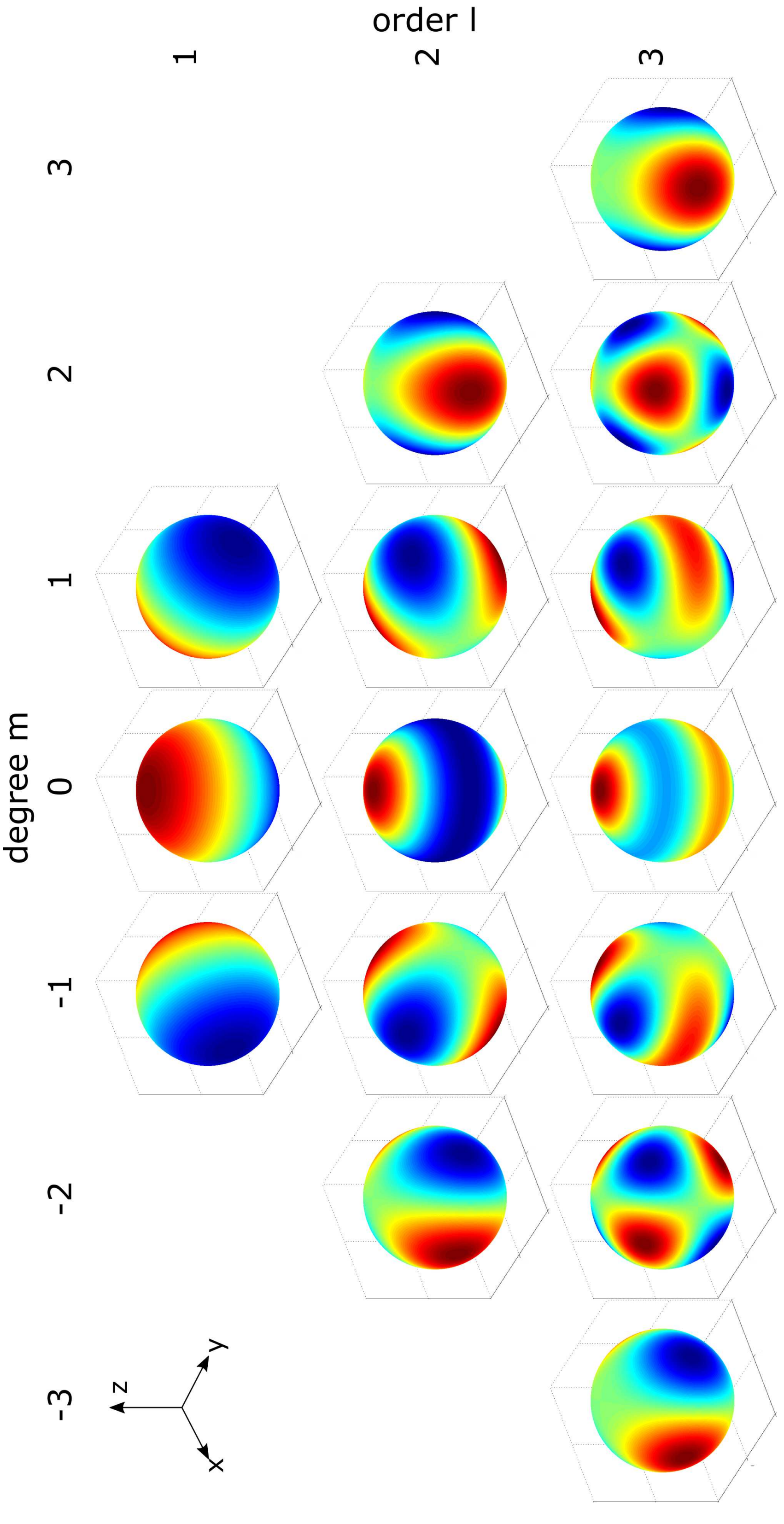

Figure A.1: Spherical harmonics shown on the surface of a sphere for order $l \leq 3$.

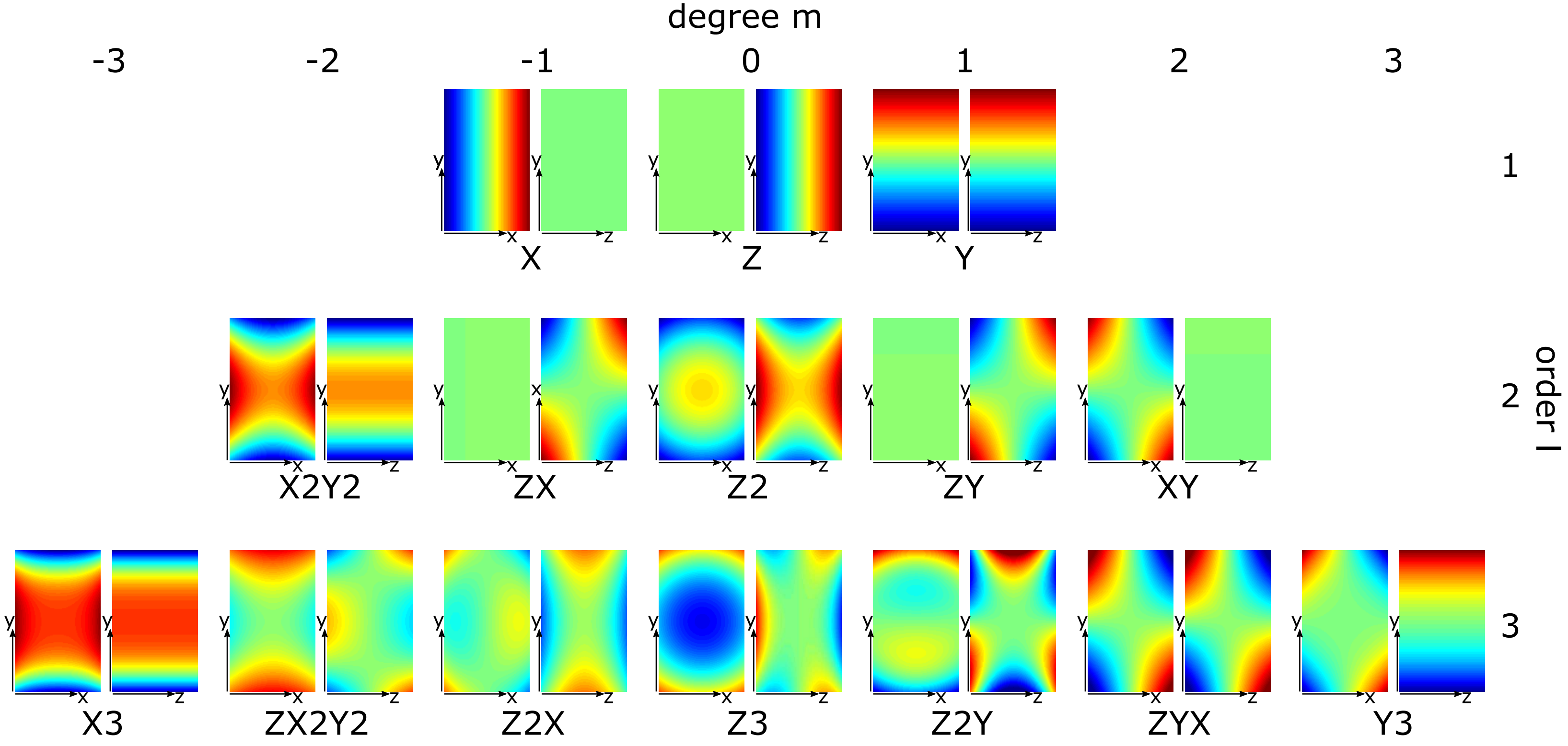

Figure A.2: Spherical harmonics shown as cross section in Cartesian coordinates for order $l \leq 3$.

A.2 Definitions

A.2.1 Rotation Matrices

Definition 1: Rotation matrices along the three axes of the Cartesian coordinate system for an arbitrary angle ζ:

$$\mathbf{R}_x(\zeta) = \begin{pmatrix} 1 & 0 & 0 \\ 0 & \cos\zeta & \sin\zeta \\ 0 & -\sin\zeta & \cos\zeta \end{pmatrix} \tag{A.10}$$

$$\mathbf{R}_y(\zeta) = \begin{pmatrix} \cos\zeta & 0 & -\sin\zeta \\ 0 & 1 & 0 \\ \sin\zeta & 0 & \cos\zeta \end{pmatrix} \tag{A.11}$$

$$\mathbf{R}_z(\zeta) = \begin{pmatrix} \cos\zeta & \sin\zeta & 0 \\ -\sin\zeta & \cos\zeta & 0 \\ 0 & 0 & 1 \end{pmatrix} \tag{A.12}$$

A.2.2 Norms

Definition 2: L_2 norm of vector u with a number of N elements:

$$\|u\|_2 = \sqrt{\sum_{i=1}^{N} |u_i|^2} \tag{A.13}$$

Definition 3: L_1 norm of vector u with a number of N elements:

$$\|u\|_1 = \sum_{i=1}^{N} |u_i| \tag{A.14}$$

Definition 4: L_p norm of vector u with a number of N elements:

$$\|u\|_p = \sqrt[p]{\sum_{i=1}^{N} |u_i|^p}\,, \tag{A.15}$$

Definition 5: Combination of L_1 and L_2 norm to treat gradients in an image in all three spatial directions, for an image u with a number of N elements (voxels):

$$\|\nabla_{xyz}^{+} u\|_{2,1} = \sum_{i=1}^{N} \sqrt{\sum_{l=1}^{3} \left|\left(\nabla_{xyz}^{+} u\right)_{i,l}\right|^2} = \sum_{i=1}^{N} \sqrt{\left|\left(\delta_x^{+} u\right)_i\right|^2 + \left|\left(\delta_y^{+} u\right)_i\right|^2 + \left|\left(\delta_z^{+} u\right)_i\right|^2} \tag{A.16}$$

A.2.3 Finite Differences Operators

Definition 6: Finite difference operators along all three spatial directions using forward differences with Dirchlet boundary conditions and the image resolution Δx, Δy, and Δz in each spatial direction, respectively. N_x, N_y, and N_z are the number of elements in x, y, and z direction:

$$\delta_x^+ u_{m_x,m_y,m_z} = \begin{cases} \frac{1}{\Delta x}\left(u_{m_x+1,m_y,m_z} - u_{m_x,m_y,m_z}\right) & \text{if } \; 1 \leq m_x < N_x \\ 0 & \text{if } \; m_x = N_x \end{cases} \tag{A.17}$$

$$\delta_y^+ u_{m_x,m_y,m_z} = \begin{cases} \frac{1}{\Delta y}\left(u_{m_x,m_y+1,m_z} - u_{m_x,m_y,m_z}\right) & \text{if } \; 1 \leq m_y < N_y \\ 0 & \text{if } \; m_y = N_y \end{cases} \tag{A.18}$$

$$\delta_z^+ u_{m_x,m_y,m_z} = \begin{cases} \frac{1}{\Delta z}\left(u_{m_x,m_y,m_z+1} - u_{m_x,m_y,m_z}\right) & \text{if } \; 1 \leq m_z < N_z \\ 0 & \text{if } \; m_z = N_z \end{cases} \tag{A.19}$$

Definition 7: Finite difference operators along all three spatial directions using backward differences with Dirchlet boundary conditions and the image resolution Δx, Δy, and Δz in each spatial direction, respectively. N_x, N_y, and N_z are the number of elements in x, y, and z direction:

$$\delta_x^- u_{m_x,m_y,m_z} = \begin{cases} \frac{1}{\Delta x}\left(u_{m_x,m_y,m_z} - u_{m_x-1,m_y,m_z}\right) & \text{if } \; 1 < m_x \leq N_x \\ 0 & \text{if } \; m_x = 1 \end{cases} \tag{A.20}$$

$$\delta_y^- u_{m_x,m_y,m_z} = \begin{cases} \frac{1}{\Delta y}\left(u_{m_x,m_y,m_z} - u_{m_x,m_y-1,m_z}\right) & \text{if } \; 1 < m_y \leq N_y \\ 0 & \text{if } \; m_y = 1 \end{cases} \tag{A.21}$$

$$\delta_z^- u_{m_x,m_y,m_z} = \begin{cases} \frac{1}{\Delta z}\left(u_{m_x,m_y,m_z} - u_{m_x,m_y,m_z-1}\right) & \text{if } \; 1 < m_z \leq N_z \\ 0 & \text{if } \; m_z = 1 \end{cases} \tag{A.22}$$

Definition 8: Adjoint operator to finite difference operator with forward differences. Operator is defined along all three spatial directions backward differences with Dirchlet boundary conditions and the image resolution Δx, Δy, and Δz in each spatial direction, respectively. N_x, N_y, and N_z are the number of elements in x, y, and z direction:

$$\delta_x^{*+} u_{m_x,m_y,m_z} = \frac{1}{\Delta x} \begin{cases} -u_{1,m_y,m_z} & \text{if} \quad m_x = 1 \\ u_{m_x-1,m_y,m_z} - u_{m_x,m_y,m_z} & \text{if} \quad 1 < m_x < N_x \\ u_{N_x-1,m_y,m_z} & \text{if} \quad m_x = N_x \end{cases} \tag{A.23}$$

$$\delta_y^{*+} u_{m_x,m_y,m_z} = \frac{1}{\Delta y} \begin{cases} -u_{m_x,1,m_z} & \text{if} \quad m_y = 1 \\ u_{m_x,m_y-1,m_z} - u_{m_x,m_y,m_z} & \text{if} \quad 1 < m_y < N_y \\ u_{m_x,N_y-1,m_z} & \text{if} \quad m_y = N_y \end{cases} \tag{A.24}$$

$$\delta_z^{*+} u_{m_x,m_y,m_z} = \frac{1}{\Delta z} \begin{cases} -u_{m_x,m_y,1} & \text{if} \quad m_z = 1 \\ u_{m_x,m_y,m_z-1} - u_{m_x,m_y,m_z} & \text{if} \quad 1 < m_z < N_z \\ u_{m_x,m_y,N_z-1} & \text{if} \quad m_z = N_z \end{cases} \tag{A.25}$$

Definition 9: Adjoint operator to finite difference operator with backward differences. Operator is defined along all three spatial directions backward differences with Dirchlet boundary conditions and the image resolution Δx, Δy, and Δz in each spatial direction, respectively. N_x, N_y, and N_z are the number of elements in x, y, and z direction:

$$\delta_x^{*-} u_{m_x,m_y,m_z} = \frac{1}{\Delta x} \begin{cases} -u_{2,m_y,m_z} & \text{if} \quad m_x = 1 \\ u_{m_x,m_y,m_z} - u_{m_x+1,m_y,m_z} & \text{if} \quad 1 < m_x < N_x \\ u_{N_x,m_y,m_z} & \text{if} \quad m_x = N_x \end{cases} \tag{A.26}$$

$$\delta_y^{*-} u_{m_x,m_y,m_z} = \frac{1}{\Delta y} \begin{cases} -u_{m_x,2,m_z} & \text{if} \quad m_y = 1 \\ u_{m_x,m_y,m_z} - u_{m_x,m_y+1,m_z} & \text{if} \quad 1 < m_y < N_y \\ u_{m_x,N_y,m_z} & \text{if} \quad m_y = N_y \end{cases} \tag{A.27}$$

$$\delta_z^{*-} u_{m_x,m_y,m_z} = \frac{1}{\Delta z} \begin{cases} -u_{m_x,m_y,2} & \text{if} \quad m_z = 1 \\ u_{m_x,m_y,m_z} - u_{m_x,m_y,m_z+1} & \text{if} \quad 1 < m_z < N_z \\ u_{m_x,m_y,N_z} & \text{if} \quad m_z = N_z \end{cases} \tag{A.28}$$

A.2.4 Discrete Gradient Operators

Definition 10: The 3D discrete gradient operator with forward differences ∇_{xyz}^{+}:

$$\begin{gathered} \nabla_{xyz}^{+} : \mathbb{C}^{N_x \times N_y \times N_z} \mapsto \mathbb{C}^{N_x \times N_y \times N_z \times 3} \\ \left(\nabla_{xyz}^{+} u\right)_{m_x,m_y,m_z} = \begin{pmatrix} \left(\delta_x^{+} u\right)_{m_x,m_y,m_z} \\ \left(\delta_y^{+} u\right)_{m_x,m_y,m_z} \\ \left(\delta_z^{+} u\right)_{m_x,m_y,m_z} \end{pmatrix} = \begin{pmatrix} v_x \\ v_y \\ v_z \end{pmatrix} = v \end{gathered} \tag{A.29}$$

Definition 11: The 3D discrete divergence operator div is defined as the negative transpose of the gradient operator ∇_{xyz}^{+} using the adjoint operator to the finite difference operator with forward differences:

$$\begin{aligned} \operatorname{div} = -\nabla_{xyz}^{+T} &: \mathbb{C}^{N_x \times N_y \times N_z \times 3} \mapsto \mathbb{C}^{N_x \times N_y \times N_z} \\ \left(\nabla_{xyz}^{+T} v\right)_{m_x,m_y,m_z} &= \left(\delta_x^{*+} v_x\right)_{m_x,m_y,m_z} + \left(\delta_y^{*+} v_y\right)_{m_x,m_y,m_z} + \left(\delta_z^{*+} v_z\right)_{m_x,m_y,m_z} \end{aligned} \tag{A.30}$$

Definition 12: The 3D discrete gradient operator with backward differences ∇_{xyz}^{-}:

$$\begin{aligned} \nabla_{xyz}^{-} &: \mathbb{C}^{N_x \times N_y \times N_z} \mapsto \mathbb{C}^{N_x \times N_y \times N_z \times 3} \\ \left(\nabla_{xyz}^{-} u\right)_{m_x,m_y,m_z} &= \begin{pmatrix} \left(\delta_x^{-} u\right)_{m_x,m_y,m_z} \\ \left(\delta_y^{-} u\right)_{m_x,m_y,m_z} \\ \left(\delta_z^{-} u\right)_{m_x,m_y,m_z} \end{pmatrix} = \begin{pmatrix} v_x \\ v_y \\ v_z \end{pmatrix} = v \end{aligned} \tag{A.31}$$

Definition 13: Symmetrized gradient $\mathcal{E}$ for the 3D case using backward differences:

$$\begin{aligned} \mathcal{E} : v = (v_x, v_y, v_z) &\in \mathbb{C}^{N_x \times N_y \times N_z \times 3} \mapsto \mathbb{C}^{N_x \times N_y \times N_z \times 9} \\ (\mathcal{E} v)_{m_x,m_y,m_z} &= \tfrac{1}{2} \left(\nabla_{xyz}^{-} (v)^T + \left(\nabla_{xyz}^{-} (v^{-})^T \right)^T \right)_{m_x,m_y,m_z} = \end{aligned}$$

$$\left(\begin{matrix} \left(\delta_x^{-} v_x\right)_{m_x,m_y,m_z} & \tfrac{1}{2}\left(\left(\delta_x^{-} v_y\right)_{m_x,m_y,m_z} + \left(\delta_y^{-} v_x\right)_{m_x,m_y,m_z}\right) \\ \tfrac{1}{2}\left(\left(\delta_y^{-} v_x\right)_{m_x,m_y,m_z} + \left(\delta_x^{-} v_y\right)_{m_x,m_y,m_z}\right) & \left(\delta_y^{-} v_y\right)_{m_x,m_y,m_z} \\ \tfrac{1}{2}\left(\left(\delta_z^{-} v_x\right)_{m_x,m_y,m_z} + \left(\delta_x^{-} v_z\right)_{m_x,m_y,m_z}\right) & \tfrac{1}{2}\left(\left(\delta_z^{-} v_y\right)_{m_x,m_y,m_z} + \left(\delta_y^{-} v_z\right)_{m_x,m_y,m_z}\right) \end{matrix} \right. \quad \cdots$$

$$\left. \begin{matrix} \tfrac{1}{2}\left(\left(\delta_x^{-} v_z\right)_{m_x,m_y,m_z} + \left(\delta_z^{-} v_x\right)_{m_x,m_y,m_z}\right) \\ \tfrac{1}{2}\left(\left(\delta_y^{-} v_z\right)_{m_x,m_y,m_z} + \left(\delta_z^{-} v_y\right)_{m_x,m_y,m_z}\right) \\ \left(\delta_z^{-} v_z\right)_{m_x,m_y,m_z} \end{matrix} \right) \tag{A.32}$$

Definition 14: Alternative definition of the symmetrized gradient $\mathcal{E}$ because of symmetry using backward differences:

$$\begin{aligned} \mathcal{E} : v = (v_x, v_y, v_z) &\in \mathbb{C}^{N_x \times N_y \times N_z \times 3} \mapsto \mathbb{C}^{N_x \times N_y \times N_z \times 6} \\ (\mathcal{E} v)_{m_x,m_y,m_z} &= \begin{pmatrix} \left(\delta_x^{-} v_x\right)_{m_x,m_y,m_z} \\ \left(\delta_y^{-} v_y\right)_{m_x,m_y,m_z} \\ \left(\delta_z^{-} v_z\right)_{m_x,m_y,m_z} \\ \tfrac{1}{2}\left(\left(\delta_x^{-} v_y\right)_{m_x,m_y,m_z} + \left(\delta_y^{-} v_x\right)_{m_x,m_y,m_z}\right) \\ \tfrac{1}{2}\left(\left(\delta_x^{-} v_z\right)_{m_x,m_y,m_z} + \left(\delta_z^{-} v_x\right)_{m_x,m_y,m_z}\right) \\ \tfrac{1}{2}\left(\left(\delta_y^{-} v_z\right)_{m_x,m_y,m_z} + \left(\delta_z^{-} v_y\right)_{m_x,m_y,m_z}\right) \end{pmatrix} = \begin{pmatrix} w_1 \\ w_2 \\ w_3 \\ w_4 \\ w_5 \\ w_6 \end{pmatrix} = w \end{aligned} \tag{A.33}$$

Definition 15: Symmetrized divergence:
The symmetrized divergence $\mathcal{E}^T$ is defined as the adjoint operator to the symmetrized

gradient $\mathcal{E}$ using forward differences:

$$\begin{aligned}
&\mathcal{E}^T : w = (w_1, w_2, w_3, w_4, w_5, w_6) \in \mathbb{C}^{N_x \times N_y \times N_z \times 6} \mapsto \mathbb{C}^{N_x \times N_y \times N_z \times 3} \\
&\left(\mathcal{E}^T w\right)_{m_x,m_y,m_z} = \begin{pmatrix} (\delta_x^{*-} w_1)_{m_x,m_y,m_z} + \left(\delta_y^{*-} w_4\right)_{m_x,m_y,m_z} + (\delta_z^{*-} w_5)_{m_x,m_y,m_z} \\ (\delta_x^{*-} w_4)_{m_x,m_y,m_z} + \left(\delta_y^{*-} w_2\right)_{m_x,m_y,m_z} + (\delta_z^{*-} w_6)_{m_x,m_y,m_z} \\ (\delta_x^{*-} w_5)_{m_x,m_y,m_z} + \left(\delta_y^{*-} w_6\right)_{m_x,m_y,m_z} + (\delta_z^{*-} w_3)_{m_x,m_y,m_z} \end{pmatrix}
\end{aligned} \tag{A.34}$$

A.2.5 Analytic Gradient Operators

Definition 16: Analytic gradient operator with respect to the model parameters, the intensity value in each voxel in the image u:

$$\nabla_u J(u) = \begin{pmatrix} \dfrac{\partial J(u)}{\partial u_1} \\ \vdots \\ \dfrac{\partial J(u)}{\partial u_N} \end{pmatrix} \tag{A.35}$$

Definition 17: Second order analytic gradient operator with respect to the model parameters, the intensity value in each voxel in the image u, the Hessian matrix:

$$\nabla_u^2 J(u) = \begin{pmatrix} \dfrac{\partial^2 J(u)}{\partial u_1^2} & \cdots & \dfrac{\partial^2 J(u)}{\partial u_1 \partial u_N} \\ \vdots & \ddots & \vdots \\ \dfrac{\partial^2 J(u)}{\partial u_N \partial u_1} & \cdots & \dfrac{\partial^2 J(u)}{\partial u_N^2} \end{pmatrix} \tag{A.36}$$

A.2.6 Convex Optimization

Definition 18: Convex Conjugate: The convex Conjugate $F^*(y)$ (or Fenchel duality) of a function $F(x)$, $\quad F : \mathbb{C}^N \mapsto \mathbb{R}$ is defined as:

$$F^*(y) = \sup_x \langle x, y \rangle - F(x) \tag{A.37}$$

Definition 19: Convex Conjugate of the squared L_p norm from [11]:

$$\begin{aligned} F(x) &= \frac{1}{2}\|x\|_p^2 \\ F^*(y) &= \max_x \langle x, y \rangle - \frac{1}{2}\|x\|_p^2 = \frac{1}{2}\|y\|_*^2 \end{aligned} \tag{A.38}$$

Here, $\| \cdot \|_*$ denotes the dual norm.

Definition 20: Convex Conjugate of the L_p norm from [11]:

$$\begin{aligned} &F(x) = \|x\|_p \\ &F^*(y) = \mathcal{I}_{\|\cdot\|_* \leq 1}(y) = \begin{cases} 0, & \text{if} \quad \|y\|_* \leq 1 \\ \infty, & \text{if} \quad \text{else} \end{cases} \end{aligned} \tag{A.39}$$

Here, $\|\cdot\|_*$ denotes the dual norm and $\mathcal{I}_{\|\cdot\|_* \leq 1}$ is the convex indicator function.

Definition 21: Dual norm from [32]:
The dual norm $\|\cdot\|_*$ to an L_p norm $\|\cdot\|_p$ is an L_q norm $\|\cdot\|_q$ defined as follows:

$$\frac{1}{p} + \frac{1}{q} = 1 \rightarrow q = \frac{p}{p-1} \tag{A.40}$$

This means the dual norm to an L_2 norm is again an L_2 norm and the dual norm to an L_1 norm is an L_∞ norm:

$$\|x\|_2 \xRightarrow{\text{dual norm}} \|y\|_2 \tag{A.41}$$

$$\|x\|_1 \xRightarrow{\text{dual norm}} \|y\|_\infty \tag{A.42}$$

$$\|x\|_\infty \xRightarrow{\text{dual norm}} \|y\|_1 \tag{A.43}$$

Definition 22: The convex indicator function:

$$\mathcal{I}_C(x) = \begin{cases} 0, & \text{if} \quad x \in C \\ \infty, & \text{if} \quad x \notin C \end{cases} \tag{A.44}$$

Definition 23: Convex Conjugate of the squared L_2 norm:

$$F(x) = \frac{1}{2}\|x\|_2^2 \quad \Rightarrow \quad F^*(y) = \frac{1}{2}\|y\|_2^2 \tag{A.45}$$

Definition 24: Convex Conjugate of the L_1 norm:

$$\begin{aligned} &F(x) = \|x\|_1 \\ &F^*(y) = \mathcal{I}_{\|\cdot\|_\infty \leq 1}(y) = \begin{cases} 0, & \text{if} \quad \|y\|_\infty \leq 1 \\ \infty, & \text{if} \quad \text{else} \end{cases} \end{aligned} \tag{A.46}$$

Definition 25: Special version of the convex indicator function:

$$\mathcal{I}_{\eta\|\cdot\|_\infty \leq 1}(y) = \begin{cases} 0, & \text{if} \quad \frac{1}{\eta}\|y\|_\infty \leq 1 \\ \infty, & \text{if} \quad \text{else} \end{cases} \tag{A.47}$$

Definition 26: Convex Conjugate: Multiplication with a constant coefficient α, according to [11]:

$$\begin{aligned} G(x) &= \alpha F(x) \qquad \alpha > 0 \\ G^*(y) &= \alpha F^*\left(\frac{y}{\alpha}\right) \end{aligned} \tag{A.48}$$

Definition 27: Proximal mapping, proximal operator or prox operator, definition according to [46]:

$$\hat{x} = (I + \tau \partial F)^{-1}(y) = \operatorname{prox}_F(y) = \arg\min_x \frac{\|x - y\|_2^2}{2} + \tau F(x) \tag{A.49}$$

Definition 28: The proximal mapping for the convex indicator function $\mathcal{I}_C$:

$$\begin{aligned} &F^*(y) = \mathcal{I}_C(y) \\ &\operatorname{prox}_{F^*}(\xi) = \arg\min_y \|y - \xi\|_2^2 + \mathcal{I}_C(y) = \arg\min_{y \in C} \|y - \xi\|_2^2 = P_C(\xi) \end{aligned} \tag{A.50}$$

Here, P_C is the projection operator, projecting ξ onto the convex set C.

Definition 29: The proximal mapping for the convex indicator function $\mathcal{I}_{\eta\|\cdot\|_\infty \leq 1}$:

$$\begin{aligned} &F^*(y) = \mathcal{I}_{\eta\|\cdot\|_\infty \leq 1}(y) \\ &\operatorname{prox}_{F^*}(\xi)_{m_x,m_y,m_z} = \frac{\xi_{m_x,m_y,m_z}}{\max\left(1, \frac{|\xi_{m_x,m_y,m_z}|}{\eta}\right)} \end{aligned} \tag{A.51}$$

This means the proximal operator to the convex indicator function is the voxel wise projection onto the L_∞ ball.

Definition 30: The proximal mapping the L_2 norm:

$$\begin{aligned} F^*(y) &= \frac{1}{2\lambda}\|y\|_2^2 \\ \operatorname{prox}_{F^*}(\xi) &= \frac{\xi}{1 + \frac{\tau}{\lambda}} \end{aligned} \tag{A.52}$$

B

List of Acronyms

Glossary

ACL Auto Calibration Line

ADC Analog to Digital Converter

AFI Actual Flip Angle Imaging

AI Artificial Intelligence

ASL Arterial Spin Labeling

BS Bloch-Siegert

bSSFP balanced Steady State Free Precession

CAIPI Controlled Aliasing in Parallel Imaging

CAIPIRINHA Controlled aliasing in volumetric parallel imaging

CEST Chemical Exchange Saturation Transfer

CG Conjugate Gradient

CP Circular Polarized

CS Compressed Sensing

CSF Cerebrospinal Fluid

CT Computer Tomography

DAM Double Angle Method

DCT Discrete Cosinus Transforms

DFT	Discrete Fourier Transform
DREAM	Dual Refocusing Echo Acquisition Mode
DTI	Diffusion Tensor Imaging
DWI	Diffusion Weighted Imaging
ECG	Electrocardiography
EPI	Echo Planar Imaging
EPT	Electrical Property Tomography
EPTI	Echo Planar Time-resolved Imaging
ESR	Electron Spin Resonance
FDTD	Finite Differences Time Domain
FFC	Fast Field Cycling
FFT	Fast Fourier Transform
FID	Free Induction Decay
FISTA	Fast Iterative Shrinkage and Thresholding Algorithm
FLASH	Fast Low Angle Shot
fMRI	functional MRI
FOV	Field of View
FWHM	Full Width Half Maximum
GLM	General Linear Model
GOOSE	Globally Optimal Surface Estimation
GPU	Graphics Processing Unit
GRAPPA	Generalized Auto-calibrating Partial Parallel Acquisition
GRASE	Gradient and Spin Echo
GRE	Gradient Recalled Echo
HS	Hyperbolic Secant
ICTGV	Infimal Convolution Total Generalized Variation

IDEAL Iterative Decomposition of water and fat with Echo Asymmetry and Least squares estimation

IRGN Iteratively Regularized Gauss Newton

MAE Mean Absolute Error

medAE median Absolute Error

MR Magnetic Resonance

MRI Magnetic Resonance Imaging

MSE Multiple Spin Echo

MT Magnetization Transfer

NMR Nuclear Magnetic Resonance

NSA Number of Signal Averages

NUFFT Non-Uniform Fast Fourier Transform

PCA Phase Contrast Angiography

PET Positron Emission Tomography

PI Parallel Imaging

POCS Projection Onto Convex Set

pTX parallel transmit

qMRI quantitative MRI

QSM Quantitative Susceptibility Mapping

RF Radio Frequency

RMSE Root Mean Squared Error

ROI Region Of Interest

SAR Specific Absorption Rate

satTFL Saturated Turbo FLASH

SE Spin Echo

SENSE Sensitivity Encoding

SMASH	Simultaneous Acquisition of Spatial Harmonics
SMS	Simultaneous Multi-Slice
SNR	Signal-to-Noise Ratio
SOS	Sum of Squares
SPIRiT	iterative Self-consistent Parallel Imaging Reconstruction
STE	Stimulated Echo
STEAM	Stimulated Echo Acquisition Mode
SVD	Singular Value Decomposition
SWI	Susceptibility Weighted Imaging
TE	Echo Time
TEM	Transverse Electro-Magnetic
TGV	Total Generalized Variation
TR	Repetition Time
TSE	Turbo Spin Echo
TV	Total Variation
UHF	Ultrahigh Field
VARPRO	Variable Projection
VFA	Variable Flip Angle

C

List of Symbols

Symbol	Unit	Description
a,b,c	mm	principle semi-axes of an ellipsoid
$\mathbf{a}$	–	different modeled phase contributions in the GLM
A_c	mm^2	cross sectional area of a loop coil
A_{lm}	–	weighting coefficient of spherical harmonic functions
A_n	–	pTx amplitude amplification factor for transmit channel n
$\tilde{\mathbf{A}}$	–	vector of pTx amplitude amplification factors
$A(u)$	–	MR forward operator
$A^H(u)$	–	MR backward operator
A_+, A_-	–	MR forward operators for $+\omega_{\mathrm{RF}}$ and $-\omega_{\mathrm{RF}}$ acquisition
$\mathbf{A}$	–	MR forward operator in matrix form
$\vec{B}$	T	general magnetic field vector
B_x,B_y,B_z	T	x, y and z component of the magnetic field vector
$B_\perp$,$B_\parallel$	T	magnetic field component perpendicular/parallel to a surface
$\vec{B}_0$	T	static magnetic field vector
B_0	T	magnitude of static magnetic field
$\mathbf{B}_0^{\mathrm{shim}}$	mT	field offset generated by the all shim coils
B_1	µT	general magnitude of the RF field
B_1^+	µT	magnitude of the transmit RF field
$\vec{B}_1^+$	µT	RF transmit field vector
$\vec{B}_1^-$	µT	RF receive field vector
$\mathbf{B}_1^-$	µT	vector with RF receive fields in a voxel for all N_c receive coils
$\vec{B}_{eff}$	µT	effective magnetic field vector in the rotating frame
B_{eff}	µT	magnitude of the effective magnetic field in the rotating frame
B_{eddy}	µT	transient field offset due to eddy currents
$\vec{B}_1^{lin}$	µT	linear polarized RF field

Symbol	**Unit**	**Description**
$\vec{B}_1^{cw}(t)$	µT	circular polarized RF field rotating direction clockwise
$\vec{B}_1^{ccw}(t)$	µT	circular polarized RF field rotating direction counterclockwise
$B^{+}_{1_n}$	µT	B_1^+ field of transmit channel n
$B^{+}_{1_{res}}$	µT	resulting complex B_1^+ field from multiple transmit coils
$B_{1,\text{peak}}$	µT	peak magnitude of B_1 encoding pulse for the Bloch-Siegert method
$B_{1,\text{norm}}$	–	normalized B_1^+ envelope
$\mathbf{B}^{+,norm}_{1_n}$	–	normalized B_1^+ map of transmit channel n
c_0	$\mathrm{m\,s^{-1}}$	speed of light in vacuum $c_0 \approx 3 \cdot 10^8$
C_n	–	normalized coil sensitivity profile of receive coil n
$\mathbf{C}$	–	matrix containing the coil sensitivity values of one voxel
$\vec{D}$	$\mathrm{N\,m}$	torque
$\mathbf{D}$	–	modified system matrix for CG
d	a.u.	measured data $d \in \mathbb{C}^{N_{k_x} \times N_{k_y} \times N_{k_z} \times N_c}$
d_+,d_-	a.u.	measured data for $+\omega_{\text{RF}}$ and $-\omega_{\text{RF}}$ acquisition
d_n	a.u.	measured data of receive coil n, $d_n \in \mathbb{C}^{N_{k_x} \times N_{k_y} \times N_{k_z}}$
E	J	energy
$\vec{E}$	$\mathrm{V\,m^{-1}}$	electric field vector
$E_\perp$,$E_\parallel$	$\mathrm{V\,m^{-1}}$	electric field component perpendicular/parallel to a surface
$F(x)$,$G(x)$	–	arbitrary linear operator $F : \mathbb{C}^N \mapsto \mathbb{R}^+$ and $G : \mathbb{C}^N \mapsto \mathbb{R}^+$
$F(y)^*$	–	convex conjugate to $F(x)$
FOV	mm	Field of View
FOV$_x$,FOV$_y$, FOV$_z$	mm	Field of View in x, y and z direction
G_x,G_y,G_z	$\mathrm{mT\,m^{-1}}$	gradient field strength in x, y and z direction
G_{m1},G_{m2}	ms	DREAM preparation gradient
$\mathbf{G}$	–	system matrix in the GLM
g	–	geometry factor for spatial dependent noise amplification
h	$\mathrm{J\,s}$	Planks constant $h = 6.626 \cdot 10^{-34}$
$\hbar$	$\mathrm{J\,s}$	Planks constant divided by 2π.
$\vec{H}$	$\mathrm{A\,m^{-1}}$	magnetic field strength
H_0	$\mathrm{A\,m^{-1}}$	magnitude of externally applied magnetic field strength
$H_\perp$,$H_\parallel$	$\mathrm{A\,m^{-1}}$	magnetic field strength perpendicular/parallel to a surface
H_i	$\mathrm{A\,m^{-1}}$	induced demagnetization field
I_c	A	electric current in the coil
I_{shim}	A	electric current of the shim coil
i	–	imaginary unit
$\mathbf{I}$	–	identity matrix
$J(u)$	a.u.	cost function to be minimized

Symbol	Unit	Description
$\vec{J}$	$\mathrm{J\,s}$	angular momentum of subatomic particle
J	$\mathrm{J\,s}$	magnitude of angular momentum of subatomic particle
J_z	$\mathrm{J\,s}$	z-component of subatomic particle's angular momentum
j	–	spin quantum number
$\vec{j}$	$\mathrm{A\,m^{-2}}$	electric current density
$j_\perp$,$j_\parallel$	$\mathrm{A\,m^{-2}}$	electric current density perpendicular/parallel to a surface
k	$\mathrm{J\,K^{-1}}$	Boltzmann constant $k = 1.38 \cdot 10^{-2}$
k_x,k_y,k_z	$\mathrm{mm^{-1}}$	spatial frequency in x, y and z direction
$k_{x,max}$,$k_{y,max}$,	$\mathrm{mm^{-1}}$	maximum acquired spatial frequency
$k_{z,max}$	$\mathrm{mm^{-1}}$	in x, y and z direction
K_{BS}	$\frac{\mathrm{rad}}{\mathrm{G^2}}$/ $\frac{\mathrm{rad}}{\mathrm{\mu T^2}}$	pulse dependent Bloch-Siegert constant
K	–	arbitrary operator
$\mathbf{K}$	–	matrix considering the chemical shift between fat and water, for single or multi-peak model
$\vec{L}$	$\mathrm{J\,s}$	angular momentum contribution from orbital motion
l_x,l_y,l_z	–	discrete k-space index in x, y and z direction
l,m	–	order and degree of spherical harmonic functions
$\vec{M}$	$\mathrm{A\,m^{-1}}$	general magnetization vector
M	$\mathrm{A\,m^{-1}}$	magnitude of general magnetization
$\vec{M}_0$	$\mathrm{A\,m^{-1}}$	thermal equilibrium magnetization vector
M_0	$\mathrm{A\,m^{-1}}$	magnitude of thermal equilibrium general magnetization
M_x,M_y,M_z	$\mathrm{A\,m^{-1}}$	x, y and z component of the magnetization
M_{xy}	$\mathrm{A\,m^{-1}}$	transverse magnetization
$M_\perp$	$\mathrm{A\,m^{-1}}$	complex transverse magnetization
m_j	–	magnetic quantum number
m_x,m_y,m_z	–	discrete voxel index in image space in x, y and z direction
$N_{\pm 1/2}$	–	number of parallel ($+1/2$) and antiparallel ($-1/2$) aligned spins
N_c	–	number of receive coils
N_{k_x},N_{k_y},N_{k_z}	–	number of acquired k-space samples in k_x, k_y and k_z direction
N_x,N_y,N_z	–	number of image voxels in x, y and z direction
N_{noise}	–	number of noise samples
N_{TE}	–	number of acquired echo times
N_w	–	number of coils windings
N_{Rx},N_{Tx}	–	number of receive and transmit channels
N_F	–	number of modeled fat peaks
N_S	–	number of acquired signals
$\vec{n}$	–	normal vector to loop coil cross section

Symbol	**Unit**	**Description**
p	–	general probability
$p(u\|d)$	–	posterior probability or conditional probability
$p(u)$	–	prior probability
$p(d\|u)$	–	likelihood
$p_\pm$	–	probability for a spin being in $+1/2$ or $-1/2$ state
p_k	–	search direction in steepest descent and CG in iteration k
p,q,r	a.u.	dual variables for TGV in primal dual
P	–	undersampling pattern
q	–	voxel index
$\vec{r}$	mm	vector to a certain point in space
R	mm	diameter of the coil
$\mathbf{R}_x$,$\mathbf{R}_y$,$\mathbf{R}_z$	–	rotational matrix around the x, y and z axis
R_{eff}	Ω	effective noise resistance
R_{coil}	Ω	noise resistance arising from the receive coil
$R_{\text{electronics}}$	Ω	noise resistance arising form the electronics
R_{body}	Ω	noise resistance from the body under investigation
R_{acc}	–	acceleration factor
R_2^*	s^{-1}	reduced transverse relaxation rate
$R_{2,F}^*$	s^{-1}	reduced transverse relaxation rate of the fat compartment
$R_{2,W}^*$	s^{-1}	reduced transverse relaxation rate of the water compartment
$\mathtt{R}$	–	residuum
r_a	–	ratio between independent principle axes of a rotational ellipsoid
r	mm	radius of polar coordinates
s	a.u.	measured and quadrature demodulated signal
s_1	a.u.	real part of quadrature demodulated signal
s_2	a.u.	imaginary part of quadrature demodulated signal
S	a.u.	complex MR signal in image space
S_n	a.u.	complex MR signal in image space from receive coil n
S_{comb}	a.u.	combined MR signal from different receive coils in image space
S_F	a.u.	fat signal
S_W	a.u.	water signal
S_{in}	a.u.	in-phase signal
S_{out}	a.u.	opposed-phase signal
$\mathbf{S}$	a.u.	vector containing the signal in a certain voxel for all N_c receive coils or vector containing the signal in a certain voxel for different TE
$\mathbf{S}_{W,F}$	a.u.	vector containing the water and fat signal in a certain voxel
S_{vox}	a.u.	signal from one voxel
$\mathbf{S}_\phi$	rad	phase of the multiecho acquisitions for the GLM

Symbol	Unit	Description
$\vec{S}$	J s	angular momentum contribution from the intrinsic spin
SAR	$\mathrm{W\,kg^{-1}}$	specific absorption rate, power deposition in tissue
SNR	dB	signal to noise ratio
t	ms	time
t_0	ms	starting time point
T	K	absolute temperature
T_p	ms	duration of the RF pulse
T_{G_y}	ms	duration of the phase encoding gradient
T_1	ms	longitudinal relaxation time
$T_{1,F}$	ms	longitudinal relaxation time of the fat compartment
$T_{1,W}$	ms	longitudinal relaxation time of the water compartment
T_2	ms	transverse relaxation time
T_2^*	ms	reduced transverse relaxation time
T_2'	ms	reverseable dephasing time constant
T_S	ms	DREAM preparation time
T_d	ms	DREAM delay time
T_{m1},T_{m2}	ms	DREAM preparation gradient duration
$\mathbf{T}$	–	matrix considering ΔB_0 and R_2^* in each voxel
TE	ms	echo time
TM	ms	mixing time
TR	ms	repetition time
$\mathrm{TV}(u)$	–	total variation functional
$\mathrm{TGV}_\alpha^2(u)$	–	second order total generalized variation functional
u_c	V	induced voltage in receive coil
u	a.u.	voxel values of the image to be reconstructed $u \in \mathbb{C}^{N_x \times N_y \times N_z}$
v	a.u.	vector field to be minimized in TGV functional $v \in \mathbb{C}^{N_x \times N_y \times N_z \times 3}$
u,v	a.u.	primal variables for TGV in primal dual
V	$\mathrm{mm^3}$	volume
V_s	$\mathrm{mm^3}$	sample volume
V_{vox}	$\mathrm{mm^3}$	voxel volume
X_l^m	–	spherical harmonic function of order l and degree m
$\vec{X}$	a.u.	general vector field
$X_\perp$,$X_\parallel$	a.u.	general field component perpendicular/parallel to a surface
x, y, z	mm	coordinates of the Cartesian coordinate system
$\mathbf{x}$	a.u.	vector containing the unaliased voxel values of the final image
x	–	primal variable in general primal dual formulation
$\mathbf{y}$	a.u.	vector containing the aliased voxel values of each receive coil
y	–	dual variable in general primal dual formulation

Symbol	**Unit**	**Description**
z	–	modified data for CG
α	rad / °	flip angle
α_m	%	relative signal contribution of fat peak m, multi peak model
β	rad / °	refocusing or second flip angle in a sequence
γ	$\frac{\mathrm{rad}}{\mathrm{T\,s}}$ / $\frac{\mathrm{MHz}}{\mathrm{T}}$	gyromagnetic ratio
Δf_{BW}	Hz	receive bandwidth
Δk_x,Δk_y,Δk_z	mm^{-1}	k-space resolution
Δt	µs	dwell time of receiver ADC
Δx,Δy,Δz	mm	voxel dimensions in x, y and z direction
ΔB_0	µT	static magnetic field distortion
$\Delta B_{0_{\mathrm{max}}}$	µT	maximum unambiguously resolveable field deviation for ΔTE
$\Delta B_{z_{in}}$	µT	field distortion inside the object
$\Delta B_{z_{out}}$	µT	field distortion outside the object
ΔT_F	ms	time interval between in-phase and opposed phase fat signal
$\Delta\phi$	rad	phase difference
$\Delta\chi$	–	difference in magnetic susceptibility between two objects
$\Delta\omega$	$\mathrm{rad\,s^{-1}}$	general resonance offset
$\Delta\omega_0$	$\mathrm{rad\,s^{-1}}$	resonance offset due to static magnetic field variations
$\Delta\omega_F$	$\mathrm{rad\,s^{-1}}$	chemical shift between fat and water using the single peak model
$\Delta\omega_{F,m}$	$\mathrm{rad\,s^{-1}}$	chemical shift between fat and water of fat peak m in the multi-peak model
δ_x^+,δ_y^+,δ_z^+	–	Finite difference operator using forward differences along the x, y and z direction
δ_x^-,δ_y^-,δ_z^-	–	Finite difference operator using backward differences along the x, y and z direction
δ_x^{*+},δ_y^{*+},δ_z^{*+}	–	Adjoint operator to finite difference operator using forward differences along the x, y and z direction
δ_x^{*-},δ_y^{*-},δ_z^{*-}	–	Adjoint operator to finite difference operator using backward differences along the x, y and z direction
ϵ_0	$\frac{\mathrm{A\,s}}{\mathrm{V\,m}}$	absolute permittivity in vacuum $\epsilon_0 \approx 8.8542 \cdot 10^{-12}$
ϵ_r	–	relative permittivity
ϵ	%	error map
η_k	a.u.	noise samples of receive coil k
η_s	%	fat signal fraction
θ	rad	angle between effective magnetic field and the x-axis
Θ	rad/°	angle between fat and water magnetization vector
ϑ,φ	rad	polar and azimuthal angle of polar coordinates

Symbol	**Unit**	**Description**
κ_k	–	step size in steepest descent and CG in iteration k
λ_{vac}	m	wavelength in vacuum
λ_{mat}	m	wavelength in matter
λ	–	regularization parameter
$\vec{\mu}$	$\mathrm{A\,m^2}$	magnetic moment
μ_x,μ_y,μ_z	$\mathrm{A\,m^2}$	x, y and z component of magnetic moment respectively
μ_0	$\frac{\mathrm{V\,s}}{\mathrm{A\,m}}$	magnetic permeability in vacuum $\mu_0 = 1.256637 \cdot 10^{-6}$
μ_r	–	relative magnetic permeability
ν	a.u.	noise contribution
ξ	–	demagnetization factor
ξ_a,ξ_b,ξ_c	–	demagnetization factor of an ellipsoid along the principle axis
ρ_0	$\mathrm{mm^{-3}}$	spin density
ρ_F	$\mathrm{mm^{-3}}$	spin density of the fat compartment
ρ_W	$\mathrm{mm^{-3}}$	spin density of the water compartment
ρ	$\mathrm{kg\,m^{-3}}$	mass density
ρ_c	$\mathrm{A\,s\,m^{-3}}$	charge density
ϱ	–	flip angle scaling factor
σ_{meas}	V	noise standard deviation in the measured signal
$\sigma_{W,F}$	a.u.	noise standard deviation in the water and fat signal, respectively
σ	$\mathrm{S\,m^{-1}}$	conductivity
σ,τ	–	step size in primal dual for primal and dual update, respectively
τ	s	evolution time between fat/water in-phase and readout
ϕ	rad	acquired phase angle due to a resonance offset
ϕ_0	rad	initial phase angle or transceive phase
$\phi_{B_{1n}}$	rad	phase of the B_1^+ field generated by transmit channel n
ϕ_n	rad	pTx phase shift for transmit channel n
$\mathbf{\Phi}$	rad	vector of pTx phase shifts
ϕ_{TE_n}	rad	phase at echo time n
ϕ_{HS}	rad	B_1 dependent phase shift for the hyperbolic secant method
ϕ_{BS}	rad	B_1 dependent phase shift for the Bloch-Siegert method
ϕ_{eddy}	rad	resulting phase shift due to eddy currents
$\mathbf{\Phi}_n$	rad	B_1^+ phase map of transmit channel n
χ	–	magnetic susceptibility
$\Psi_{k,l}$	a.u.	noise covariance between channel k and l
$\mathbf{\Psi}$,$\mathbf{\Psi}_n$	a.u.	noise covariance matrix
$\mathbf{\Psi}_s$	a.u.	signal covariance matrix
ω	$\mathrm{rad\,s^{-1}}$	reference angular frequency → frequency of the RF field
ω_0	$\mathrm{rad\,s^{-1}}$	Larmor frequency at a certain field strength

Symbol	**Unit**	**Description**
ω_1	$\mathrm{rad\,s^{-1}}$	angular frequency due to the RF field in the rotating frame
ω_{eff}	$\mathrm{rad\,s^{-1}}$	angular frequency around the effective magnetic field
ω_{RF}	$\mathrm{rad\,s^{-1}}$	resonance offset of the Bloch-Siegert pulse
ω_{BS}	$\mathrm{rad\,s^{-1}}$	effective Bloch-Siegert resonance offset
$\vec{\omega}$	$\mathrm{rad\,s^{-1}}$	direction and angular frequency of the coordinate system's rotation
ω'	$\mathrm{rad\,s^{-1}}$	off-resonance frequency in the rotating coordinate system
ω_F	$\mathrm{rad\,s^{-1}}$	fat resonance frequency
ω_W	$\mathrm{rad\,s^{-1}}$	water resonance frequency
Ω_q	$\mathrm{rad\,s^{-1}}$	solution domain for $\gamma B_{0,q}$ in each voxel, containing all local minima
$\mathcal{C}_m$	–	labeled region in image
$\mathcal{D}$	–	data fidelity term
$\mathcal{E}$	–	symmetrized derivative
$\mathcal{F}$	–	Fourier operator
$\mathcal{F}^{-1}$	–	inverse Fourier operator
$\mathcal{G}$	–	primal dual gap
$\mathcal{I}_C$	–	convex indicator function
$\mathcal{M}$	–	mask for score calculation of fat/water separation results
$\mathcal{R}$	–	regularization term
$\mathcal{S}$	–	Score for fat/water separation results
$\Re$	–	Real part operator
$\Im$	–	Imaginary part operator
∇X	–	continuous spatial gradient operator $\left(\frac{\partial X}{\partial x}, \frac{\partial X}{\partial y}, \frac{\partial X}{\partial z}\right)^T$
$\nabla \cdot \vec{X}$	–	continuous spatial divergence operator $\frac{\partial X_x}{\partial x} + \frac{\partial X_y}{\partial y} + \frac{\partial X_z}{\partial z}$
$\nabla \times \vec{X}$	–	continuous spatial rotor operator $\left(\frac{\partial X_z}{\partial y} - \frac{\partial X_y}{\partial z}, \frac{\partial X_x}{\partial z} - \frac{\partial X_z}{\partial x}, \frac{\partial X_y}{\partial x} - \frac{\partial X_x}{\partial y}\right)^T$
$\nabla^2 X$	–	continuous spatial Laplace operator $\frac{\partial^2 X}{\partial x^2} + \frac{\partial^2 X}{\partial y^2} + \frac{\partial^2 X}{\partial z^2}$
∇^+_{xyz}	–	discrete spatial gradient operator using forward differences
∇^-_{xyz}	–	discrete spatial gradient operator using backward differences
∇^{T-}_{xyz}	–	discrete spatial divergence operator using backward differences
∇_u	–	analytic gradient operator with respect to the model parameters u
∇^2_u	–	Hessian matrix operator with respect to the model parameters u
$\lvert\partial\mathcal{C}_m\rvert$	–	perimeter of $\mathcal{C}_m$
$\lVert \cdot \rVert_p$	–	L_p norm
$\langle\cdot\rangle$	–	scalar product
$\odot$	–	point wise multiplication
$\angle$	–	angle of a complex number

D

List of Publications

My work at the Institute of Medical Engineering led to the following peer-reviewed publications.

Journal Publications

1. A. Lesch, M. Schlögl, M. Holler, K. Bredies, and R. Stollberger. Ultrafast 3D Bloch–Siegert B_1^+-mapping using variational modeling. *Magnetic Resonance in Medicine*, 81(2):881–892, 2019. `doi:10.1002/mrm.27434`

2. M. Soellradl, J. Strasser, A. Lesch, R. Stollberger, S. Ropele, and C. Langkammer. Adaptive slice-specific z-shimming for 2D spoiled gradient-echo sequences. *Magnetic Resonance in Medicine*, 2020. (in press)

3. O. Maier, J. Schoormans, M. Schlögl, G. J. Strijkers, A. Lesch, T. Benkert, T. Block, B. F. Coolen, K. Bredies, and R. Stollberger. Rapid T1 quantification from high resolution 3D data with model-based reconstruction. *Magnetic Resonance in Medicine*, 81(3):2072–2089, 2019. `doi:10.1002/mrm.27502`

4. M. Soellradl, A. Lesch, J. Strasser, L. Pirpamer, R. Stollberger, S. Ropele, and C. Langkammer. Assessment and correction of macroscopic field variations in 2D spoiled gradient-echo sequences. *Magnetic Resonance in Medicine*, 2019. `doi:10.1002/mrm.28139`

5. B. Neumayer, A. Lesch, F. Thaler, T. Widek, S. Tschauner, J. De Tobel, T. Ehammer, B. Kirnbauer, J. Boldt, M. van Wijk, R. Stollberger, and M. Urschler. The four-minute approach revisited: accelerating MRI-based multi-factorial age estimation. *International Journal of Legal Medicine*, pages 1–11, 2019. `doi:10.1007/s00414-019-02231-w`

Conference Contributions

2020

6. A. Lesch, C. S. Aigner, and R. Stollberger. Highly accelerated 3D Bloch Siegert B_1^+ mapping at 7T. In *Proceedings of the 28th Annual Meeting of ISMRM, Virtual Meeting*, page 662, 2020
7. C. Graf, C. S. Aigner, A. Rund, A. Lesch, and R. Stollberger. Inversion pulses with B1-robustness and reduced energy by optimal control. In *Proceedings of the 28th Annual Meeting of ISMRM, Virtual Meeting*, page 3696, 2020

2019

8. A. Lesch, C. S. Aigner, S. Spann, M. Schlögl, and R. Stollberger. 3D Bloch-Siegert EPI B_1^+-mapping. In *Proceedings of the 27th Annual Meeting of ISMRM, Montreal, Quebec, Canada*, page 926, 2019

2018

9. S. M. Spann, C. S. Aigner, M. Schlögl, A. J. Lesch, K. Bredies, S. Roppele, D. Pinter, L. Pirpamer, and R. Stollberger. Acceleration of arterial spin labeling data using spatio-temporal total generalized variation (TGV) reconstruction. In *Proceedings of the 26th Annual Meeting of ISMRM, Paris, France*, 2018

2017

10. A. Lesch, M. Schlögl, and R. Stollberger. Robust accelerated reconstruction for Bloch-Siegert B1-mapping. In *Proceedings of the 25th Annual Meeting of ISMRM, Honolulu, Hawai'i, USA*, page 3918, 2017
11. O. Maier, M. Schloegl, A. Lesch, A. Petrovic, M. Holler, K. Bredies, T. Pock, and R. Stollberger. Improved accelerated model-based parameter quantification with Total-Generalized-Variation regularization. In *Proceedings of the 25th Annual Meeting of ISMRM, Honolulu, Hawai'i, USA*, volume 25, page 3855, 2017

2016

12. A. Lesch, M. Schlögl, M. Holler, and R. Stollberger. Highly accelerated Bloch-Siegert B_1^+-mapping using variational modeling. In *Proceedings of the 24th Annual Meeting of ISMRM, Singapore*, page 1875, 2016
13. A. Lesch, K. Bredies, C. Diwoky, and R. Stollberger. Chemical shift based fat-water separation using a variational approach for B0-field correction. In *Proceedings of the 24th Annual Meeting of ISMRM, Singapore*, volume 24, page 1875, 2016

14. O. Maier, M. Schlögl, A. Lesch, A. Petrovic, K. Bredies, and R. Stollberger. Accelerated DESPOT T1-mapping with iteratively TV regularized Gauss-Newton method. In *Proceedings of the 33rd Annual Meeting of ESMRMB, Vienna, Austria*, volume 33, 2016

15. K. Bredies, C. Diwoky, C. Langkammer, A. Lesch, G. Reishofer, S. Ropele, and R. Stollberger. Variational approaches for phase-image processing with applications in MRI. In *Mathematical Imaging and Surface Processing*, pages 31–33, 2016

2015

16. A. Lesch, A. Petrovic, and R. Stollberger. Robust implementation of 3D Bloch Siegert B1 mapping. In *Proceedings of the 23rd Annual Meeting of ISMRM, Toronto, Ontario, Canada*, page 2381, 2015

17. A. Lesch, A. Petrovic, T. J. Sumpf, C. S. Aigner, and R. Stollberger. Fast and accurate quantification of T1, T2 and proton density using IR bSSFP with slice profile correction and model based reconstruction. In *Proceedings of the 23rd Annual Meeting of ISMRM, Toronto, Ontario, Canada*, volume 23, page 1676, 2015

Oral Presentations

1. A. Lesch, C. S. Aigner, and R. Stollberger. Highly accelerated 3D Bloch Siegert B_1^+ mapping at 7T. In *Proceedings of the 28th Annual Meeting of ISMRM, Virtual Meeting*, page 662, 2020

2. A. Lesch, C. S. Aigner, S. Spann, M. Schlögl, and R. Stollberger. 3D Bloch-Siegert EPI B_1^+-mapping. In *Proceedings of the 27th Annual Meeting of ISMRM, Montreal, Quebec, Canada*, page 926, 2019, Power Pitch Presentation

3. A. Lesch, M. Schlögl, M. Holler, K. Bredies, R. Stollberger. Ultrafast 3D Bloch Siegert B_1^+ - mapping using variational methods. *Czech-Austrian MR Workshop, Spital am Semmering, Austria*, 2017.

4. A. Lesch, M. Holler, M. Schlögl, R. Stollberger. Highly accelerated B_1^+ mapping based on Bloch-Siegert using variational methods. *Czech-Austrian MR Workshop, Nové Hrady, Czech Republic*, 2018.

5. A. Lesch, M. Holler, M. Schlögl. Dual regularization for direct reconstruction of B_1^+-field from under-sampled data. *7th SFB Status Seminar*, 2016.

Poster Presentations

6. A. Lesch, M. Schlögl, and R. Stollberger. Robust accelerated reconstruction for Bloch-Siegert B1-mapping. In *Proceedings of the 25th Annual Meeting of ISMRM, Honolulu, Hawai'i, USA*, page 3918, 2017, E-poster
7. A. Lesch, M. Schlögl, M. Holler, and R. Stollberger. Highly accelerated Bloch-Siegert B_1^+-mapping using variational modeling. In *Proceedings of the 24th Annual Meeting of ISMRM, Singapore*, page 1875, 2016, traditional poster
8. A. Lesch, K. Bredies, C. Diwoky, and R. Stollberger. Chemical shift based fat-water separation using a variational approach for B0-field correction. In *Proceedings of the 24th Annual Meeting of ISMRM, Singapore*, volume 24, page 1875, 2016, E-poster
9. A. Lesch, A. Petrovic, and R. Stollberger. Robust implementation of 3D Bloch Siegert B1 mapping. In *Proceedings of the 23rd Annual Meeting of ISMRM, Toronto, Ontario, Canada*, page 2381, 2015, traditional poster
10. A. Lesch, A. Petrovic, T. J. Sumpf, C. S. Aigner, and R. Stollberger. Fast and accurate quantification of T1, T2 and proton density using IR bSSFP with slice profile correction and model based reconstruction. In *Proceedings of the 23rd Annual Meeting of ISMRM, Toronto, Ontario, Canada*, volume 23, page 1676, 2015, traditional poster

Awards and Stipends

1. Top downloaded paper 2018-2019 award for: A. Lesch, M. Schlögl, M. Holler, K. Bredies, and R. Stollberger. Ultrafast 3D Bloch–Siegert B_1^+-mapping using variational modeling. *Magnetic Resonance in Medicine*, 81(2):881–892, 2019. `doi:10.1002/mrm.27434`
2. MRM Highlighs 2019: Awarded as Editors pick of February 2019: A. Lesch, M. Schlögl, M. Holler, K. Bredies, and R. Stollberger. Ultrafast 3D Bloch–Siegert B_1^+-mapping using variational modeling. *Magnetic Resonance in Medicine*, 81(2):881–892, 2019. `doi:10.1002/mrm.27434`
3. ISMRM educational stipend in 2015, 2016 and 2017.

Bibliography

[1] S. Aja-Fernández, G. Vegas-Sánchez-Ferrero, and A. Tristán-Vega. Noise estimation in parallel MRI: GRAPPA and SENSE. *Magnetic Resonance Imaging*, 32(3):281–290, 2014. `doi:10.1016/j.mri.2013.12.001`. (page 90)

[2] S. Akoka, F. Franconi, F. Seguin, and A. Le Pape. Radiofrequency map of an NMR coil by imaging. *Magnetic Resonance Imaging*, 11(3):437–441, 1993. `doi:10.1016/0730-725x(93)90078-r`. (page 66)

[3] D. C. Alsop, J. A. Detre, X. Golay, M. Günther, J. Hendrikse, L. Hernandez-Garcia, H. Lu, B. J. MacIntosh, L. M. Parkes, M. Smits, M. J. P. van Osch, D. J. J. Wang, E. C. Wong, and G. Zaharchuk. Recommended implementation of arterial spin-labeled perfusion MRI for clinical applications: a consensus of the ISMRM perfusion study group and the European consortium for ASL in dementia. *Magnetic Resonance in Medicine*, 73(1):102–116, 2015. `doi:10.1002/mrm.25607`. (page 1)

[4] V. Antun, F. Renna, C. Poon, B. Adcock, and A. C. Hansen. On instabilities of deep learning in image reconstruction – Does AI come at a cost? *arXiv preprint arXiv:1902.05300*, 2019. (page 197)

[5] Y. Assaf and O. Pasternak. Diffusion tensor imaging (DTI)-based white matter mapping in brain research: a review. *Journal of Molecular Neuroscience*, 34(1):51–61, 2008. `doi:10.1007/s12031-007-0029-0`. (page 1)

[6] H. Bagher-Ebadian, Q. Jiang, and J. R. Ewing. A modified Fourier-based phase unwrapping algorithm with an application to MRI venography. *Journal of Magnetic Resonance Imaging*, 27(3):649–652, 2008. `doi:10.1002/jmri.21230`. (page 61)

[7] M. Barth, F. Breuer, P. J. Koopmans, D. G. Norris, and B. A. Poser. Simultaneous multislice (SMS) imaging techniques. *Magnetic Resonance in Medicine*, 75(1):63–81, 2016. `doi:10.1002/mrm.25897`. (page 4)

[8] T. Basse-Lüsebrink, V. Sturm, T. Kampf, G. Stoll, and P. Jakob. Fast CPMG-based Bloch-Siegert B_1^+ mapping. *Magnetic Resonance in Medicine*, 67(2):405–418, 2012. `doi:10.1002/mrm.23013`. (page 79)

[9] T. C. Basse-Lüsebrink, T. Kampf, A. Fischer, V. J. F. Sturm, D. Neumann, H. Köstler, D. Hahn, G. Stoll, and P. M. Jakob. SAR-reduced spin-echo-based Bloch–Siegert B_1^+ mapping: BS-SE-BURST. *Magnetic Resonance in Medicine*, 68(2):529–536, 2012. `doi:10.1002/mrm.23259`. (page 79)

[10] P. J. Basser, J. Mattiello, and D. LeBihan. MR diffusion tensor spectroscopy and imaging. *Biophysical Journal*, 66(1):259–267, 1994. `doi:10.1016/s0006-3495(94)80775-1`. (page 1)

[11] A. Beck. *First-order methods in optimization*, volume 25. SIAM, 2017. `doi:10.1137/1.9781611974997`. (page 105, 208, 209, 210)

[12] A. Beck and M. Teboulle. A fast iterative shrinkage-thresholding algorithm for linear inverse problems. *SIAM Journal on Imaging Sciences*, 2(1):183–202, 2009. `doi:10.1137/080716542`. (page 102)

[13] T. Benkert, L. Feng, D. K. Sodickson, H. Chandarana, and K. T. Block. Free-breathing volumetric fat/water separation by combining radial sampling, compressed sensing, and parallel imaging. *Magnetic Resonance in Medicine*, 78(2):565–576, 2017. `doi:10.1002/mrm.26392`. (page 125)

[14] J. Berglund, H. Ahlström, L. Johansson, and J. Kullberg. Two-point Dixon method with flexible echo times. *Magnetic Resonance in Medicine*, 65(4):994–1004, 2011. `doi:10.1002/mrm.22679`. (page 131)

[15] J. Berglund, L. Johansson, H. Ahlström, and J. Kullberg. Three-point Dixon method enables whole-body water and fat imaging of obese subjects. *Magnetic Resonance in Medicine*, 63(6):1659–1668, 2010. `doi:10.1002/mrm.22385`. (page 123, 185, 186)

[16] J. Berglund and J. Kullberg. Three-dimensional water/fat separation and T_2^* estimation based on whole-image optimization–application in breathhold liver imaging at 1.5 T. *Magnetic Resonance in Medicine*, 67(6):1684–1693, 2012. `doi:10.1002/mrm.23185`. (page 131)

[17] J. Berglund and M. Skorpil. Multi-scale graph-cut algorithm for efficient water-fat separation. *Magnetic Resonance in Medicine*, 78(3):941–949, 2017. `doi:10.1002/mrm.26479`. (page 134, 185, 186)

[18] M. A. Bernstein, K. F. King, and X. J. Zhou. *Handbook of MRI pulse sequences*. Elsevier, 2004. (page 23, 26)

[19] R. Bhagwandien, M. Moerland, C. Bakker, R. Beersma, and J. Lagendijk. Numerical analysis of the magnetic field for arbitrary magnetic susceptibility distributions in 3D. *Magnetic Resonance Imaging*, 12(1):101–107, 1994. `doi:10.1016/0730-725x(94)92357-4`. (page 37)

[20] R. Bhagwandien, R. Van Ee, R. Beersma, C. Bakker, M. Moerland, and J. Lagendijk. Numerical analysis of the magnetic field for arbitrary magnetic susceptibility distributions in 2D. *Magnetic Resonance Imaging*, 10(2):299–313, 1992. `doi:10.1016/0730-725x(92)90489-m`. (page 37)

[21] M. Bianciardi, J. R. Polimeni, K. Setsompop, C. Eichner, B. Bilgic, and L. L. Wald. Evaluation of dynamic off-resonance correction of respiratory instability in MRI signals for high-order spherical harmonic basis set and multivariate modeling

of respiratory sources. *Proceedings of the 22nd Annual Meeting of ISMRM, Milan, Italy*, 22:1623, 2014. (page 45)

[22] B. Bilgic, B. A. Gagoski, S. F. Cauley, A. P. Fan, J. R. Polimeni, P. E. Grant, L. L. Wald, and K. Setsompop. Wave-CAIPI for highly accelerated 3D imaging. *Magnetic Resonance in Medicine*, 73(6):2152–2162, 2015. `doi:10.1002/mrm.25347`. (page 4)

[23] J. M. Bioucas-Dias and G. Valadao. Phase unwrapping via graph cuts. *IEEE Transactions on Image Processing*, 16(3):698–709, 2007. `doi:10.1109/tip.2006.888351`. (page 61)

[24] M. Blaimer, F. Breuer, M. Mueller, R. M. Heidemann, M. A. Griswold, and P. M. Jakob. SMASH, SENSE, PILS, GRAPPA: how to choose the optimal method. *Topics in Magnetic Resonance Imaging*, 15(4):223–236, 2004. `doi:10.1097/01.rmr.0000136558.09801.dd`. (page 91)

[25] A. M. Blamire, D. L. Rothman, and T. Nixon. Dynamic shim updating: a new approach towards optimized whole brain shimming. *Magnetic Resonance in Medicine*, 36(1):159–165, 1996. `doi:10.1002/mrm.1910360125`. (page 45)

[26] F. Bloch and A. Siegert. Magnetic resonance for nonrotating fields. *Physical Review*, 57(6):522, 1940. `doi:10.1103/physrev.57.522`. (page 20, 77, 143)

[27] F. Bloch. Nuclear induction. *Physical review*, 70(7-8):460, 1946. `doi:10.1103/physrev.70.460`. (page 8)

[28] K. T. Block, M. Uecker, and J. Frahm. Undersampled radial MRI with multiple coils. Iterative image reconstruction using a total variation constraint. *Magnetic Resonance in Medicine*, 57(6):1086–1098, 2007. `doi:10.1002/mrm.21236`. (page 4, 108)

[29] F. Boada, Z.-P. Liang, and E. M. Haacke. Improved parametric reconstruction using variable projection optimization. *Inverse problems*, 14(1):19, 1998. `doi:10.1088/0266-5611/14/1/004`. (page 127)

[30] M. Bödenler, L. de Rochefort, P. J. Ross, N. Chanet, G. Guillot, G. R. Davies, C. Gösweiner, H. Scharfetter, D. J. Lurie, and L. M. Broche. Comparison of fast field-cycling magnetic resonance imaging methods and future perspectives. *Molecular Physics*, 117(7-8):832–848, 2019. `doi:10.1080/00268976.2018.1557349`. (page 29)

[31] P. Boernert, P. Koken, K. Nehrke, U. Katscher, and I. Graesslin. B1-mapping and B1L-shimming for MRI, May 27 2014. US Patent 8,736,265. (page 56)

[32] S. Boyd, S. P. Boyd, and L. Vandenberghe. *Convex optimization*. Cambridge university press, 2004. `doi:10.1017/cbo9780511804441`. (page 209)

[33] K. Bredies and T. Valkonen. Inverse problems with second-order total generalized variation constraints. In *Proceedings of SampTA*, volume 201, Singapore, 2011. (page 98)

[34] K. Bredies, C. Diwoky, C. Langkammer, A. Lesch, G. Reishofer, S. Ropele, and R. Stollberger. Variational approaches for phase-image processing with applications in MRI. In *Mathematical Imaging and Surface Processing*, pages 31–33, 2016. (page)

[35] K. Bredies and M. Holler. Regularization of linear inverse problems with total generalized variation. *Journal of Inverse and Ill-posed Problems*, 22(6):871–913, 2014. `doi:10.1515/jip-2013-0068`. (page 98)

[36] K. Bredies and M. Holler. A TGV-based framework for variational image decompression, zooming, and reconstruction. Part I: Analytics. *SIAM Journal on Imaging Sciences*, 8(4):2814–2850, 2015. `doi:10.1137/15m1023865`. (page 104)

[37] K. Bredies and M. Holler. TGV-based framework for variational image decompression, zooming and reconstruction. Part II: Numerics. *SIAM Journal on Imaging Sciences*, 8(4):2851–2886, 2015. `doi:10.1137/15m1023877`. (page 99)

[38] K. Bredies, K. Kunisch, and T. Pock. Total generalized variation. *SIAM Journal on Imaging Sciences*, 3(3):492–526, 2010. `doi:10.1137/090769521`. (page 4, 98, 145, 164, 167, 178)

[39] K. Bredies, T. Pock, and B. Wirth. Convex relaxation of a class of vertex penalizing functionals. *Journal of Mathematical Imaging and Vision*, 47(3):278–302, 2013. `doi:10.1007/s10851-012-0347-x`. (page 179)

[40] X. Bresson, S. Esedoḡlu, P. Vandergheynst, J.-P. Thiran, and S. Osher. Fast global minimization of the active contour/snake model. *Journal of Mathematical Imaging and vision*, 28(2):151–167, 2007. `doi:10.1007/s10851-007-0002-0`. (page 5)

[41] F. A. Breuer, M. Blaimer, M. F. Mueller, N. Seiberlich, R. M. Heidemann, M. A. Griswold, and P. M. Jakob. Controlled aliasing in volumetric parallel imaging (2D CAIPIRINHA). *Magnetic Resonance in Medicine*, 55(3):549–556, 2006. `doi:10.1002/mrm.20787`. (page 72, 90)

[42] F. A. Breuer, S. A. Kannengiesser, M. Blaimer, N. Seiberlich, P. M. Jakob, and M. A. Griswold. General formulation for quantitative G-factor calculation in GRAPPA reconstructions. *Magnetic Resonance in Medicine*, 62(3):739–746, 2009. `doi:10.1002/mrm.22066`. (page 90)

[43] L. M. Broche, P. J. Ross, G. R. Davies, M.-J. MacLeod, and D. J. Lurie. A whole-body Fast Field-Cycling scanner for clinical molecular imaging studies. *Scientific Reports*, 9(1):1–11, 2019. `doi:10.1038/s41598-019-46648-0`. (page 29)

[44] K. Butts, A. de Crespigny, J. M. Pauly, and M. Moseley. Diffusion-weighted interleaved echo-planar imaging with a pair of orthogonal navigator echoes. *Magnetic Resonance in Medicine*, 35(5):763–770, 1996. `doi:10.1002/mrm.1910350518`. (page 1)

[45] M. Bydder, T. Yokoo, G. Hamilton, M. S. Middleton, A. D. Chavez, J. B. Schwimmer, J. E. Lavine, and C. B. Sirlin. Relaxation effects in the quantification of fat using gradient echo imaging. *Magnetic Resonance Imaging*, 26(3):347–359, 2008. `doi:10.1016/j.mri.2007.08.012`. (page 118)

[46] A. Chambolle and T. Pock. A first-order primal-dual algorithm for convex problems with applications to imaging. *Journal of Mathematical Imaging and Vision*, 40(1):120–145, 2011. `doi:10.1007/s10851-010-0251-1`. (page 100, 102, 103, 146, 180, 210)

[47] T. F. Chan and J. Shen. Theory and computation of variational image deblurring. In *Mathematics and Computation in Imaging Science and Information Processing*, pages 93–130. World Scientific, 2007. (page 5)

[48] Y. V. Chang. Rapid B1 mapping using orthogonal, equal-amplitude radio-frequency pulses. *Magnetic Resonance in Medicine*, 67(3):718–723, 2012. `doi:10.1002/mrm.23051`. (page 74)

[49] S. Chavez, Q.-S. Xiang, and L. An. Understanding phase maps in MRI: a new cutline phase unwrapping method. *IEEE Transactions on Medical Imaging*, 21(8):966–977, 2002. `doi:10.1109/tmi.2002.803106`. (page 61)

[50] V. V. Chebrolu, C. D. Hines, H. Yu, A. R. Pineda, A. Shimakawa, C. A. McKenzie, A. Samsonov, J. H. Brittain, and S. B. Reeder. Independent estimation of T_2^* for water and fat for improved accuracy of fat quantification. *Magnetic Resonance in Medicine*, 63(4):849–857, 2010. `doi:10.1002/mrm.22300`. (page 118)

[51] J. Chen, L. Zhang, J. Luo, and Y. Zhu. MRI reconstruction from 2D partial k-space using POCS algorithm. In *3rd International Conference on Bioinformatics and Biomedical Engineering*, pages 1–4. IEEE, 2009. (page 87)

[52] C. Cheng, C. Zou, C. Liang, X. Liu, and H. Zheng. Fat-water separation using a region-growing algorithm with self-feeding phasor estimation. *Magnetic Resonance in Medicine*, 77(6):2390–2401, 2017. `doi:10.1002/mrm.26297`. (page 134, 185, 186)

[53] J. Chi, F. Liu, L. Xia, T. Shao, and S. Crozier. An improved cylindrical FDTD algorithm and its application to field-tissue interaction study in MRI. *IEEE Transactions on Magnetics*, 47(2):466–470, 2010. `doi:10.1109/tmag.2010.2100098`. (page 54)

[54] Z. Cho, Y. Ro, and T. Lim. NMR venography using the susceptibility effect produced by deoxyhemoglobin. *Magnetic Resonance in Medicine*, 28(1):25–38, 1992. `doi:10.1002/mrm.1910280104`. (page 38)

[55] S. Chung, D. Kim, E. Breton, and L. Axel. Rapid B_1^+ mapping using a preconditioning RF pulse with TurboFLASH readout. *Magnetic Resonance in Medicine*, 64(2):439–446, 2010. `doi:10.1002/mrm.22423`. (page 68)

[56] C. M. Collins, S. Li, and M. B. Smith. SAR and B1 field distributions in a heterogeneous human head model within a birdcage coil. *Magnetic Resonance in Medicine*, 40(6):847–856, 1998. `doi:10.1002/mrm.1910400610`. (page 54)

[57] B. D. Coombs, J. Szumowski, and W. Coshow. Two-point Dixon technique for water-fat signal decomposition with B0 inhomogeneity correction. *Magnetic Resonance in Medicine*, 38(6):884–889, 1997. `doi:10.1002/mrm.1910380606`. (page 121)

[58] N. Corbin, J. Acosta-Cabronero, S. J. Malik, and M. F. Callaghan. Robust 3D Bloch-Siegert based B_1^+ mapping using multi-echo general linear modeling. *Magnetic Resonance in Medicine*, 82(6):2003–2015, 2019. `doi:10.1002/mrm.27851`. (page 79, 196)

[59] C. Cui, A. Shah, X. Wu, and M. Jacob. A rapid 3D fat–water decomposition method using globally optimal surface estimation (R-GOOSE). *Magnetic Resonance in Medicine*, 79(4):2401–2407, 2018. `doi:10.1002/mrm.26843`. (page 134, 183, 185, 186)

[60] C. Cui, X. Wu, J. D. Newell, and M. Jacob. Fat water decomposition using globally optimal surface estimation (GOOSE) algorithm. *Magnetic Resonance in Medicine*, 73(3):1289–1299, 2015. `doi:10.1002/mrm.25193`. (page 133, 183, 185, 186)

[61] C. H. Cunningham, J. M. Pauly, and K. S. Nayak. Saturated double-angle method for rapid B_1^+ mapping. *Magnetic Resonance in Medicine*, 55(6):1326–1333, 2006. `doi:10.1002/mrm.20896`. (page 65)

[62] D. Darnell, T.-K. Truong, and A. W. Song. Integrated parallel reception, excitation, and shimming (iPRES) with multiple shim loops per radio-frequency coil element for improved B0 shimming. *Magnetic Resonance in Medicine*, 77(5):2077–2086, 2017. `doi:10.1002/mrm.26267`. (page 46)

[63] I. Daubechies. The wavelet transform, time-frequency localization and signal analysis. *IEEE transactions on information theory*, 36(5):961–1005, 1990. `doi:10.1515/9781400827268.442`. (page 108)

[64] R. A. De Graaf, P. B. Brown, S. McIntyre, D. L. Rothman, and T. W. Nixon. Dynamic shim updating (DSU) for multislice signal acquisition. *Magnetic Resonance in Medicine*, 49(3):409–416, 2003. `doi:10.1002/mrm.10404`. (page 45)

[65] S. C. L. Deoni, B. K. Rutt, and T. M. Peters. Rapid combined T1 and T2 mapping using gradient recalled acquisition in the steady state. *Magnetic Resonance in Medicine*, 49(3):515–526, 2003. `doi:10.1002/mrm.10407`. (page 3, 118, 134, 135)

[66] J. A. Detre, J. S. Leigh, D. S. Williams, and A. P. Koretsky. Perfusion imaging. *Magnetic Resonance in Medicine*, 23(1):37–45, 1992. `doi:10.1002/mrm.1910230106`. (page 1)

[67] W. T. Dixon. Simple proton spectroscopic imaging. *Radiology*, 153(1):189–194, 1984. `doi:10.1148/radiology.153.1.6089263`. (page 2, 6, 30, 119, 120, 121, 175)

[68] M. Doneva, P. Börnert, H. Eggers, A. Mertins, J. Pauly, and M. Lustig. Compressed sensing for chemical shift-based water–fat separation. *Magnetic Resonance in Medicine*, 64(6):1749–1759, 2010. `doi:10.1002/mrm.22563`. (page 130, 132, 178, 196)

[69] D. L. Donoho. Compressed sensing. *IEEE Transactions on Information Theory*, 52(4):1289–1306, 2006. `doi:10.1109/TIT.2006.871582`. (page 108)

[70] N. G. Dowell and P. S. Tofts. Fast, accurate, and precise mapping of the RF field in vivo using the 180 degrees signal null. *Magnetic Resonance in Medicine*, 58(3):622–630, 2007. `doi:10.1002/mrm.21368`. (page 69, 70)

[71] Q. Duan, I. J. Souheil, P. van Gelderen, P. Sunil, and D. H. Jeff. Implementation and validation of fast whole-brain B1 mapping based on Bloch-Siegert shift and EPI readout. In *Proceedings of the 21st Annual Meeting of ISMRM, Melbourne, Victoria, Australia*, page 609, 2012. (page 79, 139, 163)

[72] Q. Duan, P. van Gelderen, and J. Duyn. Fast simultaneous B0/B1 mapping by Bloch-Siegert shift with improved gradient scheme and pulse design. In *Proceedings of the 20th Annual Meeting of ISMRM, Melbourne, Australia*, volume 2504, 2012. (page 79, 81, 196)

[73] Q. Duan, P. van Gelderen, and J. Duyn. Improved Bloch-Siegert based B1 mapping by reducing off-resonance shift. *NMR in Biomedicine*, 26(9):1070–1078, 2013. `doi:10.1002/nbm.2920`. (page 80)

[74] C. Dumoulin, S. Souza, M. Walker, and W. Wagle. Three-dimensional phase contrast angiography. *Magnetic Resonance in Medicine*, 9(1):139–149, 1989. `doi:10.1002/mrm.1910090117`. (page 2)

[75] P. Ehses, D. Brenner, R. Stirnberg, E. D. Pracht, and T. Stöcker. Whole-brain B1-mapping using three-dimensional DREAM. *Magnetic resonance in medicine*, 82(3):924–934, 2019. `doi:10.1002/mrm.27773`. (page 72)

[76] R. Ernst and W. Anderson. Application of Fourier transform spectroscopy to magnetic resonance. *Review of Scientific Instruments*, 37:93, 1966. `doi:10.1063/1.1719961`. (page 54)

[77] M. J. Fair, F. Wang, Z. Dong, T. G. Reese, and K. Setsompop. Propeller echo-planar time-resolved imaging with dynamic encoding (peptide). *Magnetic Resonance in Medicine*, 2019. `doi:10.1002/mrm.28071`. (page 4)

[78] D. Feinberg, C. Mills, J. Posin, D. Ortendahl, N. Hylton, L. Crooks, J. Watts, L. Kaufman, M. Arakawa, and J. Hoenninger. Multiple spin-echo magnetic resonance imaging. *Radiology*, 155(2):437–442, 1985. `doi:10.1148/radiology.155.2.3983396`. (page 3)

[79] J. A. Fessler and B. P. Sutton. Nonuniform fast Fourier transforms using min-max interpolation. *IEEE Transactions on Signal Processing*, 51(2):560–574, 2003. `doi:10.1109/tsp.2002.807005`. (page 96)

[80] J. A. Fessler, D. Yeo, and D. C. Noll. Regularized fieldmap estimation in MRI. In *3rd IEEE International Symposium on Biomedical Imaging: Nano to Macro*, pages 706–709. IEEE, 2006. (page 110)

[81] G. Fornaro and E. Sansosti. A two-dimensional region growing least squares phase unwrapping algorithm for interferometric SAR processing. *IEEE Transactions on Geoscience and Remote Sensing*, 37(5):2215–2226, 1999. `doi:10.1109/36.789618`. (page 61)

[82] M. Freiberger, F. Knoll, K. Bredies, H. Scharfetter, and R. Stollberger. The agile library for biomedical image reconstruction using GPU acceleration. *Computing in Science & Engineering*, 15(1):34–44, 2013. `doi:10.1109/mcse.2012.40`. (page 146)

[83] A. Funai, J. A. Fessler, W. Grissom, and D. C. Noll. Regularized B_1^+ map estimation in MRI. In *4th IEEE International Symposium on Biomedical Imaging: From Nano to Macro*, pages 616–619. IEEE, 2007. (page 109, 110)

[84] A. K. Funai, J. A. Fessler, D. T. Yeo, V. T. Olafsson, and D. C. Noll. Regularized field map estimation in MRI. *IEEE Transactions on Medical Imaging*, 27(10):1484–1494, 2008. `doi:10.1109/TMI.2008.923956`. (page 60, 110)

[85] C. Gabriel, S. Gabriel, and y. E. Corthout. The dielectric properties of biological tissues: I. literature survey. *Physics in Medicine & Biology*, 41(11):2231, 1996. `doi:10.1088/0031-9155/41/11/001`. (page 51)

[86] S. Gabriel, R. Lau, and C. Gabriel. The dielectric properties of biological tissues: II. Measurements in the frequency range 10 Hz to 20 GHz. *Physics in Medicine & Biology*, 41(11):2251, 1996. `doi:10.1088/0031-9155/41/11/002`. (page 51)

[87] S. Gabriel, R. Lau, and C. Gabriel. The dielectric properties of biological tissues: III. Parametric models for the dielectric spectrum of tissues. *Physics in Medicine & Biology*, 41(11):2271, 1996. `doi:10.1088/0031-9155/41/11/003`. (page 51)

[88] M. W. Garrett. Axially symmetric systems for generating and measuring magnetic fields. Part I. *Journal of Applied Physics*, 22(9):1091–1107, 1951. `doi:10.1063/1.1700115`. (page 43)

[89] M. Gebhart, S. Birnstingl, J. Bruckbauer, and E. Merlin. Properties of a test bench to verify standard compliance of proximity transponders. In *Proceedings of the 6th International Symposium on Communication Systems, Networks and Digital Signal Processing, CNSDSP*, pages 306–310. IEEE, 2008. (page 49)

[90] M. Gebhart. Einige Grundlagen der magnetischen Nahfeld-Kopplung – lecture notes in “RFID Systems”, 2011. (page 48)

[91] W. Gerlach and O. Stern. Der experimentelle Nachweis der Richtungsquantelung im Magnetfeld. *Zeitschrift für Physik*, 9(1):349–352, 1922. `doi:10.1007/bf01326983`. (page 8)

[92] D. C. Ghiglia and M. D. Pritt. Two-dimensional phase unwrapping: theory, algorithms, and software. *Wiely-Interscience, first ed.*, 1998. (page 182, 187, 188)

[93] D. C. Ghiglia and L. A. Romero. Minimum Lp-norm two-dimensional phase unwrapping. *Journal of the Optical Society of America A*, 13(10):1999–2013, 1996. `doi:10.1364/josaa.13.001999`. (page 61)

[94] G. H. Glover. Multipoint Dixon technique for water and fat proton and susceptibility imaging. *Journal of Magnetic Resonance Imaging*, 1(5):521–530, 1991. `doi:10.1002/jmri.1880010504`. (page 121, 122, 125)

[95] G. Glover and E. Schneider. Three-point Dixon technique for true water/fat decomposition with B0 inhomogeneity correction. *Magnetic Resonance in Medicine*, 18(2):371–383, 1991. `doi:10.1002/mrm.1910180211`. (page 121, 125)

[96] G. Golub and V. Pereyra. Separable nonlinear least squares: the variable projection method and its applications. *Inverse problems*, 19(2):R1, 2003. `doi:10.1088/0266-5611/19/2/201`. (page 127)

[97] N. M. Gottschling, V. Antun, B. Adcock, and A. C. Hansen. The troublesome kernel: why deep learning for inverse problems is typically unstable. *arXiv preprint arXiv:2001.01258*, 2020. (page 197)

[98] C. Graf, C. S. Aigner, A. Rund, A. Lesch, and R. Stollberger. Inversion pulses with B1-robustness and reduced energy by optimal control. In *Proceedings of the 28th Annual Meeting of ISMRM, Virtual Meeting*, page 3696, 2020. (page)

[99] M. A. Griswold, P. M. Jakob, R. M. Heidemann, M. Nittka, V. Jellus, J. Wang, B. Kiefer, and A. Haase. Generalized autocalibrating partially parallel acquisitions (GRAPPA). *Magnetic Resonance in Medicine*, 47(6):1202–1210, 2002. `doi:10.1002/mrm.10171`. (page 4, 72, 85, 90)

[100] M. A. Griswold, D. Walsh, R. M. Heidemann, A. Haase, and P. M. Jakob. The use of an adaptive reconstruction for array coil sensitivity mapping and intensity normalization. In *Proceedings of the 10rd Annual Meeting of ISMRM, Honolulu, Hawai'i, USA*, page 2410, 2002. (page 107)

[101] R. Gruetter. Automatic, localized in vivo adjustment of all first- and second-order shim coils. *Magnetic Resonance in Medicine*, 29(6):804–811, 1993. `doi:10.1002/mrm.1910290613`. (page 44)

[102] R. Gruetter and C. Boesch. Fast, noniterative shimming of spatially localized signals. In vivo analysis of the magnetic field along axes. *Journal of Magnetic Resonance*, 96(2):323–334, 1992. `doi:10.1016/0022-2364(92)90085-l`. (page 44)

[103] E. M. Haacke, N. Y. Cheng, M. J. House, Q. Liu, J. Neelavalli, R. J. Ogg, A. Khan, M. Ayaz, W. Kirsch, and A. Obenaus. Imaging iron stores in the brain using magnetic resonance imaging. *Magnetic Resonance Imaging*, 23(1):1–25, 2005. `doi:10.1016/j.mri.2004.10.001`. (page 37)

[104] E. Haacke, R. Brown, M. Thompson, and R. Venkatesan. *Magnetic Resonance Imaging: Physical Principles and Sequence Design*. Wiley, 1999. `doi:10.1002/9781118633953`. (page 2, 8, 9, 10, 11, 12, 13, 14, 17, 20, 22, 23, 26, 38, 40, 41, 42)

[105] A. Haase, J. Frahm, D. Matthaei, W. Hanicke, and K.-D. Merboldt. FLASH imaging. Rapid NMR imaging using low flip-angle pulses. *Journal of Magnetic Resonance*, 67(2):258 – 266, 1986. `doi:https://doi.org/10.1016/0022-2364(86)90433-6`. (page 3)

[106] J. Hadamard. Sur les problèmes aux dérivées partielles et leur signification physique. *Princeton University Bulletin*, pages 49–52, 1902. (page 93)

[107] E. L. Hahn. Spin echoes. *Physical Review*, 80(4):580, 1950. `doi:10.1063/1.3066708`. (page 3)

[108] G. Hamilton, T. Yokoo, M. Bydder, I. Cruite, M. E. Schroeder, C. B. Sirlin, and M. S. Middleton. In vivo characterization of the liver fat ^{1}H MR spectrum. *NMR in Biomedicine*, 24(7):784–790, 2011. `doi:10.1002/nbm.1622`. (page 115, 116, 117)

[109] K. Hammernik, M. Schloegl, E. Kobler, R. Stollberger, and T. Pock. Dynamic multicoil reconstruction using variational networks. In *Proceedings of the 27th Annual Meeting of ISMRM, Montreal, Quebec, Canada*, volume 27, page 4656, 2019. (page 5, 197)

[110] K. Hammernik, T. Klatzer, E. Kobler, M. P. Recht, D. K. Sodickson, T. Pock, and F. Knoll. Learning a variational network for reconstruction of accelerated MRI data. *Magnetic Resonance in Medicine*, 79(6):3055–3071, 2018. `doi:10.1002/mrm.26977`. (page 4, 197)

[111] H. Han, A. W. Song, and T.-K. Truong. Integrated parallel reception, excitation, and shimming (iPRES). *Magnetic Resonance in Medicine*, 70(1):241–247, 2013. `doi:10.1002/mrm.24766`. (page 46)

[112] W. Hänicke and H. U. Vogel. An analytical solution for the SSFP signal in MRI. *Magnetic Resonance in Medicine*, 49(4):771–775, 2003. `doi:10.1002/mrm.10410`. (page 3)

[113] L. G. Hanson. Is quantum mechanics necessary for understanding magnetic resonance? *Concepts in Magnetic Resonance Part A: An Educational Journal*, 32(5):329–340, 2008. `doi:10.1002/cmr.a.20123`. (page 11)

[114] P. A. Hardy, R. S. Hinks, and J. A. Tkach. Separation of fat and water in fast spin-echo MR imaging with the three-point Dixon technique. *Journal of Magnetic Resonance Imaging*, 5(2):181–185, 1995. `doi:10.1002/jmri.1880050213`. (page 122, 125)

[115] M. Hedley and D. Rosenfeld. A new two-dimensional phase unwrapping algorithm for MRI images. *Magnetic Resonance in Medicine*, 24(1):177–181, 1992. `doi:10.1002/mrm.1910240120`. (page 61)

[116] E. Heine. Handbuch der Kugelfunctionen, Vol. ii. *Reimer, Berlin,*, 1878. (page 200, 201)

[117] F. Hennel and S. Köhler. Improved phase-based adiabatic B1 mapping. In *Proceedings of the 18th Annual Meeting of ISMRM, Stockholm, Sweden*, page 237, 2010. (page 74)

[118] F. Hennel, S. Köhler, and M. Janich. Phase-sensitive B1 mapping with adiabatic excitation. In *Proceedings of the 17th Annual Meeting of ISMRM, Honolulu, Hawai'i, USA*, page 2610, 2009. (page 74)

[119] J. Hennig, A. Nauerth, and H. Friedburg. RARE imaging: a fast imaging method for clinical MR. *Magnetic Resonance in Medicine*, 3(6):823–833, 1986. `doi:10.1002/mrm.1910030602`. (page 3, 46)

[120] J. Hennig and O. Speck. *High-field MR imaging*. Springer, 2011. `doi:10.1007/978-3-540-85090-8`. (page 2, 29, 30, 38, 41, 48, 49, 52, 54, 56)

[121] D. Hernando, P. Kellman, J. Haldar, and Z.-P. Liang. A network flow method for improved MR field map estimation in the presence of water and fat. In *30th Annual International Conference of the IEEE Engineering in Medicine and Biology Society*, pages 82–85. IEEE, 2008. (page 130)

[122] D. Hernando, J. Haldar, B. Sutton, J. Ma, P. Kellman, and Z.-P. Liang. Joint estimation of water/fat images and field inhomogeneity map. *Magnetic Resonance in Medicine*, 59(3):571–580, 2008. `doi:10.1002/mrm.21522`. (page 126, 127, 130)

[123] D. Hernando, P. Kellman, J. Haldar, and Z.-P. Liang. Robust water/fat separation in the presence of large field inhomogeneities using a graph cut algorithm. *Magnetic Resonance in Medicine*, 63(1):79–90, 2010. `doi:10.1002/mrm.22177`. (page 130, 131, 133, 185, 186)

[124] D. Hernando, Z.-P. Liang, and P. Kellman. Chemical shift–based water/fat separation: A comparison of signal models. *Magnetic Resonance in Medicine*, 64(3):811–822, 2010. `doi:10.1002/mrm.22455`. (page 119)

[125] M. R. Hestenes and E. Stiefel. *Methods of conjugate gradients for solving linear systems*, volume 49. NBS, 1952. `doi:10.6028/jres.049.044`. (page 101, 146)

[126] K. G. Hollingsworth. Reducing acquisition time in clinical MRI by data undersampling and compressed sensing reconstruction. *Physics in Medicine & Biology*, 60(21):R297, 2015. `doi:10.1088/0031-9155/60/21/r297`. (page 108)

[127] D. Holz, D. Jensen, R. Proksa, M. Tochtrop, and W. Vollmann. Automatic shimming for localized spectroscopy. *Medical Physics*, 15(6):898–903, 1988. `doi:10.1118/1.596173`. (page 43, 44)

[128] J. L. Honorato, V. Parot, C. Tejos, S. Uribe, and P. Irarrazaval. Chemical species separation with simultaneous estimation of field map and t_2^* using a k-space formulation. *Magnetic Resonance in Medicine*, 68(2):400–408, 2012. `doi:10.1002/mrm.23237`. (page 132)

[129] J. P. Hornak, J. Szumowski, and R. G. Bryant. Magnetic field mapping. *Magnetic Resonance in Medicine*, 6(2):158–163, 1988. `doi:10.1002/mrm.1910060204`. (page 64)

[130] D. I. Hoult. Sensitivity and power deposition in a high-field imaging experiment. *Journal of Magnetic Resonance Imaging*, 12(1):46–67, 2000. `doi:10.1002/1522-2586(200007)12:1<46::aid-jmri6>3.0.co;2-d`. (page 54)

[131] T.-Y. Huang, H.-W. Chung, F.-N. Wang, C.-W. Ko, and C.-Y. Chen. Fat and water separation in balanced steady-state free precession using the Dixon method. *Magnetic Resonance in Medicine*, 51(2):243–247, 2004. `doi:10.1002/mrm.10686`. (page 125)

[132] M. I. Iacono, E. Neufeld, E. Akinnagbe, K. Bower, J. Wolf, I. V. Oikonomidis, D. Sharma, B. Lloyd, B. J. Wilm, M. Wyss, K. P. Pruessmann, A. Jakab, N. Makris, E. D. Cohen, N. Kuster, W. Kainz, and L. M. Angelone. MIDA: a multimodal imaging-based detailed anatomical model of the human head and neck. *PloS one*, 10(4):e0124126, 2015. `doi:10.1371/journal.pone.0124126`. (page 51, 52)

[133] T. S. Ibrahim. Ultrahigh-field MRI whole-slice and localized RF field excitations using the same RF transmit array. *IEEE Transactions on Medical Imaging*, 25(10):1341–1347, 2006. `doi:10.1109/tmi.2006.880666`. (page 57)

[134] T. S. Ibrahim, R. Lee, B. A. Baertlein, A. M. Abduljalil, H. Zhu, and P.-M. L. Robitaille. Effect of RF coil excitation on field inhomogeneity at ultra high fields: a field optimized TEM resonator. *Magnetic Resonance Imaging*, 19(10):1339–1347, 2001. `doi:10.1016/s0730-725x(01)00404-0`. (page 57)

[135] E. Insko and L. Bolinger. Mapping of the radiofrequency field. *Journal of Magnetic Resonance, Series A*, 103(1):82–85, 1993. `doi:10.1006/jmra.1993.1133`. (page 64)

[136] M. Jacob and B. P. Sutton. Algebraic decomposition of fat and water in MRI. *IEEE Transactions on Medical Imaging*, 28(2):173–184, 2008. `doi:10.1109/TMI.2008.927344`. (page 131)

[137] M. Jankiewicz, J. C. Gore, and W. A. Grissom. Improved encoding pulses for Bloch–Siegert B_1^+ mapping. *Journal of Magnetic Resonance*, 226:79–87, 2013. `doi:10.1016/j.jmr.2012.11.004`. (page 79)

[138] M. Jenkinson. Fast, automated, N-dimensional phase-unwrapping algorithm. *Magnetic Resonance in Medicine*, 49(1):193–197, 2003. `doi:10.1002/mrm.10354`. (page 61)

[139] P. Jezzard and R. S. Balaban. Correction for geometric distortion in echo planar images from B0 field variations. *Magnetic Resonance in Medicine*, 34(1):65–73, 1995. `doi:10.1002/mrm.1910340111`. (page 111)

[140] J. Jin and J. Chen. On the SAR and field inhomogeneity of birdcage coils loaded with the human head. *Magnetic Resonance in Medicine*, 38(6):953–963, 1997. `doi:10.1002/mrm.1910380615`. (page 54)

[141] J. Jin, J. Chen, W. C. Chew, H. Gan, R. Magin, and P. Dimbylow. Computation of electromagnetic fields for high-frequency magnetic resonance imaging applications. *Physics in Medicine & Biology*, 41(12):2719, 1996. `doi:10.1088/0031-9155/41/12/011`. (page 54)

[142] F. Jiru and U. Klose. Fast 3D radiofrequency field mapping using echo-planar imaging. *Magnetic Resonance in Medicine*, 56(6):1375–1379, 2006. `doi:10.1002/mrm.21083`. (page 66)

[143] W. Joines, Y. Zhang, C. Li, and R. Jirtle. The electrical properties of normal and malignant human tissues from 50 to 900 MHz. In *Thirty-fifth annual Meeting of the Radiation Research Society (Abstracts)*, 1987. (page 51)

[144] K. V. Jordanova, D. G. Nishimura, and A. B. Kerr. Lowering the B1 threshold for improved BEAR B1 mapping. *Magnetic Resonance in Medicine*, 75(3):1262–1268, 2016. `doi:10.1002/mrm.25711`. (page 77)

[145] R. Joseph and E. Schlömann. Demagnetizing field in nonellipsoidal bodies. *Journal of Applied Physics*, 36(5):1579–1593, 1965. `doi:10.1063/1.1703091`. (page 36)

[146] C. Juchem, T. W. Nixon, S. McIntyre, V. O. Boer, D. L. Rothman, and R. A. de Graaf. Dynamic multi-coil shimming of the human brain at 7 T. *Journal of Magnetic Resonance*, 212(2):280–288, 2011. `doi:10.1016/j.jmr.2011.07.005`. (page 45)

[147] C. Juchem, S. U. Rudrapatna, T. W. Nixon, and R. A. de Graaf. Dynamic multi-coil technique (DYNAMITE) shimming for echo-planar imaging of the human brain at 7 Tesla. *Neuroimage*, 105:462–472, 2015. `doi:10.1016/j.neuroimage.2014.11.011`. (page 46)

[148] S. Kanayama, S. Kuhara, and K. Satoh. In vivo rapid magnetic field measurement and shimming using single scan differential phase mapping. *Magnetic Resonance in Medicine*, 36(4):637–642, 1996. `doi:10.1002/mrm.1910360421`. (page 43, 44, 61, 62)

[149] U. Katscher, P. Boernert, C. Leussler, and J. S. van den Brink. Transmit SENSE. *Magnetic Resonance in Medicine*, 49(1):144–150, 2003. `doi:10.1002/mrm.10353`. (page 3, 57)

[150] U. Katscher, T. Voigt, C. Findeklee, P. Vernickel, K. Nehrke, and O. Dössel. Determination of electric conductivity and local SAR via B1 mapping. *IEEE Transactions on Medical Imaging*, 28(9):1365–1374, 2009. `doi:10.1109/tmi.2009.2015757`. (page 51)

[151] B. Keong Li, F. Liu, and S. Crozier. Focused, eight-element transceive phased array coil for parallel magnetic resonance imaging of the chest – theoretical considerations. *Magnetic Resonance in Medicine*, 53(6):1251–1257, 2005. `doi:10.1002/mrm.20505`. (page 57)

[152] M. Khalighi, G. Glover, P. Pandit, S. Hinks, A. Kerr, M. Saranathan, and B. Rutt. Single-shot spiral based Bloch-Siegert B_1^+ mapping. In *Proceedings of the 19th Annual Meeting of ISMRM, Montreal, Quebec, Canada*, page 578, 2011. (page 79, 139, 163)

[153] M. M. Khalighi, B. K. Rutt, and A. B. Kerr. RF pulse optimization for Bloch-Siegert B_1^+ mapping. *Magnetic Resonance in Medicine*, 68(3):857–862, 2012. `doi:10.1002/mrm.23271`. (page 79)

[154] M. M. Khalighi, B. K. Rutt, and A. B. Kerr. Adiabatic RF pulse design for Bloch-Siegert B_1^+ mapping. *Magnetic Resonance in Medicine*, 70(3):829–835, 2013. `doi:10.1002/mrm.24507`. (page 79)

[155] D.-H. Kim, E. Adalsteinsson, G. H. Glover, and D. M. Spielman. Regularized higher-order in vivo shimming. *Magnetic Resonance in Medicine*, 48(4):715–722, 2002. `doi:10.1002/mrm.10267`. (page 45)

[156] J. Kim, Y. Wu, Y. Guo, H. Zheng, and P. Z. Sun. A review of optimization and quantification techniques for chemical exchange saturation transfer MRI toward sensitive in vivo imaging. *Contrast Media & Molecular Imaging*, 10(3):163–178, 2015. `doi:10.1002/cmmi.1628`. (page 112)

[157] Y. Kim, C. Mun, and Z. Cho. Chemical-shift imaging with large magnetic field inhomogeneity. *Magnetic Resonance in Medicine*, 4(5):452–460, 1987. `doi:10.1002/mrm.1910040506`. (page 121)

[158] L. M. Klassen and R. S. Menon. Robust automated shimming technique using arbitrary mapping acquisition parameters (RASTAMAP). *Magnetic Resonance in Medicine*, 51(5):881–887, 2004. `doi:10.1002/mrm.20094`. (page 44, 63)

[159] F. Knoll, K. Bredies, T. Pock, and R. Stollberger. Second order total generalized variation (TGV) for MRI. *Magnetic Resonance in Medicine*, 65(2):480–491, 2011. `doi:10.1002/mrm.22595`. (page 4, 99, 105, 109, 146, 164, 167)

[160] F. Knoll, C. Clason, K. Bredies, M. Uecker, and R. Stollberger. Parallel imaging with nonlinear reconstruction using variational penalties. *Magnetic Resonance in Medicine*, 67(1):34–41, 2012. `doi:10.1002/mrm.22964`. (page 107, 109)

[161] F. Knoll, C. Clason, C. Diwoky, and R. Stollberger. Adapted random sampling patterns for accelerated MRI. *Magnetic Resonance Materials in Physics, Biology and Medicine*, 24(1):43–50, 2011. `doi:10.1007/s10334-010-0234-7`. (page 139)

[162] F. Knoll, M. Holler, T. Koesters, R. Otazo, K. Bredies, and D. K. Sodickson. Joint MR-PET reconstruction using a multi-channel image regularizer. *IEEE Transactions on Medical Imaging*, 36(1):1–16, 2017. `doi:10.1109/TMI.2016.2564989`. (page 99)

[163] K. M. Koch, S. McIntyre, T. W. Nixon, D. L. Rothman, and R. A. de Graaf. Dynamic shim updating on the human brain. *Journal of Magnetic Resonance*, 180(2):286–296, 2006. `doi:10.1016/j.jmr.2006.03.007`. (page 45)

[164] K. Kwong. *Functional magnetic resonance imaging with echo planar imaging.* Springer, 1996. `doi:10.1007/978-88-470-2194-5_16`. (page 2)

[165] M. E. Ladd, P. Bachert, M. Meyerspeer, E. Moser, A. M. Nagel, D. G. Norris, S. Schmitter, O. Speck, S. Straub, and M. Zaiss. Pros and cons of ultra-high-field MRI/MRS for human application. *Progress in Nuclear Magnetic Resonance Spectroscopy*, 109:1–50, 2018. `doi:10.1016/j.pnmrs.2018.06.001`. (page 3)

[166] C. Langkammer, K. Bredies, B. A. Poser, M. Barth, G. Reishofer, A. P. Fan, B. Bilgic, F. Fazekas, C. Mainero, and S. Ropele. Fast quantitative susceptibility mapping using 3D EPI and total generalized variation. *Neuroimage*, 111:622–630, 2015. `doi:10.1016/j.neuroimage.2015.02.041`. (page 99, 111)

[167] C. Langkammer, N. Krebs, W. Goessler, E. Scheurer, F. Ebner, K. Yen, F. Fazekas, and S. Ropele. Quantitative MR imaging of brain iron: a postmortem validation study. *Radiology*, 257(2):455–462, 2010. `doi:10.1148/radiol.10100495`. (page 37)

[168] J. Langley and Q. Zhao. Unwrapping magnetic resonance phase maps with Chebyshev polynomials. *Magnetic Resonance Imaging*, 27(9):1293–1301, 2009. `doi:10.1016/j.mri.2009.05.013`. (page 61)

[169] D. J. Larkman, J. V. Hajnal, A. H. Herlihy, G. A. Coutts, I. R. Young, and G. Ehnholm. Use of multicoil arrays for separation of signal from multiple slices simultaneously excited. *Journal of Magnetic Resonance Imaging*, 13(2):313–317, 2001. `doi:10.1002/1522-2586(200102)13:2<313::aid-jmri1045>3.0.co;2-w`. (page 4)

[170] K. J. Layton, S. Kroboth, F. Jia, S. Littin, H. Yu, J. Leupold, J.-F. Nielsen, T. Stöcker, and M. Zaitsev. Pulseq: a rapid and hardware-independent pulse sequence prototyping framework. *Magnetic Resonance in Medicine*, 77(4):1544–1552, 2017. `doi:10.1002/mrm.26235`. (page 163)

[171] D. Le Bihan, E. Breton, D. Lallemand, P. Grenier, E. Cabanis, and M. Laval-Jeantet. MR imaging of intravoxel incoherent motions: application to diffusion and perfusion in neurologic disorders. *Radiology*, 161(2):401–407, 1986. `doi:10.1148/radiology.161.2.3763909`. (page 1)

[172] Y. Lee, Y. Han, H. Park, H. Watanabe, M. Garwood, and J.-Y. Park. New phase-based B1 mapping method using two-dimensional spin-echo imaging with hyperbolic secant pulses. *Magnetic Resonance in Medicine*, 73(1):170–181, 2015. `doi:10.1002/mrm.25110`. (page 75)

[173] A. Lesch, C. S. Aigner, S. Spann, M. Schlögl, and R. Stollberger. 3D Bloch-Siegert EPI B_1^+-mapping. In *Proceedings of the 27th Annual Meeting of ISMRM, Montreal, Quebec, Canada*, page 926, 2019. (page)

[174] A. Lesch, C. S. Aigner, and R. Stollberger. Highly accelerated 3D Bloch Siegert B_1^+ mapping at 7T. In *Proceedings of the 28th Annual Meeting of ISMRM, Virtual Meeting*, page 662, 2020. (page)

[175] A. Lesch, K. Bredies, C. Diwoky, and R. Stollberger. Chemical shift based fat-water separation using a variational approach for B0-field correction. In *Proceedings of the 24th Annual Meeting of ISMRM, Singapore*, volume 24, page 1875, 2016. (page 183)

[176] A. Lesch, A. Petrovic, and R. Stollberger. Robust implementation of 3D Bloch Siegert B1 mapping. In *Proceedings of the 23rd Annual Meeting of ISMRM, Toronto, Ontario, Canada*, page 2381, 2015. (page 81, 162)

[177] A. Lesch, A. Petrovic, T. J. Sumpf, C. S. Aigner, and R. Stollberger. Fast and accurate quantification of T1, T2 and proton density using IR bSSFP with slice profile correction and model based reconstruction. In *Proceedings of the 23rd Annual Meeting of ISMRM, Toronto, Ontario, Canada*, volume 23, page 1676, 2015. (page 134)

[178] A. Lesch, M. Schlögl, M. Holler, and R. Stollberger. Highly accelerated Bloch-Siegert B_1^+-mapping using variational modeling. In *Proceedings of the 24th Annual Meeting of ISMRM, Singapore*, page 1875, 2016. (page 148)

[179] A. Lesch, M. Schlögl, and R. Stollberger. Robust accelerated reconstruction for Bloch-Siegert B1-mapping. In *Proceedings of the 25th Annual Meeting of ISMRM, Honolulu, Hawai'i, USA*, page 3918, 2017. (page 149)

[180] A. Lesch, M. Schlögl, M. Holler, K. Bredies, and R. Stollberger. Ultrafast 3D Bloch–Siegert B_1^+-mapping using variational modeling. *Magnetic Resonance in Medicine*, 81(2):881–892, 2019. `doi:10.1002/mrm.27434`. (page)

[181] S. Li, B. J. Dardzinski, C. M. Collins, Q. X. Yang, and M. B. Smith. Three-dimensional mapping of the static magnetic field inside the human head. *Magnetic Resonance in Medicine*, 36(5):705–714, 1996. `doi:10.1002/mrm.1910360509`. (page 37)

[182] W. Li, B. Wu, A. V. Avram, and C. Liu. Magnetic susceptibility anisotropy of human brain in vivo and its molecular underpinnings. *Neuroimage*, 59(3):2088–2097, 2012. `doi:10.1016/j.neuroimage.2011.10.038`. (page 32)

[183] Z. Li, A. F. Gmitro, A. Bilgin, and M. I. Altbach. Fast decomposition of water and lipid using a GRASE technique with the IDEAL algorithm. *Magnetic Resonance in Medicine*, 57(6):1047–1057, 2007. `doi:10.1002/mrm.21232`. (page 124)

[184] Z.-P. Liang. A model-based method for phase unwrapping. *IEEE Transactions on Medical Imaging*, 15(6):893–897, 1996. `doi:10.1109/42.544507`. (page 61)

[185] T. Liebig. openEMS - open electromagnetic field solver, Published August 10, 2015. Updated February 18, 2017. Accessed March 10, 2017., `http://openEMS.de`. (page 49, 50, 51, 52)

[186] T. Liebig, A. Rennings, S. Held, and D. Erni. openEMS – a free and open source equivalent-circuit (EC) FDTD simulation platform supporting cylindrical coordinates suitable for the analysis of traveling wave MRI applications. *International Journal of Numerical Modelling: Electronic Networks, Devices and Fields*, 26(6):680–696, 2013. `doi:10.1002/jnm.1875`. (page 49, 50, 51, 52)

[187] B. Liu, K. King, M. Steckner, J. Xie, J. Sheng, and L. Ying. Regularized sensitivity encoding (SENSE) reconstruction using bregman iterations. *Magnetic Resonance in Medicine*, 61(1):145–152, 2009. `doi:10.1002/mrm.21799`. (page 109)

[188] C.-Y. Liu, C. A. McKenzie, H. Yu, J. H. Brittain, and S. B. Reeder. Fat quantification with IDEAL gradient echo imaging: correction of bias from T1 and noise. *Magnetic Resonance in Medicine*, 58(2):354–364, 2007. `doi:10.1002/mrm.21301`. (page 118)

[189] F. Liu and S. Crozier. Electromagnetic fields inside a lossy, multilayered spherical head phantom excited by MRI coils: models and methods. *Physics in Medicine & Biology*, 49(10):1835, 2004. `doi:10.1088/0031-9155/49/10/001`. (page 54)

[190] B. A. Lloyd. *Tissue Properties Database V3.1*. IT'IS Foundation, Published October 13, 2016. Accessed March 10, 2017., `https://www.itis.ethz.ch/virtual-population/tissue-properties/downloads/database-v3-1/`. (page 51, 52)

[191] C. C. Lodes, J. P. Felmlee, R. L. Ehman, C. M. Sehgal, J. F. Greenleaf, G. H. Glover, and J. E. Gray. Proton MR chemical shift imaging using double and triple phase contrast acquisition methods. *Journal of Computer Assisted Tomography*, 13(5):855–861, 1989. `doi:10.1097/00004728-198909000-00020`. (page 121)

[192] W. Lu and B. A. Hargreaves. Multiresolution field map estimation using golden section search for water-fat separation. *Magnetic Resonance in Medicine*, 60(1):236–244, 2008. `doi:10.1002/mrm.21544`. (page 131, 132, 185, 186)

[193] W. Lu and Y. Lu. JIGSAW: Joint inhomogeneity estimation via global segment assembly for water–fat separation. *IEEE Transactions on Medical Imaging*, 30(7):1417–1426, 2011. `doi:10.1109/tmi.2011.2122342`. (page 131)

[194] M. Lustig, D. Donoho, and J. M. Pauly. Sparse MRI: The application of compressed sensing for rapid MR imaging. *Magnetic Resonance in Medicine*, 58(6):1182–1195, 2007. `doi:10.1002/mrm.21391`. (page 4, 108, 148, 149, 154)

[195] M. Lustig, D. L. Donoho, J. M. Santos, and J. M. Pauly. Compressed sensing MRI. *IEEE Signal Processing Magazine*, 25(2):72–82, 2008. `doi:10.1109/msp.2007.914728`. (page 4, 108)

[196] M. Lustig and J. M. Pauly. SPIRiT: Iterative self-consistent parallel imaging reconstruction from arbitrary k-space. *Magnetic Resonance in Medicine*, 64(2):457–471, 2010. `doi:10.1002/mrm.22428`. (page 90, 110, 139, 161)

[197] A. Lutti, J. Stadler, O. Josephs, C. Windischberger, O. Speck, J. Bernarding, C. Hutton, and N. Weiskopf. Robust and fast whole brain mapping of the RF transmit field B1 at 7T. *PLoS One*, 7(3):e32379, 2012. `doi:10.1371/journal.pone.0032379`. (page 66)

[198] J. Ma. Breath-hold water and fat imaging using a dual-echo two-point Dixon technique with an efficient and robust phase-correction algorithm. *Magnetic Resonance in Medicine*, 52(2):415–419, 2004. `doi:10.1002/mrm.20146`. (page 123, 126, 134)

[199] J. Ma. Dixon techniques for water and fat imaging. *Journal of Magnetic Resonance Imaging*, 28(3):543–558, 2008. `doi:10.1002/jmri.21492`. (page 113, 121)

[200] J. Ma, S. K. Singh, A. J. Kumar, N. E. Leeds, and L. D. Broemeling. Method for efficient fast spin echo Dixon imaging. *Magnetic Resonance in Medicine*, 48(6):1021–1027, 2002. `doi:10.1002/mrm.10306`. (page 122, 125)

[201] J. Ma, J. B. Son, J. A. Bankson, R. J. Stafford, H. Choi, and D. Ragan. A fast spin echo two-point Dixon technique and its combination with sensitivity encoding for efficient T2-weighted imaging. *Magnetic Resonance Imaging*, 23(10):977–982, 2005. `doi:10.1016/j.mri.2005.10.005`. (page 123)

[202] J. Ma, J. B. Son, and J. D. Hazle. An improved region growing algorithm for phase correction in MRI. *Magnetic Resonance in Medicine*, 76(2):519–529, 2016. `doi:10.1002/mrm.25892`. (page 134)

[203] J. Ma, J. B. Son, Y. Zhou, H. Le-Petross, and H. Choi. Fast spin-echo triple-echo dixon (fTED) technique for efficient T2-weighted water and fat imaging. *Magnetic Resonance in Medicine*, 58(1):103–109, 2007. `doi:10.1002/mrm.21268`. (page 123, 125)

[204] J. Ma, F. Wehrli, H. Song, and S. Hwang. A single-scan imaging technique for measurement of the relative concentrations of fat and water protons and their transverse relaxation times. *Journal of Magnetic Resonance*, 125(1):92–101, 1997. `doi:10.1006/jmre.1996.1086`. (page 122)

[205] I. Mackenzie, E. Robinson, A. Wells, and B. Wood. A simple field map for shimming. *Magnetic Resonance in Medicine*, 5(3):262–268, 1987. `doi:10.1002/mrm.1910050307`. (page 44)

[206] F. Maier, D. Fuentes, J. S. Weinberg, J. D. Hazle, and R. J. Stafford. Robust phase unwrapping for MR temperature imaging using a magnitude-sorted list, multi-clustering algorithm. *Magnetic Resonance in Medicine*, 73(4):1662–1668, 2015. `doi:10.1002/mrm.25279`. (page 61)

[207] O. Maier, M. Schloegl, A. Lesch, A. Petrovic, M. Holler, K. Bredies, T. Pock, and R. Stollberger. Improved accelerated model-based parameter quantification with Total-Generalized-Variation regularization. In *Proceedings of the 25th Annual Meeting of ISMRM, Honolulu, Hawai'i, USA*, volume 25, page 3855, 2017. (page 134)

[208] O. Maier, M. Schlögl, A. Lesch, A. Petrovic, K. Bredies, and R. Stollberger. Accelerated DESPOT T1-mapping with iteratively TV regularized Gauss-Newton method. In *Proceedings of the 33rd Annual Meeting of ESMRMB, Vienna, Austria*, volume 33, 2016. (page)

[209] O. Maier, J. Schoormans, M. Schlögl, G. J. Strijkers, A. Lesch, T. Benkert, T. Block, B. F. Coolen, K. Bredies, and R. Stollberger. Rapid T1 quantification from high resolution 3D data with model-based reconstruction. *Magnetic Resonance in Medicine*, 81(3):2072–2089, 2019. `doi:10.1002/mrm.27502`. (page 134, 135)

[210] P. Mansfield and A. A. Maudsley. Planar spin imaging by NMR. *Journal of Magnetic Resonance*, 27(1):101–119, 1977. `doi:10.1016/0022-2364(77)90197-4`. (page 3)

[211] W. Mao, M. B. Smith, and C. M. Collins. Exploring the limits of RF shimming for high-field MRI of the human head. *Magnetic Resonance in Medicine*, 56(4):918–922, 2006. `doi:10.1002/mrm.21013`. (page 57)

[212] A. Maudsley. Multiple-line-scanning spin density imaging. *Journal of Magnetic Resonance*, 41(1):112–126, 1980. `doi:10.1016/0022-2364(80)90207-3`. (page 4)

[213] G. Metzger, P. Van de Moortele, C. Snyder, J. Vaughan, and K. Ugurbil. Local B1 shimming for imaging the prostate at 7 Tesla. In *Proceedings of the 15nd Annual Meeting of ISMRM, Berlin, Germany*, page 799, 2007. (page 57)

[214] D. Miklavčič, N. Pavšelj, and F. X. Hart. Electric properties of tissues. *Wiley Encyclopedia of Biomedical Engineering*, 2006. `doi:10.1002/9780471740360.ebs0403`. (page 51)

[215] H. Moriguchi, J. S. Lewin, and J. L. Duerk. Dixon techniques in spiral trajectories with off-resonance correction: a new approach for fat signal suppression without spatial-spectral RF pulses. *Magnetic Resonance in Medicine*, 50(5):915–924, 2003. `doi:10.1002/mrm.10629`. (page 125)

[216] H. Moriguchi, J. S. Lewin, and J. L. Duerk. Fast spiral two-point Dixon technique using block regional off-resonance correction. *Magnetic Resonance in Medicine*, 52(6):1342–1350, 2004. `doi:10.1002/mrm.20269`. (page 125)

[217] G. Morrell and D. Spielman. Dynamic shimming for multi-slice magnetic resonance imaging. *Magnetic Resonance in Medicine*, 38(3):477–483, 1997. `doi:10.1002/mrm.1910380316`. (page 45)

[218] G. R. Morrell. A phase-sensitive method of flip angle mapping. *Magnetic Resonance in Medicine*, 60(4):889–894, 2008. `doi:10.1002/mrm.21729`. (page 73)

[219] K. Nehrke and P. Börnert. Fast B1 mapping using a STEAM-based Bloch-Siegert preparation pulse. In *Proceedings of the 19th Annual Meeting of ISMRM, Montreal, Quebec, Canada*, volume 19, page 4411, 2011. (page 79)

[220] K. Nehrke and P. Börnert. DREAM – a novel approach for robust, ultrafast, multislice B1 mapping. *Magnetic Resonance in Medicine*, 68(5):1517–1526, 2012. `doi:10.1002/mrm.24158`. (page 70, 71, 72)

[221] K. Nehrke, M. J. Versluis, A. Webb, and P. Börnert. Volumetric B_1^+ mapping of the brain at 7T using DREAM. *Magnetic resonance in medicine*, 71(1):246–256, 2014. `doi:10.1002/mrm.24667`. (page 72)

[222] B. Neumayer, A. Lesch, F. Thaler, T. Widek, S. Tschauner, J. De Tobel, T. Ehammer, B. Kirnbauer, J. Boldt, M. van Wijk, R. Stollberger, and M. Urschler. The four-minute approach revisited: accelerating MRI-based multi-factorial age estimation. *International Journal of Legal Medicine*, pages 1–11, 2019. `doi:10.1007/s00414-019-02231-w`. (page)

[223] H. Nyquist. Certain topics in telegraph transmission theory. *Transactions of the American Institute of Electrical Engineers*, 47(2):617–644, 1928. (page 4, 86)

[224] M. O'donnell. NMR blood flow imaging using multiecho, phase contrast sequences. *Medical Physics*, 12(1):59–64, 1985. `doi:10.1118/1.595736`. (page 2)

[225] J. Osborn. Demagnetizing factors of the general ellipsoid. *Physical Review*, 67(11-12):351, 1945. `doi:10.1103/physrev.67.351`. (page 36)

[226] J. W. Pan, K.-M. Lo, and H. P. Hetherington. Role of very high order and degree B0 shimming for spectroscopic imaging of the human brain at 7 Tesla. *Magnetic Resonance in Medicine*, 68(4):1007–1017, 2012. `doi:10.1002/mrm.24122`. (page 45)

[227] J. W. Pan, D. B. Twieg, and H. P. Hetherington. Quantitative spectroscopic imaging of the human brain. *Magnetic Resonance in Medicine*, 40(3):363–369, 1998. `doi:10.1002/mrm.1910400305`. (page 67)

[228] W. Pauli. Über den Zusammenhang des Abschlusses der Elektronengruppen im Atom mit der Komplexstruktur der Spektren. *Zeitschrift für Physik*, 31(1):765–783, 1925. `doi:10.1007/978-3-322-90270-2_23`. (page 9)

[229] H. Peng, C. Zou, C. Cheng, C. Tie, Y. Qiao, Q. Wan, J. Lv, Q. He, D. Liang, X. Liu, et al. Fat-water separation based on transition region extraction (TREE). *Magnetic Resonance in Medicine*, 82(1):436–448, 2019. `doi:10.1002/mrm.27710`. (page 134)

[230] A. R. Pineda, S. B. Reeder, Z. Wen, and N. J. Pelc. Cramér–Rao bounds for three-point decomposition of water and fat. *Magnetic Resonance in Medicine*, 54(3):625–635, 2005. `doi:10.1002/mrm.20623`. (page 125)

[231] R. Pohmann and K. Scheffler. A theoretical and experimental comparison of different techniques for B1 mapping at very high fields. *NMR in Biomedicine*, 26(3):265–275, 2013. `doi:10.1002/nbm.2844`. (page 64)

[232] K. Preis. Lecture notes in “Elektrodynamik TE”, 2012. (page 33, 42, 49, 53)

[233] K. P. Pruessmann, M. Weiger, P. Börnert, and P. Boesiger. Advances in sensitivity encoding with arbitrary k-space trajectories. *Magnetic Resonance in Medicine*, 46(4):638–651, 2001. `doi:10.1002/mrm.1241`. (page 94, 96, 108)

[234] K. P. Pruessmann, M. Weiger, M. B. Scheidegger, and P. Boesiger. SENSE: sensitivity encoding for fast MRI. *Magnetic Resonance in Medicine*, 42(5):952–962, 1999. `doi:10.1002/(sici)1522-2594(199911)42:5<952::aid-mrm16>3.0.co;2-s`. (page 4, 85, 90, 92)

[235] J. B. Ra and C. Rim. Fast imaging using subencoding data sets from multiple detectors. *Magnetic Resonance in Medicine*, 30(1):142–145, 1993. `doi:10.1002/mrm.1910300123`. (page 90)

[236] S. Reeder, C. Hines, H. Yu, C. McKenzie, and J. Brittain. On the definition of fat-fraction for in vivo fat quantification with magnetic resonance imaging. In *Proceedings of the 17th Annual Meeting of ISMRM, Honolulu, Hawai'i, USA*, page 211, 2009. (page 119)

[237] S. B. Reeder, B. A. Hargreaves, H. Yu, and J. H. Brittain. Homodyne reconstruction and IDEAL water–fat decomposition. *Magnetic Resonance in Medicine*, 54(3):586–593, 2005. `doi:10.1002/mrm.20586`. (page 124)

[238] S. B. Reeder, M. Markl, H. Yu, J. C. Hellinger, R. J. Herfkens, and N. J. Pelc. Cardiac CINE imaging with IDEAL water-fat separation and steady-state free precession. *Journal of Magnetic Resonance Imaging*, 22(1):44–52, 2005. `doi:10.1002/jmri.20327`. (page 124)

[239] S. B. Reeder, C. A. McKenzie, A. R. Pineda, H. Yu, A. Shimakawa, A. C. Brau, B. A. Hargreaves, G. E. Gold, and J. H. Brittain. Water–fat separation with IDEAL gradient-echo imaging. *Journal of Magnetic Resonance Imaging*, 25(3):644–652, 2007. `doi:10.1002/jmri.20831`. (page 2, 124, 125)

[240] S. B. Reeder, A. R. Pineda, Z. Wen, A. Shimakawa, H. Yu, J. H. Brittain, G. E. Gold, C. H. Beaulieu, and N. J. Pelc. Iterative decomposition of water and fat with echo asymmetry and least-squares estimation (IDEAL): application with fast spin-echo imaging. *Magnetic Resonance in Medicine*, 54(3):636–644, 2005. `doi:10.1002/mrm.20624`. (page 124, 125, 128)

[241] S. B. Reeder and C. B. Sirlin. Quantification of liver fat with magnetic resonance imaging. *Magnetic Resonance Imaging Clinics of North America*, 18(3):337–357, 2010. `doi:10.1016/j.mric.2010.08.013`. (page 117, 118)

[242] S. B. Reeder, Z. Wen, H. Yu, A. R. Pineda, G. E. Gold, M. Markl, and N. J. Pelc. Multicoil Dixon chemical species separation with an iterative least-squares estimation method. *Magnetic Resonance in Medicine*, 51(1):35–45, 2004. `doi:10.1002/mrm.10675`. (page 123, 124, 125, 126)

[243] J. Ren, I. Dimitrov, A. D. Sherry, and C. R. Malloy. Composition of adipose tissue and marrow fat in humans by ^{1}H NMR at 7 Tesla. *Journal of Lipid Research*, 49(9):2055–2062, 2008. `doi:10.1194/jlr.d800010-jlr200`. (page 116, 117)

[244] S. D. Robinson, K. Bredies, D. Khabipova, B. Dymerska, J. P. Marques, and F. Schweser. An illustrated comparison of processing methods for MR phase imaging and QSM: combining array coil signals and phase unwrapping. *NMR in Biomedicine*, 30(4):e3601, 2017. `doi:10.1002/nbm.3601`. (page 59)

[245] F. Roméo and D. Hoult. Magnet field profiling: analysis and correcting coil design. *Magnetic Resonance in Medicine*, 1(1):44–65, 1984. `doi:10.1002/mrm.1910010107`. (page 43)

[246] P. B. Römer, W. A. Edelstein, C. E. Hayes, S. P. Souza, and O. M. Mueller. The NMR phased array. *Magnetic Resonance in Medicine*, 16(2):192–225, 1990. `doi:10.1002/mrm.1910160203`. (page 47, 58)

[247] L. I. Rudin, S. Osher, and E. Fatemi. Nonlinear total variation based noise removal algorithms. *Physica D: Nonlinear Phenomena*, 60(1-4):259–268, 1992. `doi:10.1016/0167-2789(92)90242-f`. (page 4, 5, 98)

[248] L. Sacolick, S. Lee, W. Grissom, and M. Vogel. Fast spin echo Bloch-Siegert B1 mapping. In *Proceedings of the 19th Annual Meeting of ISMRM, Montreal, Quebec, Canada*, page 2927, 2011. (page 79, 139)

[249] L. I. Sacolick, F. Wiesinger, I. Hancu, and M. W. Vogel. B1 mapping by Bloch-Siegert shift. *Magnetic Resonance in Medicine*, 63(5):1315–1322, 2010. `doi:10.1002/mrm.22357`. (page 77, 79, 143, 147)

[250] M. Saranathan, M. M. Khalighi, G. H. Glover, P. Pandit, and B. K. Rutt. Efficient Bloch-Siegert B_1^+ mapping using spiral and echo-planar readouts. *Magnetic Resonance in Medicine*, 70(6):1669–1673, 2013. `doi:10.1002/mrm.24599`. (page 79, 139, 163)

[251] J. Savage and K. Chen. On multigrids for solving a class of improved total variation based staircasing reduction models. *Image Processing Based on Partial Differential Equations*, pages 69–94, 2007. `doi:10.1007/978-3-540-33267-1_5`. (page 97)

[252] J. F. Schenck. Health and physiological effects of human exposure to whole-body four-tesla magnetic fields during MRI. *Annals of the New York Academy of Sciences*, 649(1):285–301, 1992. `doi:10.1111/j.1749-6632.1992.tb49617.x`. (page 33)

[253] J. F. Schenck. The role of magnetic susceptibility in magnetic resonance imaging: MRI magnetic compatibility of the first and second kinds. *Medical Physics*, 23(6):815–850, 1996. `doi:10.1118/1.597854`. (page 32, 33, 36)

[254] M. Schlögl, M. Holler, K. Bredies, and R. Stollberger. A variational approach for coil-sensitivity estimation for undersampled phase-sensitive dynamic MRI reconstruction. In *Proceedings of the 23rd Annual Meeting of ISMRM, Toronto, Ontario, Canada*, page 3692, 2015. (page 107)

[255] M. Schlögl, M. Holler, A. Schwarzl, K. Bredies, and R. Stollberger. Infimal convolution of total generalized variation functionals for dynamic MRI. *Magnetic Resonance in Medicine*, 78:142–155, 2017. `doi:10.1002/mrm.26352`. (page 4, 109, 146)

[256] M. A. Schmidt and K. M. Fraser. Two-point Dixon fat–water separation: Improving reliability and accuracy in phase correction algorithms. *Journal of Magnetic Resonance Imaging*, 27(5):1122–1129, 2008. `doi:10.1002/jmri.21310`. (page 123)

[257] P. Schmitt, M. A. Griswold, P. M. Jakob, M. Kotas, V. Gulani, M. Flentje, and A. Haase. Inversion recovery TrueFISP: quantification of T1, T2, and spin density. *Magnetic Resonance in Medicine*, 51(4):661–667, 2004. `doi:10.1002/mrm.20058`. (page 3, 134, 135)

[258] E. Schneider and G. Glover. Rapid in vivo proton shimming. *Magnetic Resonance in Medicine*, 18(2):335–347, 1991. `doi:10.1002/mrm.1910180208`. (page 44, 61, 62, 121)

[259] K. Sekihara, S. Matsui, and H. Kohno. A new method of measuring static field distribution using modified Fourier NMR imaging. *Journal of Physics E: Scientific Instruments*, 18(3):224, 1985. `doi:10.1088/0022-3735/18/3/013`. (page 60)

[260] R. Sepponen, J. Sipponen, and J. Tanttu. A method for chemical shift imaging: demonstration of bone marrow involvement with proton chemical shift imaging. *Journal of Computer Assisted Tomography*, 8(4):585–587, 1984. `doi:10.1097/00004728-198408000-00001`. (page 119)

[261] K. Setsompop, Q. Fan, J. Stockmann, B. Bilgic, S. Huang, S. F. Cauley, A. Nummenmaa, F. Wang, Y. Rathi, T. Witzel, and L. L. Wald. High-resolution in vivo diffusion imaging of the human brain with generalized slice dithered enhanced resolution: Simultaneous multislice (gSlider-SMS). *Magnetic Resonance in Medicine*, 79(1):141–151, 2018. `doi:10.1002/mrm.26653`. (page 4)

[262] K. Setsompop, B. A. Gagoski, J. R. Polimeni, T. Witzel, V. J. Wedeen, and L. L. Wald. Blipped-controlled aliasing in parallel imaging for simultaneous multislice echo planar imaging with reduced g-factor penalty. *Magnetic Resonance in Medicine*, 67(5):1210–1224, 2012. `doi:10.1002/mrm.23097`. (page 4)

[263] C. E. Shannon. A mathematical theory of communication. *Bell System Technical Journal*, 27(3):379–423, 1948. `doi:10.1109/9780470544242.ch1`. (page 4, 86)

[264] C. E. Shannon. Communication in the presence of noise. *Proceedings of the IRE*, 37(1):10–21, 1949. `doi:10.1109/jrproc.1949.232969`. (page 4, 86)

[265] A. Sharma, S. Tadanki, M. Jankiewicz, and W. A. Grissom. Highly-accelerated Bloch-Siegert $|B_1^+|$ mapping using joint autocalibrated parallel image reconstruction. *Magnetic Resonance in Medicine*, 71(4):1470–1477, 2014. `doi:10.1002/mrm.24804`. (page 110, 139, 147, 161)

[266] S. D. Sharma, H. H. Hu, and K. S. Nayak. Accelerated water–fat imaging using restricted subspace field map estimation and compressed sensing. *Magnetic Resonance in Medicine*, 67(3):650–659, 2012. `doi:10.1002/mrm.23052`. (page 132)

[267] S. D. Sharma, H. H. Hu, and K. S. Nayak. Chemical shift encoded water–fat separation using parallel imaging and compressed sensing. *Magnetic Resonance in Medicine*, 69(2):456–466, 2013. `doi:10.1002/mrm.24270`. (page 132)

[268] D. Simunic, P. Wach, W. Renhart, and R. Stollberger. Spatial distribution of high-frequency electromagnetic energy in human head during MRI: numerical results and measurements. *IEEE Transactions on Biomedical Engineering*, 43(1):88, 1996. `doi:10.1109/10.477704`. (page 54)

[269] T. E. Skinner and G. H. Glover. An extended two-point Dixon algorithm for calculating separate water, fat, and B0 images. *Magnetic resonance in medicine*, 37(4):628–630, 1997. `doi:10.1002/mrm.1910370426`. (page 121)

[270] J. G. Sled and G. B. Pike. Correction for B1 and B0 variations in quantitative T2 measurements using MRI. *Magnetic Resonance in Medicine*, 43(4):589–593, 2000. `doi:10.1002/(sici)1522-2594(200004)43:4<589::aid-mrm14>3.0.co;2-2`. (page 65)

[271] D. S. Smith, J. Berglund, J. Kullberg, H. Ahlström, and B. E. Welch. Optimization of fat-water separation algorithm selection and options using image-based metrics with validation by ISMRM fat-water challenge datasets. In *Proceedings of the 21st Annual Meeting of ISMRM, Salt Lake City, Utah, USA*, page 2413, 2013. (page 183, 185, 186)

[272] N. Soda, T. Horii, and M. Kobayashi. Magnetometric demagnetizing factors for various shapes of rotational symmetry. *IEEE Transactions on Magnetics*, 45(12):5289–5295, 2009. `doi:10.1109/tmag.2009.2023117`. (page 36)

[273] D. K. Sodickson and W. J. Manning. Simultaneous acquisition of spatial harmonics (SMASH): fast imaging with radiofrequency coil arrays. *Magnetic Resonance in Medicine*, 38(4):591–603, 1997. `doi:10.1002/mrm.1910380414`. (page 90)

[274] M. Soellradl, A. Lesch, J. Strasser, L. Pirpamer, R. Stollberger, S. Ropele, and C. Langkammer. Assessment and correction of macroscopic field variations in 2D spoiled gradient-echo sequences. *Magnetic Resonance in Medicine*, 2019. `doi:10.1002/mrm.28139`. (page 136)

[275] M. Soellradl, J. Strasser, A. Lesch, R. Stollberger, S. Ropele, and C. Langkammer. Adaptive slice-specific z-shimming for 2D spoiled gradient-echo sequences. *Magnetic Resonance in Medicine*, 2020. (in press). (page 136)

[276] A. S. Soliman, J. Yuan, K. K. Vigen, J. A. White, T. M. Peters, and C. A. McKenzie. Max-IDEAL: a max-flow based approach for IDEAL water/fat separation. *Magnetic resonance in medicine*, 72(2):510–521, 2014. `doi:10.1002/mrm.24923`. (page 133, 176)

[277] A. S. Soliman, J. Yuan, J. A. White, T. M. Peters, and C. A. McKenzie. A convex relaxation approach to fat/water separation with minimum label description. In *International Conference on Medical Image Computing and Computer-Assisted Intervention*, pages 519–526. Springer, 2012. (page 133)

[278] S. M.-H. Song, S. Napel, N. J. Pelc, and G. H. Glover. Phase unwrapping of MR phase images using Poisson equation. *IEEE Transactions on Image Processing*, 4(5):667–676, 1995. `doi:10.1109/83.382500`. (page 61)

[279] S. M. Spann, K. S. Kazimierski, C. S. Aigner, M. Kraiger, K. Bredies, and R. Stollberger. Spatio-temporal TGV denoising for ASL perfusion imaging. *Neuroimage*, 157:81–96, 2017. `doi:10.1016/j.neuroimage.2017.05.054`. (page 99)

[280] S. M. Spann, X. Shao, D. J. Wang, C. S. Aigner, M. Schloegl, K. Bredies, and R. Stollberger. Robust single-shot acquisition of high resolution whole brain ASL images by combining time-dependent 2D CAPIRINHA sampling with spatio-temporal TGV reconstruction. *NeuroImage*, 206:116337, 2020. `doi:10.1016/j.neuroimage.2019.116337`. (page 99)

[281] S. M. Spann, C. S. Aigner, M. Schlögl, A. J. Lesch, K. Bredies, S. Roppele, D. Pinter, L. Pirpamer, and R. Stollberger. Acceleration of arterial spin labeling data using spatio-temporal total generalized variation (TGV) reconstruction. In *Proceedings of the 26th Annual Meeting of ISMRM, Paris, France*, 2018. (page)

[282] D. M. Spielman, E. Adalsteinsson, and K. O. Lim. Quantitative assessment of improved homogeneity using higher-order shims for spectroscopic imaging of the brain. *Magnetic Resonance in Medicine*, 40(3):376–382, 1998. `doi:10.1002/mrm.1910400307`. (page 43)

[283] J. P. Stockmann and L. L. Wald. In vivo B0 field shimming methods for MRI at 7 T. *Neuroimage*, 168:71–87, 2018. `doi:10.1016/j.neuroimage.2017.06.013`. (page 46)

[284] J. P. Stockmann, T. Witzel, B. Keil, J. R. Polimeni, A. Mareyam, C. LaPierre, K. Setsompop, and L. L. Wald. A 32-channel combined RF and B0 shim array for 3T brain imaging. *Magnetic Resonance in Medicine*, 75(1):441–451, 2016. `doi:10.1002/mrm.25587`. (page 46)

[285] R. Stollberger, P. Wach, G. McKinnon, E. Justich, and F. Ebner. RF-field mapping in vivo. In *Proceedings of the 7th Annual Meeting of SMRM, San Francisco, California, USA*, volume 3 (works-in-progress), page 106, 1988. (page 64, 65)

[286] R. Stollberger and P. Wach. Imaging of the active B1 field in vivo. *Magnetic Resonance in Medicine*, 35(2):246–251, 1996. `doi:10.1002/mrm.1910350217`. (page 65, 141)

[287] E. C. Stoner. XCVII. The demagnetizing factors for ellipsoids. *The London, Edinburgh, and Dublin Philosophical Magazine and Journal of Science*, 36(263):803–821, 1945. `doi:10.1080/14786444508521510`. (page 36)

[288] H. Sun, W. A. Grissom, and J. A. Fessler. Regularized estimation of Bloch-Siegert $|B_1^+|$ maps in MRI. In *IEEE International Conference on Image Processing (ICIP)*, pages 3646–3650. IEEE, 2014. (page 109)

[289] A. J. Surowiec, S. S. Stuchly, J. R. Barr, and A. Swarup. Dielectric properties of breast carcinoma and the surrounding tissues. *IEEE Transactions on Biomedical Engineering*, 35(4):257–263, 1988. `doi:10.1109/10.1374`. (page 51)

[290] J. Szumowsiu and D. Plewes. Fat suppression in the time domain in fast MR imaging. *Magnetic Resonance in Medicine*, 8(3):345–354, 1988. `doi:10.1002/mrm.1910080312`. (page 120)

[291] J. Szumowski, W. Coshow, F. Li, B. Coombs, and S. F. Quinn. Double-echo three-point-Dixon method for fat suppression MRI. *Magnetic Resonance in Medicine*, 34(1):120–124, 1995. `doi:10.1002/mrm.1910340118`. (page 120)

[292] J. Szumowski, W. R. Coshow, F. Li, and S. F. Quinn. Phase unwrapping in the three-point Dixon method for fat suppression MR imaging. *Radiology*, 192(2):555–561, 1994. `doi:10.1148/radiology.192.2.8029431`. (page 120)

[293] A. N. Tihonov. Solution of incorrectly formulated problems and the regularization method. *Soviet Mathematics*, 4:1035–1038, 1963. (page 92, 95, 97)

[294] T.-K. Truong, D. W. Chakeres, D. Q. Beversdorf, D. W. Scharre, and P. Schmalbrock. Effects of static and radiofrequency magnetic field inhomogeneity in ultra-high field magnetic resonance imaging. *Magnetic Resonance Imaging*, 24(2):103–112, 2006. `doi:10.1016/j.mri.2005.09.013`. (page 38)

[295] T.-K. Truong, B. D. Clymer, D. W. Chakeres, and P. Schmalbrock. Three-dimensional numerical simulations of susceptibility-induced magnetic field inhomogeneities in the human head. *Magnetic Resonance Imaging*, 20(10):759–770, 2002. `doi:10.1016/s0730-725x(02)00601-x`. (page 37)

[296] T.-K. Truong, D. Darnell, and A. W. Song. Integrated RF/shim coil array for parallel reception and localized B0 shimming in the human brain. *Neuroimage*, 103:235–240, 2014. `doi:10.1016/j.neuroimage.2014.09.052`. (page 46)

[297] J. Tsao and Y. Jiang. Hierarchical IDEAL: fast, robust, and multiresolution separation of multiple chemical species from multiple echo times. *Magnetic Resonance in Medicine*, 70(1):155–159, 2013. `doi:10.1002/mrm.24441`. (page 132, 185, 186)

[298] R. Turner and D. Le Bihan. Single-shot diffusion imaging at 2.0 Tesla. *Journal of Magnetic Resonance*, 86(3):445–452, 1990. `doi:10.1016/0022-2364(90)90023-3`. (page 1)

[299] M. Uecker. Parallel magnetic resonance imaging. *arXiv preprint arXiv:1501.06209*, 2015. (page 91)

[300] M. Uecker, T. Hohage, K. T. Block, and J. Frahm. Image reconstruction by regularized nonlinear inversion – joint estimation of coil sensitivities and image content. *Magnetic Resonance in Medicine*, 60(3):674–682, 2008. `doi:10.1002/mrm.21691`. (page 107, 109)

[301] M. Uecker, P. Lai, M. J. Murphy, P. Virtue, M. Elad, J. M. Pauly, S. S. Vasanawala, and M. Lustig. ESPIRiT–an eigenvalue approach to autocalibrating parallel MRI: where SENSE meets GRAPPA. *Magnetic Resonance in Medicine*, 71(3):990–1001, 2014. `doi:10.1002/mrm.24751`. (page 59, 91, 107)

[302] M. Uecker, F. Ong, J. I. Tamir, D. Bahri, P. Virtue, J. Y. Cheng, T. Zhang, and M. Lustig. Berkeley advanced reconstruction toolbox. In *Proceedings of the 23rd Annual Meeting of ISMRM, Toronto, Ontario, Canada*, page 2486, 2015. (page 146)

[303] J. Ulloa, P. Irarrazaval, and J. Hajnal. Exploring 3D RF shimming for slice selective imaging. In *Proceedings of the 13th Annual Meeting of ISMRM, Miami Beach, Florida, USA*, page 21, 2005. (page 3)

[304] T. Valkonen, K. Bredies, and F. Knoll. Total generalized variation in diffusion tensor imaging. *SIAM Journal on Imaging Sciences*, 6(1):487–525, 2013. `doi:10.1137/120867172`. (page 99)

[305] P.-F. Van de Moortele, C. Akgun, G. Adriany, S. Moeller, J. Ritter, C. M. Collins, M. B. Smith, J. T. Vaughan, and K. Uğurbil. B1 destructive interferences and spatial phase patterns at 7T with a head transceiver array coil. *Magnetic Resonance in Medicine*, 54(6):1503–1518, 2005. `doi:10.1002/mrm.20708`. (page 83)

[306] C. A. Van den Berg, B. Van den Bergen, J. B. Van de Kamer, B. W. Raaymakers, H. Kroeze, L. W. Bartels, and J. J. Lagendijk. Simultaneous B_1^+ homogenization and specific absorption rate hotspot suppression using a magnetic resonance phased array transmit coil. *Magnetic Resonance in Medicine*, 57(3):577–586, 2007. `doi:10.1002/mrm.21149`. (page 57)

[307] B. Van Den Bergen, C. A. Van den Berg, L. W. Bartels, and J. J. Lagendijk. 7 T body MRI: B1 shimming with simultaneous SAR reduction. *Physics in Medicine & Biology*, 52(17):5429, 2007. `doi:10.1088/0031-9155/52/17/022`. (page 57)

[308] P. Van Gelderen, J. De Zwart, P. Starewicz, R. Hinks, and J. Duyn. Real-time shimming to compensate for respiration-induced B0 fluctuations. *Magnetic Resonance in Medicine*, 57(2):362–368, 2007. `doi:10.1002/mrm.21136`. (page 45)

[309] A. L. Van Lier, D. O. Brunner, K. P. Pruessmann, D. W. Klomp, P. R. Luijten, J. J. Lagendijk, and C. A. van den Berg. B_1^+ phase mapping at 7T and its application for in vivo electrical conductivity mapping. *Magnetic Resonance in Medicine*, 67(2):552–561, 2012. `doi:10.1002/mrm.22995`. (page 81, 82)

[310] M. Walker, S. Souza, and C. Dumoulin. Quantitative flow measurement in phase contrast MR angiography. *Journal of Computer Assisted Tomography*, 12(2):304–313, 1988. `doi:10.1097/00004728-198803000-00021`. (page 2)

[311] D. O. Walsh, A. F. Gmitro, and M. W. Marcellin. Adaptive reconstruction of phased array MR imagery. *Magnetic Resonance in Medicine*, 43(5):682–690, May 2000. `doi:10.1002/(sici)1522-2594(200005)43:5<682::aid-mrm10>3.0.co;2-g`. (page 59, 89, 107, 146, 147)

[312] D. Wang, S. Zuehlsdorff, and A. C. Larson. Rapid 3D radiofrequency field mapping using catalyzed double-angle method. *NMR in Biomedicine*, 22(8):882–890, 2009. `doi:10.1002/nbm.1403`. (page 65)

[313] F. Wang, Z. Dong, T. G. Reese, B. Bilgic, M. Katherine Manhard, J. Chen, J. R. Polimeni, L. L. Wald, and K. Setsompop. Echo planar time-resolved imaging (EPTI). *Magnetic Resonance in Medicine*, 81(6):3599–3615, 2019. `doi:10.1002/mrm.27673`. (page 4)

[314] J. Wang, M. Qiu, and R. T. Constable. In vivo method for correcting transmit/receive nonuniformities with phased array coils. *Magnetic Resonance in Medicine*, 53(3):666–674, 2005. `doi:10.1002/mrm.20377`. (page 65)

[315] Y. Wang, D. Li, E. M. Haacke, and J. J. Brown. A three-point Dixon method for water and fat separation using 2D and 3D gradient-echo techniques. *Journal of Magnetic Resonance Imaging*, 8(3):703–710, 1998. `doi:10.1002/jmri.1880080329`. (page 122, 125)

[316] Y. Wang and T. Liu. Quantitative susceptibility mapping (QSM): decoding MRI data for a tissue magnetic biomarker. *Magnetic Resonance in Medicine*, 73(1):82–101, 2015. `doi:10.1002/mrm.25358`. (page 2, 37)

[317] P. Webb and A. Macovski. Rapid, fully automatic, arbitrary-volume in vivo shimming. *Magnetic Resonance in Medicine*, 20(1):113–122, 1991. `doi:10.1002/mrm.1910200112`. (page 44, 62)

[318] S. Weingärtner, F. Zimmer, G. J. Metzger, K. Uğurbil, P. F. van de Moortele, and M. Akçakaya. Motion-robust cardiac B_1^+ mapping at 3T using interleaved Bloch-Siegert shifts. *Magnetic Resonance in Medicine*, 78(2):670–677, 2017. `doi:10.1002/mrm.26395`. (page 81, 163)

[319] C. Westbrook. *MRI at a Glance*. John Wiley & Sons, 2016. (page 10)

[320] C. N. Wiens, C. M. McCurdy, J. D. Willig-Onwuachi, and C. A. McKenzie. R_2^*-corrected water–fat imaging using compressed sensing and parallel imaging. *Magnetic Resonance in Medicine*, 71(2):608–616, 2014. `doi:10.1002/mrm.24699`. (page 132)

[321] S. Williams, M. Horsfield, and L. Hall. True water and fat MR imaging with use of multiple-echo acquisition. *Radiology*, 173(1):249–253, 1989. `doi:10.1148/radiology.173.1.2781016`. (page 120)

[322] S. Witoszynskyj, A. Rauscher, J. R. Reichenbach, and M. Barth. Phase unwrapping of MR images using ΦUN–A fast and robust region growing algorithm. *Medical Image Analysis*, 13(2):257–268, 2009. `doi:10.1016/j.media.2008.10.004`. (page 61)

[323] S. Wright, A. G. Webb, S. Pittard, D. Klomp, R. Kimmlingen, R. De Graaf, C. Collins, B. Balcom, and W. Price. *Magnetic resonance technology: hardware and system component design*. Royal society of chemistry, 2016. (page 201)

[324] Q.-S. Xiang. Two-point water-fat imaging with partially-opposed-phase (POP) acquisition: an asymmetric dixon method. *Magnetic Resonance in Medicine*, 56(3):572–584, 2006. `doi:10.1002/mrm.20984`. (page 122)

[325] Q.-S. Xiang and L. An. Water-fat imaging with direct phase encoding. *Journal of Magnetic Resonance Imaging*, 7(6):1002–1015, 1997. `doi:10.1002/jmri.1880070612`. (page 122)

[326] W. Xu and I. Cumming. A region-growing algorithm for InSAR phase unwrapping. *IEEE Transactions on Geoscience and Remote Sensing*, 37(1):124–134, 1999. `doi:10.1109/igarss.1996.516883`. (page 61)

[327] V. L. Yarnykh. Actual flip-angle imaging in the pulsed steady state: a method for rapid three-dimensional mapping of the transmitted radiofrequency field. *Magnetic Resonance in Medicine*, 57(1):192–200, 2007. `doi:10.1002/mrm.21120`. (page 67)

[328] H. N. Yeung and D. W. Kormos. Separation of true fat and water images by correcting magnetic field inhomogeneity in situ. *Radiology*, 159(3):783–786, 1986. `doi:10.1148/radiology.159.3.3704157`. (page 120)

[329] L. Ying, Z.-P. Liang, D. C. Munson, R. Koetter, and B. J. Frey. Unwrapping of MR phase images using a Markov random field model. *IEEE Transactions on Medical Imaging*, 25(1):128–136, 2005. `doi:10.1109/tmi.2005.861021`. (page 61)

[330] I. Young, S. Khenia, D. Thomas, C. Davis, D. Gadian, I. Cox, B. Ross, and G. Bydder. Clinical magnetic susceptibility mapping of the brain. *Journal of Computer Assisted Tomography*, 11(1):2–6, 1987. `doi:10.1097/00004728-198701000-00002`. (page 2, 37)

[331] H. Yu, C. A. McKenzie, A. Shimakawa, A. T. Vu, A. C. Brau, P. J. Beatty, A. R. Pineda, J. H. Brittain, and S. B. Reeder. Multiecho reconstruction for simultaneous water-fat decomposition and T_2^* estimation. *Journal of Magnetic Resonance Imaging*, 26(4):1153–1161, 2007. `doi:10.1002/jmri.21090`. (page 118, 124, 181)

[332] H. Yu, S. B. Reeder, A. Shimakawa, J. H. Brittain, and N. J. Pelc. Field map estimation with a region growing scheme for iterative 3-point water-fat decomposition. *Magnetic Resonance in Medicine*, 54(4):1032–1039, 2005. `doi:10.1002/mrm.20654`. (page 124, 126, 131, 185, 186)

[333] H. Yu, S. B. Reeder, A. Shimakawa, C. A. McKenzie, and J. H. Brittain. Robust multipoint water-fat separation using fat likelihood analysis. *Magnetic Resonance in Medicine*, 67(4):1065–1076, 2012. `doi:10.1002/mrm.23087`. (page 132)

[334] H. Yu, A. Shimakawa, C. A. McKenzie, E. Brodsky, J. H. Brittain, and S. B. Reeder. Multiecho water-fat separation and simultaneous R_2^* estimation with multifrequency fat spectrum modeling. *Magnetic Resonance in Medicine*, 60(5):1122–1134, 2008. `doi:10.1002/mrm.21737`. (page 116, 117, 124)

[335] X. Zhang, S. Zhu, and B. He. Imaging electric properties of biological tissues by RF field mapping in MRI. *IEEE Transactions on Medical Imaging*, 29(2):474–481, 2010. `doi:10.1109/tmi.2009.2036843`. (page 51)

[336] F. Zhao, J. A. Fessler, S. M. Wright, and D. C. Noll. Regularized estimation of magnitude and phase of multi-coil B_1 field via Bloch–Siegert B_1 mapping and coil combination optimizations. *IEEE Transactions on Medical Imaging*, 33(10):2020–2030, 2014. `doi:10.1109/TMI.2014.2329751`. (page 82, 109, 139)

[337] Y. Zhu. Parallel excitation with an array of transmit coils. *Magnetic Resonance in Medicine*, 51(4):775–784, 2004. `doi:10.1002/mrm.20011`. (page 3, 57)

[338] Y. Zur, S. Stokar, and P. Bendel. An analysis of fast imaging sequences with steady-state transverse magnetization refocusing. *Magnetic Resonance in Medicine*, 6(2):175–193, 1988. `doi:10.1002/mrm.1910060206`. (page 3)